Electromagnetic field analysis in coils, used for high-field NMR experiments in HR-MAS probes.

Baudouin Dillmann

Université Louis Pasteur, Strasbourg

Institut de Chimie de Strasbourg **École doctorale de Chimie-Physique**

Analyse du champ électromagnétique, dans les bobines des sondes de HR-MAS utilisées pour la RMN à haut-champ

THÈSE

présentée et soutenue publiquement le 25 mai 2007

pour l'obtention du

Titre de Docteur Ingénieur de l'Université Louis Pasteur

(spécialité Chimie-Physique)

par

Baudouin Dillmann

Composition du jury

Président :	Pr. Daniel Canet (Université Henri Poincaré)
Rapporteurs :	Pr. Hervé Desvaux (Université d'Evry Val d'Essonne) Pr.Pierre Panissod (Institut de Physique Chimie des Materiaux de Strasbourg)
Examinateurs :	Dr. Martial Piotto (Directeur d'Applications, Bruker Wissembourg) Dr.Frank Engelke (Directeur BEENPK, Bruker Elektronik Karlsruhe)
Présents :	Dr. Jacques Laeuffer Pr. Bruno Kieffer
Directeur :	Dr. Karim El Bayed

Laboratoire de RMN et Biophysique des Membranes LC3-UMR7177

Mis en page avec la classe thloria.

A mes parents.

Table des matières

Part II

Fundamental concepts, derived from classical Electrodynamics, to be employed in Probe design. Engineering approach of $\mathbf{B}_1$ 19

2
Maxwell equations

3
Description of waveguides used in NMR probes

Introduction générale

La résonance magnétique nucléaire (RMN) est une technique d'analyse puissante d'une très grande polyvalence. Peu de spectroscopies peuvent en effet se prévaloir d'une gamme aussi riche d'applications. De l'imagerie médicale à l'analyse physico-chimique, le matériel étudié peut aller des gaz aux métaux, en passant par les polymères, les peptides en solution ou dans leur milieu membranaire. Ils peuvent être aussi des amalgames complexes tels que les tissus et cellules. Dans ce cas, le mélange de petites molécules dans une matrice anisotrope exige une technique très particulière : la rotation à l'angle magique (MAS), afin d'obtenir un spectre de haute-résolution (HR-MAS). C'est grâce à une approche électromagnétique et quantique que peut s'établir une compréhension approfondie de la nature du signal recueilli. L'expérience de RMN, en effet, nécessite la mise en oeuvre de deux champs magnétiques : le champ statique $\mathbf{B}_o$ qui peut être créé par des bobines supraconductrices, et un champ radio-fréquence (RF) appelé $\mathbf{B}_1$, de moindre intensité, qui est créé par la bobine dans la sonde de RMN (un exemple d'un tel circuit est donné par [154]). Le champ $\mathbf{B}_1$ irradie le volume de l'échantillon soumis à $\mathbf{B}_o$ et permet les transitions de rééquilibrage des moments cinétiques nucléaires, peuplant les états d'énergie quantique du spin observé. En général et idéalement, les bobines de RMN se doivent de satisfaire simultanément les conditions suivantes portant sur $\mathbf{B}_1$:

(i) Produire un maximum de champ RF dans une orientation qui est perpendiculaire au champ statique ($\mathbf{B}_o$).

(ii) Produire une distribution de champ aussi homogène que possible dans des échantillons qui peuvent être de nature très différente.

(iii) Atténuer autant que faire se peut les composantes du champ électrique indissociable du champ $\mathbf{B}_1$ à l'intérieur du volume occupé par l'échantillon et ainsi réduire le risque d'échauffement provoqué par la dispersion dans les milieux polarisés.

C'est pour cela qu'après une brève introduction de notre application spécifique de la RMN (partie I) nous aborderons certains concepts issus de la théorie classique de l'électromagnétisme (partie II) qui nous semblent nécessaires afin de mieux décrire l'impact de l'inhomogénéité du champ $\mathbf{B}_1$ sur le signal RMN (partie III). Ensuite nous avons examiné

les effets d'échaufement qui s'opposent a la réciprocité et peuvent compromettre des experiences de RMN (partie IV). Finallement (partie V) nous introduirons un résonateur innovant qui ameillore l'homogénéité du champ $\mathbf{B}_1$ et reduit le champ électrique $\mathbf{E}_1$.

***

Notre intérêt pour la cartographie du champ RF dans les bobines des sondes HR-MAS a commencé en 2001, à partir de résultats surprenants obtenus après application d'une séquence dite TOCSY couramment utilisée sur une série d'échantillons étudiés par HR-MAS. En effet, une même séquence donne un signal d'intensité amoindrie et de phase décalée à certaines fréquences de rotation mécanique bien précises et toujours en relation avec l'intensité du champ magnétique $\mathbf{B}_1$ [48]. Après une étude approfondie mêlant une connaissance de la distribution de champ magnétique et une description de l'évolution de la Matrice Densité (équation de Liouville-von Neumann), il s'est avéré que l'origine du problème est l'interférence entre l'évolution spatiale d'un noyau de spin 1/2 dans son mouvement de rotation à l'intérieur de la bobine, et la séquence d'impulsions elle-même. Par ailleurs le même type d'observation fut reproduite en changeant les conditions expérimentales, comme par exemple :

(i) le type de séquence TOCSY d'abord, puis de type COSY ($90^o{}_x$-délai-$90^o{}_{-x}$-acquisition), ensuite. Plus tard ce type de phénomène fut aussi observé dans le cas d'une expérience de nutation, telle qu'elle peut être utilisée dans presque tous les laboratoires pour évaluer l'amplitude et l'homogénéité du champ RF ;

(ii) des échantillons de nature différente furent utilisés, aussi bien solides que liquides. Ce même effet est reproductible à partir du moment ou les noyaux se déplacent à la même vitesse angulaire autour du centre de la bobine ;

(iii) enfin différentes variantes de bobines RF furent utilisées pour s'affranchir d'un artéfact qui serait propre à un solénoïde particulier.

Ainsi une généralisation à toutes les bobines de géométrie hélicoïdale fut possible. Il a été établi, qu'au cours de sa période de révolution à l'intérieur du rotor, l'échantillon est amené dans des régions de champs $\mathbf{B}_1$ distincts, du fait de la distribution inhomogène de celui-ci dans le plan transverse. En effet, par définition geométrique, une hélice ne possède pas d'axe de symétrie autour duquel le champ serait identique. Cette inhomogénéité 'périodique' donne lieu à une modulation dans l'évolution de l'observable qui décrit la valeur moyenne de l'aimantation, telle qu'elle est détectée par RMN. Des calculs basés sur la résolution de l'équation maîtresse de l'évolution de l'opérateur densité ont permis de reproduire les résultats observés expérimentalement.

Dans la troisième partie ces recherches sont menées de l'avant en introduisant une description simplifiée du champ radial applicable à toute bobine de géométrie hélicoïdale, dans un circuit bien équilibré. Ces modèles de distribution du champ $\mathbf{B}_1$ ont été validés par la résolution aussi bien analytique que numérique des équations de Maxwell à la fois pour des bobines régulières, des solénoïdes à pas progressif et des bobines enroulées à partir d'une spirale. Il est important de signaler qu'aucune explication satisfaisante du point de vue de l'électromagnétisme n'avait été proposée. Depuis, des effets semblables ont été rapportés par d'autres équipes.

En RMN l'impact de la composante électrique du champ RF ($\mathbf{E}_1$) sur les échantillons dispersifs, est particulièrement interessante à haute-fréquence. Il y a au moins quatre effets observables qui sont causés par la conductivité de l'échantillon :

(i) celui-ci représente l'introduction d'un élément dispersif dans le schéma électrique de la sonde. Il en résulte donc une grande influence sur la fréquence de résonance, celle-ci étant fortement decalée vers le bas par l'introduction d'un rotor contenant un tel échantillon. Celui-ci est l'élément le plus fortement couplé au champ électrique de la bobine. La conséquence de ce premier effet est que, pour une bobine classique, il convient d'élargir vers le haut la gamme d'accord pour toutes les voies d'une sonde (la voie ^{1}H en particulier), pour leur permettre de 'rattraper' la perturbation produite par cette influence du champ électrique sur l'échantillon ;

(ii) la présence d'un milieu dispersifs dégrade fortement le facteur de qualité (Q) des voies d'irradiation et par conséquent dégrade aussi la sensibilité de la mesure, quantifiable en termes de rapport signal-sur-bruit ;

(iii) si des échantillons dispersifs sont introduits dans un champ RF, le profil de la distribution de celui-ci sera sensiblement modifié, et cela en contribuant à augmenter les effets produits par l'inhomogénéité $\mathbf{B}_1$;

(iv) les pertes dont l'origine est la polarisabilité de l'échantillon, se traduisent toujours en dissipation énergétique par effet joule, et donc par un échauffement de l'échantillon conduisant rapidement à sa dénaturation.

L'établissement de cet effet indésirable au champ électrique pour un échantillon visqueux a pu être observé directement par RMN dans une expérience décrite sur des Bicelles [36]. Ce problème, qui a été pris en compte dès les débuts de la RMN, a connu récemment un regain d'intérêt, en particulier dans les applications biologiques. L'étude des Biopsies à haut-champ (dès 500MHz) est confronté à des élévations de température qui ne sont pas encore maîtrisées. La quatrième partie introduit donc quelques-uns des mécanismes d'échauffement, que ce soit à cause de la vitesse de rotation, avec propagation de la chaleur

par convection, ou par irradiation à cause du champ $\mathbf{E}_1$.

Ainsi, les efforts faits pour trouver une bobine à faible inhomogénéité $\mathbf{B}_1$ et donc au champ $\mathbf{E}_1$ réduit se trouvent justifiés par l'étude de l'impact d'une élévation de la température sur l'échantillon. C'est pourquoi, dans cette dernière partie de notre étude, est introduit un nouveau type de bobine hélicoïdale appelée *Z-Coil* ([152]). Ce résonateur fait partie de la famille des hélices. Il peut se substituer au solénoïde dans le même circuit d'accord. Pour éloigner le champ électrique du centre de l'échantillon, l'usage de spirales qui contiennent celui-là dans le plan radial, est tout à fait adapté. Au centre, un cylindre fendu accumule le champ magnétique alors plus homogène et réduit l'échauffement des échantillons conducteurs ; enfin ces propriétés remarquables seront présentées dans la cinquième partie, grâce à une étude comparative realisée sur plusieurs bobines dans un même circuit.

***

Cette thèse, qui a débutée par une problématique liée à l'inhomogeneité du champ magnétique, se conclu sur l'invention d'un résonateur à faible champ électrique. En cherchant à comprendre le profil du champ $\mathbf{B}_1$ nous en sommes venus à essayer de trouver un résonateur qui diminuerait l'inhomogeneité transversale. L'intérêt d'un tel effort à été, finalement, de pouvoir ainsi obtenir une réduction du champ électrique à l'intérieur du volume occupé par l'échantillon. Mais cette démarche prouve aussi que, dans une onde électromagnétique, les composantes électriques et magnétiques ne sont pas indépendantes les unes des autres. D'une part elles sont gérés par les équations de Maxwell ; d'autre part, la géométrie de la bobine ou du résonateur, ainsi que le circuit et le positionnement de l'échantillon (sa localisation et son extension dans la bobine) sont autant de 'conditions aux limites' dont il faut prêter attention. Dans la dernière partie l'étude détaillée d'un résonateur à faible champ électrique montre que, le fait d'aller vers une symétrie du champ électromagnétique est une condition nécessaire pour réduire l'échauffement. En poussant ce raisonnement jusqu'au bout, on pourrait dire qu'un résonateur dont l'axe principal serait aussi axe de symétrie (comme par exemple un cylindre fermé), ne donnerait certes plus de champ électrique, mais malheureusement il ne pourrait pas non plus fournir de composante magnétique $\mathbf{B}_1$. On comprend ce compromis qui est fondé sur la première équation de Maxwell (Maxwell-Ampère) et qui peut se formuler de la façon suivante : *toute amélioration de l'homogénéité spatiale du champ magnétique RF dans le volume de l'échantillon implique une diminution de la quantité d'énergie électrique accumulée dans celui-ci.*

Part I
Hardware aspects of the High Resolution Magic Angle Spinning Spectroscopy : coils and rotors

1

General principles of HR-MAS experiments

HR-MAS experiments are usually performed on standard liquid-state NMR spectrometers equipped with a dedicated HR-MAS probe that allows to spin the sample at the magic angle. Likewise, the gradient coil generates a gradient field strength similar to what is found on a liquid state probe (ie. $50\,G.cm^{-1}$). HR-MAS probes are not designed to run cross-polarization, nonwithstanding certain CP-MAS probes can be employed to perform HR-MAS-like experiments. The shape of the sample and the sample container itself (MAS rotor) are designed to minimize the effect of the different sources of $\mathbf{B}_o$ field inhomogeneities in order to obtain an intrinsic linewidth similar to the one obtained on standard liquid high resolution probes. In the following sections, some general considerations concerning the design of HR-MAS probes will be presented starting from the most important : the RF coil.

1.1 RF Solenoidal coils

Helices and solenoids are synonyms for a passive structure commonly employed in electronics called "inductances" : two-port elements with positive imaginary complex impedance. Inductors find their place together with capacitors in any oscillating circuit for analog electric designs. These structures, exhibiting a particular symmetry, are used as delay lines in travelling wave tubes [129] or as filters [144] for radio-frequency electronics applications. As a mere example, they are present in nowadays mobile phone technologies, as antenna components. A significant number of publications exist for the various models and fields of applications for solenoidal coil structures. For the early work the reader is referred to the review of reference [121], while some of the more recent research literature relevant for magnetic resonance can be found in reference [49].

The use of inductors is the most common way of generating magnetic fields, as they allow maximum current density. Solenoidal coils have been used to generate the radio-frequency field $\mathbf{B}_1$ since the beginning of NMR in the late 1940's. It is reported in the experiments of Purcell and Torrey (see the review of Soutif and Gabillard [5]) that 1 microhenry inductors were used to produce a RF field at 30 MHz for ^{1}H resonance frequency. Nowadays only a few tens of a nanohenry are required to generate fields at 900 MHz. The principle of reciprocity, formulated for NMR by Hoult [74], was presented first by the use of solenoidal coils. It was shown that, in principle, such coils possess a performance significantly higher than Helmholtz coils (saddle coils) in terms of achievable signal-to-noise ratio, provided that the same cylindrical dimensions are applied. In the 1970's, the development of cross polarization, magic angle spinning and proton high-power decoupling techniques led to the development of multi-tuned single-coil NMR probes for solid-state NMR. Double-resonance MAS probes and probes suitable for ^{1}H CRAMPS experiments emerged, homebuilt as well as commercially available, and became a standard instrumentation in solid-state NMR spectroscopy [27, 131, 55, 107, 106, 101, 9, 59]. It was not until the end of the 1980's with the invention of REDOR techniques [67, 69], that the necessity arose to have access to single-coil triple-resonance MAS probes - and here, again, the versatility of solenoidal coils represented an obvious and efficient technical solution for these solid-state NMR MAS probes. An alternative idea to find a technically efficient solution to fulfill the different requirements for circuits and coils for widely differing frequencies (e.g., for ^{1}H and ^{13}C) was pursued by Doty [42, 44]. He departed from the strategy of a multiply tuned single coil and used instead a dedicated resonator structure for the high-frequency channel and a solenoidal coil for the low frequencies in his HR-MAS probe. Since the 1980's RF homogeneity of coils was given increased attention. One approach to increase the RF homogeneity of the solenoidal coil was to vary the pitch angle of the solenoidal windings or the width of the coil wire [76, 133, 115]. Leifer [89] proposed an inverse strategy to optimize homogeneity of the RF field in 6 and 10 turn coils with diameters larger than 10 mm operating at frequencies of 85 and 21 MHz, respectively. By using Chebyshev polynomials to describe the field, he uses an inverse technique proposed by Turner [138] to derive the current distribution that generates the desired field and, in turn, from the current distribution the positioning of the nonequidistant windings can be derived. Sun and Maciel [133] have proposed and built an RF coil for MAS probes where the plane of each coil turn is tilted such that the amplitude of the transverse RF field is increased while the coil axis is oriented at the magic angle. They claimed, that for such a coil the signal-to-noise ratio could be improved by 17% compared to a standard solenoidal coil oriented along the MAS axis. Apart from the detailed coil geometry,

electrical balance of the coil is another important point to achieve good homogeneity of the RF magnetic field inside the coil, high sensitivity of the probe circuits as well as a minimum coupling of electric fields to the sample dielectric. Electrical balance means, that at a given frequency the two ports of a solenoidal coil are connected to a circuit that provides equal complex impedance to each port such that the reflection factors on both ports are equal to each other and a symmetric standing wave appears with the oscillating maximum RF magnetic field in the coil center. In early spectrometer designs, where the transmitter and/or preamplifier were usually integrated much closer to the oscillator circuit that made up the probe, symmetric operation of both was much more common (see, e.g., [103, 28, 21]). In order to reduce losses in biological samples having relatively high conductivity caused by the presence of the RF electric field of coils implanted in biological tissues, Murphy-Boesch and Koretzky [108] apply symmetrization or balancing of the coil using additional capacitors in a single-resonance circuit. As a result they demonstrate a significantly increased Q factor of the probe circuit and a drastic increase of signal-to-noise ratio of ^{31}P spectra at 97 MHz. Decorps et al. [31] have shown that well balanced circuits can be achieved as well by inductive coupling of the NMR coil to the RF circuit. The key point for these two applications is that balancing leads to a minimization of the electric RF fields inside the coil and therefore dielectric and conductive losses appearing in the NMR sample can be aleviated. Another case where a balanced circuit is advantageous is when the NMR coil has to be matched to the transmission line connecting the coil to a liquid nitrogen cooled preamplifier. This set-up was studied by Conradi and Edwards [22] in their low-temperature probe with the goal to minimize Johnson noise originating from line losses. Finally, as mentioned above, a balanced coil possesses a well defined location where the electrical field is minimum and the voltage to ground is equal to zero. This cold point can be used to tap the coil, for example, with a shield whose purpose is to remove stray fields from the coil [32]. Solenoidal coils have been used as RF coils in NMR probes dedicated for small samples with volumina in the range of a few microliters and for sub-microliter samples as well [145, 104, 105]. The main advantage of these micro-solenoidal coils with sub-mm diameters is that they provide high filling factors and therefore allow a relatively high signal-to-noise ratio per volume unit for small NMR samples. A common characteristic for solenoidal coils of sub-mm diameter for microliter samples as well as for solenoidal coils in the mm range of diameter applied as RF coils in HR-MAS probes consists in the fact that their presence leads to a perturbation of the homogeneous static field, since (a) usually the magnetic susceptibility of the coil materials is different from the magnetic susceptibility of their environment and (b) these coils do not represent cylinders with homogeneous walls and are not aligned with their main axis along. Technical solu-

tions to minimize the resulting field distortions will be discussed in the following sections, but before we will focus on the sample inside the rotor.

1.2 The sample container : The 4 mm rotor

The rotor is an essential component of the hardware used to run HR-MAS experiments. Due to the strong centrifugal forces that exert themselves on the walls of the rotor at high spinning speeds, the rotor has to be extremely resistant. For that reason the material of choice is usually ZrO_2 ceramics. In order to optimize the sensitivity of the probe, the rotor can be designed with an inner volume that matches the detection volume of the solenoidal coil. This experimental set-up allows to detect all the material contained in the rotor. The signal to noise ratio also (SNR) will depend on the amount of material involved. Good sample positionning in the rotor is an important pre-requisite for (1) collecting the best homogeneous magnetic field, (2) avoiding air-bubbles that would spoil the mechanical equilibrium [1] and finally (3) preventing part of the sample to be denatured through heating produced by electric fields at the ends of the coil.

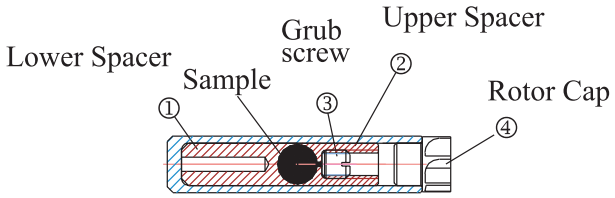

FIG. 1.1 – *Description of the different parts required to pack the sample in a 4 mm Rotor used for HR-MAS experiments. Bottom Spacer (1), Upper Spacer (2), Grub screw (3) and Rotor Cap (4) are engineered to reduce the perturbation of both* $\mathbf{B}_o$ *and* $\mathbf{B}_1$ *field. The sample remains the most critical part.At the time beeing HR-MAS rotors (both 12* μl *and 50* μl*) do not have a bottom spacer but a massive* ZrO_2 *bottom. See Fig. 1.3.*

Since the detection volume is unfortunately smaller than the total volume of the rotor, sample restriction is required de facto [16]. To know the position of the samples and their volumes, is a prerequisite for a good HR-MAS experiment.

The Fig.1.2 shows a rotor for 4 mm stators, used for samples with up to 50 μl volume. The left side denotes the bottom of the rotor and the right side represents the top where the sample is to be inserted, followed by a Teflon plug to restrict the sample volume. The axial extend of the coil is refered from the bottom part at the left side. This has been measured in the case of a 5-turns coil, made out of flat wire, at the upper part of the coil,

[1] Piotto and al. [112] have clearly shown that the resolution of the HR-MAS spectrum is not affected by the air bubbles present in the sample

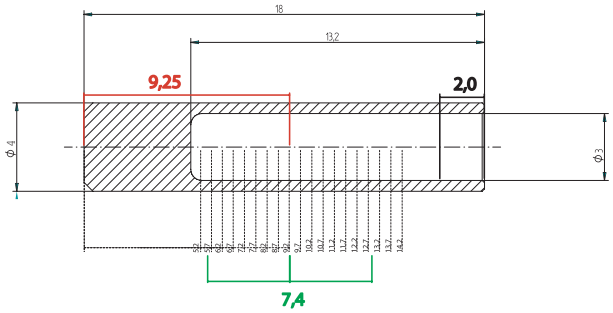

FIG. 1.2 – *Rotor 4 mm positioned in a coil holder, used in this work.*

opposed to the coil leads. There is a mark in red to signalize the middle of any 4 mm coil from the bottom of the rotor. The 2 mm height, represented at the right end, corresponds to the absolute minimum volume that must be keept free in order to allow the insertion of the cap(3 mm are required for safety in Fig. 1.3). The cilindrical rotor and the coil around him are positionned as described by Fig. 1.5.

Two different types of inserts are often employed, we present here two : a 50 μl that fits the detection volume of the coil (Fig.1.2 without the upper Teflon plug) and a 12 μl spherical sample that allows to position a smaller quantity at the magnetic center of the coil (9.5 mm from the bottom). The inserts for 15 μl were originaly made out of teflon as shown in Fig.1.1, with the disagreement of sacrifiing the bottom plug each time. This has changed since, the new 4 mm rotors are of different types as presented in Fig. 1.3, and the bottom is filled up with $Zr0_2$ with a better mechanical and electromagnetic behavior. The inner sample can occupy a diameter of maximum 3 mm in these configurations, other rotors can be provided with thicker walls in order to reduce the centrifugal force, in such case the sample is restricted in the radial dimension (2 mm).

In the following two sections we will see that the magnetic perturbation affecting the ultimate resolution of a HR-MAS spectra can be divided in two different categories : perturbations external to the rotor system (macroscopic) and perturbations originating from the rotor system (microscopic). The main differences between these two sources of perturbation is that the former is not modulated by MAS while the later is averaged out to zero by MAS.

1.3 Macroscopic susceptibility differences

The experimental set-up of a MAS experiment consists of a sample in a ceramic rotor placed inside a solenoid coil. The solenoid itself is embedded inside a ceramic stator. Placed in the static magnetic field $\mathbf{B}_o$ the coil assembly is unfortunately not transparent

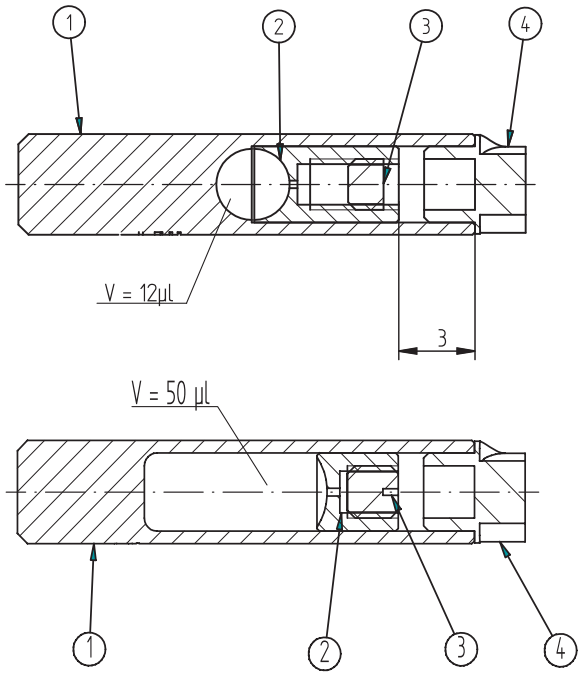

FIG. 1.3 – *Rotor 4 mm used for HR-MAS experiments, and inserts employed for an ellipsoidal sample.*

to the magnetic flux lines. The magnetic field discontinuities present at the surface of the different parts of the MAS set-up may result in a severe line broadening of the spectra. In order to alleviate this problem, the following strategy is employed : First, the magnetic susceptibility (χ_m defined in the next chapter by Eq. 2.10) jumps are reduced during probe construction by susceptibility compensation or by susceptibility matching of the different elements of the probe. Secondly, the residual weak magnetic susceptibility jumps are shimmed out using dedicated shim coils.

1.3.1 Susceptibility compensation

The material in HR probes should not exceed 3 ppm in susceptibility when disposed close to the samples [41]. Since the coil wires are less that 0.5 mm far from the rotor wall, susceptibility compensation is required. This technique consists of adapting the coil susceptibility to the local environment in order to cancel the discontinuity of the magnetic permeability. The most popular material used to produce NMR coils is the copper-clad based wire[2] [42], eventually platted with a golden alloy to increase the conductivity and compensate the weak susceptibility of the copper. The quality of this technique can be

[2]Copper has a magnetic susceptibility χ_m of -9.6 ppm, we refer to the tables given by Doty for different compounds such as metals, dielectrics and solvents

evaluated by the half line width of the ^{13}C in adamantane samples which should not exceed 5 Hz. Surface coating is intended to allow susceptibility compensation. Zelaya's experimental article [155] on Rh-plated copper cylinders proves, experimentally and theoretically, that for a defined coating surface the additional magnetization introduced by the copper is totally compensated adding a certain layer of rhodium.

1.3.2 Susceptibility matching

According to electromagnetic field theory [145, 155], a perfectly uniform and infinitely long hollow cylinder arranged perpendicular to a static magnetic field will give a perfectly uniform, albeit reduced in magnitude, magnetic field inside the cylinder. Compensation or matching techniques make it possible to neglect the demagnetization field produced in the coil due to susceptibility jumps. The case of MAS requires to consider finite length for the rotors and Barbara [8] has proved that the modulation of the demagnetization fields, perturbing the $\mathbf{B}_o$ homogeneity, is around 5 times greater at the rotors edges than at the center of the rotor. Through graphical representation of the magnetic fields lines obtained by numerically solving the Laplace equation of the magnetic scalar potential [78], Kuchel et al. [84] shows that the best suited geometries are infinitely long cylinders aligned parallel to the magnetic field $\mathbf{B}_o$. In the practice of HRNMR matching plugs are used to enlarge the apparent longitudinal dimension of a sample (Shigemi and Doty are references among others for these products). Kubo et al. [83] have proved that the shape of the sample, has a direct influence on the number of sidebands in NMR : a prolate like sample within a length to diameter ratio of 12 : 1 will show almost no side bands, and same rotation frequency an oblate like sample with geometric ratio equal to 0.8 : 1 will exhibit almost 20 satellites.

1.3.3 Shimming gradients

Proper shimming will reduce the discontinuities produced by the presence of any body in the vicinity of the rotor. Shimming a sample spinning at the magic angle requires to create gradients in the tilted frame along the MAS axis [50]. The standard shim system found on most high resolution NMR instruments can be used to correct the shims of a HR-MAS probe along the MAS axis to third order [128]. For a HR-MAS probe with a stator along the x axis, the zonal shims along the MAS axis $B_{Z^1}^{MAS}$, $B_{Z^2}^{MAS}$ and $B_{Z^3}^{MAS}$ are related to the laboratory frame shims by the following relations :

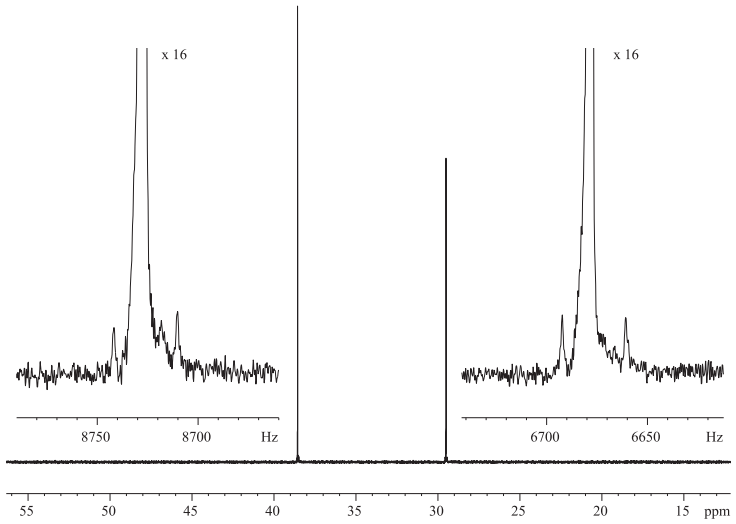

FIG. 1.4 – *^{13}C resolution and lineshape of a 31.8 mg sample of adamantane. Spinning speed at 5 kHz. ^{13}C RF field amplitude during CP of 83 kHz, is followed by a ^{1}H decoupling at ∼30 kHz during 800 ms. The probe used was a 900 MHz H/C/N SB BL3.2 with a Macor stator. Linewidth at 50% : less than 2.0 Hz; at 10% : less than 8 Hz; at 5%, 13 Hz.*

$$\begin{aligned} B_{Z^1}^{MAS} &= \frac{1}{\sqrt{3}} B_{Z^1}^{LAB} - \sqrt{\frac{2}{3}} B_X^{LAB} \\ B_{Z^2}^{MAS} &= B_{(X^2-Y^2)}^{LAB} - 2\sqrt{2} B_{ZX}^{LAB} \\ B_{Z^3}^{MAS} &= -\frac{2}{3\sqrt{3}} B_{Z^3}^{LAB} - \frac{1}{\sqrt{6}} B_{Z^2X}^{LAB} + \frac{5}{\sqrt{3}} B_{Z(X^2-Y^2)}^{LAB} - \frac{5}{3\sqrt{6}} B_{X^3}^{LAB} \end{aligned} \tag{1.1}$$

The set of shims described in Eq.1.1 is sufficient to shim a well designed HR-MAS probe [112].

Here we present a good shimming setup that can be obtained from the ^{13}C signal of adamantane. This technique is in principle far better than using the lock of deuterated water, due to the strong thermal gradients present during the mechanical rotation. The figure 1.4, obtained at 900 MHz shows two different carbon peaks, present in adamantane, and the corresponding satellites. The scalar coupling of two adjacent Carbons ^{13}C (1% in natural abundance) can be observed after 16 scans ($J \sim 30$Hz). Background signals from

the probe circuit itself are avoided [3]. As presented by Fig.1.4, spinning at the magic angle is of primary importance for the averaging of microscopic inhomogeneites.

1.4 Microscopic susceptibility differences under MAS

1.4.1 General considerations on the averaging on magnetic susceptibilities differences under MAS

As it was mentioned in the introduction, the averaging of magnetic susceptibility differences by MAS is an essential aspect of HR-MAS spectroscopy. In this section, we evaluate the static magnetic field seen by a spin in a medium consisting of a magnetic susceptibilities distribution. If the differences in magnetic susceptibilities are reasonably small and, if they are isotropic, the additional magnetic field created by a volume element of magnetization $\vec{\mathcal{M}}_j$ of coordinates $\mathbf{r}_j = (r_j, \theta_j, \phi_j)$ at a point $\mathbf{r}_i = (r_i, \theta_i, \phi_i)$ can be treated as a dipolar interaction. In the laboratory frame and for static samples, this dipolar field is given by [93, 90] :

$$\mathbf{B}\left(r_i, \theta_i, \phi_i\right) = \frac{\mu_o}{4\pi} . \sum_j \frac{\vec{\mathcal{M}}_j}{r_{ij}^3} \frac{\left(3\cos^2(\theta_{ij}) - 1\right)}{2} \tag{1.2}$$

Where r_{ij} is the distance between the points $\mathbf{r_i}$ and $\mathbf{r_j}$,θ_{ij} is the angle between $\mathbf{B}_o$ and the vector joining $\mathbf{r_i}$ to $\mathbf{r_j}$, and the summation expresses the fact that point $\mathbf{r_i}$ experiences the sum of all the different magnetic dipoles $\vec{\mathcal{M}}_j$ in its vicinity.

When the sample is rotated at an angle β respect to the main magnetic field $\mathbf{B}_o$ at a speed ω_r, Eq.1.2 can be rewritten as in [4] :

$$\begin{aligned} \mathbf{B}\left(r_i, \theta_i, \phi_i; t\right) &= \frac{\mu_o}{4\pi} . \sum_j \frac{\vec{\mathcal{M}}_j}{r_{ij}^3} \Big[\frac{1}{4} (3\cos^2\beta - 1)(3\cos^2\beta_{ij}^d - 1) \\ &+ \frac{3}{4} \sin 2\beta \, \sin 2\beta_{ij}^d \, \cos(\omega_r t + \phi_{ij}) \\ &+ \frac{3}{4} \sin^2\beta \, \sin^2\beta_{ij}^d \, \cos(2\omega_r t + 2\phi_{ij}) \Big] \end{aligned} \tag{1.3}$$

Where β_{ij}^d is the angle between the vector joining $\mathbf{r_i}$ to $\mathbf{r_j}$ and the axis of rotation of the sample and ϕ_{ij} is a phase factor describing the angular position of $\mathbf{r_i}$. If β is set to the

[3] MAS probes based on transmission line (TL) circuits, permit remote tunning and matching, and help to eliminate spurious probe signals. The adventage of the TL design [154], is that it removes lumped elements, as chip-capacitors which may produce succeptibility jumps close to the stator, as discussed previously.

magic angle (54.7^o) in Eq.1.3, the term $3(\cos^2\beta - 1)$ vanishes and only two time-dependent terms modulated in ω_r and $2\omega_r$ remain. These two terms lead to spinning side bands at frequencies ω_r and $2\omega_r$ with respect to the main peak. Under magic angle rotation, the contribution of $\mathbf{B}\left(r_i, \theta_i, \phi_i; t\right)$, and consequently of volume elements of different magnetic susceptibilities, to the width of the NMR resonance vanishes and only spinning side bands remain in the spectrum. The fact that inhomogeneous bulk magnetic susceptibility can be efficiently removed by MAS was demonstrated both experimentally and theoretically by Doskocilova [38], VanderHart [142], and Garroway [62] in the case of liquids and solids with random orientation.More recently, Barbara [6] used arguments based on electromagnetic calculations to explain this averaging process of MAS. However, the magnetic susceptibility χ_m is not always purely isotropic [142, 141, 30] and a substantial amount of anisotropy can be present in the sample. The magnetic susceptibility χ_m is no longer a scalar and must be described by a tensor. As an example, consider the well known anisotropy of the benzene ring. In the presence of a magnetic field, the intensity of the ring currents of the benzene ring depends on the orientation of the ring with respect to $\mathbf{B}_o$. This implies that the intensity of the magnetic dipole $\mathbf{M}$ of the aromatic ring depends on its orientation with respect to $\mathbf{B}_o$. During the MAS averaging process, the magnitude of $\mathbf{M}$ will vary and will interfere with the quality of the averaging process. This time-dependence of $\mathbf{M}$ during sample rotation has important consequences, as it can be shown that MAS can only average out the isotropic (scalar) part of the *chemical shift dispersion* tensor, but not the anisotropic part [141]. In the case of a sample like a peptide bound to a polystyrene-based Wang resin with a large amount of heterogeneity, the chemical environment of each peptide molecule will be unique : The number, the distance and the orientation of the neighboring aromatic molecules will be different for each peptide molecule. As previously seen, the magnetic dipole created locally by all these phenyl rings cannot be completely averaged out to zero by MAS. The combination of these two effects will result in a broad NMR line made of a superposition of different chemical shifts (inhomogeneous broadening). These considerations are extremely important for HR-MAS when considering the nature of a Wang resin which is made essentially of highly anisotropic cross-linked aromatic groups. The diffusion processes can modify the trajectory of spins and therefore interfere in an incoherent way with the rotation [120]. These additional complications will not be considered here.

1.4.2 Averaging of magnetic susceptibilities present at the sample-rotor interfaces under MAS

The previous section explains how MAS efficiently removes the line broadening due to magnetic susceptibility gradients present inside heterogeneous systems. MAS plays also a very important role in averaging out magnetic susceptibility gradients present at the sample-rotor interface. A typical HR-MAS arrangement is such that the whole sample is contained within the detection volume of the solenoid coil. In some cases, the sample is confined inside a 15 μl volume of a 4 mm rotor (Fig.1.1). This is a remarkable feature since this experimental set-up allows the whole sample to be detected and allows for the highest sensitivity. Under these experimental conditions, magnetic susceptibility jumps exist at the sample-rotor interface along the long axis of the rotor and at the top and bottom of the sample. Typically, this interfaces are between a solvent containing heterogeneous substances and the rotor material (ZrO_2 and Teflon for the insert). On a static sample, these magnetic susceptibility jumps give rise to important magnetic field gradients which are uncorrectable with the shim system of the spectrometer. MAS has the very unique property of being also able to average out these magnetic susceptibility to zero. This property can be explained using arguments similar to those developed in section 1.4.1. The consequence is that the rotor material which is the source of the magnetic perturbations is rotating at the same time as the sample and its effect on the sample vanishes. This very important property of MAS explains why the shim of HR-MAS is almost sample and solvent independent provided that the rotor is always at the same position in the probe and that the volume detected is always the same. One set of shims is sufficient for all the solvents used in HR-MAS. It is important to note that perturbations external to the rotor, and therefore not rotating at the magic angle, will not be averaged out by MAS and will have to be corrected by the shim system. This is true, as mere example, for a capacitor placed in the neighborhood of the sample. Its dipolar field will perturb the magnetic field seen by a spin packet travelling on a thin circle in a plan perpendicular to the main axis of the rotor. These spins will see a periodic modulation of the main magnetic field that will result in a sharp line flanked by spinning side bands. Another spin packet taken at the different position along the main axis of the rotor will resonate at different frequencies. The resulting frequency distribution along the main axis of the rotor can only be corrected using a combination of shims that act along the magic angle axis [128].

1.5 Gradient coil technologies for MAS

1.5.1 Specificity of the HR-MAS gradients

Pulsed field gradients are widely used in modern high-resolution liquid-state NMR spectroscopy. The selection of coherence order pathways with gradient pulses in a single scan allows to obtain faster results than with a phase cycling procedure. Gradients are particularly useful for inverse experiments and solvent suppression [75, 140, 113, 114]. With the advent of HR-MAS probes equipped with gradients, similar experiments may be envisioned on in HR-MAS [95, 18]. A variety of designs for gradient coils were proposed for MAS probes. The design of a gradient coil for MAS NMR spectroscopy differs in a number of points from traditional gradient coil designs used in standard high-resolution NMR. First, the orientation of the sample (MAS rotor axis inclined at 54.7^o with respect to the main static field) violates the overall symmetry dictated by $\mathbf{B}_o$. Secondly, the sample is rapidly spinning, such that a given spin in the sample travels along a macroscopic spatial pathway and therefore may reach a quite distinct spatial regions after a gradient pulse. Mathematically, while the magnetic field itself represents a vector field with intuitive and relatively simple properties when we consider a rotation of the coordinate reference frame, the situation is more complicated with gradient fields since they have to be described by second-rank tensors. Although we are eventually only interested in three components of such a nine-component field, namely $\partial B_z/\partial x$,$\partial B_z/\partial y$,and $\partial B_z/\partial z$ the complete second-rank tensor has to be taken into account if we are performing a coordinate transformation from the laboratory frame with the z axis parallel to the static field $\mathbf{B}_o$ to the MAS frame with the $0Z$ axis inclined at the magic angle relative to $\mathbf{B}_o$ (Lab frame is represented in the figure 1.5).

This complication when performing rotations of the reference frame reflects itself quite explicitly when designing gradient coil geometries. Gradient coils in conjunction with MAS were proposed originally by Wind, et al.[148], and implemented experimentally by Cory, et al. [25], (using, at that time, Golay coils centered around the spinner axis) and Schauss, et al. [119], (using anti-Helmholtz coils and also Golay coils centered around the spinner axis) for imaging of solid samples spinning at the magic angle. For these imaging experiments, the currents through the gradient coils need to be modulated in order to generate rotating gradient fields synchronously to the MAS rotor motion. Apart from the idea to wind the gradient coils on surfaces of cylinders with axes inclined at the magic angle, Bowtell and Peters [13] went to pursuit the goal to find a gradient coil configuration with wires wound on a cylinder with an axis parallel to $\mathbf{B}_o$, but generating a z gradient along the direction OZ oriented at the magic angle relative to Oz (magic angle gradient). In order to find

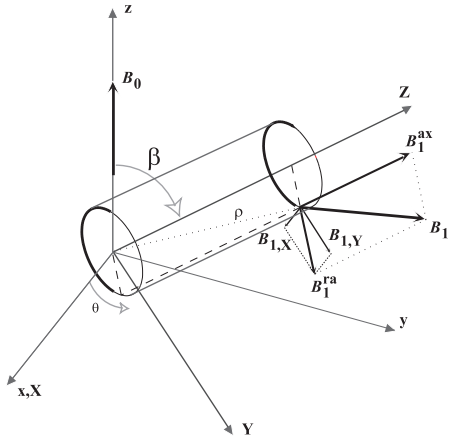

FIG. 1.5 – *Representation of the (x, y, z) laboratory frame (gray) and of the (X, Y, Z) coil frame (black). The radial and axial components of the magnetic field $\mathbf{B}_1$, are projected into the coil frame. Only the upper part of the rotor is displayed for clarity. As an illustration, for a given angle θ, the spin at a distance ρ from the center, experiences a field $\mathbf{B}_1$ that admits as projections in the coil frame the vectors $\mathbf{B}_1^{ax}$ and $\mathbf{B}_1^{ra}$.*

the coil-wire paths on the cylinder along z, two techniques were used : (i) the usage of a combination of an anti-Helmholtz pair with Golay coils, and (ii) the application of the 'target-field approach' as proposed by Turner [138].Experimental results were obtained and discussed, including imaging data and NMR spectra. Magic angle gradients were applied in high-resolution 2D NMR in order to suppress long-range dipolar couplings.

Based upon the transformation properties mentioned above of the second-rank gradient field tensor, Cory et al. [95, 23], derived a gradient coil geometry that was (i) compatible with existing MAS stator geometries, (ii) generating a z component of the static magnetic field that increased linearly along the MAS spinner axis, and (ii) where the z component of the gradient was uniform in planes perpendicular to the spinner axis $0Z$. Such a gradient, when properly adjusted, should not lead to temporally modulated NMR signal. One particular rotating spin will always sample the same magnetic field strength.

Fyfe and coworkers [60] as well as Schnell, et al. [53], proposed a design for their modified MAS system by winding an anti-Helmholtz coil pair concentric to the spinner axis. In that case, however, the rotating spin will experience a gradient modulation.

Barbara, et al. [8, 7] took a different approach to find coil geometries for magic angle gradients by extending the technique proposed by Bowtell and Peters [13]. In their design of magic angle gradient coils they rely on Turner's [138] inverse target field method.

To our knowledge, both types of gradient fields, either with magic angle gradients as proposed by Cory et al. [95, 23], and Barbara et al. [8, 7], or with concentric anti-

Helmholtz gradient coils as proposed by Fyfe, et al. [60], and Schnell, et al. [53], have found applications in solid-state MAS NMR in quite a variety of different NMR experiments. For example, coherence pathway selection was achieved by means of pulsed gradients in ^{1}H MAS double quantum experiments in the work of Spiess, et al. [58] on dipolar solids and in ^{27}Al 3QMAS experiments on zeolites by Fyfe [60]. Similar experiments were performed as well for gradient heteronuclear correlation experiments by Maas, et al. [94], Because field gradients provide spatial selectivity, they can be applied to map the RF field generated by the RF coil in MAS probes. Since ^{1}H FSLG decoupling in solids sensitively depends on RF homogeneity, experiments with pulsed field gradients can be designed [16] that either restrict the sample volume to a homogeneous region of the RF field, or alternatively, can be used to map the RF field distribution. Finally, similar to high-resolution NMR, in organic solids with residual solvents like in microcrystalline proteins, the need arises to suppress the solvent peak in ^{1}H MAS NMR experiments applying $\mathbf{B}_o$ pulsed gradients [53, 17].

1.5.2 Pulsed field gradient inhomogeneities under MAS

The application of field gradient pulses to a sample spinning at the magic angle leads to a specific set of constraints regarding the spatial characteristics of the gradient pulse. Under MAS, a spin packet will travel along a circle in a plane perpendicular to the main rotor axis oriented at the magic angle. During their journey along the circular path, the spins should experience a constant field gradient so that each of the spins in the circle experiences the same gradient. Ideally the field gradient should therefore be oriented exactly along the axis of the magic angle. This ideal configuration means that a second refocusing gradient pulse can be applied at any time during the rotation of the sample to refocus the entire magnetization. If this condition is not satisfied, magnetization losses will be observed since the second gradient pulse will be not exactly reverse the effect of the first gradient pulse. Signal losses were observed by Lippens et al. [147] in HSQC and diffusion experiments when using non rotor-synchronized gradient pulses. The remedy to this problem is to use pulse sequences where gradient pulses are applied only when the rotor is located at a given position. This solution requires that the delay separating two gradients pulses is set to an integer number of rotor periods. It is worth noting that a gradient coil generating a gradient exactly at the magic angle may be less affected by these effects than a gradient coil consisting of two anti-Helmhotz coils.

1.6 Conclusions to this introduction to HR-MAS

Here we briefly describe the basis of HR-MAS instrument, starting from the sample holder in an inside-out explanation : the rotor, the coil, the MAS gradients. Our goal is to pin-point the main characteristics of the different probes that can be used in an HR-MAS experiment. The versatility of HR-MAS makes it compatible with MAS hardware originally designed for high-power applications, as it is the case along this study. Nevetheless from this first part it is clear that the coil remains the central challenge of an HR-MAS application. In order to reach a good resolution, the issues concerning susceptibility and good shimming will be assumed from now. In this thesis, we focus on the task of developping new coil-structures, to improve the $\mathbf{B}_1$ homogeneity but also to reduce the thermal effects produced in visquous, electricaly dispersive samples, as those used in biomedical applications.

Part II
Fundamental concepts, derived from classical Electrodynamics, to be employed in Probe design. Engineering approach of B_1

2

Maxwell equations

The set of Maxwell equations appears for the first time in 1864, as a synthesis of Faraday's laws of induction, the laws Ampere discovered during the first half of the nineteenth century, as well as Gauss laws on charges. The original article went so far in the description that it gave birth to the first unification of electric and magnetic phenomena in the frame of the so called 'Electromagnetic Waves' [100]. The equation of light, an the general equations of wave propagation [4], were already derived by J.C Maxwell in his founding paper.

2.1 Maxwell equations and the description of circuits

We pretend here, only to introduce their range of applications for the present work, and also to prove that all calculations and models used for electrical calculations, as for nodal analysis, can be finally refered to Maxwell's field theory. In this work we will use a macroscopic description of these equations that allows us to consider spatially localized sources of current denoted by the surface density of current J_s and defined point-charges denoted by q. The benefits of this classic description are seen in a frame where circuit theory has it's place. But in addition, we need to consider the variation of magnetic flux produced by the spin fluctuations as a field distribution. Indeed, the spins can not be purely described as localized particles. A field's approach should be employed at the microscopic level to characterize the interactions between the sources of magnetization and the signal detection. This plays a role in the sequel to what we have to say later regarding reciprocity (deriving the equation 9.7), and dielectric dispersion in the part IV (10.2).

[4] we will develop later in the subsection 3.1.2 of this part

After these prerequisites, Maxwell equations are rewritten as :

$$\begin{aligned} \overrightarrow{rot}\vec{H} &= \vec{J}_s + \frac{\partial \vec{D}}{\partial t} \\ -\overrightarrow{rot}\vec{E} &= \frac{\partial \vec{B}}{\partial t} \\ div\vec{D} &= q_\Omega \\ div\vec{B} &= 0 \end{aligned} \tag{2.1}$$

here J_s is defined in A/m^2 , q_Ω the volumic density of charge in Coulomb.m^{-3} , $\vec{E}$ is the electric field vector (also called $\mathbf{E}_1$) in V/m , $\vec{D}$ is the electric flux density vector in As/m^2 , $\vec{H}$ corresponds to the magnetic field expressed in A/m , $\vec{B}$ is the magnetic flux expressed in Gauss (CGS) or Vs/m^2 (SI).

To illustrate these notations, we can use the following circuits models. We find them usefull to introduce the sources of EM field. These what correspond to local phenomenae and lay down in some (precise) part of the circuit. The physical circuit will admit a certain thickness, so the conductors will define a volume (called Ω_1). With this statements the two first Maxwell equations from 2.1 can be respectively illustrated with a parallel and a series circuit.

2.1.1 Maxwell-Ampere in a parallel circuit

The first Maxwell equation, also called Maxwell-Ampere equation deals with currents flowing in parallel branches. As a application of the Kirchhoff's node law the current in the main branch is a sum of the current flowing in the two other branches.

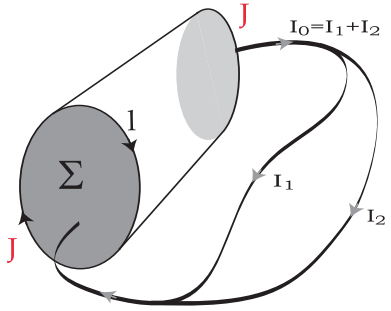

FIG. 2.1 – *Volume circuit used to illustrate the first equation of 2.1.*

In addition, the surface is the cross-section of the wire, and a closed loop l, is defined to surround this surface, as described by picture 2.1. The current density J flows through

this surface Σ.

I_o denotes the current bound to the circulation along a closed loop path, of a magnetic excitation vector $\vec{H}$ .It is stated by Ampere's law. This closed loop, as it circumvents the electrical branch, defines a Stokes surface (Σ in fig. 2.1) in such a way that the following surface integral can be formed :

$$I_o = \oint_{\Sigma} \overrightarrow{H}\, dl = \int_{\Sigma} \overrightarrow{\nabla} \times \overrightarrow{H}\, d\vec{\Sigma} \tag{2.2}$$

by application of the Stokes integral transformation. Where $\oint$ is a closed path on a surface Σ.

The other two branches carry a displacement current (I_2) and a source of current (I_1). This source is produced by the flux of the surface density J_s. So we may write :

$$I_1 = \int_{\Sigma} \overrightarrow{J_s}\, d\vec{\Sigma} \tag{2.3}$$

And at displacement current, produced by the variation of charges at the surface of a conductor yields to :

$$I_2 = \int_{\Sigma} \frac{\partial \vec{D}}{\partial t}\, d\vec{\Sigma} \tag{2.4}$$

I_2 has nothing to do with moving point charges because as defined by J.C Maxwell 'Electrical Displacement consists in the opposite electrification of the sides of a molecule, or particles of a body which may or may not be accompanied with transmission through the body'[100]. That's why we illustrate I_2 as the current in a condenser capacitor, called *displacement current*

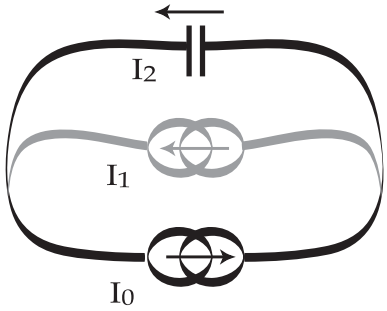

FIG. 2.2 – *Equivalent circuit used to describe the Maxwell-Ampere equation.*

The node equation is applied in the two last branches in such a way that we have, after removing the surface integral, and if we replace the rotational operator ($\vec{rot}$) by its

vectorial pendant $(\vec{\nabla}\times)$:

$$\overrightarrow{\nabla} \times \overrightarrow{H} = \overrightarrow{J_s} + \frac{\partial \overrightarrow{D}}{\partial t} \tag{2.5}$$

In this equation we should pay attention to the fact that both localized and field terms are mixed. $\overrightarrow{J_s}$ is a density of current, at one point of the circuit. On the other hand $\vec{D}$ and $\vec{H}$ are fields i.e., spacial distributions.

2.1.2 Maxwell-Faraday equation in a series circuit

The derivation which can be done for the second equation, named Maxwell-Faraday equation, looks the same. We use the Kirchhoff equation for meshes, which means that the vector sum of voltages equals zero.

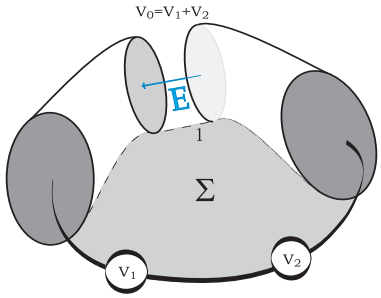

FIG. 2.3 – *Volume circuit used to describe the second equation.*

In addition the surface is area defined by the circuit, and the closed loop path l, is the circuit path as described by picture 2.3. If we assume there is no field in the conductors, V_o denotes a voltage source . The conservative field $\vec{E}$ stands perpendicular between the two surfaces of a gap considered in the bulk circuit. Since the closed loop l encompass the electrical circuit, a Stokes surface is definded, and so the potential V_o can be written :

$$V_o = -\oint_{\Sigma} \vec{E}\, dl = -\int_{\Sigma} \vec{\nabla} \times \vec{E}\, d\vec{\Sigma} \tag{2.6}$$

Here again we consider two contributions to this voltage V_o, induced by the variation of magnetic flux. We assume two different sources of magnetic flux variation. The first one is produced by the self inductance of the circuit, called the magnetic flux density and denoted by $\vec{B}$. The second one is somehow interacting with the considered circuit, by means of mutual inductance (right hand of Fig.2.4). In the present case this *actuator* will be the distribution of spins present in the sample volume.It represents the sample magnetization $\vec{\mathcal{M}}$, obviously not delivered with the probe and at the same time, strongly coupled to it. Both fluctuations of the inductance act over the same surface (Σ). We

distinguish them in the following equations :

$$\begin{aligned} V_1 &= \frac{\partial}{\partial t}\int_\Sigma \vec{B}\, d\vec{\Sigma} \\ V_2 &= \frac{\partial}{\partial t}\int_\Sigma \vec{\mathcal{M}}\, d\vec{\Sigma} \end{aligned} \tag{2.7}$$

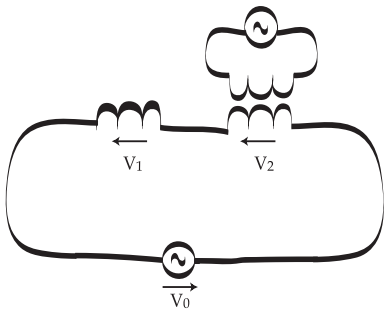

FIG. 2.4 – *Volume circuit used to describe Maxwell-Faraday equation.*

The meshes equation of Kirchhoff is applied in the circuit described by figure 2.4, since the surface Σ is the same for all we write the second Maxwell equation :

$$-\vec{\nabla} \times \vec{E} = \frac{\partial \vec{B}}{\partial t} + \frac{\partial \vec{\mathcal{M}}}{\partial t} \tag{2.8}$$

incorporating the magnetization as cause of NMR signal, and as field distribution, as it will be clear while deriving the signal equation later (in section 5.2 of this part).

2.1.3 EM field distribution and circuit simulation

From the preceding, we see how Kirchhoff laws can give a nice illustration of the two first Maxwell equations. This analogy serves us to refer circuit simulation to electromagnetism. During this study a large number of probe circuits have been designed and analyzed in the frequency domain using a freeware program called 'Vipec' [5]. It consists of a light C^{++} code used to calculate the impedance matrix on a linear system. Nodal analysis easily treats capacitances (C), inductances (L) as well as sources of voltage and of current, as lumped elements. The geometry dependance of C and L is the reason why nodal analysis requires some prior knowledge, based on Maxwell equations. A good example, to

[5] Vipec is developed under the terms of the GNU license, by J.Rossouw and E.Jansen, and can be obtained at the following homepage http ://vipec.sourceforge.net

show the dependency of a nodal-analysis model on $\mathbf{E}_1$ field distribution, is the problem of *stray capacitances* to ground. These are of great influence in the circuit behavior and can only be revealed when solving the full 3D electromagnetic distribution for the considered structure. Nevertheless, as soon as sources of current, and voltage, as well as the elements generating $\vec{B}$ fields (Inductances L) and $\vec{E}$ fields (capacitances C) have been localized, an equivalent circuit can be set to describe the impedance, resonance frequency, and quality factors of a real circuit.

Most network analysis programs will form an admittance matrix (Y-matrix) internally and invert the matrix to find a solution of the basic equation :

$$V = Y^{-1}.I$$

The network of lumped elements has no length. Dephasing through propagation is not considered there. The physical phenomena are propagated immediately. This hypothesis may be true for a large number of problems when the excitation made by electric waves is larger than the distances characteristics of the considered network. For example at 900 MHz the wavelength in free space equals 30 cm. In other words, as soon as we consider devices longer than 3 cm, we should consider a transmission-line equivalent model in the circuit, below these distances stray inductances and capacitances satisfy the network approach. Only in case of TEM mode the quasi-static approach behind circuit analysis is valid. Resonance appears when a standing mode is established. This mode allows to solve 3D problems in a plane as soon as the direction of propagation is known and supposed to be infinite. The limitation stands in the fact that most EM field distribution present a different pattern than the TEM, and so they do not admit the quasi-static approach, this is the case of most coils. Modeling a coil as an inductance in circuit analysis may be possible in a first approximation, but turns decieving at high frequencies, the usage of a helical transmission line model is recommended instead.

2.1.4 Maxwell equations for the microscopic Field

The equations given by Eq. 2.1 are suited for macroscopic detection and, therefore, they cover the engineering approach of the present part. The auxiliary field $\vec{D}$ and $\vec{B}$ are introduced when not all charges are included as sources. These fields however contain implicitely parts of the sources, namely the bound charge and current densities, in the form of polarization fields and currents. These auxiliary fields include the material response (the electric polarization and the magnetization) to the applied fields ; they are connected with $\vec{E}$ and $\vec{H}$ by relations depending on the constitution of matter . In the simplest constitutive

relations $\vec{D}$ is parallel and proportional to $\vec{E}$, and the same collinearity applies for $\vec{H}$ and $\vec{B}$. This first condition is well established in the probe circuit where all elements are carefully selected for their low-loss characteristics. But, of course, this can not be the case inside the coil due to the nature of samples used for HR-MAS (at it will be seen in Part IV). There, electric polarization $\vec{P}$ needs to be introduced in order to consider the dielectric response.

Here $\vec{P}$ is the the average polarization, sum of the microscopic $\vec{p_i}$ components of the sample. It is the response of matter to an electric excitation :

$$\vec{P} = \epsilon_o . \chi_e \vec{E} \ ; \ \vec{D} = \epsilon_o (1 + \chi_e) \vec{E} \tag{2.9}$$

where χ_e is the electric susceptibility, and ϵ_o the permittivity of vacuum.

The magnetic part admits a similar reasoning, and the magnetic susceptibility χ_m is introduced by :

$$\vec{B} = \mu_o . (1 + \chi_m) \vec{H} \ ; \ \vec{M} = \chi_m \vec{H} \tag{2.10}$$

where χ_m is the electric susceptibility, and μ_o the vacuum permeability. Fortunately for NMR in general and, as explained in the previous chapter, for HR-MAS in particular χ_m is canceled in the coil volume. It is therefore justified to consider the magnetic flux as being *collinear* with the magnetic field.

Finally the microscopic formulation of Maxwell equations needed for quantum electrodynamics, saves the problem of material equations :

$$\begin{aligned} \nabla \times \mathbf{b} &= \mu_o \mathbf{j}_s + \frac{1}{c^2} \frac{\partial \mathbf{e}}{\partial t} \\ -\nabla \times \mathbf{e} &= \frac{\partial \mathbf{b}}{\partial t} \\ \nabla \cdot \mathbf{e} &= \frac{q}{\epsilon_o} \\ \nabla \cdot \mathbf{b} &= 0 \end{aligned} \tag{2.11}$$

where c is the speed of light in vacuum ($c^2 = 1/\epsilon_o \mu_o$), $\mathbf{b}$ and $\mathbf{e}$ are the microscopic pendants of the electromagnetic fields introduced in Eq. 2.1.

This is not a justification of the usage of the microcopic magnetic induction $\mathbf{b}$ to denote *magnetic field*. Such practice is incorrect from the strict views of electrical engenieering. Nevertheless the link between both in free space and in most of our NMR samples is so obvious ($\mathbf{b} = \mu_\mathbf{o} \mathbf{h}$) that most people agree in mentioning one for the other. At the

end of this chapter and in Part III, we will understand how usefull it is to designate the distribution associated with the magnetic field induced in the sample by $\mathbf{B}_1$, and the corresponding RF magnetic excitation by $\mathbf{H}_1$.

2.2 Continuity equations

2.2.1 General definition of the continuity equations

Continuity equations are well suited for the description of the electromagnetic field boundary conditions when the media is divided in several regions each one of distinct permittivity and permeability.

The surface separates the free space, whose index is a and material constants are ϵ_o and μ_o, from a second medium of index b. This second medium can be metal or dielectric material. In the following, we will consider as boundary the cover shield surrounding the probe. The shield is made in such a way that conductivity can be assumed to be infinite, so the skin depth at the considered frequencies is considered to be negligibly small.

Application of Stokes theorem

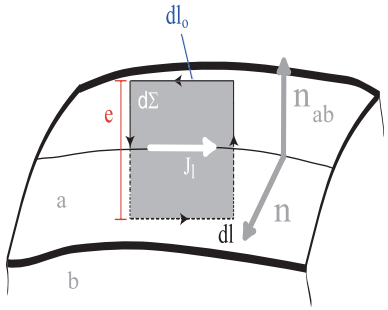

FIG. 2.5 – *Integration pathway for the application of the Stokes transformation.*

The Maxwell-Ampere equation can be written as follows in its integral form :

$$\int_\Sigma \vec{\nabla} \times \vec{H}\, d\vec{\Sigma} = \int_\Sigma \vec{J}_s\, d\vec{\Sigma} + \int_\Sigma \frac{\partial \vec{D}}{\partial t}\, d\vec{\Sigma} \tag{2.12}$$

with $\vec{J}_s$ a current at the surface of the material.

The same integration path is invoked as before, so the equation 2.12 will have the following form after the application of the Stokes theorem :

$$\oint_l \vec{H}\, \vec{dl} = \int_\Sigma \vec{J}_s\, d\vec{\Sigma} + \int_\Sigma \frac{\partial \vec{D}}{\partial t}\, d\vec{\Sigma} \tag{2.13}$$

it is important to insist on the fact that on the first approximation (skin effect negligible) there is no current in the bulk conductor, and obviously none in the free space, the surface integral can easily be transformed into a linear integral (hereby the linear current density is defined as J_l). The closed loop path which encompass the surface is defined as in figure 2.5, again e is the smallest distance we can imagine. By integrating the equation 2.13 as shown in the figure 2.5 using the fact that $d\Sigma = e.dl_o$ one obtains after decomposition of the path over dl_o and e :

$$\overrightarrow{n_{ab}}.(\vec{H}_b - \vec{H}_a).e + (H_{bT} - H_{aT}).dl_o = J_l.dl_o + \vec{n}.\frac{\partial \vec{D}}{\partial t}.e.dl_o \tag{2.14}$$

At the limit of e close to 0, half of the terms of this equation vanish :

$$H_{bT} - H_{aT} = J_l \tag{2.15}$$

Currents exist also at the surface of dielectrics, this is a remarkable property of dielectric resonators.

On the other hand, but always on the same contour defined by Fig.2.5, the Faraday-Maxwell equation can be written as follows :

$$\int_\Sigma \vec{\nabla} \times \vec{E}\, d\vec{\Sigma} = -\int_\Sigma \frac{\partial \vec{B}}{\partial t}\, d\vec{\Sigma} \tag{2.16}$$

The element surface $d\Sigma$ is defined as a surface crossing the interface of length dl_o and of height e.

By applying the Stokes theorem 2.16 becomes :

$$\oint_l \vec{E}\, d\vec{l} = -\int_\Sigma \frac{\partial \vec{B}}{\partial t}\, d\vec{\Sigma} \tag{2.17}$$

Again a contour loop around the surface element is taken. This loop is small enough to estimate that $\vec{B}$ is constant over the surface defined by it. With this statements Eq.2.17 admits this derivation :

$$\overrightarrow{n_{ab}}.(\vec{E}_b - \vec{E}_a).e + (E_{bT} - E_{aT}).dl_o = -\vec{n}.\frac{\partial \vec{B}}{\partial t}.e.dl_o \tag{2.18}$$

At the limit of e close to 0 only the second term doesn't cancel and the second continuity equation appears :

$$E_{bT} - E_{aT} = 0 \tag{2.19}$$

Application of Ostrogradsky-Gauss theorem

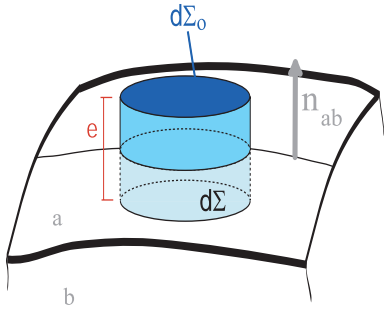

FIG. 2.6 – *Integration pathway for the application of Ostrogradsky transformation.*

The Gauss's law can be expressed by the following equation, this time with a volume integral, whose volume is represented by the figure 2.6 :

$$\int_{\Omega} \vec{\nabla}.\vec{D}\, d\Omega = \int_{\Omega} q_{\Omega}\, d\Omega \tag{2.20}$$

As presented in the figure 2.6 the volume element is a cylinder of infinitesimal height e. We assume the surface of the sides small in comparison to the surface at the intersection with the interface (we call it $d\Sigma_o$).The bulk electric charge q is the point charge introduced in the previous section, related to q_σ the charge per unit surface, and q_Ω introduced here is the volume charge. By means of the Ostrogradsky-transformation one gets from the preceding equation :

$$\oint_{\Sigma} \vec{D}\, d\vec{\Sigma} = \int_{\Sigma_o} q_\sigma\, d\Sigma_o \tag{2.21}$$

Finally, as we assume e becoming infinitesimal, and the contribution of the tangential part of the electric displacement density $\vec{D}$ cancels : this equation becomes the third continuity equation :

$$D_{bN} - D_{aN} = q_\sigma \tag{2.22}$$

At last (but not at least) the conservation of the magnetic induction, which is expressed by the Gauss-magnetic fourth Maxwell equation stands like that :

$$\int_{\Omega} \vec{\nabla}.\vec{B}\, d\Omega = 0 \tag{2.23}$$

Equivalent by means of the same theorem to the following surface integral,

$$\oint_{\Sigma} \vec{\nabla}.\vec{B}\, d\Sigma = 0 \tag{2.24}$$

where Σ is the closed surface surrounding the above mentioned volume. When the surface formed by the cylinder approaches the two disks (as e is approaching 0) the equation 2.24, will admit as expression the fourth continuity equation :

$$B_{bN} - B_{aN} = 0 \tag{2.25}$$

2.2.2 Application to the case of an NMR probe shielding

We have to consider these equations to approach the EM field distribution within an NMR probe, and especially the influence of the probe cover. We can consider the probe's shield as a perfect conductor, whose thickness is such that at a certain depth neither charges nor currents can be induced.

The results displayed in the table 2.1 show the boundary condition imposed by the shield at the probe's cover surface, in the ideal case of a shield whose conductivity is perfect. In practice it is good to consider a transitional region where E_T and B_N do not cancel. This is the so called *skin depth* defined as :

$$\delta_s = \sqrt{\frac{2}{\mu_c \omega \sigma}} \tag{2.26}$$

where μ_c is the permeability of the conductor, ω the frequency of the wave, and σ the conductivity in Siemens per meter .

Flux of energy

These results are essential to prove that the flux of a Poynting vector cancels when passing through a good conductor. Electromagnetic energy will not go through a probe cover. This is the reason why despite of the high power used inside an NMR probe will never be a good RF antenna. With the same element of surface $d\vec{\Sigma}$ defined as in fig. 2.7 taken infinitely close to conductor's walls, we can write :

$$\lim_{e \to 0} \oint_{\Sigma} \vec{E_1} \times \vec{H_2}.\, d\vec{\Sigma} = 0 \tag{2.27}$$

Where (1) and (2) are denoting two wave sources in the free space volume.

TAB. 2.1 – *Field distribution at the interface with a perfect conductor.*

Electric field	$E_T = 0$	$D_N = q_\sigma$
Magnetic field	$H_T = J_l$	$B_N = 0$

Image charge theorem

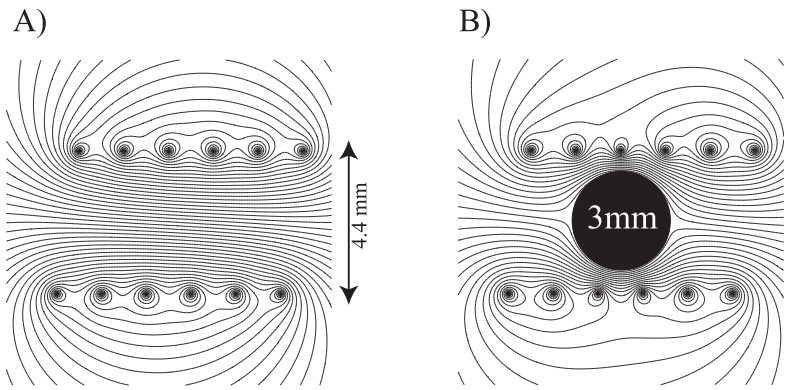

FIG. 2.7 – *Illustration of the image-charge theorem, considering infinitely thin wires in an empty space (A) and when an inner circular shield mimics the conductive ball used to probe the magnetic induction. The flux lines are calculated using this electrostatic theorem.*

The Gauss theorem can be employed to replace point charges by spheres, and linear distribution of charges by infinitely long cylinders, as a direct implication of the two last continuity equations.

It is well known that the equipotential lines of a two-charges distribution are a family of spheres (S) , whose centers are contained on a symmetry axis passing by the charges. The *Image charge* theorem, also called substitution theorem, states the following :

'If any of those spheres (S) surrounding the charge is metalized with a layer of perfect conductor then, according to the screening properties of electrostatic charges, the surface on it will be charged with the same, but opposite value. And therefore, a screening surface can be substituted by the corresponding punctual image charge without altering the equipotential distribution.'

If O is the center of a shield whose radius is R, and $|OM|$ the distance from O to the charge creating a distribution of potential, then another charge of opposite value can be found at M' aligned with O and M. The relation between these values is given by the algebraic product :

$$|OM|.|OM'| = R^2 \tag{2.28}$$

This image charge can be defined to remove the shield, and still keep the same electrostatic distribution.

A direct application of the image charges theorem, is given by the case of TEM waves traveling inside the probe's cover :

As the direction of propagation is longitudinal, along the probe's shielding considered infinitely long, the decomposition of the wave components becomes trivial. The fields

can be solved in transverse plane using the quasistatic approximation, and the voltage distribution is calculated easily using this technique. Another pedadogical application would be the description of the flux lines distorded by a conductive body inside the coil simulated with point charges. Fig. 2.7 pretends only to illustrate, with a quasitatic approximation, the field lines inside of a coil. This pattern corresponds to a perturbation of the $\mathbf{B}_1$ when inserting a ball. Such a perturbation technique is employed to map the field inside of the NMR coil.

2.3 Field mapping by perturbation methods : the Ball-shift

In order to experimentally determine the H_1 field magnitude inside resonators or coils, small metallic (e.g., spherical) bodies are positioned into the region of interest to induce a local perturbation of this field and to increase the resonance frequency of a tuned and matched circuit. Such frequency variation is called Δf_{bs}. The so-defined 'ball shift' measurements provide an accurate field mapping [97, 109]. The value of the frequency shift is a (monotonous) function of the magnetic field amplitude at the same location. In this work, we used a set of cylindrical dielectric inserts with embedded copper balls (of diameter 3 mm) to probe the magnetic filling factor (η_{bs}) by introducing and positioning these inserts along the main axis of the coil with incremental steps of 0.5 mm (an example of such curves is given by the Fig. 11.9 where three different resonators are to be compared). We consider a cavity of initial volume Ω_1, as depicted by Fig. 2.8 the initial area of the cavity walls is Σ_1, now we modify the surface of such a resonator by inserting a ball in the center of this cavity, so we perturb the electromagnetic field distribution inside this volume. The new volume is then called Ω_2. By extension we will define by index '1' all variables without perturbation (before inserting the ball) and by '2' the variables with perturbation.

This description is symmetric, and the calculations are done under the assumption that the perturbation is small, so that the field lines in the probe can be assumed to remain more or less the same after the insertion of a metallic ball.

Now let us take the complex conjugate of the field $\vec{E}_1$, we write it as $\vec{E}_1^*$ and multiply it by the Maxwell-Ampere equation in the state 1, it will be the first equation of 2.29 and then take the complex conjugate of the Maxwell Faraday equation in the state 2, and multiply it by $\vec{H}_2$, the pair of equations obtained are :

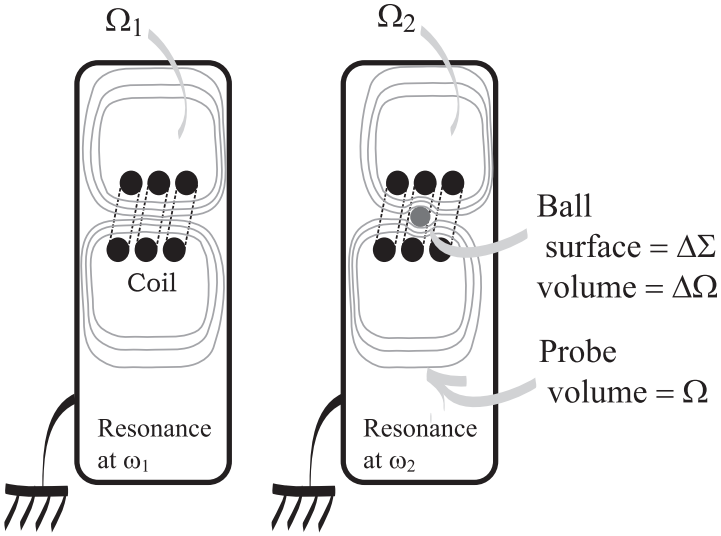

FIG. 2.8 – *Deformation of equipotential lines, due to the presence of a metal ball inside the coil.*

$$\begin{aligned} \vec{E}_1^*.\vec{\nabla}\times\vec{H}_2 &= i\omega_2\,\vec{E}_1^*\vec{D}_2 \\ -\vec{H}_2.\vec{\nabla}\times\vec{E}_1^* &= -i\omega_1\,\vec{H}_2\vec{B}_1^* \end{aligned} \tag{2.29}$$

Taking into account the well know vector relation :

$$\vec{\nabla}.(\vec{A}\times\vec{B}) = \vec{B}.\vec{\nabla}\times\vec{A} - \vec{A}.\vec{\nabla}\times\vec{B} \tag{2.30}$$

We can sum the two preceding equations 2.29, the result of the term to term sum is the first equation in 2.31, and the second one is deduced by simple symmetry.

$$\begin{aligned} \vec{\nabla}.(\vec{H}_2\times\vec{E}_1^*) &= i\omega_2\,\epsilon_o\vec{E}_1^*\vec{E}_2 - i\omega_1\,\mu_o\vec{H}_2\vec{H}_1^* \\ \vec{\nabla}.(\vec{H}_1^*\times\vec{E}_2) &= i\omega_2\,\mu_o\vec{H}_2\vec{H}_1^* - i\omega_1\,\epsilon_o\vec{E}_1^*\vec{E}_2 \end{aligned} \tag{2.31}$$

Now we add these two equations, and we perform the volume integration over the volume Ω_2 of the perturbed cavity.

$$\int_{\Omega_2} \vec{\nabla}.(\vec{H}_2 \times \vec{E}_1^*) + \vec{\nabla}.(\vec{H}_1^* \times \vec{E}_2)\, d\Omega = i(\omega_2 - \omega_1) \int_{\Omega_2} (\epsilon_o \vec{E}_1^* \vec{E}_2 + \mu_o \vec{H}_2 \vec{H}_1^*)\, d\Omega \qquad (2.32)$$

Finally let us apply the Gauss-Ostrogradski transformation on the right-hand side of this equation, to replace it by :

$$\oint_{\Sigma_2} (\vec{H}_2 \times \vec{E}_1^*)\, d\vec{\Sigma} + \underbrace{\oint_{\Sigma_2} (\vec{H}_1^* \times \vec{E}_2)\, d\vec{\Sigma}}_{0} \qquad (2.33)$$

Both terms of this expression represent the flux of Poynting vectors through a closed surface, the second term of this expression vanishes at the surface Σ_2 of the conductor because of the continuity relations we have mentioned in the section 2.2. The first term does not cancel at all due to the fact that Σ_2 considers also the surface of the ball, and in this precise region, $\vec{E}_1^*$ is not, as it is at the probe shielding, normal to the surface ($\vec{E} \neq E_N.\vec{U}_r$). Of course it will still be the case at the surface of the conductive walls, in both states. We reformulate these statements into the following equations :

$$\oint_{\Sigma_2} (\vec{H}_2 \times \vec{E}_1^*)\, d\Sigma = \underbrace{\oint_{\Sigma_1} (\vec{H}_2 \times \vec{E}_1^*)\, d\Sigma}_{0} - \oint_{\Delta\Sigma} (\vec{H}_2 \times \vec{E}_1^*)\, d\Sigma \qquad (2.34)$$

So at the end, Eq.2.32 is rewritten in such a way that a frequency shift appears to be :

$$(\omega_2 - \omega_1) = \frac{i \oint_{\Delta\Sigma} (\vec{H}_2 \times \vec{E}_1^*)\, d\Sigma}{\int_{\Omega_2} (\epsilon_o \vec{E}_2.\vec{E}_1^* + \mu_o \vec{H}_2.\vec{H}_1^*)\, d\Omega} \qquad (2.35)$$

This equation is the general formula obtained assuming no losses. The crude approximation to be made in 2.35 is that of substituting the fields pattern ($\vec{E}_2$,$\vec{H}_2$) by the one from the unperturbated state ($\vec{E}_1$,$\vec{H}_1$). For small perturbations, this is certainly reasonable for the denominator (we are performing an integration over the whole space) and should be valid if the deformation on the equipotential lines is shallow and smooth. In practice this theory is quite robust, nobody need to look for an infinitely small ball for the measurement. In addition for some experimental reasons, the ball has to be sufficiently large in order to allow a practical measurement with the wobbler or the network analyzer. Indeed, an infinitely small ball would produce an exact but fully unmeasurable result.

$$\oint_{\Delta\Sigma} (\vec{H}_2 \times \vec{E}_1^*)\, d\Sigma \approx \oint_{\Delta\Sigma} (\vec{H}_1 \times \vec{E}_1^*)\, d\Sigma \qquad (2.36)$$

By using the first equation of 2.31, with the proper index 1, instead of 2, we end up

with the following ratio :

$$\frac{f_2 - f_1}{f_1} = \frac{\omega_2 - \omega_1}{\omega_1} = \frac{-\int_{\Delta\Omega}(\epsilon|E_1|^2 - \mu|H_1|^2)\, d\Omega}{\int_{\Omega}(\epsilon|E_1|^2 + \mu|H_1|^2)\, d\Omega} \tag{2.37}$$

Ball shift measurements are easy to measure and they have proved to be very useful in order to estimate the sensitivity of a probe, by comparing one channel to another, but nevertless they will not be included 'as it' into our expression of the signal to noise ratio. For this, some other characteristic parameters, like filling factor ζ or quality factor Q are better suited. We are going to introduce them now,

2.3.1 Magnetic filling factor

The portion of the magnetic field energy stored in the volume equal to the ball volume (without ball) may serve to define the magnetic filling factor [97]. By the preceeding demonstration we have clearly exposed that the ball-shift difference in frequencies is proportional to the variation of energy inside of the NMR coil (whose impedance is defined by L_{NMR}). The fraction of the magnetic field energy stored in the ball volume ($\Delta\Omega$), serves to define the *magnetic filling factor* ζ_{bs}. Starting from Eq. 2.37 with the simplification introduced by the abscence of electric field in a pure inductor :

$$\zeta_{bs} = \frac{\int_{\Delta\Omega} |\mathbf{B}_1|^2\, d\tau}{\int_{\Omega} |\mathbf{B}_1|^2\, d\tau} = \frac{\Delta\mathcal{E}_m}{\mathcal{E}_m} = \frac{\Delta L_{NMR}}{L_{NMR}} \tag{2.38}$$

where $\mathcal{E}_m$ is the magnetic energy, stored in the NMR coil, and related to its inductance, and $\Delta\mathcal{E}_m$ an infinitesimal variation of volumic energy.

We can write the preceding equation in a simpler way to relate ζ to a directly measurable quantity :

$$\zeta_{bs} = 1 - \Big(\frac{f_1}{f_1 + \Delta f_{bs}}\Big)^2 \tag{2.39}$$

where f_1 denotes the circuit resonance frequency measured with an empty insert. If we want to compare different coils, it is the magnetic filling factor that turns out to be relevant to relate $\mathbf{B}_1$ field magnitudes to each other at a given position inside the respective coil.

The formula given by Eq.2.38 is specially useful when predicting the sensitivity of a circuit simulated by nodal analysis. The frequency increase obtained when decreasing the inductance of the NMR coil described as a lumped elements, serves, as first approximation, to predict the amount of field inside of the coil. In fact this means also that : the field distorsion produced by a ball inside of the coil, results in a new coil inductance called $L^K_{NMR} = L_{NMR} - \Delta L_{NMR}$ and providing that the electric field is not modified in this region (by hypothesis), the equivalent parallel capacitance of the resonant circuit will

stay unmodified. So invoking Thomson's law : $LC.\omega^2 = 1$ we can finally link the new inductance to the resonance shift :

$$\zeta_{bs} = \frac{\Delta L_{NMR}}{L_{NMR}} = 1 - \frac{L^K_{NMR}}{L_{NMR}} = 1 - \frac{\omega_1^2}{\omega_2^2} = 1 - \Big(\frac{f_1}{f_1 + \Delta f_{bs}}\Big)^2 \tag{2.40}$$

where f_1 is the resonance frequency measured with an empty holder, f_2 the resonance frequency of a loaded coil, and Δf_{bs} the increase of frequency when inserting a conductive sphere in the resonator. This expression is to be compared to the initial one in Eq. 2.37.

2.4 Quality factor

The Q factor is related to the electromagnetic energy stored in a resonator or circuit divided by the dissipated power. As known from classical electromagnetic theory [78, 68], the quality factor is defined by :

$$Q = \frac{\omega \times \text{energy stored}}{\text{average power dissipated}} \tag{2.41}$$

where ω refers to the resonance frequency.

For high quality factors, $\frac{1}{Q}$ can be also called *power factor*. A general expression of stored and dissipated energy is :

$$\frac{1}{Q_s} = \frac{\int_{sample\,volume} \overline{\sigma(\vec{\rho})E(\vec{\rho},t)\cdot E(\vec{\rho},t)^*}\, d\Omega + \mathcal{P}_d}{\omega \int_{sample\,volume} \overline{B(\vec{\rho},t)\cdot H(\vec{\rho},t)^*}\, d\Omega} \tag{2.42}$$

where Q_s is the measured quality factor of a probe containing a sample,the first term in the numerator is dissipation, caused by conductive currents in the sample, to be distinguished from other kinds of sources of dissipation, like dielectric dispersion (denoted by $\mathcal{P}_d$). This introduces σ, the conductivity, expressed in S/m. The overbar designates the time average over one cyle.

Therefore it describes quite exhaustively the losses in the probe and in the sample [33, 136, 79]. From this definition we derive that, in the presence of distinct sources of dissipation, the Q factor will be decomposed as follows :

$$\frac{1}{Q_s} = \frac{1}{Q_l} + \frac{1}{Q_u} \tag{2.43}$$

where Q_l is due to the specific loss in the conductive load which can not be accessed directly, and Q_u is the measured loss of an unloaded probe. The ratio of quality factors of the loaded resonator to the empty resonator $(1 - Q_u/Q_s)$ as used in Fig.11.16 focuses on

the specific influence of the conductive load, and can be found in the literature elsewhere [92, 132] as an indicator of how strong the coupling of the electric field to the sample is. It serves to evaluate the decrease of the loaded quality factor when increasing the conductivity σ of the sample. The smaller the importance of the electric field is, the smaller will be the influence of the conductivity on the quality factor.

2.5 Macroscopic Magnetization : classical description

As it will be clarified through quantum theory in chapter 6, the magnetic field acts on the spin magnetization as a rotation operator. Such rotations are called *Nutations* when caused by the RF field, to distinguish them from the rotations called *Precessions* from the static $\mathbf{B}_o$. Such terms are part of a jargon employed in classical mechanics. In this section, to stick to the macroscopic formulation of Maxwell equations (Eq. 2.1) we will stick to $\mathbf{H}$ to designate the magnetic field. In this classical frame, the NMR experiment can be understood thanks to a mechanical analogy. The basis of signal detection in NMR can be explained through the now explained *nutation* experiment.

This one is to be separated in three sequential steps :

- a starting *precession* to stabilize the sample denoted by index 0 ;
- a pulsing time, called *flipping* as RF emission period denoted by index 1 ;
- the *acquisition* period (or measuring time) of index 2.

The relaxation during the pulsing, and acquisition times exits, and can be accessed through the Bloch equations. In this section we follow the formalism used by Abragam to relate nutation speed to the magnetic excitation (chapter II in [1])

The pulse is an electromagnetic wave expressed as :

$$\vec{H_1} = 2\omega_1.cos(\omega_{rf}t_1 + \phi).\vec{y} \tag{2.44}$$

from now $2\omega_1$ is the magnitude of the oscillating field in the laboratory frame, ω_{rf} is the pulsation of the RF wave (we assume monochomatic), and ϕ is the phase of the wave, taken as a constant over all the sample. This last point will be justified at the end of the fourth part.

Larmor Equation : The spin is submited to the static magnetic field H_o which produces a precession on the magnetization in such a way that :

$$\vec{\omega_o} = -\gamma_r.\vec{H_o}$$

$$\nu_o = \frac{\gamma_r}{2.\pi}.H_o \tag{2.45}$$

where γ_r is the gyromagnetic ratio of the spin nucleus.

The Magnetization vector : Many atomic nuclei in their ground state have a non-zero spin angular momentum[6] and a *dipolar magnetic moment*$\hbar\mathbf{I}$ colinear with it, so

$$\boldsymbol{\mu} = \gamma_r.\hbar.\mathbf{I} \tag{2.46}$$

Thus the magnetic field produces a torque of strengh G with :

$$\mathbf{G} = \boldsymbol{\mu} \times \mathbf{H} \tag{2.47}$$

lending to twist $\boldsymbol{\mu}$ and to forces the spin vector to precess around a cone of axis Oz (Fig. 2.9).

The classical equation of motion is written as :

$$\frac{d}{dt}(\boldsymbol{\mu}) = -\gamma_r(\boldsymbol{\mu} \times \mathbf{H}) \tag{2.48}$$

the sign is a matter of conventions, it indicates that the 'right-hand' rotation should be used to predict the evolution of the dipolar magnetic moment. Since the bulk magnetic moment $\vec{\mathcal{M}}$ is the sum of all the individual nuclear moments $\boldsymbol{\mu}$, we introduce the evolution of magnetization in the following first order differential equation :

$$\frac{d\vec{\mathcal{M}}}{dt} = -\gamma_r(\vec{\mathcal{M}} \times \vec{H}) \tag{2.49}$$

2.5.1 The Nutation experiment

The preparation time

We consider, as in Fig.1.5, the lab frame defined as (x, y, z). The coil axis is the y axes of this frame. During this time the spin motion is solely due to the static fields so :

$$\frac{d\vec{\mathcal{M}}_o}{dt} = -\gamma_r(\vec{\mathcal{M}}_o \times \vec{H}_o) \tag{2.50}$$

resulting in a distribution of spins rotating in a cone.

[6] integer or half integer in units of $\hbar$

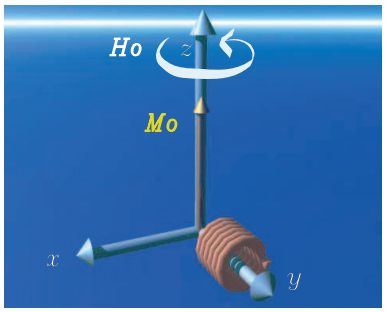

FIG. 2.9 – Preparation state of the magnetic moment, using the convention that the Larmor precession is conterclockwise.

The flipping with a nutation angle

The following is the evolution during a RF pulse of phase[7] x. During this time, H_1 is superimposed to the static field H_o. The nutation speed ω_1 (associated with the RF field H_1) is of some few kHz. This is negligible in front of the precession speed ω_o, of several hundreds of MHz. We introduce then, the *rotating frame* of axis (x', y', z'), rotating around Oz at an angular speed of ω_o. This mathematical treatment enlightens the usefulness of *on-resonance* pulsing, to understand how does the RF field to influence effectively the NMR experiment.

The pulsation of the applied RF field H_1 is fluctuating at the pulsation ω_{rf}. In the case of *linear polarization*, the RF field given in Eq. 2.44 can be decomposed in two compoments of strength ω_1, rotating at ω_{rf} in two oposite directions. The component synchronized with $+\omega_o$ is locked along the axis Oy'.

According to the general law of relative motion, the time derivative (d/dt) in the laboratory frame, and its derivative $(\partial/\partial t)$ computed in the moving frame, are related trough the so called *Coriolis correction* :

$$\frac{d\vec{\mathcal{M}}}{dt} = \frac{\partial\vec{\mathcal{M}}}{\partial t} + \vec{\omega}_o \times \vec{\mathcal{M}} \tag{2.51}$$

Combining 2.50 for a linearily polarized RF field (Eq. 2.44), and the equation. 2.51, the motion of the magnetic moment in the rotating frame becomes :

$$\frac{\partial\vec{\mathcal{M}}}{\partial t} = -\gamma_r\Big(\vec{\mathcal{M}}' \times (\vec{H}_o - \frac{\vec{\omega}_{rf}}{\gamma_r})\Big) - \frac{\gamma_r}{2}(\vec{\mathcal{M}}' \times \vec{H}_1) \tag{2.52}$$

to condensate notations we introduce the effective magnetic field, static in the rotating

[7]The meaning of the phase notations will be treated later in this Part (Section 5.1) . It is sufficient for the present to asume that phase x, means that the magnetization vector will be rotated towards Ox

frame :

$$\gamma_r.\vec{H}_{eff} = -(\vec{\omega}_{rf} - \vec{\omega}_o) + \vec{\omega_1} \tag{2.53}$$

the difference in pulsation is called offset $\Delta\omega_o = \omega_{rf} - \omega_o = 2\pi\Delta\nu$, this last is the off-resonance factor considered in Part III. (Our notation of $\Delta\omega_o$ is the same but opposite as the one employed by Desvaux [34])

Finally the flipping is evaluated by its *nutation angle* :

$$\theta = \gamma_r.H_{eff}.t_1 \tag{2.54}$$

The figure 2.10 gives a schematic overview of this classical description.

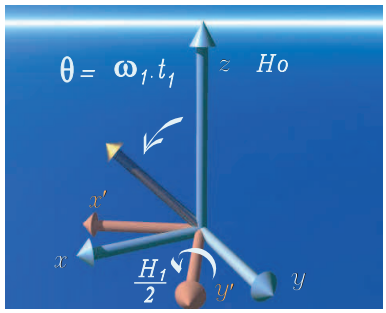

FIG. 2.10 – The application of an RF pulse on-resonance, produces the flipping of the magnetization in the transverse plane.

If the relaxation starts playing a role during this period, the Bloch differential equation has to be expanded in the rotating frame. Using matrix algebra we chose to write Eq. 2.49 in such a way :

$$\frac{\partial}{\partial t}\begin{pmatrix} M_{x'} \\ M_{y'} \\ M_{z'} \end{pmatrix} = \begin{pmatrix} -1/T_2 & -\Delta\omega_0 & \omega_{1y'} \\ \Delta\omega_0 & -1/T_2 & -\omega_{1x'} \\ -\omega_{1y'} & \omega_{1x'} & -1/T_1 \end{pmatrix}\begin{pmatrix} M_{x'} \\ M_{y'} \\ M_{z'} \end{pmatrix} + \begin{pmatrix} 0 \\ 0 \\ M_0/T_2 \end{pmatrix} \tag{2.55}$$

The strength of the radio field in the plane is represented by $\omega_{1x'}$ and $\omega_{1y'}$. $\Delta\omega_0$ is the offset of H_1 to the Larmor frequency of the nucleous, as seen before in Eq. 2.53. T_1 (spin-lattice relaxation) and T_2 (spin-spin transverse relaxation) are time constants for the exponential decay of M_z respectively M_x and M_y. They are specific properties of the sample and normally $T_1 \gg T_2$.

When the purpose in RF field mapping, the choice of the sample is intended to obtain long relaxation time compared to the pulse length. Regarding the longitudinal relaxation

time (T_1), the length of the prepartion has to be enlarged correspondingly. For what concerns the transverse relaxation (T_2), the nutation frequency has to be several orders of magnitude bigger than the half-line width of the observed peak.

Acquisition of the magnetization : At the end of this flipping period, the magnetization is detected by the probe. During the acquisition time t_2, a modulation by a cosine function, is performed to come back to the laboratory frame. If the relaxation is not considered the magnetization recorded along x is simply given by :

$$M_x = M_o \sin(\omega_1.t_1).\cos(\omega_o.t_2) \tag{2.56}$$

this is one component of the so called Free Induction Decay (FID). In practice the FID is fourier transformed, and the first point ($t_2 \to 0$) is accessed by measuring the area of the spectra. This is a first approximation to evaluate the intensity of the field H_1 by finding the correct pulse length t_1 associated with the projection of magnetization in the transverse plane.

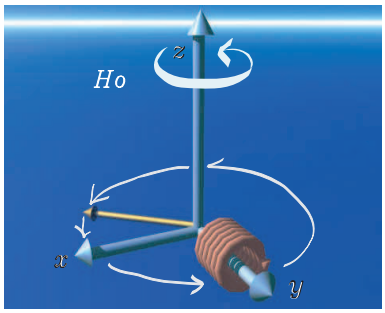

FIG. 2.11 – *During the evolution time, the projection of the Magnetization evolves and produces an Voltage at both ends of the coil by nuclear Faraday-induction.*

Finally $\mathbf{B}_1$ can be called 'Nutation field' and still considerd to refer to a magnetic field H_1. This is justified, form the point of view of microscopic Maxwell equations. We refer to the explanation given at the end of section 3.4.

2.6 $\mathbf{B}_1$ field as a function of the input power

We have seen that the perturbation of the distribution of magnetic energy produces a shift of the self resonant frequency of the circuit. Such energy can be written in two different manners :

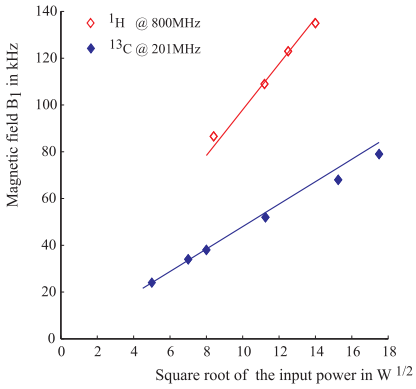

FIG. 2.12 – *Intensity of the* $\mathbf{B}_1$ *field as a function of the input power measured, in* $\sqrt{W}$*, for each channel using the same adamantane sample. The field intensity* $\mathbf{B}_1$ *was measured from the first 0 crossing of a nutation curve.*

$$\Delta\mathcal{E}_m = \frac{1}{2}\Delta L_{NMR}.I_o^2 \tag{2.57}$$

$$\Delta\mathcal{E}_m = \mu_o\vec{H}_1.\vec{H}_1^*\,\Delta\Omega = \frac{1}{\mu_o}|\mathbf{B}_1|^2\,\Delta\Omega \tag{2.58}$$

I_o is the current circulating in the NMR coil, whose expression is derived from the probe circuit's analysis :

$$I_o = \sqrt{\frac{2.\mathcal{P}^e Q_l}{\omega_o.L_{NMR}}} \tag{2.59}$$

here the RF field $\mathbf{B}_1$ is tuned to frequency $f_o = 2\pi.\omega_o$, whose quality factor is Q_l, and such channel is attacked by a pulse of power $\mathcal{P}^e$

From the fact that the magnetic energy density $\mathbf{B}_1^2/2\mu_o$ is equal to the RF power $\mathcal{P}^e$ supplied to the probe, multiplied by the magnetic filling factor ζ_{bs} divided by the frequency bandwidth ω_o/Q_l of the probe and divided by the volume of the element referring to ζ_{bs}, the expression for the field magnitude $\mathbf{B}_1$ is given by :

$$\mathbf{B}_1 = k\sqrt{\frac{2\mu_o\mathcal{P}^e\zeta_{bs}Q_l}{\omega_o\,\Delta\Omega}} \tag{2.60}$$

where Q_l denotes the quality factor of the circuit with the lossy sample inside the RF coil, and ω_o is equal to the angular RF frequency. The filling factor ζ_{bs} is measured relative to the volume element $\Delta\Omega$. In an already cited paper from Doty $k\sqrt{2\mu_o\zeta_{bs}}$ is linked to a 'geometry factor', in our case the factor k takes into account the orientation of the coil

or resonator axis relative to the precession field $\mathbf{B}_o$. It considers also the linear relation between the magnetic field produced in the coil and the nutation frequency in the lab frame.

Finally in Eq. 2.60 we identify the volume $\Delta\Omega$ which has been already defined. This quantity can also be declared to be the *coil volume*[8]. Since it is clear for us that the volume perturbed is small in comparison the the entire volume under the NMR probe-cover, this is perfectly acceptable under the statement of the perturbation approach. But in fact $\Delta\Omega$ already corresponds to a significant fraction of the NMR coil. When the $\mathbf{B}_1$ field distribution follows a Gaussian distribution, the point values probed by the ball shift at the coils center, correspond to the volume actually seen by a well positioned sample (as for example the 12 μl sample presented in Fig. 1.1).

To conclude this chapter, we introduce the following parameters describing the performance of a specific probe circuit, with a particular coil-sample arrangement. Some power $\mathcal{P}^e$ is sent to the probe channel. We can relate the square root of Power sent to the probe to the measured nutation field $\mathbf{B}_1$, as predicted by Eq. 2.60. Here the figure 2.12 presents results obtained for an 800 MHz probe used in solid-state MAS esperiments. The power was measured with a scope DS06102A (Agilent technologies). Conversion of the power level at the 50Ω cables from the preamplifer was done through an attenuator of almost -50dB (frequency dependent value). The power is taken at the probe connector. The definition of power efficiency, or power conversion factor η used in the last chapter can be introduced here as the nutation frequency rate squared per unit of power $\mathcal{P}^e$.

[8] as done in Eq. 7 of the article from Doty [44]

3

Description of waveguides used in NMR probes

3.1 Propagation of Electromagnetic field in TEM

The analysis of transmision line probes [154] must be considered as a particular case of the broader problem of propagation in waveguides. As in many RF electronics problems, this implies solving Maxwell equations to calculate the electromagnetic (EM) spacial field distribution. As stated by J.C Slatter ' When ideas of transmission lines lead to the same results as Maxwell's equations they are right, thought superfluous, when they lead to different results they are wrong[9]'

3.1.1 Maxwell equation for monochromatic waves

Supposing a monochromatic wave of angular frequency ω propagating in a medium whose physical properties are such that it is considered linear, homogeneous and isotropic. In macroscopic media the electric $\vec{E}$ and magnetic fields $\vec{H}$ are linked to the electric displacement $\vec{D}$ and the magnetic induction $\vec{B}$ (simply called the magnetic field in most of the NMR litterature) through permitivity and the permeability thanks to the simplification of the material equations seen in the previous chapter (Eqs. 5.15 and 5.16), to denote propagation in vacuum :

$$\vec{B} = \mu_o \mu \vec{H} \tag{3.1}$$

$$\vec{D} = \epsilon_o \epsilon \vec{E} \tag{3.2}$$

[9]Pr. J.C Slatter, in 'Microwave transmission 1st ed.' p 79 Dover Pub. Inc.

the wave of electric or magnetic field can be described respectively by complex vectors as :

$$\vec{E} = \vec{E}_o e^{i\omega t}$$
$$\vec{B} = \vec{B}_o e^{i\omega t}$$

if there are charges (ρ) and currents ($\vec{J}$) in the propagating media, the Maxwell equation writes :

$$\begin{aligned} -r\vec{o}t\vec{E} = \frac{\partial \vec{B}}{\partial t} &= i\omega\vec{B} \\ r\vec{o}t\vec{H} = \frac{\partial \vec{D}}{\partial t} + \vec{J} &= i\omega\vec{D} + \vec{J} \\ div\vec{D} &= \rho \\ div\vec{B} &= 0 \end{aligned} \tag{3.3}$$

In the following we consider no charges nor currents in the propagating media and we simplify the equations, introducing the speed of light as $c = 1/\sqrt{\epsilon_o \mu_o}$, we get :

$$\begin{aligned} -\vec{\nabla} \times \vec{E} &= i\omega\vec{B} \\ \vec{\nabla} \times \vec{B} &= i\omega\frac{\mu\epsilon}{c^2}\vec{E} \\ \vec{\nabla}.\vec{E} &= 0 \\ \vec{\nabla}.\vec{B} &= 0 \end{aligned} \tag{3.4}$$

3.1.2 Isotropic Propagation

The most general case of EM waves is the case of a point source spreading. No boundary condition is considered to guide it.The EM wave is then called 'spherical'. In this case the propagation is isotropic in all directions of space.

The EM field distribution is calculated through a pair of elliptical differential equations, called Helmholtz equations. These are obtained from the two first maxwell equations

by application of $\vec{\nabla}$ at both sides of them. From vectorial analysis we know that,

$$\vec{\nabla} \times (\vec{\nabla} \times \vec{E}) = \vec{\nabla} (\vec{\nabla}.\vec{E}) - \nabla^2 \vec{E} \tag{3.5}$$

since there are no free charges, the third Maxwell equation applies and

$$div(\vec{E}) = 0$$

and then the combination of the two first equations writes :

$$\begin{aligned} \nabla^2 \vec{E} + \mu\epsilon(\frac{\omega}{c})^2 \vec{E} = & \quad 0 \\ \nabla^2 \vec{B} + \mu\epsilon(\frac{\omega}{c})^2 \vec{B} = & \quad 0 \end{aligned} \tag{3.6}$$

∇^2 is also called the Laplacian. In order to simplify the equations we introduce the factor k called wave factor and defined in this case as

$$k^2 = \mu\epsilon(\frac{\omega}{c})^2 \tag{3.7}$$

3.1.3 Separation of axial and longitudinal components in (X, Y, Z) frame.

Introducing separation of axial (Z) and transverse (t) components of the EM fields appears as a requirement to analyse the distribution field distribution in any NMR coil. To do this we can select a cartesian frame, whose transverse plane is such that the electrical (and magnetic) part write as :

$$\vec{E} = \begin{bmatrix} \vec{E}_t \\ \vec{Z} \times \vec{E}_t \\ E_Z \end{bmatrix} ; \vec{B} = \begin{bmatrix} \vec{B}_t \\ \vec{Z} \times \vec{B}_t \\ B_Z \end{bmatrix}$$

In this frame the direction of each of the two first components, representing the transverse field is not relevant, what counts is the vector $\vec{Z}$ which denotes the direction of propagation. In addition $\nabla_Z = \frac{\partial}{\partial Z}$, and the $\vec{\nabla}$ vectorial operator expresses himself as :

$$\vec{\nabla} = \begin{bmatrix} \vec{\nabla}_t \\ \vec{Z} \times \vec{\nabla}_t \\ \frac{\partial}{\partial Z} \end{bmatrix} \tag{3.8}$$

The vectorial product is here used as an algebraic trick to define a third component orthogonal to the two others. To simplify this notation we state that $\vec{\nabla}_t$ is the vectorial sum of the two first components.The choice of notations made here become interesting when we express in (X, Y, Z) the vectorial product $\vec{\nabla}_t \times \vec{B}$ as follows :

$$\vec{\nabla}_t \times \vec{B} = \begin{bmatrix} \vec{\nabla}_t \\ \vec{Z} \times \vec{\nabla}_t \\ 0 \end{bmatrix} \times \begin{bmatrix} \vec{B}_t \\ \vec{Z} \times \vec{B}_t \\ B_Z \end{bmatrix} = \begin{bmatrix} \vec{Z} \times \vec{\nabla}_t B_Z \\ -\vec{\nabla}_t B_Z \\ \vec{\nabla}_t . \vec{Z} \times \vec{B}_t - \vec{Z} \times \vec{\nabla}_t . \vec{B}_t \end{bmatrix} \tag{3.9}$$

The Maxwell-Fararay equation from 3.4 will be decomposed using the previous expression of the rotational from $\vec{E}$:

$$-\vec{\nabla}_t E_Z + \frac{\partial \vec{E}_t}{\partial Z} = -i\omega \vec{Z} \times \vec{B}_t \tag{3.10}$$

$$\vec{Z}.(\vec{\nabla}_t \times \vec{E}_t) = -i\omega . B_Z \tag{3.11}$$

and the Maxwell-Ampère will admit a similar decomposition :

$$-\vec{\nabla}_t B_Z + \frac{\partial \vec{B}_t}{\partial Z} = i\omega \frac{\mu\epsilon}{c^2} \vec{Z} \times \vec{E}_t \tag{3.12}$$

$$\vec{Z}.(\vec{\nabla}_t \times \vec{B}_t) = i\omega \frac{\mu\epsilon}{c^2} . E_Z \tag{3.13}$$

the third Maxwell equation (Gauss) will be written then as follows :

$$\vec{\nabla}_t . \vec{E}_t + \frac{\partial E_Z}{\partial Z} = 0 \tag{3.14}$$

Considerations on low-E field coil

Low-E field coils as Z-coils, loop-gaps, scroll-coils, dielectric resonators and other resonators of cylindrical geometry provide a pratical example of how to use the previous decomposition.

Here we intend to demonstrate, in a quite phenomenological way, that any improvement of the field homogeneity will have an impact on the sample heating. Magnetic field created in such coil is produced by superposition of propagating waves. Geometry of NMR coils used for HR-MAS induce in a favorized direction of propagation, and the frame described in this Section an vizualized in Fig. 1.5 can be involved to decompose the axial and transverse parts of the fields. Our aim is to derive a general principle concerning $\mathbf{B}_1$ homogeneity and $\mathbf{E}_1$ field for cylindrical geometries.

In case of a wave propagation along OZ, the transverse divergence of the magnetic field writes as the electric field in Eq. 3.14 :

$$\vec{\nabla}_t \cdot \vec{B}_t = -\frac{\partial B_Z}{\partial Z} \tag{3.15}$$

If $\vec{B}_t$ is constant in space, all components of $\mathbf{B}_1$ in the transverse plane (OXY), will cancel their derivatives ($\partial/\partial X$ and $\partial/\partial Y$ will be equal to 0). From this we deduce the two following properties of the magnetic field :

$$\vec{\nabla}_t \cdot \vec{B}_t = 0 \tag{3.16}$$

$$\frac{\partial B_Y}{\partial X} - \frac{\partial B_X}{\partial Y} = 0 \tag{3.17}$$

First, from equation 3.16), we derive that if there is no radial inhomogenity then $\partial B_Z/\partial Z$ must also cancel. In other words, *transverse homogeneity implies axial homogeneity*. And then, from the second equation 3.17, we realize that since Maxwell Ampère says :

$$(\vec{\nabla} \times \vec{B})_Z = \frac{\partial B_Y}{\partial X} - \frac{\partial B_X}{\partial Y} = -i\omega.\frac{\epsilon\mu}{c^2}.E_Z$$

we can then state that transverse homogeneity means no $\mathbf{E}_1$ field projection along the coil axis. For all above mentioned resonators we can state the folowing phenomenological rule : *Good Magnetic transverse homogeneity* $\Longrightarrow$ *Less Electric energy in the coil*

3.1.4 Derivation of the Helmholtz problem in the case of guided propagation

Supposing now that a perfect electric conductor extends infinitely in one direction ($\vec{Z}$). We distinguish the longitudinal dimension given by Z and the transverse plane (X, Y) denoted by the subscript t. Then with this assumption $\vec{E}$, and $\vec{B}$ fields will be writen using the principle of the separation of variables :

$$\begin{aligned} \vec{E}_{(X,Y,Z,t)} &= \vec{E}_{(X,Y)}.e^{\pm\gamma Z+i\omega t} \\ \vec{B}_{(X,Y,Z,t)} &= \vec{B}_{(X,Y)}.e^{\pm\gamma Z+i\omega t} \end{aligned} \tag{3.18}$$

where γ is the longitudinal propagation factor of the EM wave, and $\pm\gamma$ denotes that both forward and backward propagation are possible. γ is a complex number, whose real part designates the damping of the traveling wave.

With these notations the Laplacian operator will be, according to the separation in two normal components :

$$\vec{\nabla}^2 = \vec{\nabla}_t^2 + \frac{\partial^2}{\partial Z^2}.\vec{Z} \tag{3.19}$$

The new pair of Helmhotlz equations is obtained directly from the one defined previously (3.6). The Laplacian is applied to the forward traveling wave $(+Z)$, and we obtain :

$$\begin{aligned} \nabla_t^2\vec{E} + (k^2+\gamma^2)\vec{E} &= 0 \\ \nabla_t^2\vec{B} + (k^2+\gamma^2)\vec{B} &= 0 \end{aligned} \tag{3.20}$$

Now we use the decomposition of the field vectors defined previously to express the transverse part of the field ($\vec{E}_t$, and $\vec{B}_t$) as a linear combination of the longitudinal part of the field (E_Z,B_Z).

We derive the Helmoltz equation as for the isotropic case, but applying the transverse part of the rotational to both sides of the two first Maxwell equations. The full derivation follows :

$$\begin{aligned} \vec{\nabla}\times\vec{E} &= -i\omega\vec{B} \quad \Leftrightarrow \\ \vec{\nabla}_t\times(\vec{\nabla}\times\vec{E}) &= -i\omega(\vec{\nabla}_t\times\vec{B}) \quad \Leftrightarrow \end{aligned}$$

$$\vec{\nabla}_t(\vec{\nabla}_t.\vec{E}) - (\nabla_t^2\vec{E}) = \quad -i\omega(\vec{\nabla}_t \times \vec{B}) \quad \Leftrightarrow \tag{3.21}$$

Now invoquing equations 3.14, and 3.20, this last simplifies and we write :

$$\gamma.(\vec{\nabla}_t E_Z) + (k^2+\gamma^2)\vec{E}_t = -i\omega(\vec{\nabla}_t \times \vec{B}) \tag{3.22}$$

This result is quite independent of the frame as long as the longitudinal component remains the $\vec{Z}$ direction. We remark that $\vec{\nabla}_t E_Z$ does not cancel in most cases. The former equation can be generalized to a two component transverse field, and an analogous reasoning will drive us to a similar expression of the transverse part of the magnetic field, finally this gives, after projecting in the frame defined by Eq. 3.9 :

$$\begin{aligned} \vec{E}_t &= \frac{1}{(k^2+\gamma^2)}.[-\gamma\vec{\nabla}_t E_Z - i\omega Z \times \vec{\nabla}_t B_Z] \\ \vec{B}_t &= \frac{1}{(k^2+\gamma^2)}.[-\gamma\vec{\nabla}_t B_Z - i\frac{k^2}{\omega} Z \times \vec{\nabla}_t E_Z] \end{aligned} \tag{3.23}$$

These equations are the general solution of the Helmoltz equation for a longitudinal propagation. The EM wave can be guided by a single conductor like a waveguide or a helix it can also be guided inside of a two conductor structure like in a transmission line. We distinguish many modes of longitudinal propagation, TE (transverse electric) or TM (transverse magnetic) or a mixture of both. The characteristics of those modes are summarized in one table 3.1. We take note of a degenerate or special type of solution, called the transverse electromagnetic (TEM) wave. This solution has only field components transverse to the direction of propagation.

3.2 The TEM wave

The Transverse Electromagnetic (TEM) mode also called *Lecher wave* applies when $k^2 + \gamma^2 = 0$ in this case the longitudinal components E_Z and B_Z must cancel. The caracteristic propagation factor γ of the TEM writes

$$\gamma = i\sqrt{\mu\epsilon}\,\frac{\omega}{c}$$

3.2.1 Orthogonality of $\vec{E}_t$ and $\vec{B}_t$

From Eqs.3.11 and 3.12 it is seen that if $E_Z = 0$ and $B_Z = 0$ then $\vec{E}_t = \vec{E}_{TEM}$ satisfies :

$$\vec{\nabla}_t \times \vec{E}_{TEM} = 0 \ ; \ \vec{\nabla}_t . \vec{E}_{TEM} = 0 \tag{3.24}$$

This means that $\vec{E}_{TEM}$ is a solution of an electrostatic problem in two dimensions. Since the boundaries at the conductor surface impose, $\vec{E}_t = 0$ and $H_n = 0$ the orthogonality of electric and magnetic part are extended to all the volume and therefore :

$$\vec{E}.\vec{B} = 0$$

The second consequence is that the magnetic field deduced from Eq.3.10 , is

$$\vec{B}_{TEM} = \pm \frac{\vec{k} \times \vec{E}_{TEM}}{\omega} \tag{3.25}$$

based on the fact that $k = \sqrt{\mu\epsilon}\frac{\omega}{c}$

3.2.2 Phase Velocity

The phase velocity of the wave is given by

$$V_\phi = \frac{\omega}{|\gamma|} \tag{3.26}$$

Then the definition of the longitudinal propagation factor, allow us to write the first constant of the TEM waves :

$$V_\phi = \frac{c}{\sqrt{\epsilon\mu}} \tag{3.27}$$

It can be demonstrated that whenever a couple of conductors propagates TEM modes the velocity of this wave will be a constant. We note that if L and C are the inductance and the capacitance between these conductors the product $\sqrt{LC}$ is homogeneous to a time constant, and when dividing the conductors lenght by this product we will obtain a speed. This is equal to the phase velocity of the equation 3.27 and the velocity is the same whatever inductance and capacitance we can imagine. Therefore the factor $\sqrt{\epsilon\mu}$ is encountered as soon as the time constant ($\sqrt{LC}$) is expressed for the TEM lines.

3.2.3 Wave impedance

The derivation of the second constant of the TEM waves involves the introduction of the concept of wave impedance. It results an expression of the TEM field as in the equation 3.18. We show now that we can express the first maxwell equation 3.4 as follows in a cartesian frame :

$$\vec{\nabla}_t \times \vec{B} = -i\omega\vec{B} \Rightarrow \begin{bmatrix} \gamma E_Y \\ \gamma E_X \end{bmatrix} = \begin{bmatrix} -i\omega\mu_o\mu H_X \\ i\omega\mu_o\mu H_Y \end{bmatrix}$$

whose components simplifies using the definition of γ, and the wave impedance is introduced as :

$$\frac{E_X}{H_Y} = \sqrt{\frac{\mu\mu_o}{\epsilon\epsilon_o}} \approx 377.\sqrt{\frac{\mu}{\epsilon}} = Z_{TEM} \tag{3.28}$$

as for the previous factor, this ratio appears in the definition of the characteristic impedance and this whatever propagating structure is considered, as soon as the TEM wave is propagated. In the vacuum the wave impedance is a constant equal to $337\,\Omega$, this is a mathematical limit because in the free space we are in an isotropic propagation, and therefore we must refer to the simplified Helmholtz equations 3.6. This is the reason why, whenever we want to calculate the impedance from the distributed inductance and capacitance in a TEM problem, we invoque :

$$Z_{TEM} = \sqrt{\frac{L}{C}} \tag{3.29}$$

3.3 Application of the TEM description to various geometries

3.3.1 Application to the spiral

The strip-line model is a geometry that can be applied to all transmission lines containing a dielectric of rectangular transverse section (thickness d and width w.) The spiral inductor can be treated, as well with this approach as soon as the bending do not prevent the TEM mode to propagate. We first calculate the length of the dielectric band, and after derivation of the distributed capacitance and inductance we evaluate the self resonance frequency when being in the range of the quarter of the frequency wavelength.

Length of the dielectric band for the scroll-coil This model consider the radius of the spiral as a function of the turns, in the mathematical description this radius increases linearly in such a way that the distance from turn to turn is kept identical. The linear integral over the number of tuns (n_t) of a spiral with starting radius (r_i) and outer radius (r_o) is the following :

$$l_{spiral} = \pi.n_t.(r_o + r_i) \tag{3.30}$$

Distributed capacitance and inductance The capacitance and the inductance estimated for any strip line are directly related to the transmission line theory, stating that there is a TEM mode propagating trought the strip transverse section. The wave propagates in a dielectric of relative permitivity and permeability ϵ and μ.

$$\begin{cases} C = \epsilon_o \epsilon \frac{w}{d} .l_{spiral} \\ \\ L = \mu_o \mu \frac{d}{w} .l_{spiral} \end{cases} \tag{3.31}$$

In general the dielectric is not magnetic and μ can be taken equal to unity. C is expressed in Farad, and L in Henry.

Self-resonance The Thomson law is used in order to derive the self resonance for the previous electrical parameters. In the frame of the transmission line theory this resonance corresponds to the first lambda quarter mode and can be experimentally measures by connecting one end of the scroll coil to the ground and leaving the other one to a high potential.

$$f_o = \frac{1}{2.\pi} \frac{1}{\sqrt{\epsilon}} . \frac{c}{l_{spiral}} \tag{3.32}$$

this is the case of all transmission lines of this section. This approach can be used also in scroll coils as the wave propagated in the dielectric between the turns is simply a TEM mode.

3.3.2 Application to the Coaxial line

The coaxial line model can be applied to all transmission lines whose transverse section contains a inner conductor and a surrounding shield. In general these are two concentric conductors of circular transverse section and we define the outer radius of the central conductor as a and inner radius of the outer conductor as b.

Distributed capacitance and inductance The capacitance and the inductance estimated for any concentric coaxial line are derived as in the preceding subsection.

$$\begin{cases} C = \epsilon_o \epsilon \frac{2\pi}{\ln(b/a)} . l_{coaxial} \\ \\ L = \mu_o \mu \frac{\ln(b/a)}{2\pi} . l_{coaxial} \end{cases} \tag{3.33}$$

The equation 3.32 applies here again, with $l_{coaxial}$. The impedance of the coaxial line is given by the well known formula :

$$Z_o = \frac{60}{\sqrt{\epsilon}} . \ln\left(\frac{b}{a}\right) \tag{3.34}$$

3.3.3 Application to the pair of coupled lines

The coupled lines problem refers to a cathegory of transmission lines having two conductors, which are not concentric. In such case, transverse section considers two inner conductor and no surrounding shield.In the The simpliest case we define a common diameter of the two conductors : a and a distance between the center of each of them : h. Again the lenght is defined as $l_{bifilar}$

Distributed capacitance and inductance The capacitance and the inductance estimated for any bifilar line is in the simplest case :

$$\begin{cases} C = \epsilon_o \epsilon \frac{\pi}{\ln(2.h/a-1)} . l_{bifilar} & \approx \epsilon_o \epsilon \frac{\pi}{\ln(2.h/a)} . l_{bifilar} \\ \\ L = \mu_o \mu \frac{\ln\left(h/a+\sqrt{(h/a)^2-1}\right)}{\pi} . l_{bifilar} & \approx \mu_o \mu \frac{\ln(2.h/a)}{\pi} . l_{bifilar} \end{cases} \tag{3.35}$$

Whithin the approximation made when the diameter of the line a becomes infinitely small the equation 3.32 applies here again, with $l_{bifillar}$.

3.4 Propagation in hollow waveguide, and resonant cavities

The cavities can be produced by placing end faces on a length of cylindrical waveguides. Our objective is to place the study of resonators in the same theoretical frame as the analysis of NMR coils.In hollow cylinders, and most coils can be treated as such, there occur two types of field configuration : the transverse magnetic (TM) and the transverse

electric (TE) waves. These are both solutions from the wave equation 3.6. Boundary conditions at the wall surface $\mathcal{S}$ as decribed previously in section 2.2 allows to summarize them in the table 3.1.

The scalar E_Z (for TM) and H_Z (for TE) satisfies the two-dimensional wave equation :

$$\begin{aligned}(\nabla_t^2 + \gamma^2).E_Z &= 0 \\ (\nabla_t^2 + \gamma^2).H_Z &= 0\end{aligned} \tag{3.36}$$

where different solutions called the *modes of the guide* may be considered as eigen values γ_m. The wave factor writes in this case of guided propagation :

$$k_m^2 = \mu\epsilon(\frac{\omega}{c})^2 - \gamma_m^2 \tag{3.37}$$

If we define the cutoff frequency of a mode ω_m,

$$\omega_m = \frac{\gamma_m}{\sqrt{\mu\epsilon}}c \tag{3.38}$$

then the wave factor of Eq. 3.37 can be written :

$$k_m = \sqrt{\mu\epsilon}.\frac{\sqrt{\omega^2 - \omega_m^2}}{c} \tag{3.39}$$

When the wave factor is imaginary, the modes are then called *evanescent modes*, such modes cannot propagate. The dimensions of the guide allow certain modes to apperar at certain frequencies. The eigen modes are those where the storage of EM energy is the highest. Since the wave factor k_m is always less than the free-space value $\omega\sqrt{\mu\epsilon}$, the wavelenght in the resonnant waveguide is always greater than the free-space wavelength.

TAB. 3.1 – *Important identities for TE and TM modes*

Mode	Axial Field	Boundary condition at $\mathcal{S}$	Transverse field
TM	$B_Z = 0$	$E_Z\|_{\mathcal{S}} = 0$	$\mathbf{E}_t = \pm\frac{ik}{\gamma^2}\nabla_t.E_Z$
TE	$E_Z = 0$	$\frac{\partial B_Z}{\partial n}\|_{\mathcal{S}} = 0$	$\mathbf{H}_t = \pm\frac{ik}{\gamma^2}\nabla_t.H_Z$

In turn the phase velocity V_ϕ is larger than the infinite space value :

$$V_\phi = \frac{\omega}{k_m} = \frac{1}{\sqrt{\mu\epsilon}} \frac{1}{\sqrt{1 - (\frac{\omega_m}{\omega})}} > \frac{1}{\sqrt{\mu\epsilon}} \tag{3.40}$$

This does not mean that some signal could propagate faster than the speed of light (p 337 [78]). The group velocity, associated to transmission of energy, or information is always smaller than the speed of light.

In the the frame of NMR resonators, it is interesting to note that the difference between coils and cavities, is done regarding the wave factor k. In the case of coil the compression of the wavelenght obtained along the propagation direction allows to shorten the physical lenght of the traveling wave. To understand this, a complette derivation of Helmholtz equation involving *periodic boundary conditions*, is needed. This task will require the introduction of an additional propagation factor β considering a longitudinal and a transverse propagation.

3.5 The helix model

RF electromagnetic fields in solenoidal coils can be calculated on the basis of a variety of models. The simplest one consists in adopting the quasi-stationary approximation and to apply Biot-Savart's formula. This approach yields reasonable results for coils with diameters below 10 mm and NMR frequencies below 100 MHz. It does not take into account the dielectric response of the NMR sample and it also neglects effects caused by shielding the coil. For higher frequencies it is necessary to consider explicitly that

(i) the effective electromagnetic wavelength in the coil is shorter than the free wavelength ;

(ii) this compressed wavelength may become comparable to the coil dimensions (thus the quasi-stationary approximation breaks down) ;

(iii) the dielectric and/or conductive properties of the NMR sample become more and more noticeable.

Inductances as distributed elements should be treated as transmission lines [117] at high frequency. This section gives an analitical approach to wavelengh compression and impedance, in infinitely long helices.

In order to treat this situation adequately and to find out the actual RF field distribution in the solenoidal coil, it is necessary to start calculations from first principles, either by solving Maxwell's equations with numerical solution methods, or by calculating the wave equation derived from them, analytically. Such numerical methods like, for example,

finite-element or finite-difference techniques are based on discrete models and powerful algorithms exist for a wide variety of electromagnetic phenomena. A straightforward alternative to numerical solutions exists for geometries with high symmetry. Here analytical or semi-analytical approaches can be applied where the specific coil geometry and sample shape can be taken into account as analytical boundary constraints to the solutions of the inhomogeneous Helmholtz equation. In the following we will address the simulation of the RF fields in solenoidal coils by referring to this latter technique. For the case of cylindrical symmetry it results that if the longitudinal components (directed along the cylinder axis) of the electric and magnetic fields are known solutions of the homogeneous Helmholtz equation, then the transverse field components can be calculated from these longitudinal components. In first approximation the helix coil can be considered as a cylinder where the current along its circumference is tilted by a pitch angle ψ and along the cylinder axis the coil exhibits a translational symmetry with the period p (pitch length). This model is referred to as sheath helix model, it allows to predict the effective wave propagation factor for solenoidal coils with remarkable precision in the NMR frequency range up to 1 GHz and for coils with diameters below 10 mm. The longitudinal period length of the helix (pitch length p) yields an equation expressing the periodic boundary condition for the longitudinal (electric E_Z and magnetic H_Z) field components $\mathcal{X}$ expressed in cylindrical coordinates (ρ, Z, θ) :

$$\mathcal{X}\Big(\rho, Z + Z_1, \theta + \frac{2\pi Z_1}{p}\Big) = \mathcal{X}(\rho, Z, \theta)\exp(+j\beta_e Z_1) \tag{3.41}$$

$\mathcal{X}$ is equal to E_Z or H_Z, Z_1 denotes a translation along the helix axis, while $2\pi Z_1/p$ is equal to a simultaneous rotation around that axis. Eq. 3.41 states that the electromagnetic field in a helix changes only by a phase factor $\exp(+j\beta_e Z_1)$ when such a rotation is performed. The origin of Eq. 3.41 as a symmetry condition can be understood from the fact that solving the homogeneous Helmholtz equation $\Delta\mathcal{X}(\rho, Z, \theta) + \beta^2\mathcal{X}(\rho, Z, \theta) = 0$ with a propagation factor β *periodically varying in space* (because the helix is a periodic structure) is equivalent to solving the Helmholtz equation $\Delta\mathcal{X}(\rho, Z, \theta) + \beta_e^2\mathcal{X}(\rho, Z, \theta) = 0$ with the *effective and spatially constant* propagation factor β_e and requiring Eq.3.41 as a periodic boundary condition. This is mathematically expressed in Floquet's theorem[54], a general theorem about the solution of linear differential equations with periodic coefficients. Based on the overall cylindrical symmetry (as solution to the Helmholtz equation) the following mathematical statement expressible as a Fourier series of a space periodic function can be made for the longitudinal field components :

$$E_{Z,m}(\rho, Z, \theta; t) \;=\; \Big(A_m I_m(h_m\rho) + B_m K_m(h_m\rho)\Big)\exp\Big(i(\omega t - \beta_m Z + m\theta)\Big)$$

$$E_{Z,m}(\rho, Z, \theta; t) = \Big(A_m I_m(h_m\rho) + B_m K_m(h_m\rho)\Big) \exp\Big(i(\omega t - \beta_m Z + m\theta)\Big) \tag{3.42}$$

where I_m and K_m denote modified Bessel functions of first and second kind, $\beta_e = \beta_0$ is equal to the effective propagation factor, $\beta_m = \beta_e + 2\pi m/p$, with Fourier order m, and the quantity h_m is equal to the transverse propagation factor (of mode order m) defined as

$$h_m^2 = \beta_m^2 - k^2 > 0$$

with k equal to the firstly defined wave vector in free space (Eq. 3.7). If the longitudinal field components are known, the transverse components result from the same calculations than 3.23 [49, 78]

$$\begin{aligned} H_\rho &= \frac{1}{k^2+\gamma^2}\Big[-\gamma\frac{\partial H_Z}{\partial\rho} + i\omega\epsilon_o\epsilon\frac{1}{\rho}\frac{\partial E_Z}{\partial\theta}\Big], \qquad H_\theta = \frac{1}{k^2+\gamma^2}\Big[-\gamma\frac{1}{\rho}\frac{\partial H_Z}{\partial\theta} - i\omega\epsilon_o\epsilon\frac{\partial E_Z}{\partial\rho}\Big], \\ E_\rho &= \frac{1}{k^2+\gamma^2}\Big[-\gamma\frac{\partial E_Z}{\partial\rho} - i\omega\mu_o\mu\frac{1}{\rho}\frac{\partial H_Z}{\partial\theta}\Big], \qquad E_\theta = \frac{1}{k^2+\gamma^2}\Big[-\gamma\frac{1}{\rho}\frac{\partial E_Z}{\partial\theta} + i\omega\mu_o\mu\frac{\partial H_Z}{\partial\rho}\Big], \end{aligned} \tag{3.43}$$

ϵ, μ and γ are the permitivity, the permeability and the wave factor in guided propagation,respectively. The constant coefficients A, B, C, D, appearing in Eqs.3.42 have to be determined by taking into account the transverse boundary conditions separating various spatial regions in radial direction -(a) the region outside the helix, (b) the region outside of that cylinder, but still inside the helix, and (c) the region inside the dielectric NMR sample (assumed to be of cylindrical shape). The resulting constraints for tangential and normal field components read : (i) fields have to remain finite for $\rho = 0$, i.e., at the helix axis. (ii) For the surface of a dielectric cylinder (for example, constituting the NMR sample) inside the helix coil we require the tangential components of the magnetic and electric field to be continuous, provided that the conductivity of the dielectric cylinder is equal to zero (which we assume in the following). (iii) At the surface of the radially thin, helically wound conductor (supposed to have very high conductivity), we require that the electric field component parallel to the current direction vanishes, i.e., the tangential electric field may have only a component perpendicular to direction of the current traveling through the helix. (iv) For that component perpendicular to the helix current we require that the tangential electric field component perpendicular to the direction of the helix current is continuous inside the helix and in the outer space surrounding the helix. (v) Finally, the tangential component of the magnetic field parallel to the helix (current) direction is continuous inside and outside the helix [144, 49]. In the sequel only the zero order mode

is considered as the dominant mode, which is justified as long as the wavelength is large compared to the helix diameter (denoted by $2a$). From equations 3.42-3.43 and the radial boundary condition outlined above, the following characteristic equation can be derived :

$$\frac{2\pi a \cot\psi}{\lambda_0} = h_0 a \sqrt{\frac{I_0(h_0 a)K_0(h_0 a)}{I_1(h_0 a)K_1(h_0 a)}} \tag{3.44}$$

From that transcendental equation the radial propagation factor h_0 can be determined which defines the wavelength compression factor of the helix to be :

$$\frac{\lambda_0}{\lambda} = \sqrt{1 + \left(\frac{\lambda_0}{2\pi} h_0\right)^2} \tag{3.45}$$

By Eqs. 3.42,3.43 and 3.44 all field components inside the helix can be determined. If these are known, we are able to derive the current distribution J_Σ along the helix surface (Σ) that would generate the field just calculated, because the discontinuity of the tangential magnetic field component at the helix surface is proportional to that current density

$$|\mathbf{H}_{bT} - \mathbf{H}_{aT}| \propto J_\Sigma$$

$\mathbf{n}$ denotes the vector normal to the helix surface, $\mathbf{H}_{aT}$ is equal to the tangential field outside the helix at its surface, $\mathbf{H}_{bT}$ is equal to the tangential field at the surface inside the metal conductor. For very high conductivity $\mathbf{H}_{bT}$ decays rapidly to zero, (infinitesimally small skin depth), such that practically $\mathbf{H}_{aT} \propto |J_\Sigma|$. In order to obtain the field distribution for a solenoidal coil of finite length, the following approximation can be made : we take the current distribution along the helix surface obtained from the above sheath helix model to be equal to the current distribution of a wire helix. It can be shown that parameters like, wave compression and field distribution inside the solenoidal coil of finite length are characterized correctly by making this assumption [49]. The current distribution known, it can be used to recalculate the detailed magnetic field of the finite solenoidal coil [96]. The solutions of the Helmholtz equations with current as source term, are the so called retarded potentials :

$$\mathbf{B}(\mathbf{r},t) = \frac{\mu_o \mu}{4\pi} . e^{i\omega t} \int_l e^{-i.\frac{\omega}{c}\sqrt{\epsilon\mu}|\mathbf{r}'-\mathbf{r}|} \times \Big(-\frac{i\omega\sqrt{\epsilon\mu}}{c} \frac{1}{|\mathbf{r}'-\mathbf{r}|^2} - \frac{1}{|\mathbf{r}'-\mathbf{r}|^3} \Big) (\mathbf{r}'-\mathbf{r}) \times J_l(\mathbf{r}') d\mathbf{r} \tag{3.46}$$

where J_l, the linear current distribution along the helix wire, can be obtained directly from the current distribution J_Σ. Position vector $\mathbf{r}$ specifies the point in space where

the field is to be evaluated, position vector $\mathbf{r}'$ the point at the helix wire with current $J_l(\mathbf{r}')$. By introducing cylindrical coordinates (ρ, Z, θ) Eq.3.46 will now provide the basis to obtain the magnetic induction field $\mathbf{B}_1 = f(\rho, Z, \theta; t)$. The computation of the $\mathbf{B}_1$ fields inside a solenoidal coil using Eq.3.46 provides some reliable information on the spacial field distribution. In this equation phenomenae like helix wave compression and fringe fields are included, however the dielectric properties of the sample and its detailed shape inside and outside the coil are not considered. Also the more distant vicinity of the coil is not taken into account (e.g., MAS stator and shielding of the probe).

4

Numerical methods to solve Maxwell equations

4.1 Introduction to Finite integration technique

The present chapter provides some information regarding fundamental assumptions involved in the numerical simulations. These where performed with the commercial program Microwave Studio^{TM} [10]. Some example and applications of CST can be found in NMR literature [43, 44, 70]. This is indeed the better alternative we found to finite element (FEM) codes also successfully employed in coil design and RF mapping [123].

Time domain solvers are those using the forward and backward propagation of waves in order to establish a standing electromagnetic wave over a structure in the time. These techniques provide a spatial discretization scheme, applicable to various electromagnetic problems,over a broad frequency domain. What is specific of CST is the FIT (Finite Integration Technique) now presented. The integral form of the Maxwell equations 2.1 is developed in the following way :

$$\begin{aligned}
\oint_l \vec{H}\,\vec{dl} &= \int_\Sigma (\vec{J_s} + \frac{\partial \vec{D}}{\partial t})\, d\vec{\Sigma} \\
\oint_l \vec{E}\,\vec{dl} &= -\int_\Sigma (\frac{\partial \vec{B}}{\partial t})\, d\vec{\Sigma} \\
\oint_\Sigma \vec{D}.d\vec{\Sigma} &= \int_\Omega q\, d\Omega \\
\oint_\Sigma \vec{B}.d\vec{\Sigma} &= 0
\end{aligned}$$

[10] Version 2006B from Computer Simulation technology, Darmstadt. From now refer here uniquely as CST

(4.1)

the definition of the fields is the same as what has been given previously in Eq.2.1

The two last equations are introduced using Gauss-Ostrogradski's transformation of the divergence operator, similar to the Stokes transformation for the rotational operator. In order to solve these equations numerically all finite difference time domain codes will define a finite calculation domain enclosing the considered application. By creating a suitable rectangular mesh system, this domain can be split up into several small parallelograms so-called grid cells, for mere simplicity reasons we propose here the example of a cubic[11]cell.

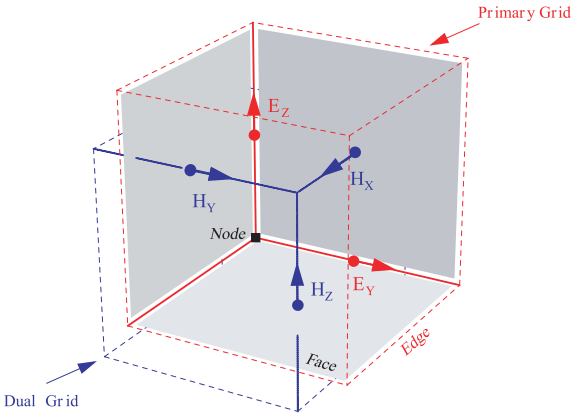

FIG. 4.1 – *Dual grid known as Yee's cell.*

Presented in Fig. 4.1 is the first or *primary* mesh. It can be visualized and refined with manual, or automatic algorithms. An important parameter is the mesh ratio per wavelength to be entered manually, other refinements are done from automatic identification of edges, vertices, singular points in the device under test. In addition to this primary mesh a dual grid mesh is generated to solve the complementary part of the EM wave.

The spatial discretization of Maxwell's equations is finally performed on this two orthogonal grid systems : the primary $\mathcal{G}$ and dual $\tilde{\mathcal{G}}$. Referring to the following figure 4.2, the Maxwell-Ampere equation is solved considering a magnetic field on the contour edges of the dual grid, and the electric displacement (plus the current in the case of conductive media) is derived at the faces of the primary grid. The resolution of the Maxwell-Faraday equation is solved in analogous way using the primary grid for the electric field and the nodes of the dual grid at the surface of this first one (figure 4.3 illustrates this). The advantage of such approach, called Leap-Frog scheme, is that time propagation of signal

[11]This rectangular meshing is deprecated and has been replaced by hexagonal or tetrahedral meshes

from one mesh to another in either primary or dual grid, is feasible for any kind of input signal.

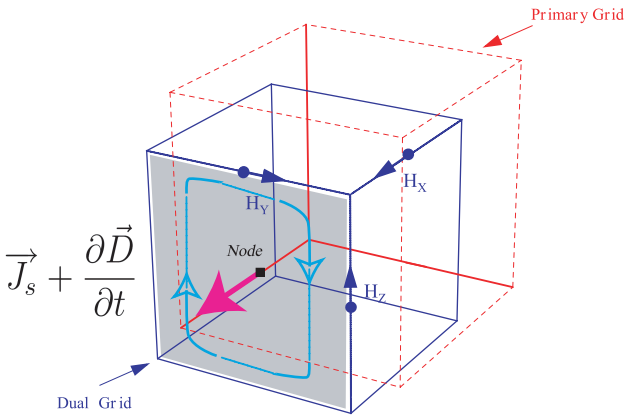

FIG. 4.2 – *Loops of magnetic field used to derive currents.*

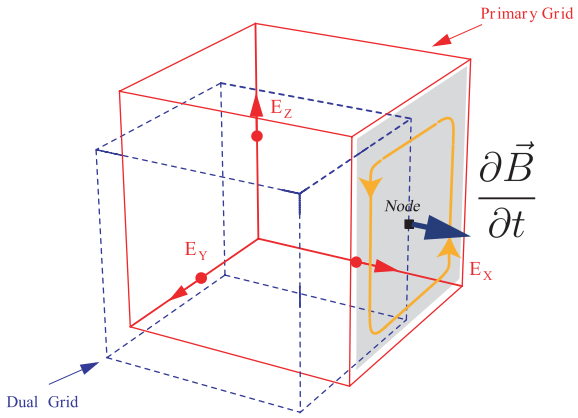

FIG. 4.3 – *Circulation of the Electric field in order to derive the flux* Φ.

In practice FIT formalism formulates the fields involved in Maxwell's equations, for each edge of the cell facets as vectors of a discretized space. The magnetic excitation (**h**) and the corresponding electric displacement **d** are assigned to the dual grid, as shown in figure 4.2 and the electric grid voltage **e** and magnetic induction **b** are allocated to the primary grid as presented by 4.3. Considering Ampere's law, the closed integral on the equation's left side can be rewritten as a sum of four grid magnetic potentials h_i, h_j, h_k, h_l, without introducing any supplementary quantification error. Consequently, the surface currents if present, and time derivative of the displacement currents at the surface defined on the enclosed cell facet represents the right-hand side of the equation, as illustrated by the figure 4.2. By repeating this procedure for all available cell facets, the calculation rule can be summarized in an elegant matrix formulation, involving the matrix **C** whose

coefficients are $C_{ij} \in \{-1, 0, 1\}$. This is a discretized representation of the rotational operator '$\nabla\times$' in the space $\tilde{\mathcal{G}}$ which includes all topological information of the structure to analyze [20]. In equivalent way, the divergence '$\nabla.$' is substituted by a matrix $\mathcal{S}$. The discretization of the four Maxwell equations introduced discrete operators $\mathcal{S}$ and $\tilde{\mathcal{S}}$, belonging respectively to the primary and dual grids. The complete set of discrete matrix equations, the so-called Maxwell-Grid-Equations (MGE) is now given by :

$$\begin{aligned} \tilde{\mathcal{C}}\mathbf{h} &= \mathbf{j} + \frac{d}{dt}\mathbf{d} \\ \mathcal{C}\mathbf{e} &= -\frac{d}{dt}\mathbf{b} \\ \tilde{\mathcal{S}}\mathbf{d} &= \mathbf{q} \\ \mathcal{S}\mathbf{b} &= \mathbf{0} \end{aligned} \tag{4.2}$$

At this point it is interesting to note that numerical resolution of both $\mathbf{h}$ and $\mathbf{e}$ can be driven only through a rectangular 3D meshing. Finally the missing material equations introduce the inevitable numerical inaccuracy due to spatial discretization. By defining the necessary relations between voltages and fluxes their respective integral values have to be approximated over the grid edges and the cell areas. Consequently, the resulting coefficients depend on the averaged material parameters as well as on the spatial resolution of the grid and are summarized again in the correspondent matrices :

$$\begin{aligned} \mathbf{b} &= \mathbf{M}_\mu \mathbf{h} \\ \mathbf{d} &= \mathbf{M}_\epsilon \mathbf{e} \\ \mathbf{j} &= \mathbf{M}_\sigma \mathbf{e} + \mathbf{j_S} \end{aligned} \tag{4.3}$$

This specific formulation of Maxwell equations allows solving electromagnetic problems from quasi-statics to high frequency using transient analysis where n denotes the time-period step. When time derivatives are replaced by central differences then the following propagation equations appear :

$$\begin{aligned} \mathbf{e^{n+1/2}} &= \mathbf{e^{n-1/2}} + \Delta t \mathbf{M}_\epsilon^{-1}[\tilde{\mathcal{C}}\mathbf{M}_\mu^{-1}\mathbf{b^n} + \mathbf{j_S^n}] \\ \mathbf{b^{n+1}} &= \mathbf{b^n} - \Delta t \mathcal{C}\mathbf{e^{n+1/2}} \end{aligned}$$

(4.4)

Yielding this explicit update formulation for the simplest loss-free case is common to many other time domain algorithms (the FDTD codes), including the case of FIT, but also CFDTD [35], among others. Most time domain simulators employ the method proposed originally by Yee [149] in 1966. While Yee simply replaces the partial derivatives in Maxwell's rotational equations by central finite differences, Weiland [146] went further ahead and derived an equivalent discretization approach using finite integration of Maxwell equations in 1977 (Eq. 4.1).

Nevertheless it is important to distinguish FIT from other time domain methods. The development from Weiland is based indeed on Yee's first approach but only regarding the idea of a scattering of pulse. The discretization proposed by Yee was based on the differential form of the Maxwell equations, as it was the case for the early CFDTD [35], and most FDTD methods, but this is not the case of FIT which start directly with the integral form of the Maxwell equations. This is much better adapted to volumic circuits, since no approximation is made while solving the Maxwell equations in free space.

4.2 Considering Material properties for numerical simulation

All components get a physical assignment in order to fill the material property matrices $\mathbf{M}_\mu, \mathbf{M}_\epsilon, \mathbf{M}_\sigma$. Materials can be defined either as *normal*, describing isotropic media, or as *anisotropic* with consideration of their tensor of anisotropy. Conductivity in dielectrics and the introduction of material losses leads to define complex relative permittivity [12] as :

$$\epsilon = \epsilon' - i\epsilon''$$

here we stick to time dependence convention of preceding chapters with $\exp(i\omega t)$. Dispersion, defined as a frequency dependance of materials is often encountered in lossy samples. Time domain methods are particularly adapted to solve Maxwell equations in complex dispersive media. Later, in a chapter dedicated to thermal effects, we will investigate the RF irradiation process. Dispersive material have a frequency dependent relative dielectric conductivity called σ_{eff} :

$$\sigma_{eff} = (\sigma_{ion} + \omega\epsilon_o\epsilon'') + i\omega\epsilon' \tag{4.5}$$

[12] The material permeability is described in an analogous way, but since material used in NMR sample tend to be transparent to magnetic field we will not insist on μ

This definition of conductivity was found elsewere in the literature [126, 12, 70]. The analysis of conductivity performed in this thesis is in fact based on the effective permitivity, and considers again the two contributions :

$$\epsilon_{eff} = \epsilon' - i(\frac{\sigma_{ion}}{\omega\epsilon_o} + \epsilon'') \tag{4.6}$$

the static conductivity σ_{ion} depends strongly on the salt concentration, or more precisely to the ionic strenght, in practice this term decays rapidly at high frequencies and the dominant term is ϵ''. Here ϵ_{eff} is a relative permitivity and ϵ_o the already defined permitivity of vacuum. When considering a first order Deby model for the imaginary part of the permittivity, as it has been proposed for polar solvants [70], as well as for bicelle sample [126, 82] the precedent equation becomes :

$$\epsilon(\omega) = \epsilon_\infty + \frac{(\epsilon_s - \epsilon_\infty)}{1 + i\,\omega\tau^c} \tag{4.7}$$

were ϵ_s is the static permittivity, ϵ_∞ is given at an infinite frequency. This phenomenological model introduced by the Physical Chemist Peter Debye (1884-1966) considers relaxation process τ^c and can be applied to most NMR samples [70].

For a model including the ionic conductivity a general dispersion model of second order can be involved :

$$\epsilon(\omega) = \epsilon_\infty + \frac{\beta_o + i\omega\beta_1}{\alpha_o + i\omega\alpha_1 - \omega^2} \tag{4.8}$$

, this model is used in the program to describe dispersive materials, the coefficients to be entered are written according to the following formulas :

$$\begin{aligned} \beta_o &= \frac{\sigma}{\epsilon_o\tau^c} \\ \beta_1 &= \frac{\sigma}{\epsilon_o} + \frac{\Delta\epsilon}{\tau^c} \\ \alpha_o &= 0 \\ \alpha_1 &= \frac{1}{\tau^c} \end{aligned} \tag{4.9}$$

The plot of figure 10.3B was done using this model.

4.3 Practical aspects of CST-based EM calculations

The programming task involved to solve the integral form of Maxwell equation given by Eq. 4.1, can not be done by a single person in the time frame of a thesis. CST, based on the fundamental concepts expressed here, present some particularities. For instance, the way structures are excitated, or the means to check convergence, and even the possibility to chose between time domain or eigen mode solving, is valuable information for our study.

4.3.1 Role of the different type of excitation ports in CST

Excitation waves are the inputs of the time domain solvers. In CST the amplitude of those time dependent stimulations are normalized to one (in $W^{\frac{1}{2}}$ as signal amplitudes) for the wave guides ports mostly used in this work. Four types of signals can be applied to the structure as described in the following :

Wave guide port

Waveguide ports represent a special kind of boundary condition of the calculation domain, enabling the emission as well as the absorption of energy. Note that these boundaries do not need to be at the edge of the meshing region. They can be selected for example, around a contour of the inner TL shield, or in the end face of the dielectric filling a waveguide. The ports have to be aligned with the Cartesian frame's directions. CST allows calculating possible higher modes at the wave guide port plane with the help of a 2D eigen-mode solver. The superposition of an infinite number of those modes represents all possible electromagnetic field solutions in the port region, certain waveguides are designed to carry many different modes and this can be explicitly addressed by the solver. In RF also, degenerate modes need to be considered when using two conductors coupled inside a shield (odd and even modes of the ^{1}H WB tunning-matching parallel TL's for instance). Usually the TEM mode is sufficient for most problems involving coaxial lines as feed-troughs. The number of modes to be considered in the solver calculation can be defined in the waveguide port dialog. Out of that S-parameters are to be derived, with possible renormalization of the wave impedance or of the physical length of the TL during the post-processing of the results.

Plane waves

The *plane wave* tool simulate an incident wave from a source located far away to the observed object. The propagation vector, as the polarization of the waves can be

set. These excitations are of great importance when optimizing immunity behind a shielding, or reciprocally the radiation pattern of a Probe. CST can be used prior to acquire measurements required for electromagnetic compatibility validation.[13]

Discrete ports

Beside waveguide ports or plane waves the discrete ports offers another possibility to feed the calculation domain with power. Three different types of discrete ports are available. The excitation can be considered as (i) a voltage or (ii) current source or (iii) as an impedance element which absorbs some power and enables S-parameter calculation. Voltage port realizes a voltage source, exciting with a constant voltage amplitude. In case that this port is not stimulated during the transient analysis the voltage along the wire is set to 0 (short-circuit). The voltage excitation signal will be recorded during the solver run. Current port type realizes a current source, exciting with a constant current amplitude. S-Parameter port is modeled by a lumped element, consisting of a current source with an inner impedance, which excites and absorbs power. This port delivers as default a Gaussian signal of 14.14 V peak (pure source of 10 V RMS), which provides 0.5 W to the coil when matched to 50 Ω [44]. This is compatible to what has been said before because the source impedance is also matched to 50 Ω and the current circulating is 0.1 A RMS (calculated with 10 V RMS in series with 100 Ω). In addition to the calculation of S parameters, it is also possible to monitor the voltage across and the current trough the discrete ports, note that the orientation of the port is used to determine the phase of the S-parameters. Discrete ports are contained in the volume of a single mesh and applied to the two points thanks to the shortest possible perfectly conducting wire, therefore positioning the discrete ports should be done carefully to avoid any other element of the structure to be short-circuited.

Excitation signals

The pulses applied to the structure can be of various shapes depending on the frequency domain to stimulate. The default is Gaussian, but arbitrary shapes can be designed. A macro allows to define arbitrary shapes. The fields amplitude as a function of frequency has to be multiplied by the envelope of the frequency window, it is known that CST enlarges the boundaries of the frequency domain asked by the user, so the window function is not to be considered by the user when comparing data.

[13] These measures are done according to the norm IEC 61326, which refers to RF immunity and emissions for electrical equipment.

Pulse response analysis, use of field probes

CST performs transient analysis to compute the discrete $\mathbf{e}_i$ and $\mathbf{h}_i$ vectors from an input time signal. The FT is computed from the pulse signals, the time signal therefore imposes it's own excitation profile as in NMR pulse sequences, so some care has to be taken in choosing the pulse shape. Since all $\mathbf{e}_i$ and $\mathbf{h}_i$ vectors are computed after each time step of the pulse we could follow the build up of the EM fields in time by just setting a *field probe* at a specific location and storing the updated calculated fields as an ASCII file at this specific time step. It is in principle inherent to the time domain method employed by CST to give access to transient analysis or pulse response of a tested structure. But the time-lengths of the probing pulse is 10^3 smaller than the NMR pulse lengths.

Excitation of ports in order to simulate standing waves and Balance

Excitation of two port as NMR and ESR coils in a balanced situation requires that standing waves can be simulated. The advantage of two port excitation is the ability to reproduce balance, by influencing the phase of each excitation, and by adding on the calculated solutions for each of the two excitations, the definition of electrical balance states that a standing wave $\mathcal{X}$ is the superposition of two waves called forward and backward, in such a way that one can write, introducing the superposition :

$$\mathcal{X}_{standing} = \mathcal{X}_{forward}.e^{i\pi/2} + \mathcal{X}_{backward}.e^{-i\pi/2} \tag{4.10}$$

In practice it is possible by stimulating one after the other the two ports, incident waves from one port to the other are the forward and backward waves are needed to compute the standing wave. The way to proceed is straightforward : (i) In the transient mode solver the source type has to be all selected ports, so the ports will be stimulated sequentially.(ii)One of the special solver Parameters states per default that the two-port reciprocity should be considered, if needed (when the sample is dispersive) this can be deselected in order to force two independent excitations.(iii) After the simulation is done, calculation results are combined, at this point the combination can be done considering a phase shift of $\pm\pi/2$ in order to represent a symmetric loading. Amplitude can also be modified for the considered frequency. If we can estimate by perturbation means the Electric field at the end of both TL, this can enter into the consideration of a well-balanced situation. Finally (iv), for S-parameters calculations, there is the possibility to renormalize the Impedance at the port (wave impedance) to other values. In addition de-embedding of S-parameters allows to enlarge the TL length arbitrarily without increasing the number of mesh cells. This will allow observation of resonances observed by connecting the coil to

two parallel TL's.

The simulation of the circuit impedance at both ends of the coil can also be intended by inserting RLC circuits at the end of both ports, in the standard version of CST ; more complex circuits will involve nodal analysis (Vipec, Touchstone, Microwave Office, CST Design Studio, etc...). Our experience is that nodal analysis is sometimes the fastest way to get to the right resonant frequency. But since it requires some assumptions based on the EM field distribution, nodal analysis has to refer to a resolution of the Maxwell equations.

4.3.2 Means to evaluate convergence

Convergence means that all stability criteria are meet so we can consider the solution to be reproducible from one experiment to another. CST provides means to validate results within each single transient analysis pass, and over an adaptive mesh refinement. This last problem needs to be solved systematically in order to ensure that EM field solutions are almost independent from the meshing, they involve at least two or three iterations.

In the case of CST there is an two important monitors to follow : (i) The so called 'energy' of the system, this function of time represents the travel of EM energy over the structure. In the time-dependent process initiated after the pulse there is a build-up during the first period (corresponding to the pulse length) and after the curves passes a maximum of energy stored, a logarithmic decay is observed due to absorption of energy in the ports. Indeed when considering S-parameters, the energy dissipation in the ports is the main criteria for assuming steady state. This energy is the sum of what is inserted i_n at port n minus what gets out from j ports $o_{n1}; o_{n2}, ...o_{nj}$. Like ports, open space will also radiate energy. The convergence of the solver is bounded to this decay, but if the system is resonant the energy will be stored in the structure, as described by the physical definition of the quality factor : *the energy stored divided by the energy dissipated per cycle (Eq. 2.41)*. Therefore no energy dissipation will be detected and the convergence may be worse or even not possible.(ii) Another criteria is the 'balance' defined as $\sqrt{|S_{nn}|^2 + |S_{jj}|^2 + ...}$ this parameter is an amplitude expressed over the frequency range. The closer to unity we are, the less radiations will be shown in the structure. The dispersion from this value at other frequencies proves that the structure gets lossy or dispersive there. The convergence criteria is again based on the difference on scattering parameters from one the results obtained after one pass to the next one, default convergence error for the adaptive mesh refinement is less than 2%.

4.3.3 Eigen mode calculations

For eigen-mode calculations, ie. to predict the self resonances of the considered structure, or for frequency domain analysis, the two first Maxwell equations are needed, as soon as all conductors are lossless, and no induced charges are considered. The Helmholtz differential equation is derived as presented afterwords in Chapter 3. There this calculations involves the discrete formulation of the rotational differential operator. This is a matrix inversion problem, as it can be solved by any FEM code, with complex inversion algorithms. In the case of CST, thanks to incorporated eigen-mode and frequency domain analysis on full hexagonal meshcells (tetrahedral mesh is possible as an option) Helmholtz equation can be solved even in the static case (Laplace equation) for electrostatic comparisons. In oder to do this the space has to be closed with perfect electric boundaries obeying $\vec{E}_t = 0$, corresponding to a Faraday cage, the perfect shielding box, or magnetic boundaries obeying $\vec{H}_t = 0$ (and where no currents loops can be induced in the shield) to avoid shield resonances. Far field radiation is a specific problem involving absorbing boundaries (called *open*) and absorbing boundary conditions called also perfectly matched layers.

For CST using the discretization of the rotational operator in the primary grid $\mathcal{C}$ and in the dual grid $\tilde{\mathcal{C}}$, the simplest form of Helmholtz equation writes :

$$\tilde{\mathcal{C}}\,\mathbf{M}_{\mu}^{-1}\,\mathcal{C}\,\mathbf{e} = \omega^2\,\mathbf{M}_{\epsilon}\,\mathbf{e} \tag{4.11}$$

where $\mathbf{M}_{\mu}$ is the matrix of permeabilities over the meshcells, and $\mathbf{M}_{\epsilon}$ the matrix of permittivities. The eigenmode solver is based on this eigenvalue equation for non-driven and loss free harmonic problems. The solution of this second order differential equation is obtained in the loss-free case via a Krylov-Subspace (AKS) or Jacobi-Davidson method (JDS) for lower frequencies when losses need to be taken in account. The solving method is not a time domain anymore, but the mesh stays the same as for the transient analysis. This specific matrix inversion may require more RAM than in the transient case, therefore we may have to decrease the mesh size. For the frequency domain analysis the currents need to be addressed at the different interfaces :

$$(\tilde{\mathcal{C}}\,\mathbf{M}_{\mu}^{-1}\,\mathcal{C} - \omega^2\,\mathbf{M}_{\epsilon})\mathbf{e} = -i\omega\mathbf{j} \tag{4.12}$$

where $\mathbf{j}$ is the current vector over the different meshcells.

4.4 Strengths and weaknesses of Finite time domain methods, and in particular to FIT used by CST

The RAM storage requirements for Finite difference Time domain (FDTD) and Transmission Line matrix method (TLM) are considerably lower than for other techniques like Method of Moments (MoM) or FEM. Propagation methods we mention first are time consuming but got no large matrix to invert. This means, in practice, that a personal computer is well suited for solving such problems. As a mere example, with rather small amount of RAM (512M) a Pentium IV can solve the field distribution in a resonant structure involving more than 450.10^3 meshcells in 3 hours (but not at the self resonance). The time domain response is subject to a so called *Discrete Fourier Fast Transform* to generate broadband frequency domain data in a single simulation.It permits the identification of various resonances along the frequency axis. This feature should very useful to identify modes, and specially for a comparison of what is measured by the network analyzer. The ability to inject arbitrary waveforms into a discretized structure allows us to simulate transient effects when applying an RF pulse. Another strength of time domain simulators is their ability to model nonlinear materials, boundaries, and devices in a natural way, this is particularly useful for the measures of SAR (specific absorption rate) in relation with human body, but can be even more easily employed for simulation of the coupling of lossy dielectric samples. On the other hand the convergence of FDTD depends on the size of the mesh, the number of required time steps, and the Q of the structure. The algorithm of convergence involves the decay of energy stored in a system under test, this is why high quality cavities are quite challenging for CST. In practice we can be overcome this by separating the port and un-matching the structure. Problems were operating at the self resonance frequency is required are quite seldom. For problems with very large aspect ratios we proved, that it is not easier to generate an FEM mesh than a FIT one (in spite of the situation described in Swanson and Höpfer's EM survey, CST has progressed considerably in the past few years [134]). Without doubt the evolution of most codes will continue in the next few months. This survey of FIT in regards to other programs will need to be updated. In particular nobody doubts in the future of the availability of promising Open Source EM field solvers distributions (EMAP4,NEC...), with brilliant academic perspectives. Such software would offer the best for our applications when adapted to our needs.

5

Equation of reciprocity and mathematical expression of the signal in NMR

The design and production of NMR probes faces the chalenge of sensitivity. Improvement of signal to noise is the probe developpers 'Daily bread'. Instruments such as NMR probes are concieved to recieve a signal from nuclear relaxation which is indeed weaker as a few tens of mV. In this section we try to explain the 'how' of the signal's detection at the probe's end. We will prove these derivations usefull when trying to extrapolate a certain $\mathbf{B}_1$ field distribution from a series of NMR measures'.

5.1 Polarization of the RF field pulses

In most cases the MAS coil generates a field linearily polarizated. Over the time period associated with the RF frequency (whose pulsation is set to ω) the field components will oscillate along OZ, if such is the polarization direction. It is convenient, for the calculation of density matrix evolution, to work in the so called 'rotating' frame. In order to do that, the linearily polarized field is decomposed in two rotating vectors (co-rotating components) of half the amplitude, inverse phase and pulsation ω. The component rotating in the inverse direction is considered to be non-effective for the NMR experiment. Such it is, that the amplitude of the voltage in the reciever coil is increased a factor of $\sqrt{2}$ when replacing the linear by circular polarized coil (p 77 in [1]).

The phase of the RF wave is critical to project the spin magnetization along the axis of this rotating frame, for example (the reference is arbitrary) hard pulses of phases ϕ

equal to $0^o, 90^o, 180^o, 270^o$ will project the magnetization along $y, -x, -y, x$ respectively. A clear tutorial of this fundamental property of the RF pulses can be found in p 53 of [14]. This justifies the introduction of the following general mathematical formulation of the time-harmonic field :

$$\mathbf{X}(r,t) = \mathbf{X}_c(r)\cos(\omega t) + \mathbf{X}_s(r)\sin(\omega t) \tag{5.1}$$

which includes the cases of linear and circular polarization. For convenience it is usual to bring this out by introducing complex vectors. Here we give then the notation $\mathcal{F}$. These are defined by :

$$\begin{aligned} \mathbf{X}(r,t) &= \Re e(\vec{\mathcal{X}}(r)e^{+i(\omega t+\varphi)}) \\ \vec{\mathcal{X}}(r) &= \mathbf{X}_c(r) + i\mathbf{X}_s(r) \end{aligned} \tag{5.2}$$

usage of these harmonic 'phasors' in differential equations will be usefull here.

.

5.2 Reciprocity as derived from the Maxwell equations

The signal is detected at the probe's 50 Ω connector.It is convenient to think of the connector as the hookup point of a tuned and matched resonant probe (not just a coil), that will be connected through a lossless transmission line and duplexer to an actual transmitter and reciever system.

To give a mathematical equation of the signal based on the physical phenomenon, we need to analyse the two sources acting during the excitation-reception cycle. We have to consider also the contribution of the electromagnetic sources in the Maxwell equations presented in the second chapter.

5.2.1 Sources at the emission stage and at the reception

On the other hand, the main source acting during the emission is a current $\vec{J}_s$, during the reception period the spin magnetization will induce a FEM accordingly to Faraday's law and the magnetic displacement flux source associated with nuclear magnetization writes :

$$\vec{\dot{B}}_s = \frac{\partial \vec{B}_s}{\partial t} = \mu_o.i\omega.\vec{\mathcal{M}}_s \tag{5.3}$$

where $\mathcal{M}_s$ is the spin magnetization described as a phasor.

Assuming for the moment that we are in a linear homogeneous and isotropic media. The Ampere and Faraday Maxwell equations admits the following expression during the emission $i = 1$ and reception $i = 2$ states :

$$\begin{aligned} \vec{\nabla} \times \vec{H}_i &= \vec{\dot{D}}_i + \vec{J}_{si} \quad (5.4) \\ -\vec{\nabla} \times \vec{E}_i &= \vec{\dot{B}}_i + \vec{\dot{B}}_{si} \quad (5.5) \end{aligned}$$

Now lets take the sum of products $\vec{E}_1$ by Eq. 5.4 with $i = 2$ and $\vec{H}_2$ by Eq. 5.4 with $i = 1$ the result is the first equation of 5.6. Proceeding with similar combinations, the following pair of equations appears using vectorial product properties :

$$\begin{aligned} \vec{\nabla}.(\vec{H}_2 \times \vec{E}_1) &= \vec{E}_1\vec{\dot{D}}_2 + \vec{H}_2\vec{\dot{B}}_1 + \vec{E}_1\vec{J}_{s2} + \vec{H}_2\vec{\dot{B}}_{s1} \\ \vec{\nabla}.(\vec{H}_1 \times \vec{E}_2) &= \vec{E}_2\vec{\dot{D}}_1 + \vec{H}_1\vec{\dot{B}}_2 + \vec{E}_2\vec{J}_{s1} + \vec{H}_1\vec{\dot{B}}_{s2} \end{aligned} \quad (5.6)$$

Now we perform the differences of these two equations, and at the end, we perform the volume integration over the volume Ω. By the meanwhile one can cancel the terms such as $E_1\dot{D}_2$ and $E_2\dot{D}_1$ who are clearly the same, in the case of lossless homogeneous media.

$$\int_\Omega \vec{\nabla}.(\vec{H}_2 \times \vec{E}_1) - \vec{\nabla}.(\vec{H}_1 \times \vec{E}_2)\, d\Omega = \int_\Omega (\vec{E}_1\vec{J}_{s2} - \vec{E}_2\vec{J}_{s1} + \vec{\dot{B}}_{s1}\vec{H}_2 - \vec{\dot{B}}_{s2}\vec{H}_1)\, d\Omega \quad (5.7)$$

Now lets apply the Gauss-Ostrogradsky transformation on the first member of Eq. 5.7 which becomes :

$$\oint_\Sigma (\vec{H}_2 \times \vec{E}_1)\, d\Sigma - \oint_\Sigma (\vec{H}_1 \times \vec{E}_2)\, d\Sigma \quad (5.8)$$

Both terms represents the flux of Pointing vectors across a closed surface in front of the conductive walls of the probe. The right member of this equation cancels. So, one may

notice that Eq. 5.7 is equivalent to :

$$\int_{\Omega}(\vec{E}_2\vec{J}_{s1} - \vec{B}_{s1}\vec{H}_2)\,d\Omega = \int_{\Omega}(\vec{E}_1\vec{J}_{s2} - \vec{\dot{B}}_{s2}\vec{H}_1)\,d\Omega \tag{5.9}$$

where fields ($\vec{E}_i$,$\vec{H}_i$) are created by sources ($\vec{J}_{s\,i}$,$\vec{\dot{B}}_{s\,i}$), and 'i' is the state considered. This equation means that, the response of the system (fields $\vec{E}, \vec{H}$) to a source ($\vec{J}_s$,$\vec{\dot{B}}_s$) is unchanged if cause and it's effects are interchanged (p116 in [68]) this is the simplest sense of the reciprocity theorem. In a more general sense, reciprocity relates a response at one source due to a second source to the response at the second source due to the first source. These two sources may be different in time or space, their link is their mutual influence. A modern Electromagnetic compatibility (EMC) version of the Reciprocity states again that 'A source of perturbation will perturb the surroundings with the same Electromagnetic pattern used by the surroundings to perturb it.' Electromagnetic reciprocity as it has been introduced by Lorentz in 1895 was quite general, and the formulation for NMR was first published by D.Hoult and R.Richards in their reference paper [74] and redeveloped some years latter in various reviews [72, 71], so that this principle was known among most NMR-scientists as 'Hoult's reciprocity theorem'. More recently NMR physicists have extended this principle by deriving it to analyse retardation [77] and to discuss it in the context of linear an circular polarizations [33, 71].

In practice the NMR setup allows certain specifications to the general equation of reciprocity 5.9, for instance induction in the NMR coil prior to any pulse ($\dot{B}_{s1}H_2$) is completely negligible. In addition, the left member admits a drastic simplification as soon as we admit to be in the case of lossless samples ($J_{s2} = 0$) no current source from the sample will be present during the reception state. Other simplifications allow us to restrict the volume of integration. For instance the left member of 5.9 will be integrated only over the volume containing the spins. This comes from the fact that the field cancels in the bulk conductor, specially if conductivity is considered infinite and skin depth is negligible. The signal will be collected only from spins within a finite volume. The usage of the filling factor ζ_{bs} serves to this purpose :

To introduce the source of current used during the pulsing state and the voltage generator measuring the spin induced EMF at the reception, we used the following volumic circuit comparable to a capacitor connected to a circuit. The gap of this capacitor (defined as $d\Omega_1 = d\Sigma\, dl$) is a volume represented by Fig.5.1 which can be constructed from an extruded surface where E is spatially homogeneous.

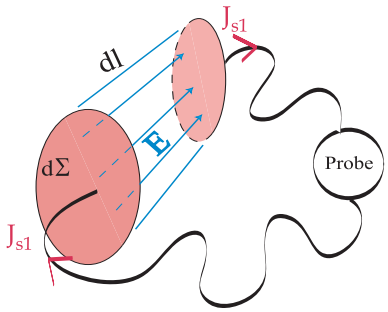

FIG. 5.1 – *Volume $d\Omega = d\Sigma.dl$ for the integration of the left side equation of reciprocity, decomposed as explained, in two regions where conduction, and displacement currents apply.*

5.2.2 First equation of the Voltage measured by the receptor

For the right hand member of Eq. 5.9, we rely on the assumption that there is no other sources of signal than the nuclei inside of the sample. The background signal of the probe is always minimized by removing materials such as Silicone, Teflon, Kapton that can add their own contribution, therefore the volume Ω can be restricted to the sample volume Ω_2 experimenting NMR of the coil.

$$\begin{aligned} \int_\Omega \vec{E}_2.\vec{J}_{s1}\, d\Omega &= -\int_\Omega \vec{H}_1.\dot{\vec{B}}_{s2}\, d\Omega \\ \Leftrightarrow \int_\Sigma \oint_l \vec{E}_2\, dl.\vec{J}_{s1}\, d\Sigma &= -\int_\Omega \vec{H}_1.\dot{\vec{B}}_{s2}\, d\Omega \\ \Leftrightarrow -V_2.I_1 &= -\int_\Omega \vec{H}_1.\dot{\vec{B}}_{s2}\, d\Omega \\ \Leftrightarrow V_2.I_1 &= i\omega \int_{\Omega_2} \vec{B}_1.\vec{\mathcal{M}}_s\, d\Omega_2 \end{aligned} \tag{5.10}$$

V_2 is the voltage detected at the probe's connector, I_1 is the RMS current sent to the coil over one cycle, Ω_2 is the sample volume, all other factors are related to the already defined electromagnetic field.

The last one of these equations is the so called *signal equation*, obtained by the application of Lorentz reciprocity principle. This equation is the general formula assuming no losses by radiation, thermal dissipation and so. Here again, the equipotential lines inside of the coil are the same during the pulse and during the reception of the signal.The schematic path represented by Fig.5.2 illustrates the approximations made : no significant counter-reaction from the spins during the pulsing, and open circuit during the acquisition of the signal.

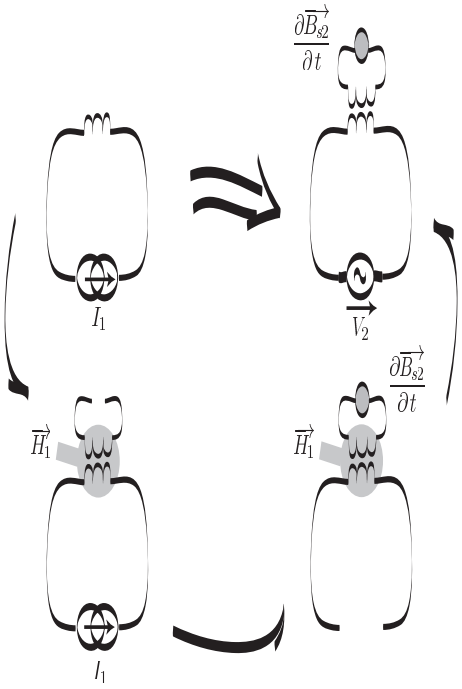

FIG. 5.2 – *Step by step description of the NMR experiment : During the pulse step (left-up) a current I_1 is applied to the coil (left-down), this produces a magnetic field $\mathbf{H_1}$, later the spin precession (right-down) will create a signal, by coupling between and the coil and the spins. Reciprocity tells us that the same magnetic profile created previously by I_1, now induces a voltage at the circuit's port (right-up).*

In fact we can prove that this situation describes indeed the real NMR signal but only as a first order approximation. It is perhaps useful to stress that this derivation of reciprocity doesn't neglect the field inhomogeneity, and can be applied for the two rotating components of the $\mathbf{B}_1$ as it has been clarified by Hoult and Van der Klink [71, 33].

5.3 Generalized reciprocity in materials

Even if the Hoult's derivation from 1976 was brillant, until a more recent work of Van der Klink in 2001 it was unclear how this equation was derived from classical electrodynamics. In addition it is perhaps useful to stress that the reciprocity theorem applies as long as Joule heating in the probe and the dissipation produced by finite conductivity in the sample is kept low. So a given I_1 will create a smaller H_1 when any of these losses becomes more important ; and the electric field E_2 at the reception diminishes. The proof starts from the formulation of Maxwell's equations in a medium, and therefore radiation and retardation effects could be included. The medium needs not to be homogeneous, but keeps everywhere linear and isotropic relations.

The NMR reciprocity implies to consider a precessing nuclear magnetic moment at point R comprising two orthogonal, linear oscillating magnetic moments in phase quadrature, and so the NMR experiment is analogous to having two coils, one pointing in the $\vec{x}$ direction and one in the $\vec{y}$ direction, through which we put currents in quadrature phase [71]. Since both components of the rotating magnetic field can be treated separately and added on afterwords using the superposition theorem. For the moment we will focus only on the 'right-hand' component in phase with the rotating frame.

The reciprocity principle has been widely discussed in antenna theory, where it means an invariance of a system when the transmitter and reciever are interchanged. It is also called 'electromagnetic reaction' by physicists [118]. Reciprocity applies to a certain type of material called *reciprocal media*. This last can be anisotropic as well. It considers, dielecric looses, as long as the permittivity and permeability of such material stay reversible so :

$$\bar{\bar{\epsilon}} = \bar{\bar{\epsilon}}^T \; ; \; \bar{\bar{\mu}} = \bar{\bar{\mu}}^T \tag{5.11}$$

where the double overbar distinguishes the dyadics, and ^{T} denotes the transpose operator, meaning in this case that time can be reversed and the same causes will produce the same effects. With this definition given by [124] reciprocal media is not necesarilly isotropic and lossless, as long as it's material properties remain in time (T-symmetry) which is a violation of the second law of thermodynamics.

Recently a new regard to the reciprocity theorem has been provided to incorporate the losses induced by the sample, and the impact on the co-rotating components of $\mathbf{B}_1$ [71, 33]. In the original formulation of reciprocity, two oscillating dipoles of moment $\vec{p}$ interact to each other in the following way : Let one dipole $\vec{p}_1 \cos(\omega t)$ be situated in a point R_1 and another $\vec{p}_2 \cos(\omega t)$ in a point R_2. Let the electric fields created by these dipoles be $\vec{E}_i(r)$. Then reciprocity is written as :

$$\vec{p}_1 \cdot \vec{E}_2(R_1) = \vec{p}_2 \cdot \vec{E}_1(R_2) \tag{5.12}$$

For the NMR application, we compare the electromagnetic fields of an electric dipole (representing the transmitter as a source of RF field) and a magnetic dipole (creating a voltage at the preamplifier's output in the probe's connector). In the transmitting case we suppose that the RF source is an electric polarization dipole $\vec{P}$ between the capacitor plates as described by Fig. 5.1, and we consider the magnetic field that it creates at some point R in the sample volume. In the receiving case, the source is a rotating magnetization dipole $\vec{\mathcal{M}}_s$ at that point R and we look for the electric field that it creates between those plates.

In the transmitter mode (index 1) :

$$\begin{aligned} \vec{P}_1(r,t) &= \vec{p}_1\delta(r)\cos(\omega t+\phi_1) \\ \vec{\mathcal{M}}_1(r,t) &= \vec{0} \end{aligned} \tag{5.13}$$

The pulse of amplitude p_1 is applied at the probe connector (denoted by a Dirac function $\delta(r)$). In addition it has a frequency given by ω and a phase ϕ_1 which serves as a reference for the following calculation.

In the receiver mode (index 2) :

$$\begin{aligned} \vec{P}_2(r,t) &= \vec{0} \\ \vec{\mathcal{M}}_2(r,t) &= m_2\,\delta(r-R)\Big(\sin(\omega t+\phi_2)\vec{x}-\cos(\omega t+\phi_2)\vec{y}\Big) \end{aligned} \tag{5.14}$$

The magnetization is measured at a point R. A spin having a magnetic moment of amplitude m_2 precesses at a frequency ω and a phase given by ϕ_2.

We consider the Maxwell equations, and the constitutive material equations as defined previously.

$$\vec{H} = (\vec{B}/\mu_o) - \vec{M} \tag{5.15}$$

$$\vec{D} = (\epsilon_o\epsilon\vec{E}) + \vec{P} \tag{5.16}$$

$$\vec{j} = \vec{j}^p + \sigma\vec{E} \tag{5.17}$$

Probe and sample are considered to have a relative permeability $\mu = 1$. The conductivity σ and relative permittivity ϵ are material properties specific to each sample. The two sets of Maxwell equations, at both steps will be developped as follows. First for transmission :

$$\vec{\nabla}\times\vec{H}_1 = \vec{j^p}_1 + \sigma\vec{E}_1 + \frac{\partial\vec{P}_1}{\partial t} \tag{5.18}$$

$$\vec{\nabla}\times\vec{E}_1 = -\mu_o\frac{\partial\vec{H}_1}{\partial t} \tag{5.19}$$

and then for reception :

$$\vec{\nabla} \times \vec{H}_2 = \vec{j^p}_2 + \sigma \vec{E}_2 + \epsilon_o \epsilon \frac{\partial \vec{E}_2}{\partial t} \tag{5.20}$$

$$\vec{\nabla} \times \vec{E}_2 = -\mu_o \frac{\partial \vec{H}_2}{\partial t} - \mu_o \frac{\partial \vec{\mathcal{M}}_1}{\partial t} \tag{5.21}$$

The terms containing the sample losses σ and the current density j^p can be incorporated in the expression of the complex effective permittivity ϵ_{eff} (refer to Eq. 4.6 and to chapter 10 for an detailled analysis of dielectric dispersion). The reciprocity is still fully valid when the losses become significant, as long as the material stays 'symmetric' in the sense given by Eq. 5.11. In linear analysis of systems based on scattering parameters S_{ij} a practical example of, how reciprocity has to be considered, is given. A two port circuit to be excited from one port to the other will need only a single calculation, because both transmission parameters (S_{12} and S_{21}) are equivalent. This is a property of linear devices that every RF engenieers dealing with pasive components understands. Hoult made use of such concept in an article published in year 2000 [71]. But when the device under test incorporates a lossy dielectric (such that the dispersion may create strong phase distorsions), the user should notify that the reciprocity may not be valid anymore.

The impact of such result in an NMR experiment can be accessed by measuring the decrease of signal to noise ratio of different salty samples when increasing the conductivity [81]. Or even simpler, by measuring the variation of the quality factor, which is related to the current density in the sample j^p [132, 92]

To derive the reciprocity from the preceding equations the calculations are similar as those employed in section 5.2. The solution for the case of linearly polarized $\mathbf{B}_1$ field is :

$$\begin{aligned} \vec{p}_1.\vec{E}_2(R) &= \vec{m}_2(R).\vec{B}_1(R) \\ \Phi_E(R) &= 2\Phi_B(R) - \pi/2 \end{aligned} \tag{5.22}$$

where Φ_E and Φ_B are the phases of the electric and magnetic vectors, we write $\vec{E}_2(R)$ to signify that the received signal is caused by a magnetic moment (a voxel) situated in R. In all cases $\vec{E}_2$ is the field that appears in the gap represented by Fig. 5.1. When considering a circularly polarized $\mathbf{B}_1$ a factor $\sqrt{2}$ multiplies the right term in Eq. 5.22.

An equation identical to Eq. 5.10 appears when expressing the dipole $\vec{p}_1$ as $q_1.\vec{l}$, with q_1 the charge and $\vec{l}$ the distance between the plates. Defining the current traveling through

the circuit as : $I_1 = q_1.\omega$. Then introducing the mesured voltage $E_2 = \Delta V_2/l$ with ΔV_2 the potential difference between the plates of Fig.5.1. And finnally considering the magnetization $m = M_o\Omega_2$ with Ω_2 the volume of the sample. But the integration of 5.22 is a delicate task due to the right member containing a vector product that can not be separated without loosing phase information.

Signal power as a function of the quality factor

Van der Klink defends that the reciprocity theorem takes care of all losses : by radiation (for inside-out NMR) by a finite quality factor of the coil, and by ohmic heating in the sample. So a given I_1 will create a smaller H_1 when any of these losses becomes more important ; and the voltage at the receptor V_2 diminishes by the same factor. The proof starts from the formulation of Maxwell's equations in medium. As the quality factor includes the sample's response, it is usefuly involved in the signal equations as follows in the next paragraphs. Quality factor is related to field distribution and it has been demonstrated in [33] that it stays the same during the reception stage as during the emission.

$$(\zeta_{bs}.Q)_1 = (\zeta_{bs}.Q)_2 \tag{5.23}$$

Using the general expression of the quality factor 2.42, and the consitutive equation 5.15, the product $\zeta_{bs}.Q$ becomes :

$$(\zeta_{bs}.Q) = 2\frac{\omega \int_{sample} \overline{B(\vec{\rho},t) \cdot M(\vec{\rho},t)}d\Omega}{\int_{space} \overline{\sigma(\vec{\rho})E(\vec{\rho},t) \cdot E^*(\vec{\rho},t)}d\Omega} \tag{5.24}$$

with the denominator containing the joule losses in the entire probe plus the dissipated power in an equivalent load, and replacing the numerator by the received power per cycle calulated in Eq. 5.2 the signal power is written :

$$\mathcal{P}^r \propto \zeta_{bs}.Q_s \tag{5.25}$$

where $\mathcal{P}^r$ is the power received in the detector according to the reciprocity principle, it refers to the product $V_2.I_1$ of Eq. 5.2, and includes the volumic amount of magnetization not explicitly designated here. Again, Q_s is the quality factor of the loaded resonator, and ζ_{bs} derives directly from the measured ball-shift perturbation as seen before (Eq. 2.40). From Eq. 5.25 is is clear that both entangled parameters Q and ζ_{bs} are products of the field inhomogeneity that undermines the sensitivity.

This is due to the influence of lossy samples on the RF distribution of non Low-E coil,

also defined as *E-field heating coils*. As we will discuss it in the last part the Q factor of a coil plays a key role in the identification of low-E field coils.

Other definitions of measured signal as the one done in instrumentation articles, like the one done by Clark[14], include a parameter where all nuclear spin properties are lumped. In Abragam (Eq 75 p 83 in [1]), the static magnetic field $\mathbf{B}_o$ is included as well. This drives us to another approach, complementary to the one here focused on reciprocity, and that is widely accepted within the NMR community : The signal intensity is proportional to $\gamma^3.\mathbf{B}_o^2$ (p 87 in [14]). The stronger the static magnetic field the better the signal. Nevertheless, at high-field, one knows from experience that the strong impact of sample losses, and the limitations of traditional RF circuits counteracts the gains expected from high supra-conductive $\mathbf{B}_o$ fields.

5.4 Conclusions on electromagnetic reciprocity

This last chapter concluded the part dedicated on electrodynamics with a description of the NMR measure, consistent with the reciprocity equation. This concept is crucial to pass from a bulk representation of $\mathbf{B}_1$ to a detailed microscopic caracterization of the fields.In the literature inferring field inhomogeneities from the nutation signal relies on a statistical description of the field distribution [66, 123, 137]. Most of the time such approach is sufficient to give a ratio of field inhomogeneity. Since we pretend to relate the signal to the *profile* of the distribution we can not bypass reciprocity. It is clear that the prediction of the nuclear magnetization states, as those discused in the next part, can be done without considering reciprocity explicitely [15], but for the coil engeniering this concepts play a key role. Specially when improving the field homogeneity for a given coil : the assumption of a signal directly proportional to the magnetization would mean that the $\mathbf{B}_1$ is the same in the entire sample volume. This is unfortunately never the case. Some inhomogeneities can be neglected, but assuming perfect homogeneity would contradict everyone pretending to improve the NMR coils. And we know that $\mathbf{B}_1$ inhomogeneity will become a limiting factor for the high-field multinuclear MAS of biological samples.

The simulations presented later in Fig. 8.7 will justify that, in the sample volume, the time-phase of the fields (ϕ) can be considered as constant. Such is not the case for the spacial-phase distribution (φ to be defined in the part III) introducted by the fact that not all field vectors are aligned in the same direction, this spacial $\mathbf{B}_1$ inhomogeneity will

[14] (Eq 8 in [19]) is based on another reference of the RF literature : Terman in 1943 [136].

[15] This approach based on the fact that signal is protortional to the magnetization can be found elsewere in excellent references [57, 156] among others already cited

be treated in the next part.

Finally we see that the limitation of the principle of reciprocity is given by the material itself. Non-reciprocal material as dispersive medium will break the exchange between the source and the absorber. As in classical mechanics, where frictions generates heat, the reciprocity is limited by the materials response. In fact this limitation is specially encoutered in highly dispersive samples often used for HR-MAS. This is the reason why sample heating will be treated in the part IV.

Part III
Influence of the Axial and Transverse components of the magnetic field on the NMR signal : Physical description

6

Density matrix approach to describe the consequences of RF field inhomogeneities

The description and understanding of NMR multi-pulse sequences can be approached trough the so called *vector treatment* as seen in previous part (section 2.5), or using the description of the evolution of magnetization, through the *density matrix formalism*. The first method is generaly restricted to simple cases, but most situations encountered in bi-dimensionnal sequences, spin-locking or complex decoupling schemes, require the second approach to be used. The density matrix is a tool employed to describe the state of an ensemble as well as its evolution in time. This formalism is usually suitable for the following effects :

(i) static field $\mathbf{B}_o$ Zeeman effect ;

(ii) RF field $\mathbf{B}_1$ transitions ;

(iii) scalar couplings ;

(iv) relaxation and exchange.

To describe the consequences of the RF field[16] inhomogeneity, on a rotating sample[17] the density matrix approach is needed, as we will see in the following. In this Part we restricted ourselves to simplified experimental conditions, involving one spin-1/2 in a deuterated water system (HDO), undergoing the both first effects (linked to the fields $\mathbf{B}_1$, $\mathbf{B}_o$). Within this frame we are going now to describe the fate of the nuclear magnetization.

[16] RF field pulsation in designated by $2\pi\nu_{rf}$

[17] Angular speed of the mechanical rotation is given by ω_r

6.1 Definition of the NMR Hamiltonian

This chapter pretends to give an introduction to density matrix calculations. The microsopic nature of the NMR experiment requires a quantum approach. Our previous electrodynamic analysis of coils has to be now involved to predict the magnetization states after pulsing with an inhomogeneous magnetic field. This last one is called $\mathbf{B}_1$ whithin the frame of such microscopic description. The experiment of Stern and Gerlach permitted the observation of a *quantized angular momentum* : the component applied along a defined axis of the intrinsic angular momentum of an atom can only take discrete values. In 1922 this experiment permitted a better analysis of the interferometric observation made by Zeeman 26 years before. Such names (among other) are related to quantum classification of nuclear, atomic, and molecular NMR spectra.

6.1.1 Nuclear spin Operator

The goal of this section is to clarify from first principles the action of the RF pulse on the evolution of the spin system. Since density matrix formalism has been extensively used to predict spin dynamics out of a particular distribution of magnetic field inside of the sample, it seems to us that this is a necessary tool to correlate the $\mathbf{B}_1$ field mapping with the NMR experiments. The operator produced by the magnetic field is an Hamiltonian $\mathcal{H}$ of energy given by :

$$\mathcal{H} = -\boldsymbol{\mu}.\mathbf{B} = -\gamma_r \hbar \, \mathbf{B}.\mathbf{I} \tag{6.1}$$

where γ_r is the already defined gyromagnetic ratio, $\hbar = h/2\pi$ the normalized Plank constant, and $\mathbf{I}$ is a dimensionless operator denoting the nuclear spin, linked to the spin angular momentum, intrinsic to the particle and often decomposed in components $\{\mathrm{I}_o, \mathrm{I}_x, \mathrm{I}_y, \mathrm{I}_z\}$, that are linked to a base of Pauli matrices $\{\tilde{\sigma}_o, \tilde{\sigma}_x, \tilde{\sigma}_y, \tilde{\sigma}_z\}$.

$$\mathcal{M} = \mathbf{I}\hbar = \frac{\hbar}{2}.\tilde{\sigma} \tag{6.2}$$

Pauli matrices

Performing operations with the angular momentum, requires a specific algebra. If we restrict ourselves to the development of a two state problem, the following set of two times two matrices forming a base of Pauli matrices, are well suited.

$$\tilde{\sigma}_o = \begin{bmatrix} 1 & 0 \\ 0 & 1 \end{bmatrix} \quad \tilde{\sigma}_x = \begin{bmatrix} 0 & 1 \\ 1 & 0 \end{bmatrix}$$
$$\tilde{\sigma}_y = \begin{bmatrix} 0 & -i \\ i & 0 \end{bmatrix} \quad \tilde{\sigma}_z = \begin{bmatrix} 1 & 0 \\ 0 & -1 \end{bmatrix} \tag{6.3}$$

6.1.2 Schrödinger's equation

The quantum state of any particle is described by it's state function or wave function Ψ a function of space coordinates and time. In addition Ψ has to satisfy the Schrödinger differential equation :

$$\mathcal{H}\,\Psi = i\hbar\,\partial\Psi/\partial t \tag{6.4}$$

One typically separates the partial differential equation by writing :

$$\Psi = \psi\,\exp(-i/\hbar E\,t) \tag{6.5}$$

where ψ is a function of the coordinates alone. Equation 6.4 becomes

$$\mathcal{H}\,\psi = E\psi \tag{6.6}$$

This is an eigen-value problem for the Hamiltonian operator $\mathcal{H}$, described by eigen values corresponding to quantified energy levels E_n and an associated base of eigenfunctions Φ_n is introduced according to the following expression :

$$\mathcal{H}\,\Phi_i = E_i\Phi_i \tag{6.7}$$

As an immediate consequence we can expand the time-independent wave function Ψ as a linear combination of time-independent eigenfunctions,

$$\Psi = \sum_k c_k\,\Phi_k \tag{6.8}$$

since the Φ_k's are constants, the coefficients c_k must carry the time dependence.

Now we briefly explain how to solve the Schrödinger equation for an Hamiltonian corresponding to the RF pulse.

6.2 Density of probability and quantum state evolution

The *density matrix* is a tool used to describe the state of a spin ensemble as well as its evolution in time. It allows the passage from a probabilistic treatment of a *system* of few spins to the statistical treatment of a large *ensemble* of such systems [99, 51, 130].

6.2.1 Expectation value of an observable

We follow here the general demonstration given by Slichter (p158-161 of [127]). The expectation value of an operator $\mathcal{F}$, which depends on the coordinates and momenta of the system, is given by :

$$\begin{aligned} < \mathcal{F} > &= < \Psi, \mathcal{F}\Psi > \\ &= \int \Psi^* \mathcal{F} \Psi \, d\tau \\ &= \sum_{i,j} c_i^* c_j (\phi_i, \mathcal{F}\phi_j) = \sum_{i,j} c_i^* c_j < \phi_i | \mathcal{F} | \phi_j > \end{aligned} \tag{6.9}$$

where the projection of the state function is obtained in a base of eigen states that has been presented in the equation 6.7.

The ensemble average of this expectation value, necessary to predict the system's macroscopical behavior, is :

$$< \overline{\mathcal{F}} > = \sum_{i,j} \overline{c_i^* c_j} < \phi_i | \mathcal{F} | \phi_j > \tag{6.10}$$

this illustrates the fact that we can conveniently arrange the coefficients introduced by Eq. 6.8, as a product $c_m^* c_n$ to form a matrix, whose properties are given now. As we already mention, if the wave function is time dependent, the time dependency is contained in the coefficients c_n. On the other hand he basis functions ϕ_n, and matrix elements such as $< \phi_i | \mathcal{F} | \phi_j >$ are time independent. In practice the matrix elements of the density matrix ϱ are introduced in such a way :

$$< n | \varrho | m > = \overline{c_m^* c_n} \tag{6.11}$$

where the bar denotes the macroscopical average.

The equation 6.10 can be expanded now considering ϱ. This matrix is an Hermitian operator, therefore $\varrho_{mn} = \varrho_{nm}^*$, $\varrho^2 \leq \varrho$ and $Tr(\varrho) = 1$, and even if not necessarily diagonal,

there exist a basis which diagonalize ϱ, and the diagonal elements must be occupation probabilities. In the calculation presented in Fig. 9.9, $\mathcal{F}$ is in practice $\mathcal{M}_x$, the magnetization along I_x in a base of Pauli matrices (Eq. 6.3).

$$\begin{aligned} < \overline{\mathcal{M}_x} > &= \sum_{n,m} < n|\varrho|m >< m|\mathcal{M}_x|n > \\ &= \sum_{n} < n|\varrho \underbrace{\Big(\sum_{m} |m >< m| \Big)}_{1} \mathcal{M}_x|n > \\ &= Tr(\varrho.\mathcal{M}_x) \end{aligned} \tag{6.12}$$

In order to obtain a mathematical expression for the *measurable* time evolution of the magnetization, we will use the now-familiar trace relation. Once $\varrho(t)$ the density matrix for a certain spin evolution is calculated, the magnetization recorded along x is given by the trace of the product with the Pauli matrix corresponding to $\tilde{\sigma}_x$:

$$< \overline{\mathcal{M}_x} > = \frac{\hbar}{2} Tr(\varrho.\tilde{\sigma}_x) \tag{6.13}$$

the utility of such an approach as been proven extensively in NMR and we will therefore make a practical usage of it for the signal calculations of Figs.9.2, 9.5, 9.9 and 9.11.

6.2.2 Transition probability

Moreover the hamiltonian accepts the following decomposition, which is very useful in NMR for the calculation of transition probabilities between two states of energy (e.g E_i and E_j).

$$\mathcal{H} = \mathcal{H}_0 + \mathcal{H}_1 \tag{6.14}$$

where $\mathcal{H}_1$ is, in some sense, small in comparison with $\mathcal{H}_0$, and where the solution to Schrödinger's equation is known if $\mathcal{H}_1 = 0$. In such cases a powerful formalism, called *perturbation theory*, is available to approximate the solution to Shrödinger's equation for the full Hamiltonian given in equation 6.14. The fundamental results depend on whether or not $\mathcal{H}_1$ is a function of time. If it is not dependent on time, its effect is to cause a small shift in the energy level for the unperturbed ($\mathcal{H}_1 = 0$) case. The shift in i^{th} level is

$$\Delta E_i = \int \phi_i^* \mathcal{H}_1 \phi_i \, d\tau =< \phi_i|\mathcal{H}_1|\phi_i > \tag{6.15}$$

where ϕ_i is the i^{th} unperturbed eigenfunction ; that is, the shift is equal to the expectation value of the perturbation with respect to the j^{th} unperturbed level. On the other hand, if $\mathcal{H}_1$ is a function of time, its effect is to induce *transitions* between the different states of the unperturbed Hamiltonian $\mathcal{H}_o$.

Only an RF pulse is able to modify the value of the coherence order. The operator $\mathcal{H}_1$ is produced by the magnetic field $\mathbf{B}_1$ as expressed by equation 6.1. The equation 6.16 links the application of the RF pulse inside of the coil to the probability of transitions between the energy levels of the spins. This equation can be formulated using the density matrix :

$$< j|\varrho(t)|i >= e^{i/\hbar(E_i - E_j)t} < j|\varrho(0)|i > \tag{6.16}$$

where t is the evolution time, from one state to the other.

The diagonal terms of the density matrix, correspond to the probability of finding the system in the corresponding state. For example, the state m is populated accordingly to the statistical distribution :

$$c_m.c_m^* = \frac{e^{-E_m/k_B\,T}}{Z} \tag{6.17}$$

where k_B is the Boltzmann constant, and Z denotes the normalization factor in a canonical distribution [37]. This equation is useful to calculate the magnetization at the equilibrium.

6.2.3 Equation of evolution of the density matrix

Case of an Hamiltonian constant in time

For the future, we shall omit the bar indicating an ensemble average to simplify the notation, but of course we realize that whenever the symbol ϱ is used, an ensemble average is intended. Naturally the wave function Ψ, describing whatever system we are considering, will develop in time. It is straightforward to find the differential equation obeyed by the coefficients c_k : this is nothing else than Schrödingers equation 6.4. Using the decomposition of Ψ of Eq. 6.8 it follows that

$$-\frac{\hbar}{i}\sum_n \frac{dc_n}{dt}\Phi_n = \sum_n c_n \mathcal{H}\Phi_n \tag{6.18}$$

We can pick out the equation for one particular coefficient, c_k, by multiplying both left sides by Φ_k^* and integrating :

$$-\frac{\hbar}{i}\frac{dc_k}{dt} = \sum_n c_n < k|\mathcal{H}|n > \tag{6.19}$$

This equation is the well-known starting point for time-dependence perturbation theory. We can use (6.19) to find a differential equation for the matrix elements of the operator ϱ, since

$$\begin{aligned}
\frac{d}{dt}< k|\varrho|m > &= \frac{d}{dt}(c_k c_m^*) \\
&= c_k \frac{dc_m^*}{dt} + \frac{dc_k}{dt} c_m^* \\
&= -\frac{i}{\hbar}\sum_n [< k|\mathcal{H}|n > c_n c_m^* - c_k c_n^* < n|\mathcal{H}|m >] \\
&= -\frac{i}{\hbar} < k|\mathcal{H}\varrho - \varrho\mathcal{H}|m >
\end{aligned} \tag{6.20}$$

Finally, the well known *equation of motion*, governing the evolution of the density matrix, appears with the following commutator :

$$\frac{d}{dt}\varrho(t) = -\frac{i}{\hbar}[\mathcal{H}, \varrho(t)] \tag{6.21}$$

When the density matrix $\varrho(t)$ evolves under this Hamiltonian. In the event that $\mathcal{H}$ is independent of time, we may obtain a formal solution of the equation of motion. The value attained after a delay Δt is given by :

$$\varrho(\Delta t) = e^{-(i/\hbar)\mathcal{H}\Delta t}\varrho(0)e^{(i/\hbar)\mathcal{H}\Delta t} \tag{6.22}$$

the integration is strayforward, and this equation predits quite well simples case as those encoutered in precession. In the case of a field whose amplitude and spacial orientation is varying in time, the resolution of Schrödingers equations turn to be far more delicate because time varying Hamiltonians obtained at different times do no commute.

Case of an RF Hamiltonian continuously evolving in time

One situation commonly encountered is that of a Hamiltonian as described by 6.14, consisting of a (i) large time-independent interaction $\mathcal{H}_0$, produced by the static field $\mathbf{B}_o$

$$\mathcal{H}_0 = -\hbar\gamma_r \mathbf{B}_o.\mathbf{I} = -\hbar\omega_o.\mathbf{I}$$

and (ii) a much smaller but time-dependent term $\mathcal{H}_1(t)$ depending of the RF coil. The equation of motion of the density matrix is then :

$$\frac{d}{dt}\varrho(t) = -\frac{i}{\hbar}[\mathcal{H}_0 + \mathcal{H}_1(t), \varrho(t)] \tag{6.23}$$

In the context of this perturbational approach it is convenient to perform a frame transformation, and to introduce the RF Hamiltonian ($\tilde{\mathcal{H}}_1$) in the rotating frame :

$$\tilde{\mathcal{H}}_1 = e^{i\mathcal{H}_0 t/\hbar}\mathcal{H}_1 e^{-i\mathcal{H}_0 t/\hbar} \tag{6.24}$$

we can after changing to the rotational frame, rewrite the equation of motion. This one was used in this work for a time dependent Hamiltonian :

$$\frac{\delta\tilde{\varrho}(t)}{\delta t} = -\frac{i}{\hbar}[\tilde{\mathcal{H}}(t), \tilde{\varrho}(t)] \tag{6.25}$$

such more general equation admits a solution similar to Eq. 6.22 :

$$\tilde{\varrho}(t+\Delta t) = e^{-(i/\hbar)\tilde{\mathcal{H}}(t)\Delta t}\tilde{\varrho}(t)e^{(i/\hbar)\tilde{\mathcal{H}}(t)\Delta t} \tag{6.26}$$

but with Δt small enough to consider the RF Hamiltonian constant during this infinitesimal delay.

In practice a numerical iteration is required to follow the time evolution of $\tilde{\varrho}$ due to the non-commutative character of the Hamiltonian. Then Δt must be, at least a factor 2 smaller that the time step of the fastest oscillation period to be observed.

The recurence problem to be solved will consider the following steps :

$$\begin{aligned}
\tilde{\varrho}(\Delta t) &= e^{-(i/\hbar)\tilde{\mathcal{H}}(0)\Delta t}\tilde{\varrho}(0)e^{(i/\hbar)\tilde{\mathcal{H}}(0)\Delta t} \\
\tilde{\varrho}(2\Delta t) &= e^{-(i/\hbar)\tilde{\mathcal{H}}(\Delta t)\Delta t}\tilde{\varrho}(\Delta t)e^{(i/\hbar)\tilde{\mathcal{H}}(\Delta t)\Delta t} \\
&\ldots \\
\tilde{\varrho}(n\Delta t) &= e^{-(i/\hbar)\tilde{\mathcal{H}}\left((n-1)\Delta t\right)\Delta t}\tilde{\varrho}\Big((n-1)\Delta t\Big)e^{(i/\hbar)\tilde{\mathcal{H}}\left((n-1)\Delta t\right)\Delta t}
\end{aligned} \tag{6.27}$$

to solve this iteration, we need to analyse the mathematical expression of $\tilde{\mathcal{H}}$ in the case of inhomogeneous $\mathbf{B}_1$ field and in presence of mechanical rotation (MAS). Rotation at the

magic angle will reintroduce time modulations in the expression of these Hamiltonian's components, and should be considered with care.

In addition, since the iteration, to be implemented numerically, may be long and repetitive, errors will propagate from one iteration to another. The principal difficulty comes from the treatement of complex *exponential* matrices :

$$\tilde{\varrho}_{n+1} = e^{-(i/\hbar)\tilde{\mathcal{H}}_1 \Delta t} \tilde{\varrho}_n e^{(i/\hbar)\tilde{\mathcal{H}}_1 \Delta t} \tag{6.28}$$

found step after step.

The convergence to a realistic solution (as opposed to a numerical artifact) is stongly dependent on the numerical implementation of this building block. To avoid drawbacks we derive an analytical expression of Eq. 6.28. This alleviates the computational burden introduced by the algorithmic treatment of the exponential matrices. In the base designated before (6.3), $\tilde{\varrho}_n$ admits the following decomposition :

$$\tilde{\varrho}_n = \mathcal{C}_x^n \tilde{\sigma}_x + \mathcal{C}_y^n \tilde{\sigma}_y + \mathcal{C}_z^n \tilde{\sigma}_z \tag{6.29}$$

at each step n where $\{\mathcal{C}_x^n, \mathcal{C}_y^n, \mathcal{C}_z^n\}$ are the coefficients corresponding to the different components of the magnetization. We notice that these coefficients are projections of the density matrix :

$$\mathcal{C}_x^n = Tr(\varrho_n . \tilde{\sigma}_x) \tag{6.30}$$

in the case of $\tilde{\sigma}_x$ here.

To derive Eq. 6.29 at each step, a simplified analytical model will be set for the RF hamiltonian. As it will be shown in the next chapter, $\tilde{\mathcal{H}}_1(t = n\Delta t)$ can be expressed as a two components operator :

$$\tilde{\mathcal{H}}_1(\vec{\rho}, t) = \varphi_x(\vec{\rho}, t)\tilde{\sigma}_x + \varphi_y(\vec{\rho}, t)\tilde{\sigma}_y \tag{6.31}$$

where $\varphi_x(\vec{\rho}, t)$ and $\varphi_y(\vec{\rho}, t)$, are based on the projection of $\mathbf{B}_1$ in the rotating frame. This is to be finally incorporated into Eq. 6.28. The analytical solution of $\tilde{\varrho}_n$ is then obtained by direct diagonalization of the exponential matrices. These strayforward calculations can be done using Maple or by any other tool to provide a general algebraic expression.

With

$$\alpha_\varphi \quad = \quad \varphi_x^2 + \varphi_y^2 \tag{6.32}$$

and

$$\delta_\varphi \quad = \quad \varphi_x^2 - \varphi_y^2 \tag{6.33}$$

Finally the new coefficients at the step $n+1$ are given as a function of the old ones at the step n, and this replaces the numerical treatment of Eq. 6.28.

$$\begin{aligned}
\mathcal{C}_x^{n+1} &= \frac{\alpha_\varphi.\cos\left(\frac{\alpha_\varphi}{4}.(\Delta t)^2\right) + \delta_\varphi.\left[1-\cos\left(\frac{\alpha_\varphi}{4}.(\Delta t)^2\right)\right]}{\alpha_\varphi}\,\mathcal{C}_x^n \\
&+ 2\,\varphi_y\,\varphi_x\frac{1-\cos\left(\frac{\alpha_\varphi}{4}.(\Delta t)^2\right)}{\alpha_\varphi}\,\mathcal{C}_y^n \\
&+ 2\,\frac{\cos(\frac{\sqrt{\alpha_\varphi}}{2}.\Delta t)\,\sin(\frac{\sqrt{\alpha_\varphi}}{2}.\Delta t)\,\varphi_y}{\sqrt{\alpha_\varphi}}\,\mathcal{C}_z^n
\end{aligned} \tag{6.34}$$

$$\begin{aligned}
\mathcal{C}_y^{n+1} &= 2\,\varphi_y\,\varphi_x\frac{1-\cos\left(\frac{\alpha_\varphi}{4}.(\Delta t)^2\right)}{\alpha_\varphi}\,\mathcal{C}_x^n \\
&+ \frac{\alpha_\varphi.\cos\left(\frac{\alpha_\varphi}{4}.(\Delta t)^2\right) - \delta_\varphi.\left[1-\cos\left(\frac{\alpha_\varphi}{4}.(\Delta t)^2\right)\right]}{\alpha_\varphi}\,\mathcal{C}_y^n \\
&- 2\,\frac{\cos(\frac{\sqrt{\alpha_\varphi}}{2}.\Delta t)\,\sin(\frac{\sqrt{\alpha_\varphi}}{2}.\Delta t)\,\varphi_x}{\sqrt{\alpha_\varphi}}\,\mathcal{C}_z^n
\end{aligned} \tag{6.35}$$

$$\begin{aligned}
\mathcal{C}_z^{n+1} &= -2\,\frac{\cos(\frac{\sqrt{\alpha_\varphi}}{2}.\Delta t)\,\sin(\frac{\sqrt{\alpha_\varphi}}{2}.\Delta t)\,\varphi_y}{\sqrt{\alpha_\varphi}}\,\mathcal{C}_x^n \\
&+ 2\,\frac{\cos(\frac{\sqrt{\alpha_\varphi}}{2}.\Delta t)\,\sin(\frac{\sqrt{\alpha_\varphi}}{2}.\Delta t)\,\varphi_x}{\sqrt{\alpha_\varphi}}\,\mathcal{C}_y^n \\
&+ \left[2\cos\left(\frac{\alpha_\varphi}{4}.(\Delta t)^2\right) - 1\right]\mathcal{C}_z^n
\end{aligned} \tag{6.36}$$

This set of equations link the coefficients $\mathcal{C}^n$ in a recurent way. For the prediction of evolution of magnetization, we have developed a C^{++} code used in the chapter 9. This software is based on the above presented analytical expressions, and customized for the various NMR sequences. For the $\mathbf{B}_1$ magnetic field profiles created by helical coils and described in chapter 8. The novelty of the here presented approach is that the $\mathbf{B}_1$ inhomogeneity is included in study of the NMR sequence, via φ_x and φ_y. Of course a

deep understanding of electromagnetic distribution is needed to provide a comprehensive model of the magnetic field distribution. These models will be introduced in chapter 7. They are based on the axial and radial decomposition already found in the previous part (chapter 3.1.2) but applied here to our problem. By solving analyticaly Maxwell equations in the regular coils, the chapter 8 will fully justify these simplified models. Finally in chapter 9 experimental evidence will be presented, based on rotatory echo, MLEV, and above all nutation experiments.

7

The RF field in a solenoid coil

The investigation of the effects of RF field inhomogeneities in HR-MAS started when it was reported that MLEV16 sequences run under HR-MAS could lead to very awkward results [111, 85]. The effects observed varied from strong phase distortions to an almost complete disappearance of the magnetization. After a careful analysis, the origin of the problem was found to be due to an interference between the mechanical spinning of the sample and the MLEV16 sequence [111]. It was noted that, in the course of its rotation, the sample is necessarily taken through regions of varying $\mathbf{B}_1$ fields, resulting in a natural periodic amplitude modulation of the $\mathbf{B}_1$ field [111]. Simulations reproducing the actual MLEV16 sequence using empirical models of $\mathbf{B}_1$ inhomogeneities were shown to be able to reproduce the experimental results. In this section this investigation is carried out a step further by using more elaborate models of the $\mathbf{B}_1$ inhomogeneity for the NMR simulations and by validating these models with electromagnetic simulations of $\mathbf{B}_1$ inside a solenoid. We show that the MLEV16 and the DIPSI2 experiments are not the only experiments affected by this $\mathbf{B}_1$ modulation. Unusual effects are also observed for a simple nutation experiment which is used in almost every laboratory to determine the amplitude and the inhomogeneity of the radio-frequency field. Unusual aspects of the rotary-echo experiment ($90^o_x - delay - 90^o_{-x} - Acquisition$) are also discussed. It is important to note that these effects have been observed in a number of laboratories but that no clear explanation was proposed in the literature until 2005 [48].

7.1 Evolution of magnetization under the RF field in MAS conditions

Magic angle spinning consists in spinning a sample around an axis forming the magic angle $\beta = \cos^{-1}(1/\sqrt{3}) = 54.7^o$ with respect to the axis of the main static field $\mathbf{B}_o$. The radio-frequency coil used to generate the $\mathbf{B}_1$ field and to observe the NMR signal is usually a solenoid oriented at the magic angle. The characteristics of the $\mathbf{B}_1$ field are most easily described in the (X, Y, Z) frame of the solenoid whereas the description of the NMR experiments requires the use of the (x, y, z) laboratory frame where the Oz axis is along the magnet's bore (Fig. 1.5). In most text books, it is stated that the $\mathbf{B}_1$ field generated by a solenoid coil is aligned along the OZ axis of the solenoid and that the field distribution is symmetrical around this axis. This is clearly an oversimplification since the main axis of a solenoid is not an axis of symmetry. The helical winding of a solenoid is such that a radial plane, taken perpendicular to the OZ axis, contains some regions that are close to the wire of the coil and some that are more remote. The $\mathbf{B}_1$ field distribution can therefore present some slight imperfections in its alignment and in its symmetry around the OZ axis. Such a $\mathbf{B}_1$ field, at a point of cylindrical coordinates (ρ, Z, θ), can be conveniently decomposed into the sum of its radial and axial components as :

$$\mathbf{B}_1(\rho, Z, \theta; t) = \mathbf{B}_1^{ra}(\rho, Z, \theta; t) + \mathbf{B}_1^{ax}(\rho, Z, \theta; t)$$

Where $(^{ax})$ denotes the axial field component along the main Z axis of the solenoid and $(^{ra})$ the radial field component in the (X,Y) plane (Fig. 1.5). The here called $\mathbf{B}_1$, is a linearly oscillating vector at an angular frequency[18] $2\pi\nu_{rf}$, of time phase ϕ and of amplitudes $2\mathbf{B}_1^{ax}$ and $2\mathbf{B}_1^{ra}$, these express the 'nutation field' and can therefore be given in kHz. It can be expressed as a function of its radial and axial components :

$$\begin{aligned} B_{1,X}(\rho, Z, \theta; t) &= 2\mathbf{B}_1^{ra}(\rho, Z, \theta)\cos(\theta)\cos(2\pi\nu_{rf}t + \phi) \\ B_{1,Y}(\rho, Z, \theta; t) &= 2\mathbf{B}_1^{ra}(\rho, Z, \theta)\sin(\theta)\cos(2\pi\nu_{rf}t + \phi) \\ B_{1,Z}(\rho, Z, \theta; t) &= 2\mathbf{B}_1^{ax}(\rho, Z, \theta)\cos(2\pi\nu_{rf}t + \phi) \end{aligned} \tag{7.1}$$

To calculate the effects of RF pulses, we need to decompose the $\mathbf{B}_1$ field, in the

[18] The notation of angular frequency ω_{rf} employed in the precedent chapters is changed here into $2\pi\nu_{rf}$ in order to keep the small case ω_r as the pulsation of the mechanical rotation.

laboratory frame as introduced in Fig. 1.5 :

$$\mathbf{B}_1 = B_{1,x}.\vec{x} + B_{1,y}.\vec{y} \tag{7.2}$$

where, $\mathbf{B}_1$ is a phasor and therefore, both B_x and B_y are complex numbers.

We can reasonably consider the same phase at every single point for B_X and B_Y, in the expression given by Eq. 7.1 only the real part is taken in account.

To predict the results of the NMR experiment, the different components of the $\mathbf{B}_1$ field must be expressed in the (x, y, z) laboratory frame. In this frame, with $\beta = 54.7^o$, Eq. 7.1 transforms into :

$$\begin{aligned}
B_{1,x}(\rho, Z, \theta; t) &= 2\mathbf{B}_1^{ra}(\rho, Z, \theta)\cos(\theta)\cos(2\pi\nu_{rf}t + \phi) \\
B_{1,y}(\rho, Z, \theta; t) &= 2\Big(\sqrt{\frac{2}{3}}\,\mathbf{B}_1^{ax}(\rho, Z, \theta) + \frac{1}{\sqrt{3}}\,\mathbf{B}_1^{ra}(\rho, Z, \theta)\sin(\theta)\Big)\cos(2\pi\nu_{rf}t + \phi) \\
B_{1,z}(\rho, Z, \theta; t) &= 2\Big(\frac{1}{\sqrt{3}}\,\mathbf{B}_1^{ax}(\rho, Z, \theta) - \sqrt{\frac{2}{3}}\,\mathbf{B}_1^{ra}(\rho, Z, \theta)\sin(\theta)\Big)\cos(2\pi\nu_{rf}t + \phi)
\end{aligned} \tag{7.3}$$

The effect of a RF-pulse on a spin system can be followed by computing the evolution of the density matrix $\varrho(t)$ whose evolution is governed by the equation of motion as seen in Eq. 6.25 of the previous section 6.2. An analogous treatment has been reported by Abragam (p 26 in [1]) or by Slichter (in Eq 5.100 in [127]).

In the case of an isolated spin system placed in a static field $\mathbf{B}_o$ and subjected to the RF field $\mathbf{B}_1$ the temporal and spatial dependence of the Hamiltonian $\mathcal{H}$ is given by :

$$\mathcal{H}(\rho, Z, \theta; t) = \mathcal{H}_0 + \mathcal{H}_1(\rho, Z, \theta; t) \tag{7.4}$$

where $\mathcal{H}(t)$ is the time-dependent Hamiltonian, in the context defined by the theory of perturbation. And where $\mathcal{H}_0$ and $\mathcal{H}_1$ are defined by :

$$\begin{aligned}
\mathcal{H}_0 &= -\gamma_r\hbar\mathbf{B}_o\mathrm{I}_z \\
\mathcal{H}_1(\rho, Z, \theta; t) &= -\gamma_r\hbar\Big(B_{1,x}(\rho, Z, \theta; t)\,\mathrm{I}_x + B_{1,y}(\rho, Z, \theta; t)\,\mathrm{I}_y + B_{1,z}(\rho, Z, \theta; t)\,\mathrm{I}_z\Big)
\end{aligned} \tag{7.5}$$

Using Eq. 7.3, the RF Hamiltonian $\mathcal{H}_1$ becomes :

$$\begin{aligned}\mathcal{H}_1 &= -2\gamma_r\hbar\Big[\mathbf{B}_1^{ra}(\rho,Z,\theta)\cos(\theta)\mathrm{I}_x \\ &+ \Big(\sqrt{\frac{2}{3}}\,\mathbf{B}_1^{ax}(\rho,Z,\theta)+\frac{1}{\sqrt{3}}\,\mathbf{B}_1^{ra}((\rho,Z,\theta)\sin(\theta)\Big)\mathrm{I}_y \\ &+ \Big(\frac{2}{\sqrt{3}}\,\mathbf{B}_1^{ax}(\rho,Z,\theta)-\sqrt{\frac{2}{3}}\,\mathbf{B}_1^{ra}((\rho,Z,\theta)\sin(\theta)\Big)\mathrm{I}_z\Big]\cos(2\pi\nu_{rf}t+\phi)\end{aligned} \tag{7.6}$$

The linearly oscillating field-components $\mathbf{B}_1$ along the x and y axes can be expressed as a superposition of two opposite, circularly polarized components rotating in the (x,y) plane. Thus, Eq. 7.6 can be written as :

$$\begin{aligned}\mathcal{H}_1(\rho,Z,\theta;t) &= -\gamma_r\hbar\Big[\mathbf{B}_1^{ra}(\rho,Z,\theta)\cos(\theta) \\ &\quad\times\Big(e^{i\left(2\pi\nu_{rf}t+\phi\right)\mathrm{I}_z}\mathrm{I}_x e^{-i\left(2\pi\nu_{rf}t+\phi\right)\mathrm{I}_z}+e^{-i\left(2\pi\nu_{rf}t+\phi\right)\mathrm{I}_z}\mathrm{I}_x e^{i\left(2\pi\nu_{rf}t+\phi\right)\mathrm{I}_z}\Big) \\ &+ \Big(\sqrt{\frac{2}{3}}\,\mathbf{B}_1^{ax}(\rho,Z,\theta)+\frac{1}{\sqrt{3}}\,\mathbf{B}_1^{ra}(\rho,Z,\theta)\sin(\theta)\Big) \\ &\quad\times\Big(e^{i\left(2\pi\nu_{rf}t+\phi\right)\mathrm{I}_z}\mathrm{I}_y e^{-i\left(2\pi\nu_{rf}t+\phi\right)\mathrm{I}_z}+e^{-i\left(2\pi\nu_{rf}t+\phi\right)\mathrm{I}_z}\mathrm{I}_y e^{i\left(2\pi\nu_{rf}t+\phi\right)\mathrm{I}_z}\Big) \\ &+ \Big(\frac{1}{\sqrt{3}}\,\mathbf{B}_1^{ax}(\rho,Z,\theta)-\sqrt{\frac{2}{3}}\mathbf{B}_1^{ra}(\rho,Z,\theta)\sin(\theta)\Big)2\cos(2\pi\nu_{rf}t+\phi)\mathrm{I}_z\Big]\end{aligned} \tag{7.7}$$

Using the convention that the counterclockwise RF field component rotates in the same sense as the Larmor precession, we can switch into the frame rotating at the frequency ν_{rf} (defined in Eq. 6.24) where the density matrix is given by $\tilde{\varrho}(t)=e^{-i2\pi\nu_{rf}t\mathrm{I}_z}\varrho(t)\,e^{i2\pi\nu_{rf}t\mathrm{I}_z}$. The equation of motion in the rotating frame becomes, the equation 6.25. Where $\mathcal{H}'_0$ and $\mathcal{H}'_1$ are expressed by :

$$\mathcal{H}'_0 = -\gamma_r\hbar\Big(\mathbf{B}_o-\frac{2\pi\nu_{rf}}{\gamma_r}\Big)\mathrm{I}_z=\Delta\nu\mathrm{I}_z \tag{7.8}$$

$$\begin{aligned}\mathcal{H}'_1(\rho,Z,\theta;t) &= -\gamma_r\hbar\Big[\mathbf{B}_1^{ra}\,(\rho,Z,\theta)\cos(\theta) \\ &\quad\times\Big(e^{i\phi\mathrm{I}_z}\mathrm{I}_x e^{-i\phi\mathrm{I}_z}+e^{-2i\left(2\pi\nu_{rf}t+\phi\right)\mathrm{I}_z}\mathrm{I}_x e^{2i\left(2\pi\nu_{rf}t+\phi\right)\mathrm{I}_z}\Big) \\ &+ \Big(\sqrt{\frac{2}{3}}\mathbf{B}_1^{ax}(\rho,Z,\theta)+\frac{1}{\sqrt{3}}\mathbf{B}_1^{ra}(\rho,Z,\theta)\sin(\theta)\Big) \\ &\quad\times\Big(e^{i\phi\mathrm{I}_z}\mathrm{I}_y e^{-i\phi\mathrm{I}_z}+e^{-2i\left(2\pi\nu_{rf}t+\phi\right)\mathrm{I}_z}\mathrm{I}_y e^{2i\left(2\pi\nu_{rf}t+\phi\right)\mathrm{I}_z}\Big)\end{aligned}$$

$$+ \quad \Big(\frac{1}{\sqrt{3}}\,\mathbf{B}_1^{ax}\,(\rho,Z,\theta) - \sqrt{\frac{2}{3}}\,\mathbf{B}_1^{ra}\,(\rho,Z,\theta)\sin(\theta)\Big)2\cos(2\pi\nu_{rf}t+\phi)\mathrm{I}_z\Big]$$

Under magic angle spinning conditions, with the sample rotating at the frequency ω_r, the spins located initially at the position (ρ, Z, θ_0) will move to the new position $(\rho, Z, \theta_{(t)})$ where $\theta_{(t)} = \omega_r \mathrm{t} + \theta_0$. Over a rotor period, since the resonance frequency $2\pi\nu_{rf}$ is much larger than ω_r , the time-dependent terms of $\mathcal{H}'_1$ modulated at a frequency $2\pi\nu_{rf}$ will be averaged out to zero. $\tilde{\mathcal{H}}$ can be finally written as :

$$\begin{aligned}
\tilde{\mathcal{H}}\,(\rho,Z,\theta_0;t) &= -\gamma_r\hbar\Big[\Big(\mathbf{B}_o - \frac{2\pi\nu_{rf}}{\gamma_r}\Big)\mathrm{I}_z \\
&+ \mathbf{B}_1^{ra}\left(\rho,Z,\theta_{(t)}\right)\cos(\theta_{(t)}) \times (\cos(\phi)\mathrm{I}_x + \sin(\phi)\mathrm{I}_y) \\
&+ \Big(\sqrt{\frac{2}{3}}\,\mathbf{B}_1^{ax}\left(\rho,Z,\theta_{(t)}\right) + \frac{1}{\sqrt{3}}\mathbf{B}_1^{ra}\left(\rho,Z,\theta_{(t)}\right)\sin\left(\theta_{(t)}\right)\Big) \\
&\quad \times(-\sin(\phi)\mathrm{I}_x + \cos(\phi)\mathrm{I}_y)\Big]
\end{aligned} \tag{7.9}$$

Where the amplitudes of the RF components are expressed in Hz units. Note that the RF Hamiltonian in Eq. 7.9 corresponds to a pulse of phase[19] ϕ. On the other hand Eq. 7.9 indicates that in the case of a RF pulse along the y axis ($\phi = 0^o$), the axial field produces, as expected, a component I_x while the radial field generates both components I_x and I_y.

The exact representation of the amplitude of the axial and radial fields $\mathbf{B}_1^{ax}(\rho, Z, \theta_0)$, and $\mathbf{B}_1^{ra}(\rho, Z, \theta_0)$ is a delicate task [129, 144, 121, 74], we note that this distribution has a spacial periodicity revealed trough rotation and, as any well behaved periodic function, could have be represented by a Fourier series, using the following decomposition [111, 48] :

$$\begin{aligned}
\mathbf{B}_1^{ax}(\rho,Z,\theta) &= \mathbf{B}_1^{ax}(\rho,Z)\sum_{n=0}^{+\infty}\Big(\alpha_n^{ax}(\rho,Z)\cos(n\theta) + \beta_n^{ax}(\rho,Z)\sin(n\theta)\Big) \\
\mathbf{B}_1^{ra}(\rho,Z,\theta) &= \mathbf{B}_1^{ra}(\rho,Z)\sum_{n=0}^{+\infty}\Big(\alpha_n^{ra}(\rho,Z)\cos(n\theta) + \beta_n^{ra}(\rho,Z)\sin(n\theta)\Big)
\end{aligned} \tag{7.10}$$

Where the coefficients $\alpha_n^{ax}, \alpha_n^{ra}, \beta_n^{ax}, \beta_n^{ra}$, are correction factors that may account for the different field inhomogeneities present in the coil.

[19] The time phase $\phi \in \{y, -x, -y, x\}$ corresponds to $\{0^o, 90^o, 180^o, 270^o\}$, respectively. This has been explained in section 5.1

7.2 Models for the RF field-spin interaction

In this section, simple models will be used to represent the distribution of the intensities $\mathbf{B}_1^{ax}$ and $\mathbf{B}_1^{ra}$. Since the deviations from an ideal field represented by $\mathbf{B}_1^{ax} = \mathbf{B}_1$ and $\mathbf{B}_1^{ra} = 0$ are obviously small, only the first terms of Eq. 7.10 will be considered. For the analysis of the effect of $\mathbf{B}_1$ inhomogeneities on the outcome of MLEV-16 experiments, only two cases will be discussed. To mimic the trajectory of a spin packet during the course of the sample rotation, the analysis will take place on a thin ring located at a position (ρ, Z) . The spin packet will start at position (ρ, Z, θ_0) and will move to a new position $(\rho, Z, \theta_{(t)})$ where $\theta_t = \omega_r t + \theta_0$. For clarity, the position parameters ρ and Z will be omitted in the following.

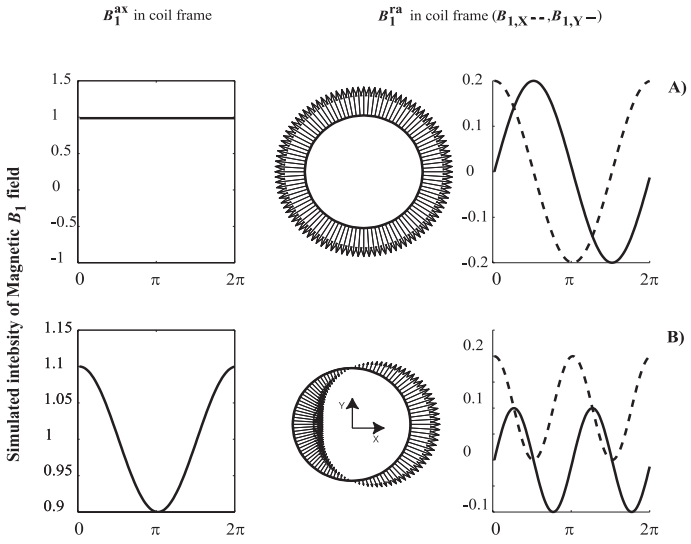

FIG. 7.1 – *Pictorial representation of the models proposed for the* $\mathbf{B}_1$ *field distribution around a given ring. A) model 1 (Eq. 7.12) and B) model 2 (Eq. 7.14). The axial, and radial components are plotted as a function of the angular position along the ring. The first column represents the evolution of the axial component along the circular trajectory followed by a packet of spins. The second column displays the orientation of the radial component in the transverse plane (X, Y) of the coil. The third column contains the projections* $\mathbf{B}_{1,X}$ *and* $\mathbf{B}_{1,Y}$ *of the two components of* $\mathbf{B}_1^{ra}$ *in this plane.*

7.2.1 Model 0 : Perfectly homogeneous RF field :

For this ideal case, only the term α_0^{ax} remains in Eq. 7.10 and $\mathbf{B}_1^{ax} = \mathbf{B}_1$ and $\mathbf{B}_1^{ra} = 0$. According to Eq. 7.9, the corresponding Hamiltonian $\tilde{\mathcal{H}}$ describing a RF-pulse along $\mathrm{I_y}$ ($\phi = 0$) is given by the usual form :

$$\tilde{\mathcal{H}}(t) = -\Delta\nu \mathrm{I}_z - \sqrt{\frac{2}{3}}\,\mathbf{B}_1\,\mathrm{I}_y \tag{7.11}$$

This expression of the $\mathbf{B}_1$ field is the one usually employed to describe NMR experiments under MAS.

7.2.2 Model 1 : Axial RF field constant and Radial RF field of constant amplitude and normal to the ring (Fig. 7.1A) :

This case corresponds to a field of the form

$$\mathbf{B}_1^{ra}(\theta_{(t)}) = |\mathbf{B}_1^{ra}|.(\cos(\theta_{(t)}).\vec{X} + \sin(\theta_{(t)}).\vec{Y})$$

and to an axial field of the form

$$\mathbf{B}_1^{ax}(\theta_{(t)}) = |\mathbf{B}_1^{ax}|.\vec{Z}$$

Meaning that all the coefficients $\alpha_n^{ax}, \beta_n^{ax}, \alpha_n^{ra}, \beta_n^{ra}$ of Eq. 7.10 are canceled, except for α_0^{ax} and α_0^{ra}. The pictorial representation of this model is represented in Fig. 7.1. The intensity of $\mathbf{B}_1^{ax}$ remains constant while the orientation of $\mathbf{B}_1^{ra}$ stays along the normal of the ring. According to Eq. 7.9, the corresponding Hamiltonian $\mathcal{H}$ for a RF pulse along $\mathrm{I_y}(\phi = 0)$ is still dependent on θ and can be written under the form :

$$\tilde{\mathcal{H}}\,(\theta_0; t) = -\Delta\nu \mathrm{I}_z + a\cos(\theta_{(t)})\mathrm{I}_x + b\Big(1 + c\sin(\theta_{(t)})\Big)\mathrm{I}_y \tag{7.12}$$

with :

$$\begin{cases} a = & -|\mathbf{B}_1^{ra}| \\ b = & -\sqrt{\frac{2}{3}}\,|\mathbf{B}_1^{ax}| \\ c = & \frac{1}{\sqrt{2}}\,|\mathbf{B}_1^{ra}|/|\mathbf{B}_1^{ax}| \end{cases} \tag{7.13}$$

These equations show that in the case of a RF-pulse along the Oy axis, the presence of a radial field of constant amplitude and symmetrical around the OZ axis will create a small amount of RF pulse along the Ox axis. Another effect of this radial field is the presence of a sine modulation of the $\mathbf{B}_1$ field at the frequency ω_r of the rotation since $\theta_{(t)} = \omega_r t + \theta_0$.

7.2.3 Model 2 : Cosine modulation of the amplitude of the axial and radial fields (Fig.7.1B) :

In this case, a cosine modulation of the intensity of the axial and radial fields, $\mathbf{B}_1^{ax}$ and $\mathbf{B}_1^{ra}$, is considered. The time phase ϕ of the RF components is assumed to be the same. This situation corresponds to a radial field of the form

$$\mathbf{B}_1^{ra}(\theta_{(t)}) = |\mathbf{B}_1^{ra}|\cos(\theta_{(t)}).(\cos(\theta_{(t)}).\vec{X} + \sin(\theta_{(t)}).\vec{Y})$$

and

$$\mathbf{B}_1^{ax}(\theta_{(t)}) = |\mathbf{B}_1^{ax}|(1 + \alpha\cos(\theta_{(t)}).\vec{Z})$$

This means that the only coefficients left from Eq. 7.10 are $\alpha_0^{ax}, \alpha_1^{ax}$ and α_1^{ra}. The pictorial representation of this model is presented in Fig.7.1B. In the case of a rotating sample,$\mathbf{B}_1^{ax}$ oscillates at a frequency ω_r around its nominal value during the rotation. The amplitude $\mathbf{B}_1^{ra}$ oscillates as well but at a frequency $2\omega_r$. According to Eq. 7.9, the corresponding Hamiltonian $\tilde{\mathcal{H}}$ describing a RF-pulse along the y axis ($\phi = 0$) can be written under the form :

$$\tilde{\mathcal{H}}(\theta_0; t) = -\Delta\nu \mathrm{I}_z + a\cos(2\theta_{(t)})\mathrm{I}_x + b\Big(1 + c\cos(\theta_{(t)}) + d\sin(2\theta_{(t)})\Big)\mathrm{I}_y \tag{7.14}$$

with :

$$\begin{cases} a = & -\frac{1}{2}|\mathbf{B}_1^{ra}| \\ b = & -\sqrt{\frac{2}{3}}|\mathbf{B}_1^{ax}| \\ c = & \alpha \\ d = & \frac{1}{\sqrt{8}}|\mathbf{B}_1^{ra}|/|\mathbf{B}_1^{ax}| \end{cases} \tag{7.15}$$

To give an order of magnitude of the two components $\mathbf{B}_1^{ra}$ and $\mathbf{B}_1^{ax}$ in this region, which is located in the middle of the coil, one can prove later that $\mathbf{B}_1^{ra}$ is a tenth of $\mathbf{B}_1^{ax}$ and that $\mathbf{B}_1^{ax}$ will follows a Gaussian distribution. Finally Eq. 7.14 shows that the presence of a modulation, at the frequency ω_r, of the axial field introduces a similar modulation in the final Hamiltonian while a cosine modulation of frequency ω_r of the radial field introduces a periodic fluctuation of $2\omega_r$ in the final Hamiltonian. These different models, relaying initially on simplified geometrical considerations, provide a very simple description of the $\mathbf{B}_1$ field inside a solenoidal coil. In order to validate them, electromagnetic simulations based on Maxwell equations are required.

7.3 Prediction of the quantum states with the master equation

Another information contained in Eq. 7.9 is that, on a spinning sample, the presence of a non-vanishing radial field $\mathbf{B}_1^{ra}$, because of its pattern of distribution generates a modulation of the amplitude of I_x and I_y at the frequency ω_r. The evolution of the density matrix is then calculated by numerical integration of the equation of motion according Eq.6.26 :

$$\tilde{\varrho}\left(\rho, Z, \theta_0; t+\Delta t\right) = e^{\left(-\frac{i}{\hbar}\tilde{\mathcal{H}}(\rho,Z,\theta_0;t)\,\Delta t\right)}\,\tilde{\varrho}\left(\rho, Z, \theta_0; t\right)\,e^{\left(\frac{i}{\hbar}\tilde{\mathcal{H}}(\rho,Z,\theta_0;t)\,\Delta t\right)} \tag{7.16}$$

Since the direction, as well as the amplitude, of the RF field vary over the sample, the calculation of the NMR signal requires integrals over all the values of the *microscopic* field $b_1(\rho, Z, \theta_0)$ and a weighted ensemble average. For a solid-type sample, the real sample distribution is not accurately known due to the centrifugal force that can concentrate the sample against the walls of the rotor, whereas for a liquid, without any air bubbles, this concentration can be assumed to be homogeneous. For analytical purposes, the analysis of the $\mathbf{B}_1$ field will be limited to thin rings of various diameters centered around the main OZ axis of the solenoid and to homogeneous samples. The ring represents the circular path that a volume element of the sample follows during the rotation.

In practice this is calculated using the iterative way introduced in chapter 6. The sequence of pulses is applied to one single spin at a defined position (ρ, Z, θ). The signal obtained is then added to 59 other angular positions, taken along a circular path, in order to gather the effects of radial inhomogeneity. Finally these results were included in a loop to scan also the axial dimension. All simulations presented in chapter 9 are done accordingly to this general principle.

8

$\mathbf{B}_1$ field simulation for solenoidal coils from first principles

8.1 Results obtained from analytical methods

The simplification proposed to map electromagnetic fields in a coil is sufficient to explain a variety of results obtained in MAS experiments for typical 4 mm probes operating at 500 MHz of ^{1}H frequency. Calculations where performed using a numerical implementation of the Eq. 3.46 in Matlab 4.2b. The scaling was chosen to give an absolute value for the magnetic field arbitrarily equal to unity in the middle of the coil (For the balance chosen here, the sign of $\mathbf{B}_1$ is taken negative). Note that the proximity of the windings introduces a discontinuity and the amplitude may diverge at the center of the infinitely thin wire. We proceed by considering a circular path describing the trajectory of the spins subjected to the RF field $\mathbf{B}_1$. This vector field can be decomposed into an axial component $\mathbf{B}_1^{ax}$ (along the coil Z axis) and a transverse or *radial* $\mathbf{B}_1^{ra}$ component, as can be seen in Fig.1.5. In modeling the field components, various spatial regions are distinguished: the vicinity of the coil ends where the radial field component dominates and the region inside the coil close to its center where the axial component governs the RF hamiltonian. For each point, we plot :

(i) $\mathbf{B}_1^{ax}$, the axial part of $\mathbf{B}_1$,

(ii) the transverse part of $\mathbf{B}_1$ around the ring

(iii) the decomposition of the transverse components $\mathbf{B}_1^{ra}$ in the coil frame (X, Y, Z) and

(iv) the same as in (iii) but in the laboratory frame (x, y, z).

The Figs. 8.1 to 8.4 are obtained by changing the variable ρ of the circular path : the ring diameters considered are $0.5, 1, 1.5$, and 3 mm respectively. The four different positions

along the Z axis presented in each figure are :

(i) the center of the coil ($Z/Z_{max} = 0\%$),

(ii) the end of the coil ($Z/Z_{max} = 100\%$),

(iii) the middle position 50% between the two

(iv) a ring definitively out of the coil at 125% to probe the radial region as in the work published by Goldman [63].

In such a way that the calculations covers a range inside and outside the coil. The rotors used in the actual experiment have a diameter of 4 mm and a total length of 20 mm as depicted by Fig. 1.1. In the case of a full rotor the sample extends beyond the end of the coil, up to 6.2 mm from the center of the coil, corresponding to the plane corresponding of the last line of each figure denoted by ratio $Z/Z_{max} = 125\%$.

The first important result of the simulations shown in first column of Figs.8.1,to 8.4 is that the axial field $\mathbf{B}_1^{ax}$ always undergoes an intensity modulation as the sample rotates during MAS experiments. Very often, this modulation is similar to an expression of the type described by the model 2, which perfectly matches the results published in [111], based solely on the MLEV16 experiments. This result is not surprising if one considers that a helical structure can not, as it is usually stated, contain an axis of symmetry along OZ. Qualitatively, as the sample moves along a given ring, the distance to the actual coil wire fluctuates in a cosine like manner.

More quantitatively the calculation shows that the modulation factor $\alpha(\rho, Z)$ of the axial part increases with the radius of the circle, such a coefficient was introduced by Eq. 7.15. This effect is shown in the first line in Figs. 8.1, to 8.4. For $Z/Z_{max} = 0\%$, the amplitude of this modulation varies from around 5% for a ring of diameter 0.5 mm (center of the rotor) to 20% for a ring of diameter 3 mm (largest inner ring of the rotor). This modulation is consistent with what is described by model 2. For Z/Z_{max} greater than 50% we note a serious discrepancy with the simple sinusoidal modulation, specially when the spins are located on a ring close to the rotor wall (3 mm) (Fig. 8.4) last two lines of the first column). As the ratio Z/Z_{max} increases from 0% to 125%, the average of $\mathbf{B}_1^{ax}$ decreases.

If we refer now to the last column we can appreciate the impact of such modulation on the principal component of the $\mathbf{B}_1$ field along Oy in the laboratory frame. The presence of a periodic variation whose period is the same as the rotor period is noticeable in particular in the first line of Fig. 8.4. This modulation of $\mathbf{B}_1^{ax}$ during the course of the sample rotation is an important information that was until now fully neglected in MAS experiments. The second result of the simulations concerns the behavior of the radial

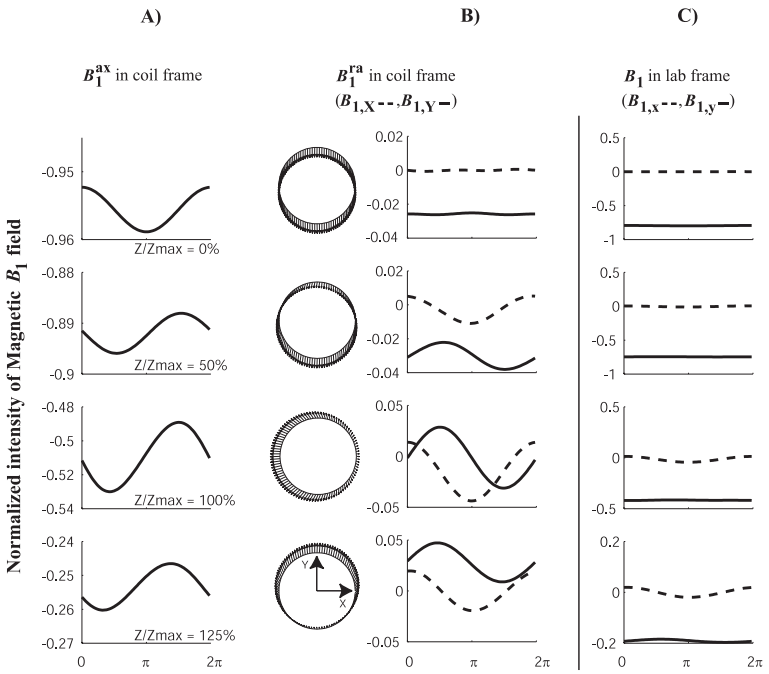

FIG. 8.1 – *Set of figures $\rho = 0.25$ mm : Magnetic field vectors calculated in the empty coil, and displayed around circular rings of diameter 0.5 mm. Each line corresponds to a transverse plane perpendicular to OZ, the main axis of the coil. The first line corresponds to the center of the coil ($Z/Z_{max} = 0\%$). The second line represents a position midway between the center and the end of the coil ($Z/Z_{max} = 50\%$), the third line represents the end of the coil ($Z/Z_{max} = 100\%$). The last line describes the field seen by the spins outside of the coil ($Z/Z_{max} = 125\%$) The first three columns represent the projection of the field in the coil frame, exactly as described in Fig. 7.1, the last column is the projection of the $\mathbf{B}_1^{ra}$ field in the (x, y, z) laboratory frame. The dashed curves correspond to the projection of the magnetic field $B_{1,X} = B_{1,x}$ .The projection $B_{1,y}$ of the last column (full line) is the dominant component of the $\mathbf{B}_1$ field in the laboratory frame.*

field : $\mathbf{B}_1^{ra}$ this component undergoes as well some modulation in the course of the sample rotation. For a ring of 0.25 mm (Fig. 8.1C) and at a value of $Z/Z_{max} = 0\%$, $\mathbf{B}_1^{ra}$ is vanishing small, ie. the field is purely axial. As the diameter of the ring increases from 0.5 mm to 3 mm, the amplitude of the radial field increases and fluctuations as a function of the rotation becomes clearly visible. When moving Z/Z_{max} from 0% to 125%, the amplitude of the radial field increases and becomes comparable in intensity to the axial field at the upper and lower edge of the coil (Fig. 8.4C). When comparing these simulations to the two previous proposed models, it is clear that model 1 is valid outside the solenoid coil (Z/Z_{max} values of 100% and 125%). In this region, the intensity of the radial and axial component of the field become comparable and the direction of $\mathbf{B}_1^{ra}$ is roughly along the normal of the ring, as shown by the two last lines of the second columns in all these figures.

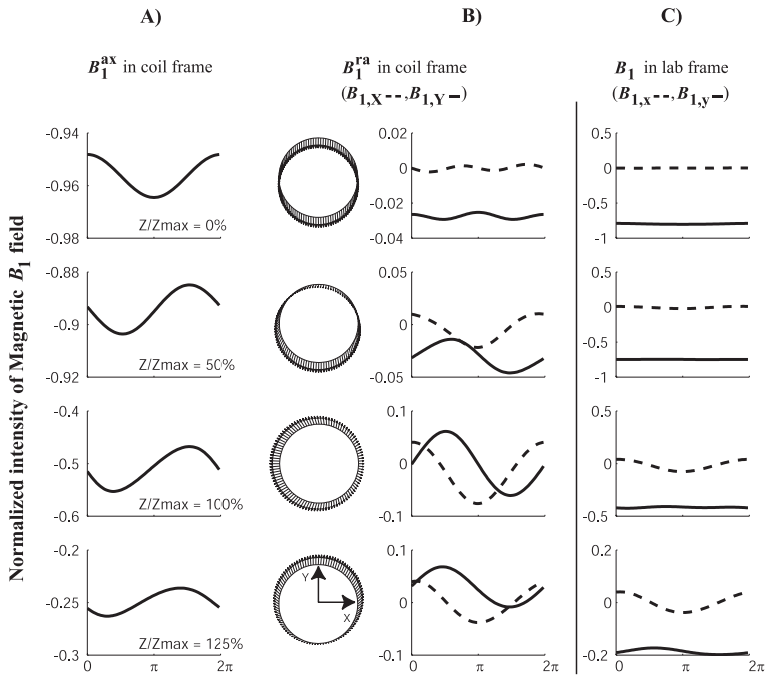

FIG. 8.2 – *Set of figures* $\rho = 0.5$ *mm : Magnetic field vectors calculated in the empty coil, and displayed around circular rings of diameter* 1 *mm.*

In the center of coil (Z/Z_{max} values of 0% and 50%), many characteristics of model 2 can be identified. The vector $\mathbf{B}_1^{ra}$ follows a cosine dependence at the frequency ω_r and $\mathbf{B}_1^{ra}$ exhibits a cosine dependence at the frequency $2\omega_r$. This is illustrated in the laboratory frame by the component along Ox of $\mathbf{B}_1$ in the first line of the last column of Fig.8.4, experimenting a modulation whose period is two times shorter than the rotation period. In the meanwhile the equation 3.46 can be also applied to a path collinear to the coil axis. Since the first source of inhomogeneity is the axial variation of $\mathbf{B}_1^{ax}$, an additional Gaussian factor can be introduced in the model to weight this effect.

The rigorous usage of this analytical derivation, requires to stay in the frame defined by the sheath helix. Obviously a tape helix-model can be still included in this frame [129], notwithstanding predictions away from this restricted ensemble of coils, could not claim to be valid. If the helix is (for instance) not equally wound [76], or of variable ribbon width [115], or finally of variable inner diameter this analytical method could not be used. For the moment we can state that electromagnetic derivation of the equation 3.46 justified the simplified models used in the quantum calculations presented in chapter 6. As a result of this we prove that the rather complex distribution of $\mathbf{B}_1$ can be analyzed -with a good accuracy- using the simple models 1 and 2 presented in section 10.2.2, which are the basis of the mathematical treatment involved in our work on field modulation in coils [48]. In the following we will prove that all helically wound structures show a similar pattern for

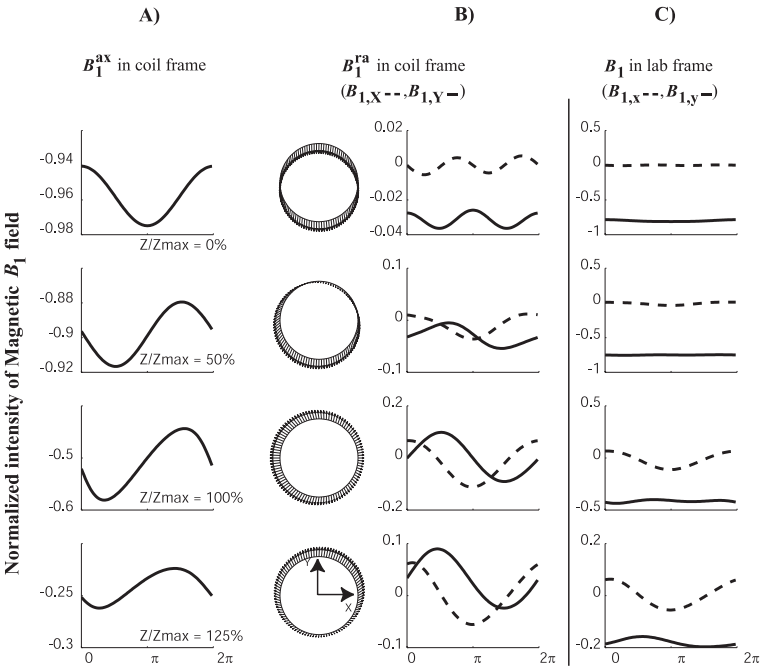

FIG. 8.3 – *Set of figures $\rho = 1$ mm : Magnetic field vectors calculated in the empty coil, and displayed around circular rings of diameter* 1.5 *mm.*

the $\mathbf{B}_1$ field, and that our models are still valid for a larger range of helices, but we will have to switch to numerical methods, to consider these more complex helical geometries that are variable pitch coils (in the next section), or to low-E field coils, which are to be presented in the chapter 11.

8.2 Results obtained using the numerical discretization of Maxwell equations from CST

The approach employed for analytical calculations, introduced an elegant and fast method to evaluate the contribution of the RF coil to the electromagnetic field on one precise point. Profiles can be easily obtained, by choosing a curve where the sum of each of the coil segments contributes to the retarded potential (Eq. 3.46). In fact the analytical model does not consider the 3D space as a medium where intricate wave relationships in any point may have a direct influence on the profile measured at another position. Only the infinitely thin coil play its role, and this is the reason why analytical methods are fast but inaccurate when the symmetry is broken. The first rupture is introduced by finite axial length, specially for the loading of the coil and the sample. Numerical methods on the opposite do not consider any kind of symmetry and the wave is propagated and

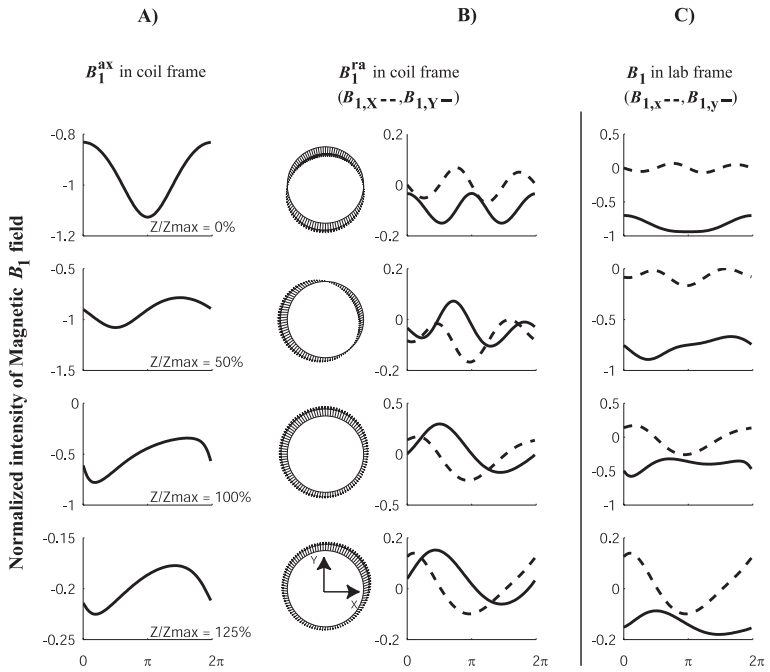

FIG. 8.4 – *Set of figures* $\rho = 1.5$ *mm : Magnetic field vectors calculated in the empty coil, and displayed around circular rings of diameter* 3 *mm.*

scattered in all the 3D space. Incident and reflected waves will give rise to charges and currents at all the discontinuities according to the boundary conditions set by Maxwell equations (Section 2.2), and at the end the electromagnetic wave pattern will emerge as the standing wave solution really present at the resonance.

The following section presents results obtained by CST 2006 in the case of a 5.5 turns coil used in a 500 MHz probe. To describe the non-equidistant winding a wire of 1 mm diameter has been created over an analytical curve representing half of the helix, this curve was created using a parameter t, so each point of the analytical helix has has the following coordinates :

$$\{\frac{D_c}{2}\sin(t); \frac{D_c}{2}\cos(t); z_c\} \tag{8.1}$$

where D_c is the diameter of the path, and z_c the height linked to the pitch by the following parametric relation :

$$z_c = a.t + b.t^2 \tag{8.2}$$

a and b are the coefficients that permit the parametrization of a variable pitch coil so :

$$a = \frac{n^2.P_L - L}{2n(n-1)\pi}$$

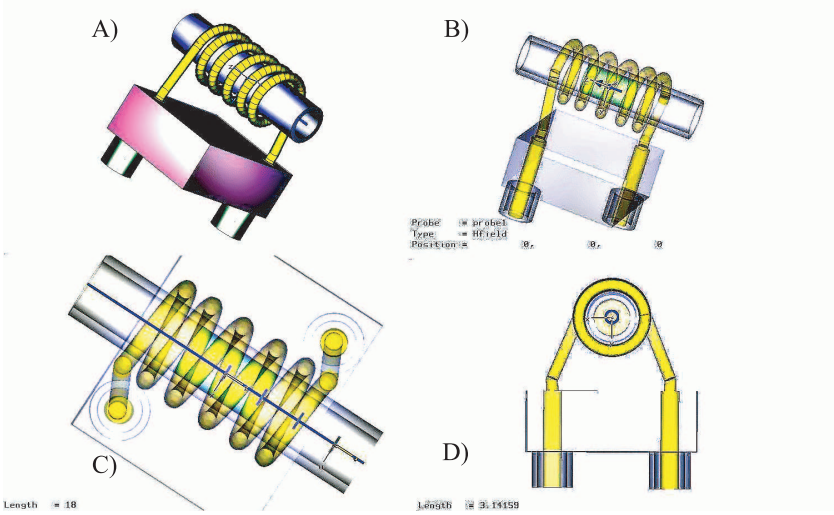

FIG. 8.5 – *Set of pictures describing the geometry of the variable pitch coil used for our simulations with CST.*

$$b = \frac{n.P_L - L}{2n(1-n)\pi^2} \tag{8.3}$$

where P_L is the length of the gap at the center, L is the length of the coil, n the number of turns and finally with a being bigger than b. In practice for the coil described here :

$$\begin{aligned} n &= 5.5\,\text{turns} \\ L &= 9.95\,\text{mm} \\ P_L &= 2.22\,\text{mm} \\ D_c &= 5.44\,\text{mm} \end{aligned} \tag{8.4}$$

The solenoid generated by the wire has an inner diameter of 4.44 mm.

This variable pitch coil is soldered to the feed-throughs of the coil holder. The simulated coil involves as input ports two TL's whose shields are not grounded together. These two TL are connected to such a holder, of rectangular shape and made of ceramic, whose permittivity influences the self resonance of the coil. Figure 8.5A, displays the considered coil, within a box filled up with 'vacuum' (ϵ_r=1,μ_r=1) and whose faces are boundary conditions for the electric field. Interesting feature of the solver employed here is the ability to consider conductive and dispersive dielectrics, here an aqueous sample with an

equivalent conductivity of 2 S/m was employed to simulate a highly dispersive sample (the dispersion curve of this sample is presented in Fig. 10.3A). The analysis of the port signal is followed over a large range of frequencies (from quasi-static up to 800 MHz), with a mesh comprising over 178,640 cells. The mode at the ports is purely TEM, and the two excitations pulses are applied through a structure one after each other, during a 8 ns pulse of Gaussian shape[20]. Fig. 8.5B shows the position of the magnetic field probe, used to track the establishment of the wave pattern during the excitation and relaxation process. The result is a frequency dependent curve of the magnetic field at this position. When the solver has reached the steady-state by minimization of the systems *energy*[21], the field can be displayed at user defined positions, for a chosen frequency comprised in the range of observation (here at 500 MHz). Figures 8.5C, and 8.5D display the linear and circular paths where the fields have to be calculated, the length of each of these is indicated in the bottom of the figure. The series of results presented in Fig. 8.6 are a display comparable to what has been shown by Fig. 8.2 of the preceding section : the fields were calculated along the circles indicated in the Fig. 8.5D.

When ploting the magnetic field along the central axis of the coil, it appears that the variable pitch has improved significantly the axial homogeneity of the magnetic field. This field is treated as a complex vector and therefore each component has a time dependency included in the phase. Dephasing of a traveling wave along the helix is known problem and a recent survey can be found in [49]. In the plots below (Fig. 8.7) we see that the variation of such time-phase is rather negligible at this frequency, even if a small lowering in the center (less than 1^o) is observable for all curves. This depth is to be related with the conductivity of the sample : in an empty coil the phase of the backward and forward H_Z components would experience a monotonous variation in the center region. Here the field can be considered 'linearly-polarized' with same phase for all field vectors. The treatment of such linerar polarization of the magnetic field is well known in NMR.

The combination presented in Fig. 8.8 is an example of how intricate the relationship between $\mathbf{B}_1$ and $\mathbf{E}_1$ may be. This last figure offers an interesting demonstration of the intricate combination of electric and magnetic field in the loaded coil. The myth of no-electric field in balanced coils is only valid at extreme low frequencies. Electric field pattern is far more complex, because the boundaries introduced by the sample, and the rotor wall modified strongly the shape we had calculated previously in an empty coil. The rotor walls are a first discontinuity, the electric field is mostly normal to the walls outside the

[20] Corresponding to the large frequency bandwidth

[21] In the sense given by CST, the convergence is reached when the power in the mesh reaches -50dB of the original input power

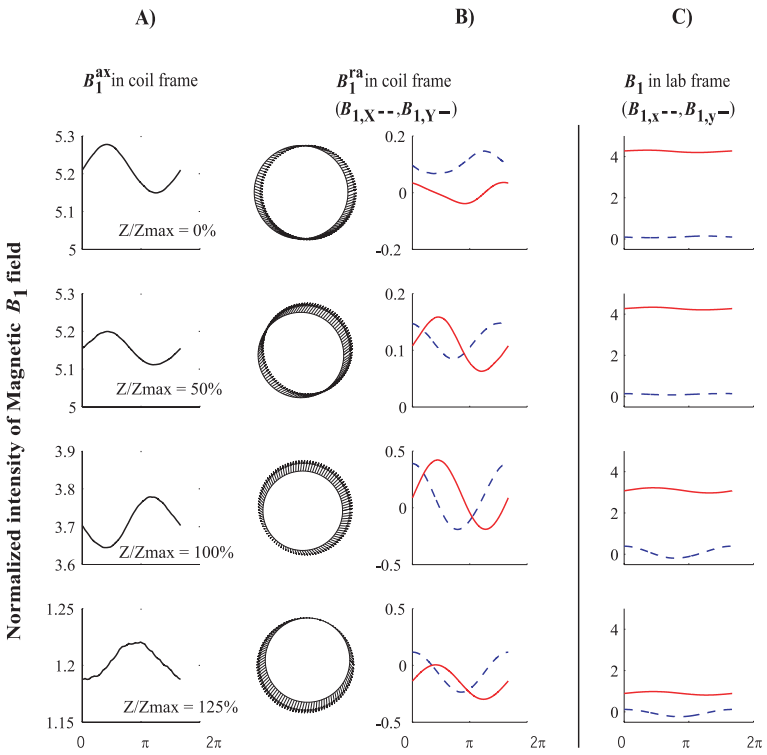

FIG. 8.6 – *Set of figures equivalent to $\rho = 0.5$ mm : Magnetic field vectors calculated in the sample (0% and 50%) but also outside (100% and 125%). The two models can be identified at the center and at the ends of the rotor.*

rotor, but becomes purely axial once it is inside the rotor, we point here that the high dielectric constant of the rotor has the advantage of lowering the electric field from outside to inside. The second, and maybe more significant, discontinuity is the step between the rotor (considered empty) and the sample volume, whose dispersion characteristics where considered by the solver. Again the effect of such sample is to lower the electric field. Notwithstanding dynamical analysis of the phase vectors shows that there is a phase retardation of almost 180^o from the field outside the sample and the field inside the sample. This phase dispersion denotes a high dielectric absorption of the sample. Therefore we reveal a strong coupling of the sample with the electric field which implies that a significant heating is expected.

This is in agreement with the experience produced by the perturbation experiment called 'water-shift'. The frequency variation produced by a rotor containing water in an empty coil is at high frequencies far more important than the frequency variation induced by a rotor alone.

It is noticeable from the right side of figure 8.8 that the magnetic field keeps tangential to the rotor walls, and of course that the surface with the sample does not alter its

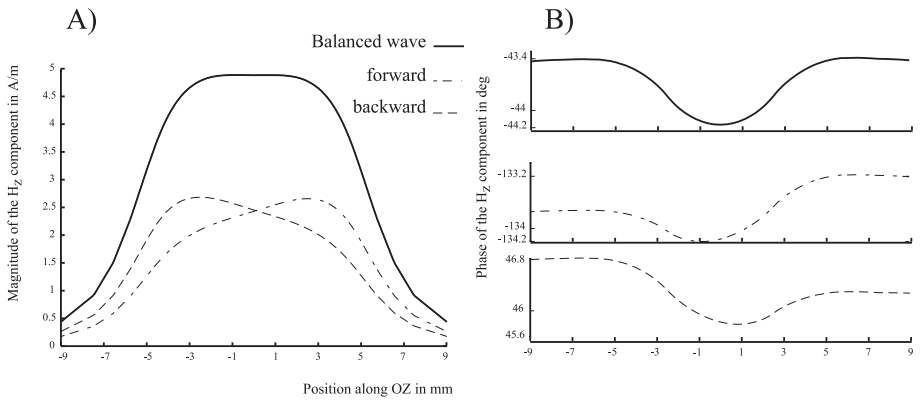

FIG. 8.7 – *Result of the EM field calculation displayed at 500 MHz along the OZ axis. The magnetic field component H_Z is a vector whose magnitude is presented at the left side (A). The field pattern is generated by the excitation of each port to simulate forward and backward waves and the sum of both according to the definition of balance given by Eq. 4.10. As the fields are treated as complex numbers, we have the possibility to plot the phase in degres of these three components in (B). This curves give the phase as a function of the position along the rotor axis.*

distribution. The strength of the magnetic field is nevertheless altered by the conductivity. It is useful for the interpretation of Fig. 8.8 to note that both fields are in phase quadrature, and therefore there respective maximum values are 90^o far away from each other.

A) B)

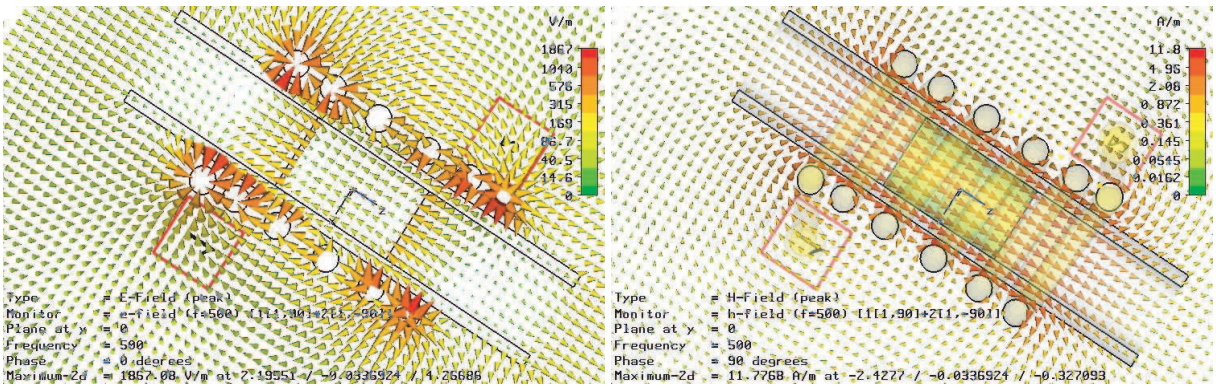

FIG. 8.8 – *Result of the EM field calculation displayed at 500 MHz in the axial OXZ plan, Electric field is presented as a vector field at the left (A), and magnetic field at the right (B).*

9

Field modulation effects induced by sample spinning : results and discussion

In the following sections, we present three experiments that can be affected by $\mathbf{B}_1$ field inhomogeneities (axial and radial) and include the effects of $\mathbf{B}_1$ modulation. The results presented in the following section are those observed first for complex pulse sequences like MLEV cycles. Later in the last section we employ nutation to reveal the simplicity of this phenomenon, and to relate it to the models introduced in the previous chapter.

9.1 Rotary Echo experiment

The rotary echo experiment is based on the simple sequence $(90^o)_{+x} - t - (90^o)_{-x}$. The data are recorded after a variable evolution time (t). In the absence of relaxation processes, RF field imperfections and offset effects, the magnetization of the spins initially aligned along the Oz axis is returned to exactly the same position at the end of the sequence. Experiments ran under static conditions in liquid-state high resolution probes clearly agree with this statement. However the outcome of the rotary echo experiment run under MAS conditions does not lead to this result. The actual results obtained under these conditions are illustrated in Fig. 9.1. The spectrum was recorded on a D_2O sample by incrementing the evolution time (t) between the two pulses and by Fourier transforming the different spectra in both dimensions. The carrier frequency was set exactly on the proton HDO resonance.

The spinning speed used for MAS was 2 kHz and the 90^o pulse-length was equal to 7.5 μs, corresponding to a RF field amplitude of 33.3 kHz. The experimental results show that the spectra consist in several lines of frequencies 2 and 4 kHz. The maximum intensity is observed for the line at twice of the spinning frequency. The high number of

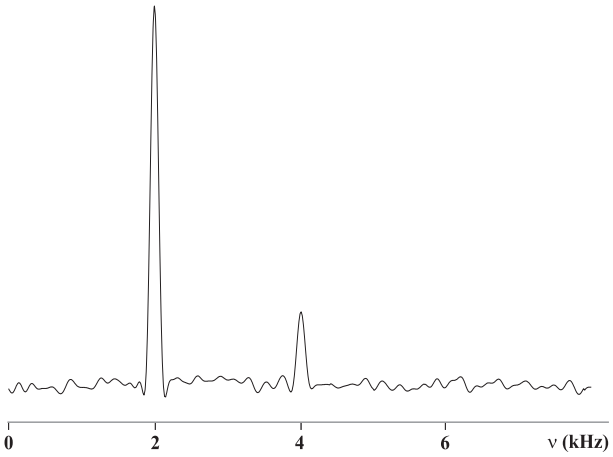

FIG. 9.1 – *Proton spectrum of resulting from a rotary echo experiment* $(90^o)_{+x} - t - (90^o)_{-x}$ *recorded on the HDO signal of a* D_2O *sample. The data are recorded after a variable evolution time* (t)*. The carrier frequency was set on the proton HDO resonance. The spinning speed used for MAS was 2 kHz and the* 90^o *pulse-length was equal to* 7.5 μs*, corresponding to a RF field amplitude of 33.3 kHz. The spectrum was recorded by incrementing the evolution time* (t) *between the two pulses and by Fourier transforming the different spectra in both dimensions. Displayed spectrum is the corresponding F1 slice extracted from 2D spectra obtained with a resolution in F1 dimension of (20 Hz). Spectra were recorded on a Bruker Avance 500 MHz equipped with a 4 mm H/C/D MAS probe. The sample was placed in a 4 mm rotor fitted with Teflon inserts delimiting an active volume of* 50 μl*.*

scans required to observe these spinning lines indicates that the transversal magnetization is weak and the magnetization is mainly returned along the Oz axis. Rotary-Echo experiments were performed on other samples leading to the same findings. This unusual behavior in a consequence of the $\mathbf{B}_1^{ra}$ inhomogeneities experienced by the sample during the rotation. This thesis will be illustrated by the following simulations. In order to simulate these experimental results, initial magnetization was exposed to a the pulse sequence $(90^o)_{+x} - t - (90^o)_{-x}$. The calculations were performed according to the procedure described above. The following parameters were used for the simulations : $\Delta_n u = 0$, $\omega_r = 2\ Hz$, $\sqrt{2/3}\mathbf{B}_1^{ax} = 33.3\ kHz$, $\mathbf{B}_1^{ra} = 0.1\mathbf{B}_1^{ax}$, and $c = 0.1$ in Eq. 7.14. The results of the simulations describing the fate of the I_x, I_y and I_z components as a function of the evolution time (t) are shown in Fig.9.2.

The spectra presented in Fig. 9.3 are obtained after Fourier Transformation of the transverse magnetizations plotted in Fig. 9.2. Incidentally figs.9.2A and 9.3A represent the simulations using model 1 while Figs.9.2B and 9.3B represents the results of the simulations using model 2.

These results show that the spinning provokes periodic oscillations of the magnetiza-

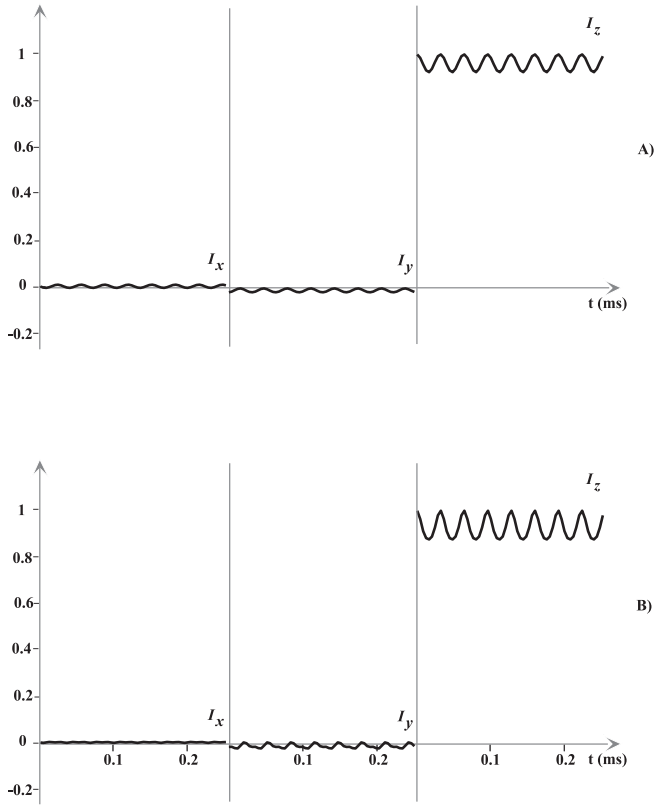

FIG. 9.2 – *NMR simulations of the magnetization evolution in the Rotary Echo experiment* $(90^o)_{+x}-t-(90^o)_{-x}$ *using model 1 (A) and model 2 (B). Eq.7.12 was used for model 1 and Eq.7.14 was used for model 2. The following parameters were used for the simulations :* $\Delta\nu = 0$, $\omega_r = 2\ Hz$, $\sqrt{2/3}\mathbf{B}_1^{ax} = 33.3\ kHz$, $\mathbf{B}_1^{ra} = 0.1\mathbf{B}_1^{ax}$, *and* $c = 0.1$ *(Eq.7.15).*I_x,I_y *and* I_z *components are plotted as function of the evolution time(t) between the flip and flop pulses.*

tion. As it can be seen, a large fraction of the magnetization is returned along the Oz axis and a non negligible part of the magnetization is shared periodically between the longitudinal and transversal components. Amplitude and frequency of the oscillations are provided by the spectra presented in Fig. 9.3. According to model 1, the spinning induces two oscillations of frequency 2 and 4 kHz. The intensities of two spinning lines indicate the preponderance of the oscillation at 2 kHz corresponding to the spinning speed. Using model 2, the calculations predict two intense oscillations of frequency 2 and 4 kHz. These predicted results agree with the experimental observations (Fig. 9.1). The inspection of the experimental data shows that the intensities of the two spinning lines fit well with the predictions of model 2.

These investigations show that for sequence $(90^o)_{+x} - t - (90^o)_{-x}$ the spinning gives rise to a weak loss of the magnetization along the Oz axis. The repetition of this sequence

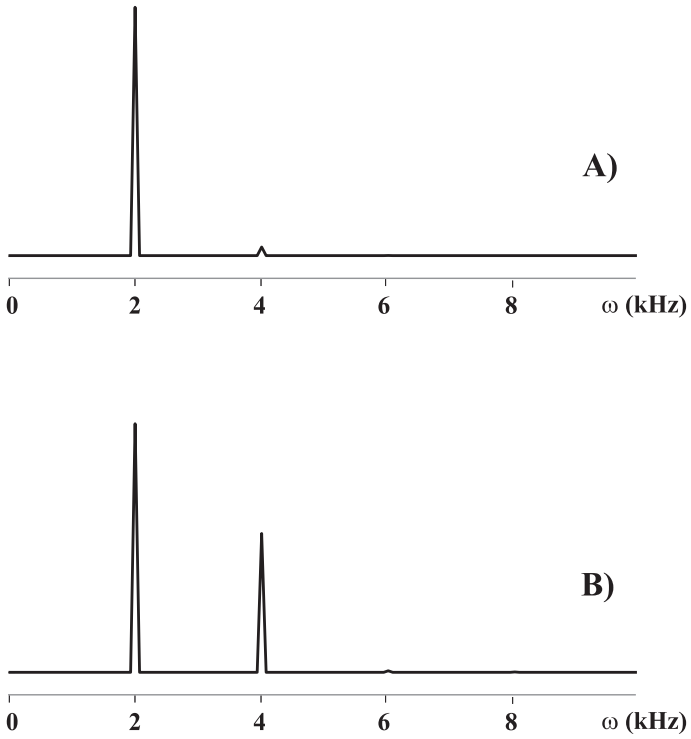

FIG. 9.3 – *Spectra obtained after Fourier Transformation of the transversal magnetizations plotted in Fig. 9.2. Spectra A and B correspond to the models 1 and 2, respectively.*

in a NMR experiment can lead to some loss of magnetization. To prevent these effects, the increment of the evolution time (t) must be set equal to a multiple of the rotor period.

9.2 MLEV16 and DIPSI2 experiments

The goal of the present section is to provide an explanation to the data shown in 9.4. These data represent the variations of the first increment of an MLEV-16 [91] experiment recorded on a sample of sucrose in D_2O as a function of the rotor spinning speed. The $\mathbf{B}_1$ field used for the MLEV-16 mixing pulses was 8 kHz which corresponds to the classical value used at moderate $\mathbf{B}_o$ fields.

Only the proton HDO resonance line, in the center of the spectrum at 4.76 ppm, is shown in Fig. 9.4. Data were recorded with a small increment of 100 Hz in order to obtain a precise description of the phenomenon. An extremely strong decrease in signal intensity is observed for sample rotation values of 2, 4, 6, 6.5 and 9.5 kHz. This phenomenon is most puzzling since the proton of the HDO resonance represents an isolated spin system whose MLEV-16 spectrum should be independent of the speed of rotation. Similar effects were observed on all the resonances of the sucrose molecule in the sample. The maximum signal

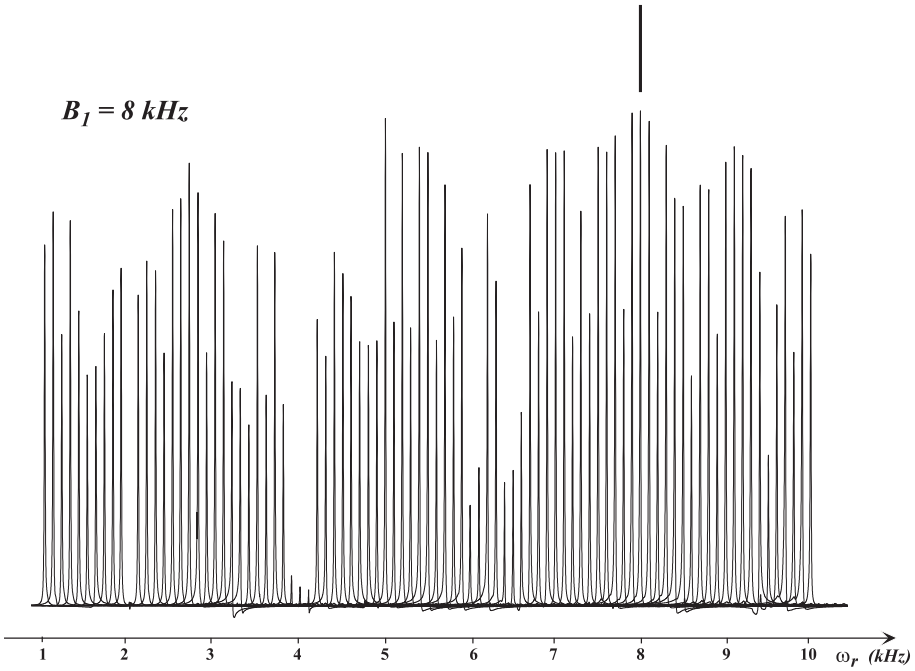

FIG. 9.4 – *Proton spectra of the first increment of an MLEV-16 experiment recorded on the HDO signal of a 2 mM sucrose sample in D_2O. The spectra were recorded at different spinning speeds, starting at 1 kHz and going to 10 kHz in 100 Hz increments. The constant field used for the MLEV-16 element was set to 8 kHz and two MLEV-16 cycles, corresponding to a 4 ms mixing time, were applied. Spectra were recorded on a Bruker Avance 500 MHz equipped with a 4 mm H/C/D HRMAS gradient probe. The sucrose sample was placed in a 4 mm rotor fitted with Teflon inserts delimiting an active volume of 50 μl.*

intensity is only obtained at a rotation speed of 8 kHz which matches exactly the value of the $\mathbf{B}_1$ field strength. Under these conditions, the time length of the basic element of the MLEV-16 cycle $R = (90^o)_{\phi_1} - (180^o)_{\phi_2} - (90^o)_{\phi_1}$ is exactly equal to one rotor period. These experimental conditions are the ones recommended to acquire MLEV-16 spectra under MAS [111]. For DIPSI-2[122] experiments, the optimum value of the $\mathbf{B}_1$ field over the speed of rotation is different and more difficult to define exactly. The data published in Ref. [111] can be used to chose the optimum value of the rotation.

MLEV-16 sequences are experiments designed to achieve coherence transfer through scalar coupled spin systems in order to assign the different spin systems present in a molecule. The basic element of our sequence is a composite 180^o_y pulse called R which is defined as :$R = (90^o)_y - (180^o)_x - (90^o)_y$ .Its opposite $\bar{R} = (90^o)_{-y} - (180^o)_{-x} - (90^o)_{-y}$ is the second basic element of the sequence. The two elements R and $\bar{R}$ are combined in the following manner to generate the MLEV-16 cycle :

$$R\bar{R}\bar{R}R\,\bar{R}\bar{R}RR\,\bar{R}RR\bar{R}\,RR\bar{R}\bar{R}$$

The magnetization of interest in these experiments is the one initially perpendicular to the RF field of the MLEV-16 element. For example, if the MLEV-16 cycle is applied along $+y$, then the magnetization of interest is I_x. Under these conditions, the initial magnetization I_x is taken successively through $-\mathrm{I}_z, \mathrm{I}_z$ and then back to I_x. The experimental results of Fig. 9.4 show that the intensity of the magnetization almost drops to zero at 2, 4 and 6 kHz. Signal losses can also be observed at 1.5, 3.25, 4.75, 6.5 and 9.5 kHz. The maximum expected intensity of the experiment is only reached at a spinning rate of 8 kHz which corresponds to the intensity of the $\mathbf{B}_1$ field used in the experiment. In order to simulate these experimental results, initial I_x magnetization was subjected to two consecutive MLEV-16 cycles of phase $\pi = y$. These particular conditions correspond to a R element given by $R = (90^o)_y - (180^o)_x - (90^o)_y$. The calculations were performed by numerical integration of Eq.7.16 and by summing the results obtained using 60 equally spaced values of θ_0. This set of values was found to be adequate to represent the spin population on the ring. The simulations were performed using models 1 and 2 of section 6, which correspond to Eqs. 7.12 and 7.14, respectively. The following parameters were used for the simulations : $\Delta\nu$, $\sqrt{2/3}\,\mathbf{B}_1^{ax} = 8\ kHz$, $\mathbf{B}_1^{qx} = 0.1\,\mathbf{B}_1^{ra}$ and $c = 0.1$ in Eq.7.15. The value of 8 kHz chosen for correspondence with the experimental conditions of Fig. 9.4 and leads to a 4 ms MLEV-16 mixing time. The calculations were performed for different spinning rates ranging from 1 to 10 kHz. The results of the simulations describing the fate of the I_x component after two MLEV-16 cycles are shown in Fig. 9.5. Fig. 9.5A represents

the simulations using model 1 while Fig. 9.5B represents the results of the simulations using model 2. These results show that, as expected, the magnetization present after the MLEV-16 cycles is strongly affected by the spinning rate. Model 1 creates important losses of magnetization at 1.5, 4, 6.5 and 9.5 kHz. Model 2, on the other hand, features intensity drops at 1.5, 2, 4, 6 and 6.5 kHz. In both cases, a small amount of I_y and I_z magnetization is created during the MLEV-16 mixing. However, this new magnetization does not compensate the much larger intensity drops observed for I_x. Everything happens as if some of the magnetization had disappeared. An analysis of the fate of the magnetization in different parts of a single ring shows that the spins behave as if they were subjected to an intense gradient pulse $\mathbf{B}_1$. Along a given ring, the MLEV-16 sequence effectively dephases all the spins, creating a state in which the magnetization points in every directions in the (x, y) plane, resulting in a net magnetization equal to zero. What is particularly striking in these simulations is that model 2 reproduces the experimental data of Fig. 9.4 to a very high degree. Most of the magnetization losses observed in Fig. 9.4 are observed in the simulations of Fig. 9.5B, which is quite remarkable considering the relative simplicity of model 2 and the fact that the simulations were carried out using a single ring. An important point is that the modulations in ω_r and $2\omega_r$ present in model 2 are essential to reproduce the behavior observed in the experimental data. On the other hand, the results of the simulations using model 1 are not complex enought to understand the experimental data. Only the intensity drops observed at 4 and 6.5 kHz are reproduced properly. These findings are consistent with the results of the electromagnetic simulations of section 8 that show that model 2 is valid inside the coil whereas model 1 is valid outside the coil. In fact model 1 and model 2 coexist, but in different regions of the solenoid. However, for most HR-MAS applications, model 2 is certainly the right one since it describes the distribution of the active volume of the solenoid coil.

The time evolution of the magnetization at 2, 4, 6 and 8 kHz is simulated in Fig. 9.6(A-D respectively) in the case of model 2. Each point on this curve represents a data point taken after one R cycle.

It is clear that when the rotation speed is 2, 4 or 6 kHz, the loss of intensity is a very fast process, requiring only a couple of milliseconds. This intriguing phenomenon of destruction of magnetization is clearly related to the spatial properties of the electromagnetic field in the solenoid coil. It should, therefore, be possible to minimize these effects by restricting the sample position. For that purpose, we have manufactured a cylindrical Teflon insert with an inner cylindrical hole of diameter 0.5 mm. This insert allows to restrict the sample location to a cylinder of diameter 0.5 mm in the center of the solenoid coil.But, of course, will reduce the filling factor and therefore the sensitivity. Under these conditions, the

effects of radial fields and the amplitude of the modulations of the axial field should be far less pronounced than in a normal 4 mm rotor. Results of MLEV-16 experiments carried out on such a sample show that virtually no magnetization losses are observed at 2, 4 and 6 kHz, thereby confirming the hypothesis developed in our review article [48]. When comparing these observations to the models proposed in section 6, it is clear that many features of model 1 are present outside the solenoid coil (Z/Z_{max} values of 100% and 125%). In this region, the intensity of the radial and axial component of the field become comparable and the direction of $\mathbf{B}_1^{ra}$ is roughly along the normal of the ring. This situation is similar to the one described by Goldman et al. [63, 135].

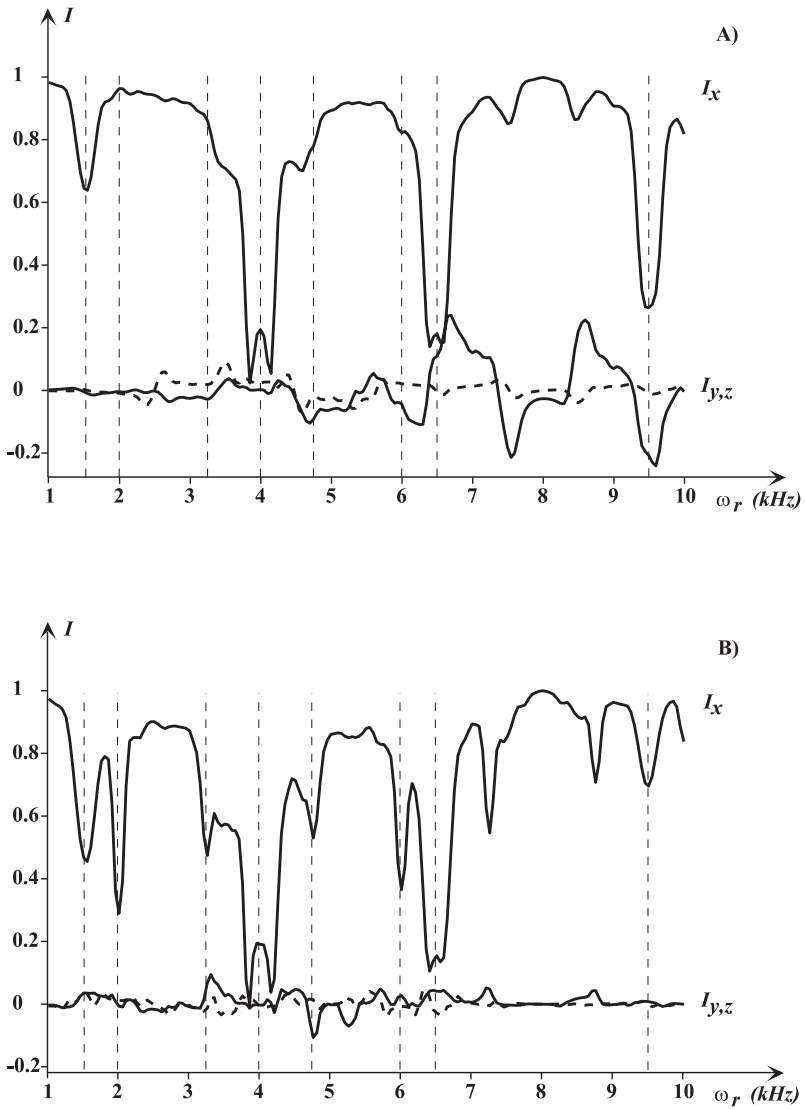

FIG. 9.5 – *NMR simulations of the magnetization of the first increment of a MLEV-16 experiment using model 1 (A) and model 2 (B) at different spinning speeds. Eq.7.12 was used for model 1 and Eq.7.14 was used for model 2. The following parameters were used for the simulations :* $\Delta\nu$, $\frac{2}{3}\mathbf{B}_1^{ax} = 8\ kHz$, $\mathbf{B}_1^{ax} = 0.1\,\mathbf{B}_1^{ra}$ *and* $c = 0.1$ *in Eq.7.15. Data points were taken after each R cycle and the average of all these values was plotted in the graph.* I_y *is represented by solid lines and* I_z *by dashed lines.*

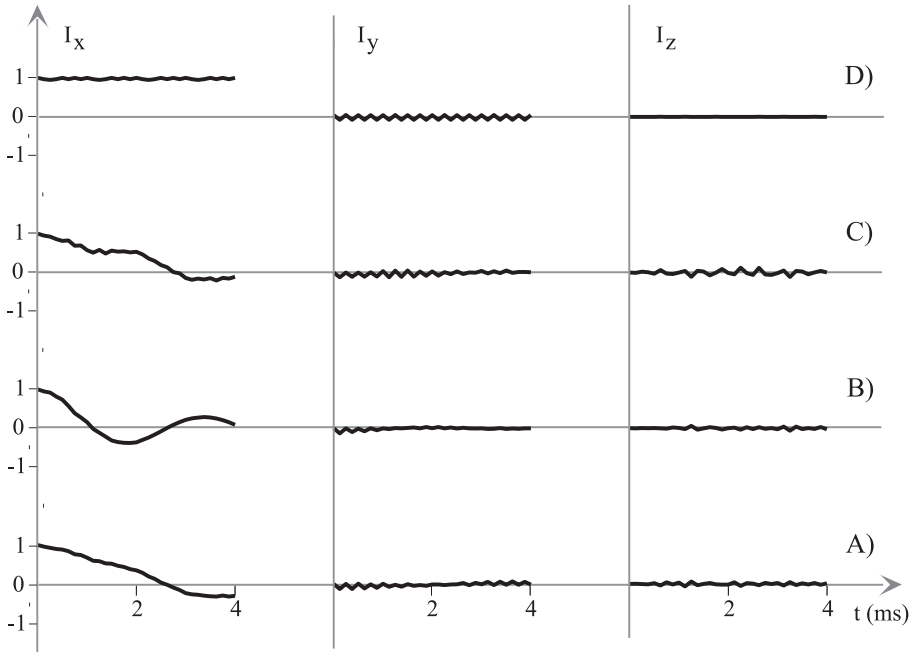

FIG. 9.6 – *NMR simulations of the magnetization of the first increment of a MLEV-16 experiment as a function of the mixing time using model 2. Simulations were performed at a speed of 2 kHz (A), 4 kHz (B), 6 kHz (C) and 8 kHz (D). Data points were taken after each R cycle. The parameters used for the simulation are the same as those used in Fig. 9.5.*

9.3 Nutation experiment

The amplitude of the RF field and an estimation of its inhomogeneity can be accessed with the so-called *nutation* experiment [137]. The nutation consists in applying a single hard pulse of increasing length (t_1), followed by an acquisition period (t_2). Fourier transformation of the NMR data in the two dimensions leads to a 2D spectrum where the F2 dimension is the regular spectrum while the F1 dimension gives the $\mathbf{B}_1$ distribution experienced by the spins in the sample.

9.3.1 Practical aspects of the adjustment of experimental nutation curves using the expression of the measured signal given by the reciprocity

We want here to describe the methodology to be employed in order to get information from a nutation curve. An short historical review of the signal equation may be interesting to understand the simplifications behind the mathematical expression of the NMR signal.

The nutation experiment is the first NMR experiment used to calibrate the 90^o pulse length in the sample under analysis. It can be separated in three sequential steps, one starting delay to stabilize the sample ($1 - 10\,s$) denoted by index '0', one pulsing time (in the range $1 - 300\,\mu s$) as RF emission period of index '1', one acquisition period ($1 - 1000\,ms$) of index '2'.

If we focus on this single pulse experiment, after a pulse of length t_1 we will describe the projection along $\vec{x}$ of the precessing magnetization $\vec{\mathcal{M}}_2$.

Abragam made an early statement of signal equation in his reference book [1], of 1960. His approach serves as starting point for later studies [74, 33]. The signal is directly linked to an EMF (electromotive force), called ϑ, deriving from Faraday's law.

$$\vartheta = -\frac{\partial \Phi}{\partial t} \tag{9.1}$$

where Φ is the flux produced by the magnetization in the transverse plane $\vec{\mathcal{M}}$ given as a phasor with a definition similar to what has been already seen in the second part :

$$\vec{\mathcal{M}} = \vec{\mathcal{M}}_2 . e^{i\omega_o t}$$

If $\vec{A}$ is the total surface of the coil, Abragam derives the EMF (page 72 of [1]) as :

$$\vartheta = 4\pi\omega_o . \vec{\mathcal{M}} . \vec{A} \tag{9.2}$$

Later, in his description, the voltage measured at the preamp (V_2) is calculated using the Quality factor of the probe Q. Finally equation 9.2 relates the magnetization to the amplitude of the signal, as a first approximation. This is supported by electromechanics as a first approximation. By the means of the geometry dependent surface vector $\vec{A}$, Eq. 9.2 provides a usefull simplified expression of signal. Numerical calculations derived from this particular approach are of great help for many purposes. Nevertheless, in this case, it is stated implicitly that the $\mathbf{B}_1$ is homogeneous in the sample volume, and this can not be accepted in the range of NMR frequencies used in high field spectrometers. Specially not, if the signal's equation has to be used to estimate the impact of the $\mathbf{B}_1$ inhomogeneity. For this, the correction introduced by the reciprocity principle is needed.

In the original article from Hoult and Richard [74] the induction field $\mathbf{B}_1$ produced by a coil C carrying unit current, generates a signal written as :

$$\vartheta = -\frac{\partial}{\partial t}\int_{\Omega_2} \vec{B}_1.\vec{\mathcal{M}}\, d\Omega_2 \tag{9.3}$$

where $\mathbf{B}_1$ and $\vec{\mathcal{M}}$ have identical time dependency and are staying in the near-field limit of electromagnetic fields [77]. It is one of those formulae that tend to be accepted without question, whereas in reality, its use in subtle. It is clear that with the simplifications introduced by *Hoult's reciprocity* the signal level of any NMR experiment can be predicted. The calculation of $\mathbf{B}_1$ is feasible for most shapes of coil, at least by numerical methods. Of course, if $\mathbf{B}_1$ is to be considered as reasonably homogeneous over the sample volume by Hoult, the calculation is considerably simplified as the integration of Eq. 9.3 becomes trivial, giving :

$$\vartheta(t_2) = K\omega_o(B_1)_{xy}\mathcal{M}_o\Omega_s\cos(\omega_o t_2) \tag{9.4}$$

where K is a bulk 'inhomogeneity' factor. $(B_1)_{xy}$ is the RF field component perpendicular in the lab frame, Ω_s is the sample volume, and the phase inhomogeneity has been neglected [74]. This may be useful for a first approximation, but not when the field mapping by NMR is at stake.

We propose here an approach based on reciprocity and focused on the fact that damping of the nutation curve is solely produced by the $\mathbf{B}_1$ inhomogeneities. When we introduce the source of magnetization in the equation of reciprocity 5.10, we assume that $\vec{\mathcal{M}}_s$ is kept in the transverse plane, this corresponds to a long relaxation time as often encountered in liquids. Indeed solving Bloch differential equations makes sense for a deeper analysis of how much does relaxation influence the signal during the nutation experiment, but we know it is not necessary for our concern. In this analysis we rely on experimental conditions that guarantee that relaxation process is not influencing the nutation signal.For

the present we keep the simplest equation of voltage signal given by :

$$\vartheta(t_2 \sim 0^+) = \frac{i.\mu_o\omega_o}{I_1\gamma_r}\mathcal{M}_o \cos(\omega_o t_2) \int_\Omega \omega_1 . \sin(\omega_1 t_1)\, d\Omega \tag{9.5}$$

$\vec{\mathcal{M}}_o$ is the initial magnetization along the $\vec{z}$ axis, it can be extracted form the volume integral because of the homogeneity of the static magnetic field $\mathbf{B}_o$.

By noticing that the limit of the Fourier transformation when $t_2 \to 0$ is equal to the integral of the spectral peak :

$$\lim_{t_2 \to 0} \quad \mathrm{FT}\Big(\vartheta(t_1, t_2)\Big) = \tfrac{\mu_o\omega_o\mathcal{M}_o}{I_1\gamma_r} . \int_\Omega \omega_1 . \sin(\omega_1 t_1)\, d\Omega \tag{9.6}$$

we can access the first point of the received signal.

This volumic integral can been transformed in a linear one by assuming an almost flat $\mathbf{B}_1$ distribution in the radial dimension. This is acceptable as long as the radial inhomogeneity is one order of magnitude smaller that the axial variation. We proved it in the precedent chapter that this is always the case. So we may transform the integral of the equation 9.6 in the following integral along OZ the main axis of the coil. The surface of the sample is derived thanks to r, the radius of the sample. When increasing the pulse length (t_1), the FT of the nutation signal $\vartheta(t_1)$ becomes :

$$\vartheta(t_1) = \vartheta_o \int_Z \omega_1 . \sin(\omega_1 t_1)\, dZ \tag{9.7}$$

with ϑ_o a scaling factor comprising $\frac{\mu_o\omega_o\mathcal{M}_o}{I_1\gamma_r}$ times πr^2.

In general this integral can not be solved analytically. In order to predict the magnetic field, an experiment has to be fitted by the matematical model given by Eq. 9.7, the adjusted parameters define the shape of the $\mathbf{B}_1$ field along the axial direction of the coil.

The simplified derivation presented here, has only the pretension of describing different simplifications involved behind our reciprocity-based adjustments.

For extracting the field distribution out of a nutation curve, a certain number of material properties need to be known. The experimental setup will, in certain cases, involve a sample like water, adamantane, or even glycine. The dissipation occuring in the matter during a long destructive pulse may alter the sample and ruin the reciprocity. On the other hand strong dipolar couplings in solids will influence the nutation curves when the pulse length become too long. Finally samples approaching the model known

as *diluted gas of spins* or diluted dipolar solids are chosen. There dipolar couplings, and some transverse relaxation mechanisms are withdrawn by chosing rare spins. Samples like deuterated adamantane or heavy water for ^{1}H, or even polycristaline C_{60} [57] for ^{13}C are a good example of this. In practice all materials whose different dipolar, exchange or relaxation times are much longer than the maximum pulse length. It is so that in the case of aqueous samples, relycling delays need to be considerably increased, and the nutation may last many hours. The static field $\mathbf{B}_o$ requires to be homogeneous in the sample region and stable, specially when nutation is measured as a 1D experiment.

9.3.2 Adjustements of nutation plots obtained in 4 mm rotors

In this experiment we illustrate the position dependency of the $\mathbf{B}_1$ introduced by the inhomogeneity. This is done by performing adjustments of two nutation curves recorded simultaneously, but from distinct regions. A set of plugs allows to isolate labeled glycine sample slices. These are designed to hold the samples at defined positions along the 4 mm rotors were machined accordingly to the numerical indications provided by Fig. 1.2. Staying with this description of the rotor seen in section 1.2, we will call *bottom region* the slice extended form 6.25 to 7.25 mm, and *middle region* the volume comprised between 10.75 and 11.75 mm.

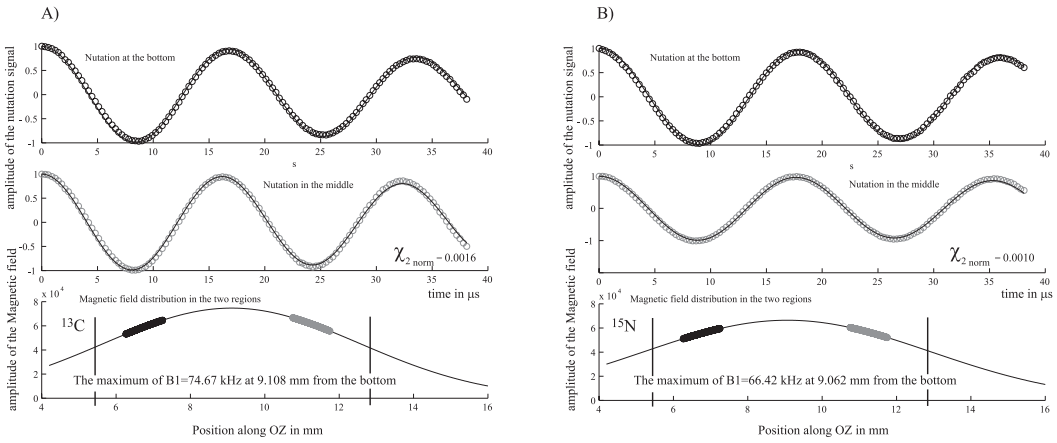

FIG. 9.7 – *Adjustement of the nutation curves of ^{13}C (A) and the ^{15}N (B) peaks from a set of labeled glycine samples packed, in a 4 mm rotor at 800 MHz. The nutation curves were obtained by increasing the 90^o pulse after the CP in steps of 0.3µs, the rotation frequency ω_r=10 kHz.*

The measures were obtained with a triple ^{1}H/^{13}C/^{15}N SB probe at 800 MHz. Nutation was achieved after a CP pulse with ^{1}H channel, by increasing a 90^o pulse at 66 kHz for ^{15}N and 74 kHz for ^{13}C. This is the reason why the periodic curves displayed by Figs.9.7

A and B are cosine like.

The plots shown in figures 9.7 A and B are described as follows : the two first curves in the top are the experimental nutation curves normalized in amplitude, so all intensities are refered to the first point, and the abscissa corresponds to the pulse lengths in μs. For each of these curves a circle corresponds to an experiment, and the continuous curve fitting the experiment is obtained by adjusting the $\mathbf{B}_1$ distribution present in the entire rotor. The last curve is a pictorial representation of the best guess for this distribution of the magnetic field $\mathbf{B}_1$ along the rotor length, including the two regions where the spins were located (*bottom* :(b) and *middle* :(m)).

The curves where obtained from single 2D experiments of nutation in presence of a weak $\mathbf{B}_o$ gradient. Such gradient allows to resolve two peaks corresponding to the two different spatial localizations of the spins. In the reconstructed dimension (F1) the maximum of each peak can be followed up in such a way that the nutation curve displays as a column. These adjustement where performed on the ^{13}C and ^{15}N nutation data. The equation 9.7 is used to model the signal amplitude, with the integration of the product magnetization times $\mathbf{B}_1$ field along the sample lenght. Here a Gaussian profile was stated for the axial distribution $\mathbf{B}_1^{ax}$ along the coil axis OZ. The integration of Eq. 9.7 was implemented in such a way that 100 points where used to obtain a discretized Gaussian profile, at the portions corresponding to each of the two spatial regions. The predicted $\mathbf{B}_1$ profiles were used to adjust simultaneously two nutation curves. A χ^2 is calculated from the simulated nutation curves produced by one adjusted gaussian $\mathbf{B}_1^{ax}$ and the experimental nutation curves. The last squares method is employed, with our following definition of χ^2_{norm} :

$$\chi^2_{norm} = \frac{\sum_i \left| \left(S(i)_{meas.(b)} - S(i)_{calc.(b)} \right) + \left(S(i)_{meas.(m)} - S(i)_{calc.(m)} \right) \right|^2}{2N - n} \tag{9.8}$$

where N is the number of experimental points of one nutation curve, and n is a number of parameters to be adjusted.

The best fit of the pair of nutation curves is achieved by a Gaussian curve whose center is found for ^{13}C (A) and ^{15}N (B) respectively at 9.10 and 9.06 mm of the rotor bottom's[22]. This corresponds to a χ^2_{norm} of 0.16 and 0.1, respectively. It is noticeable that the spins are scanning regions where $\mathbf{B}_1$ field is monotonous. In fact, bottom and middle regions are at opposite sides of the estimated maximum. The span of ^{13}C is 80% of ^{15}N, which is consistent with the fact that higher frequency will compress the field distribution.

The principle behind ajustement of nutation is based on the assumption that the static

[22] we refer to Fig. 1.2 for sample restriction in 4 mm rotors

field inhomogeneity is negligible over the sample extension, which is not contradictory with the presence of a $\mathbf{B}_o$ gradient here, due to the limited size of the sample. In addition the filtering resulting from the ^{1}H distribution during CP, is the same for both channels. And the adjustement relies on an approximated model of mainly axially distributed $\mathbf{B}_1$. This does not exclude the presence of a radial field component $\mathbf{B}_1^{ra}$ as soon as it remains small, and that is precisely what is intended by installing the samples in the middle region of the coil. We have shown that radial fields are one order of magnitude smaller compared to the axial component $\mathbf{B}_1^{ax}$ which is the main part of $\mathbf{B}_1$. When mapping the EM field with the ball shift measurments this results seem again consistent : the maximum of the $\mathbf{B}_1$ amplitude was found between 8.7 and 9.2 mm in both cases by ball shift measurement using a 3 mm ball. The adjusted parameter is within this range. The nutation gives valuable information on the overlap of ^{13}C and ^{15}N profiles.

When faced to the multinuclear experiments, involving CP the preceding approach showns it's adventage for probe calibration. Pulse schemes, as REDOR or double-CP require a good level of overlap between all 3 frequencies, namely ^{1}H, ^{13}C, and ^{15}N in order to match Hartmann-Hann conditions over the largest volume. The result of the double CP intended for this rotor confirms that the middle region whose distribution is smoother than the bottom part of the rotor gives a better enhancement. The link between the double CP efficiency and the RF field distribution has been recently discussed [109] regarding hardware developments in the field of CP-MAS probes.

9.4 Conclusions on radial field inhomogeneity

Among the different simplifications made in order to predict a model for the $\mathbf{B}_1$ distribution the most villainous appears to be the hypothesis of a flat profile in the transverse dimension. Indeed this was justified before by the fact that this variation is one order of magnitude smaller than the variation of $\mathbf{B}_1$ along the main axis of the coil. But we proved that the impact on NMR experiment was such, that a more detailed analysis was required [111, 48].

The Fourier transformation of the nutation curve obtained in F1 results in a field histogram as shown in Fig. 9.8. Such curve can also be called *density of probability* to get a certain $\mathbf{B}_1$ in the sample volume. It consists in a long ^{1}H nutation experiment (maximal pulse length is 8.6 ms), performed in an 5.5 mm long adamantane sample. The RF field strenght ranges from 128 kHz, for the fastests components at the middle of the coil, to 112 kHz for the slower ones. Interesting to note that the maximum field is more expected than the value corresponding to the avearge. This last explains why such distribution

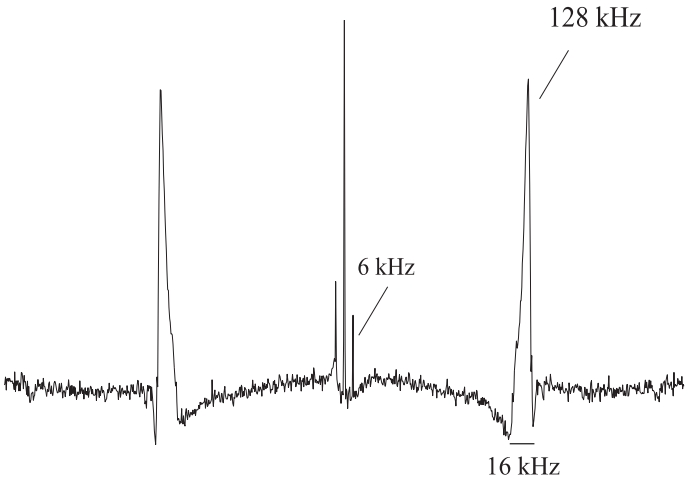

FIG. 9.8 – *Experimental field histogram acquired using 4096 increments of the 90° pulse, to reach a resolution of 116Hz. The spectra is mirrored because only the real part of the nutation signal was Fourier transformed.*

should be asymmetric.

The rotation speed of the 3.2 mm sample was set to 6 kHz. The pulse lenght increment was set to 2.1 μs, to allow the sampling of a field strenght up to 200 kHz (In general, the sampling time was set equal to p_{90^o} in order to assure that the Nyquist-Shannon theorem is fulfilled). The experimental results show that the aspect of the spectra vary strongly with the amplitude of the RF field. The shape of the NMR resonance is highly modified. The pulse was incremented 4096 times, with a recovery delay of 2 s, one single scan was acquired and Fourier transformed in F2. The experimental time was more than 5 h long. In addition to prove a good stability of the ^{1}H channel of an ^{1}H/^{13}C/^{2}D MAS probe, this experiments indicate that in such sample the span of the distribution created by a regular coil is rather small in the middle of the coil where a 3 mm long admantane sample lays. We estimated this one to be 12.5% of the maximum value of 128 kHz. Moreover the large number of points acquired allow for a resolution of 116 Hz, sufficient to distinguish the rotation peak as an additional oscillating component of the nutation curve. This spurious peak, has to be interpreted as if some spins were indeed nutating at 6 kHz. The presence of such unexpected distribution is explained by radial inhomogeneity.

To understand this, we refer to the chapters 6 to derive the master equation of the evolution Eq. 6.25 for a population of spins, and to the chapter 7 in order to get a model of field distribution. In practice we have considered an initial I_z magnetization subjected to a pulse of phase x (the coil is oriented along Oy as it has been stated in Fig. 3.1.3). These calculations were performed by numerical integration of Eq. 7.16 and by summing the results obtained using 60 equally spaced values of θ_0. The field distribution,

was calculated according to Model 1 (Eq. 7.12). The coefficients where chosen such that $\mathbf{B}_1^{ra} = 0.1\,\mathbf{B}_1^{ax}$, and $\mathbf{B}_1^{ax}$ follows a Gaussian curve of half-line witdh 8 mm, a reasonable ^{1}H span at 500 MHz.

The plot of Fig. 9.9 shows different nutation curves obtained with the same $\mathbf{B}_1$ field distribution, but at three distinct rotation frequencies ($\omega_r \in \{8, 10, 12\}$ kHz). The discrepancy of the nutation curves (B), is easy to explain thanks to the $\mathbf{B}_1$ field interferogram obtained by Fourier transformation (A). The asymmetric pattern of the field distribution, has already been observed in Fig. 9.8. In addition to this characteristic pattern the modulation introduced by the radial field, is manifested by a sharp peak in such spectral density plots, precisely at the frequency of rotation.

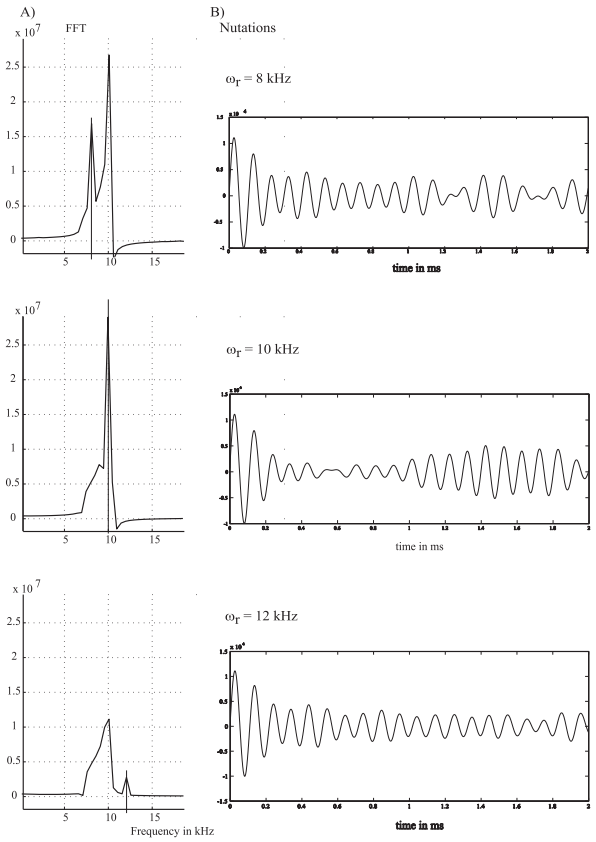

FIG. 9.9 – *Magnetic field histogram and the corresponding nutation signal. The signal was obtained with a similar algorithm as in Fig. 9.11 with a Gaussian distribution along the* $0Z$ *employed for the axial part of the field (centered, normalized and of span 10 comparable to what has been found in 9.3.2).Model 1 was used with a radial field one order of magnitude smaller than the corresponding axial field. The nutation was calculated with 2000 steps of 1 µs for 60 different angular positions around circles. The sum was done for each of the 21 circles distributed along a 5 mm long sample.*

The model 1 of chapter 7, is sufficient to describe the measurement displayed in

Fig. 9.8.

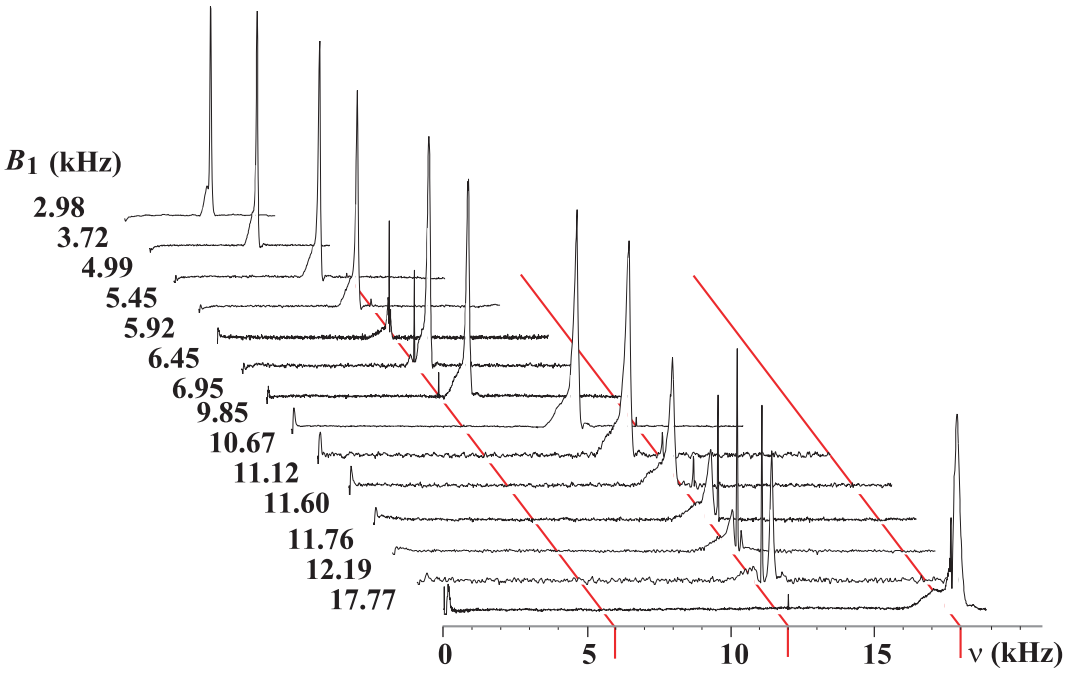

FIG. 9.10 – *Proton spectra of resulting from a nutation experiment recorded on the residual ^1H signal of a D_2O sample. The spinning speed used for MAS was 6 kHz. Spectra were recorded for different RF field amplitudes. Indicated values were determined at another spinning speed (8 kHz) to prevent the effects of sample spinning on the nutation spectra. As the nutation spectra exhibit an asymmetric shape resulting from the RF field distribution over the sample, these values correspond to the mean position of the nutation peak. Each spectrum is the corresponding F1 slice extracted from 2D nutation spectra obtained with a resolution in F1 dimension of 20 Hz. Spectra were recorded on a Bruker Avance 500 MHz equipped with a 4 mm H/C/D MAS probe. The sample was placed in a 4 mm rotor fitted with Teflon inserts delimiting an active volume of* 12 μl. *This volume corresponds to a volume which is less than the active region of the solenoid coil of the probe (* 50 μl*).*

A series of nutation experiments was performed under MAS conditions and at different RF field amplitudes. A set of nutation spectra recorded on a sample of D_2O is shown in Fig. 9.10. The carrier frequency was set on the HDO proton's resonance. The spinning speed used for MAS was 6 kHz which corresponds to the typical value used in HRMAS experiments. Nutation signals were acquired with a good digital resolution (20 Hz). An interesting experimental observation is the appearance of an additional sharp line at the frequency of the spinning speed (6 kHz) or at twice the frequency (12 kHz). The resonance observed at $\mathbf{B}_1$=6 kHz appears when the value of the RF field amplitude is close to the spinning speed. The intensity of the peak increases as the RF field amplitude approaches 6 kHz and becomes even more intense than the actual nutation peak. For a

RF field amplitude very close or equal to the spinning speed, the shape of the nutation peak is distorted. These effects are more marked for a RF field amplitude equal to twice the spinning speed (ω_r = 12 kHz). For a value equal to three times the spinning speed (18 kHz), the shape of the nutation peak is strongly affected, however the intensity of the line at the spinning frequency is low. These nutation experiments under HRMAS were performed on additional samples. The nutation spectra of molecules bound to a swollen resin show the same features mentioned above. For the solid sample adamantane, the nutation MAS spectra of ^{1}H and ^{13}C leads to similar findings. These effects seem to be general and can be predicted on the basis of $\mathbf{B}_1$ inhomogeneities as will be shown in the following simulations. The simulations were performed using models 1 and 2 of section 6, which correspondent equations are 7.12 and 7.14 The off-resonance factor $\Delta\nu$ and the spinning speed ω_r were set equal to 0 and 6 kHz respectively. The calculations were performed for different values of $\sqrt{2/3}\,\mathbf{B}_1^{ax}$ ranging from 3 to 19 kHz with (again) $\mathbf{B}_1^{ra} = 0.1\,\mathbf{B}_1^{ax}$ and imposing $c = 0.1$ in Eq. 7.15. The RF field amplitude distribution was approximated by a Gaussian function. For each value of $\sqrt{2/3}\,\mathbf{B}_1^{ax}$, the final result is the sum over a Gaussian distribution with a linewidth of 150 Hz. The results of the simulations describing the behavior of the I_x component are shown in Fig. 9.11.

After calculation, we obtain Figs. 9.11A and 9.11B, which represent the simulations using model 1 and model 2, respectively. The simulated nutation spectra are obtained after Fourier transformation of the (exponentially damped) nutation signal. These results show that, as expected, the nutation signal is strongly affected by the spinning rate. According to model 1, a line at the position of the spinning rate, 6 kHz, appears when the RF field amplitude is close to the spinning speed. The peak intensity increases when the RF field amplitude approaches the value of the spinning speed. The maximum expected intensity is reached for a RF field amplitude of 6 kHz. Deformations and perturbations on the nutation signal are also predicted. Using model 2, two spinning lines at 6 and 12 kHz appear when the RF field amplitude is close to the double of the spinning speed. The peak at 6 kHz is less intense than at 12 kHz. As for model 1, the peak intensities are maximum when the RF field amplitude is the closest to 12 kHz. Again, if the RF field amplitude is equal to 12 kHz, the nutation signal is affected.

Regarding Fig. 9.8, we have seen that the modulation presented in model 1 explains the spinning line at 6 kHz. On the other hand, both modulations in ω_r and $2\omega_r$ present in model 2 give an explanation for both spinning lines at 6 and 12 kHz in Fig. 9.10. The comparison between experimental and simulated data indicates that model 1 is less appropriate. Indeed, the calculated nutation spectra consist of one peak at 6 kHz only, whose intensity is overestimated (see Figs. 9.9 and 9.10) . From this theoretical analysis

we can say that model 2 seem to be more realistic, since the predicted nutation spectra reproduce better the experimental results. Spins experiencing an uniform RF field will nutate at the same frequency. RF field distribution amplitude due to the $\mathbf{B}_1$ inhomogeneities results in distribution in frequency nutation. Dispersion of spin flipping angles causes the damping of the signal nutation and therefore the broadening of the corresponding line (see Fig. 9.10). In addition to this, under MAS conditions, the sample spinning induces modulations in the nutation motion of spins at the frequencies $(\omega_r, 2\omega_r, 3\omega_r)$. The amplitude of these modulations and therefore the intensity of their corresponding peaks also depend on the $\mathbf{B}_1$ inhomogeneities. The fluctuations of the spinning speed can act as damping factor of these modulations. Apparently, the fluctuations are weak as indicated by the sharpness of the spinning lines at multiples of the spinning speed. Their broadening can be caused by the fluctuations of the rotation speed only. Analysis of the rotation dependant peaks in the field histogram observed in Fig. 9.10 can be seen as a clue to prove the low impact of spin relaxation on nutation curves. If the nutation damping would be governed by relaxation mechanisms in the sample before the end of the nutation (i.e for shorter pulses as those needed for 10 to 50 nutation loops) the rotation peaks would be much broader. This justifies the hypothesis formulated in 9.3.1, or in other terms it suggest that every comprehensive work on relaxation should incorporate also a careful analysis of the $\mathbf{B}_1$ field distribution.

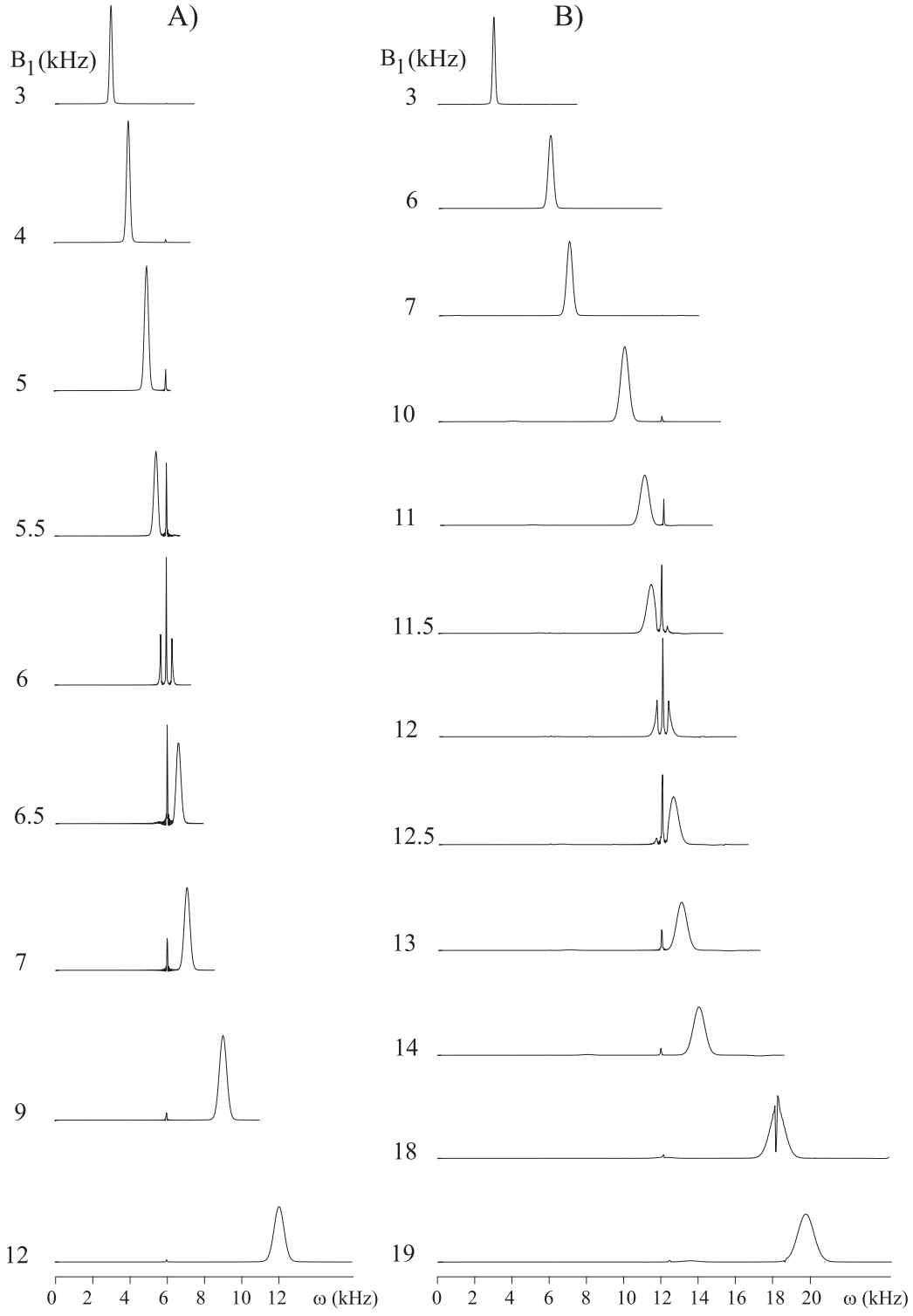

FIG. 9.11 – *NMR spectra simulations of nutation experiments using model 1 (A) and model 2 (B) at different RF field amplitudes. Eq. 7.12 was used for model 1 and Eq. 7.14 was used for model 2. The off-resonance factor* $\Delta\omega_o$ *and the spinning speed were set equal to 0 and 6 kHz respectively. The calculations were performed for different values of* $\sqrt{2/3}\,\mathbf{B}_1^{ax}$ *ranging from 3 to 19 kHz with* $\mathbf{B}_1^{ra} = 0.1\,\mathbf{B}_1^{ax}$ *and c=0.1 in Eq. 7.15. The simulated nutation curves were multiplied by an exponetial window to avoid truncation effects.*

Part IV
Origin of the Temperature increase induced by HR-MAS on samples

10

Thermal issues in samples investigated under MAS

The first law of thermodynamics tells that heat and work are both occurences of the same phenomemon called 'energy'. The first explicit statement of this, was given by Rudolf Clausius un 1850. If dU is an infinitesimal increase of the internal energy of the system, δQ in the infinitesimal amount of heat added to the system, and δW infinitesimal amount of work imposed to the system :

$$dU = \delta Q + \delta W \tag{10.1}$$

W is the work, Q the heat and U the energy of the considered system. This energy is expressed in Joules with the convention that what gets into the system is negative.

From the first principle it is clear that, NMR samples investigated by magic angle spinning experiment, present some specific heating mechanisms. We distinguish first (i) macroscopic mechanical efforts such as rotation of a sample. This work induces thermal effects, caused by frictional heating with the walls and at the air bearings. These are mechanical phenomena, because fast spinning leads to strong acceleration or deceleration of the sample (when spinning up or down) as well as to strong centrifugal forces at constant spinning speed. And then (ii) we focus on 'microscopic works' causing elevations of temperature, such as the rotational motions of water molecules due to dielectric polarization. This heating process, linked to high frequency electric polarization (and thus the $\mathbf{E}_1$ field), may destroy the sample, either in the static or the MAS case. The first of those two points will be the subject of the following section 10.1, while the second point will be discussed with respect to the classical electrodynamics theory of the last section 1. Finally some techniques employed to measure the temperature rise in the NMR

sample while pulsing will be introduced. An original example of RF heating in a model membrane, called 'bicelle', will be described.

10.1 Heat produced by mechanical effects

Fast mechanical rotation of the sample may modify physical parameters like the temperature, the concentration or the density. The distribution of these quantities can itself be modified by the rotation. Friction between the rotor and the ambient MAS bearing and drive gas surrounding the MAS rotor may result in the appearance of a gradient of temperature over the sample length. MAS rotors contain the NMR sample and must provide high mechanical strength to withstand the centrifugal forces acting upon fast spinning. The mechanical pressure resulting from the centrifugal forces acting when angular frequency rises up to ω_r,

$$\sigma_c \quad = \quad \frac{\rho_s \omega_r^2}{3}\left(R_a^2 + R_a R_i + R_i^2\right) \tag{10.2}$$

depends on the rotor material density ρ_s and outer and inner rotor radii, R_a and R_i, respectively. The equation above can also be used to estimate the centrifugal load acting on the NMR sample inside the rotor with the corresponding re-interpretation of the radii R_a and R_i , and ρ_s then denoting the sample density. For example, an NMR sample (For water $\rho_s = 1\,g/cm^3$) with an outer diameter of $2R_a$=3 mm (e.g., in a 4 mm MAS rotor) in the shape of a full cylinder ($R_i = 0$) at 15 kHz experiences a centrifugal pressure such that σ_c=6.7 MPa (=67 bar) at its outer circumference. Smaller sample diameters may reduce this effect, and thus may allow higher spinning speeds.

The results presented by Fig. 10.1 can be related to the phenomenological law of Eq. 10.2. The larger the diameter of the sample is, the strongest the pressure along the radial direction will be. An additional heating process may be present. Experience shows that the temperature rise is also caused by the mechanical friction at the end of the rotor. Acording to this second diffusion mechanism, the heat would also propagate axially from the bottom bearings along the rotor length to the rotor caps. However then, there are unexplained differences between the 12 mm long 2.5 mm rotor, which is less subjected to heat, and the 20 mm long 4 mm rotor.

Besides the spinning motion, the rotor may perform additional motions. The air cushion in the bearings has elastic properties such that the system rotor+air bearings+MAS stator housing represents a system that may exhibit mechanical vibrations (various kinds of nutational and precessional motions). Since the mass of the rotor (including the sample)

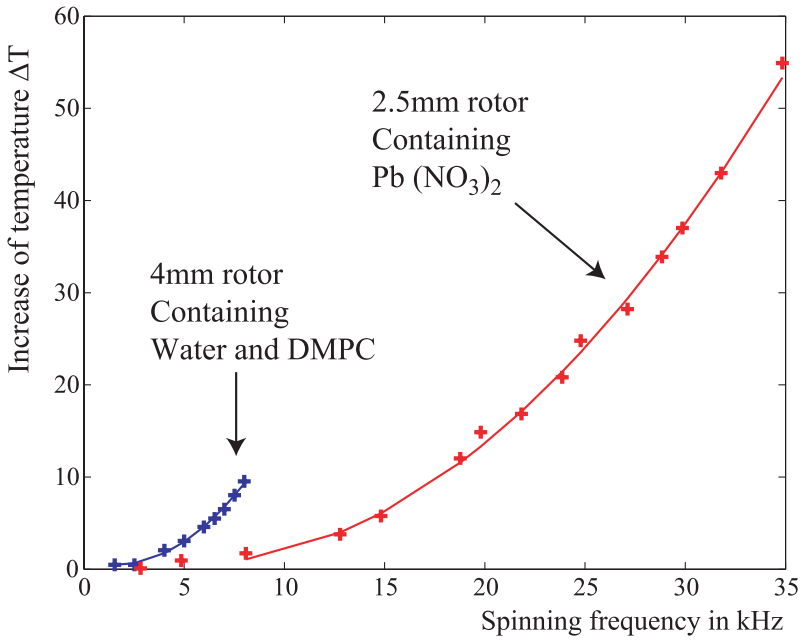

FIG. 10.1 – *Fast spinning causes a temperature increase of the NMR sample, observed directly inside the 2.5 mm rotor solid sample. In this case the nuclear thermometer is lead nitrate (2.5 mm red curve).For a 4mm rotor the water contained in a DMPC suspension indicated the temperature rise (blue curve). This last measurments are taken from [46]. Both temperature increase follow a quadratic law. The largest diameter the faster the increase of temperature will be, even at the lower spinning rates used by HR-MAS.*

is small compared to the mass of the MAS stator (the latter in turn is rigidly connected to the probe frame) the rotor will carry out tiny oscillatory motions with an amplitude larger than the amplitude of vibrations of the surrounding system. Eventhough, one of the first goals of every MAS design is to keep the amplitude of rotor vibrations under control such that no interference with the spinning occurs. Nevertheless, vibrational amplitudes are also affected by the distribution of the sample mass inside the rotor, hence an even packing of the sample is of utmost importance to ensure proper operation.

For a loosely packed, spinning solid sample, the real sample distribution is not accurately known and the sample is pressed against the walls of the rotor with the centrifugal force estimated above. For a liquid without any air bubbles in a MAS rotor, due to incompressibility of the liquid, sample density can be assumed to be homogeneous. However, for heterogeneous -semi-solid/liquid sample a heterogeneous distribution cannot be excluded. Indeed, for a system of molecules bound to a resin and swollen in solvent, NMR HR-MAS observations indicate clearly the presence of both kinds of solvents : free and solute forms. Due to centrifugal forces, the swollen resin matrix is distributed along the rotor walls

while the free solvent occupies the center of the rotor [47].

For MAS solid samples, it is clear that the whole sample spins at the same spinning rate. In the case of a viscous medium such as a heterogeneous quasi-liquid, the situation is analogous. Particular experimental conditions are used to induce flow by the spinning such as a sample placed between two horizontal concentric tubes rotating at very low spinning rates of different value [143]. After a brief transition from turbulent to laminar flow the MAS sample reach a stationary spinning state[23]. The MAS spectrum of a real liquid sample shows side-band patterns with peaks separated by the spinning frequency. The shape and the line width side-band peaks indicate clearly that the liquid sample moves uniformly. As it has been shown before, the nutation experiment leads to results supporting our findings.

Such increase of temperature produced by convection, can be prevented by cooling of the sample with an evaporator. In this work we used the Bruker BCU05 device that cools dry air or nitrogen gas. At the output of the transfer line the gas temperature may reach cold temperaures down to 233 K. Spinning stability is an issue when cooling the bearing gas. To prevent it, stators with double bearing flux have been developped (DVT). In such stators, the bearing is performed at ambient temperature while the temperature inside of the stator is maintained at lower levels. For the 4mm rotors, quite popular among HR-MAS scientists, the material of the rotor-cap is critical for going low in temperature, Kel-F caps will pop-out below 263 K (-10^{o}C), they should be replaced by polyimides ones (Velspel) which are warrantied down to 243 K. For lower tempertures ceramics such a Marcor, become a must.

For a complex system like an air-bearing MAS stator/turbine with partly laminar, partly turbulent gas flows (bearing gas flow, drive gas flow, VT gas flow, exhaust gas flows), which is thermodynamically an open and highly heterogeneous system, any reliably measurable physical quantity, that affects the efficiency and operation of the system, is of invaluable help. On the other hand, from the sample point of view, a means became available to precisely measure and calibrate the temperature of the NMR sample, i.e., for example, that it is possible to establish a unique relationship between operational parameters like bearing pressure and flow, spinning rate, and temperature of the sample. MAS design changes affect the thermal characteristics of the MAS system, and vice versa, as recently demonstrated by Doty, et al.[45], in order to change or improve the thermal features of the system, mechanical modification or even re-design might be necessary. One could have expected to solve the heat increase by cooling, this only applies for convection

[23]Heating is generated during the transient state, when the acceleration produces strength and movement

heat, where the diffusion time-period is in the range of the second, or even slower. We will see now that irradiation produced by the RF field is unfortunately much faster and can not be controled by variable temperature units of any kind.

10.2 Heat produced by the $\mathbf{E}_1$ at high frequencies

RF heating is of different nature than the rotation induced one. The irradiation, known as *microwave heating* acts faster and directly inside the material, therefore it can not be directly compensated by cooling. We pretend here to give a physical introduction of this microscopic effect. The ability of certain molecules to orient in a specific direction is called *Polarization*, the electric field as well as the displacement vector participate in this process (Eq.5.16 and 2.9). The microscopic polarization $\mathbf{p}_i$ is linked to the local electric field, through the dielectric susceptibility χ_e, defined by

$$\vec{P} = \epsilon_o . \chi_e \vec{E}$$

.

The frequency dependence of χ_e, has been solved using a time correlation approach in a statistical ensemble [102]. The polarisation of the system can be expressed as a sum over i states as :

$$\mathbf{P} = \sum_i \mathbf{p}_i |i>$$

The starting point for a quantum development of polarization is the expression of the Hamiltonian of the electric field that can be writen as :

$$\mathcal{H}_E = -\mathbf{P}.\mathbf{E} \tag{10.3}$$

where $\mathbf{E}$ is the local field. This term is to be added to the expression of the total Hamiltonian given in Eq. 7.4. From there a time correlation approach of the dielectric relaxation has been proposed to derive the Debye model from the expression of microscopic electric susceptibility (p 495 in [102]). This démarche reveals that the dispersive curves of χ_e, and ϵ obey the Kramers-Kronig equations.

The relations between microscopic dielectric factors, and the effective dielectric of an NMR sample, can be employed to solve Maxwell equations in dispersive media. The so called *mixing formulas* are the proper tool for this analysis. A survey of such techniques can be found in [124]. We simply insist on the fact that polarization $\mathbf{P}$ expressed in Debye per meter is the touchstone of RF heating mechanisms.

This approach fits quite well to the discussion of some recently published ideas in the area of bioelectromagetism. Those whose specific interest is the derivation the RF power absoption of mixtures containing lipid membranes, forming inclusions in a water buffer [126, 82]. In the following we limit ourselves to demonstrate the principal steps needed to justify the expression of the relative dielectic constant ϵ used in CST (Eq. 4.7). The FDTD methods are in general well suited to access the effective permittivity of randomly inhomogeneous mixtures [124] and so to solve the electromagnetic field distribution produced by the NMR coils in realistic biological samples. On a more macroscopical size the degradation of the $\mathbf{B}_1$ field produced by increasing salt concentration in NMR samples has been elucidated using CST. These results will be presented in the next pages.

10.2.1 Joule heating in aqueous samples

In 1842 James Prescott Joule proposed an experiment to describe how mechanical efforts can produce an increase of temperature. The system considered is a dewar (thermicaly isolated from outer world) containing a viscose liquid whose volume is constant. Inside the liquid a propeller spins the medium, and this mechanical movement can be quantified. The energy used to drive the spinner is directly converted in an increase of heat inside of the dewar (an illustration of the Joule's experiment can be found at p 503 of [37]). Such is, by analogy, the action of the average electrical polarization $< \mathbf{P} >$ inside of the sample. The variation of temperature ΔT is ruled by the following differential equation [56]

$$k_T \nabla^2 T + \mathcal{P}_j = \kappa \, \rho_s . \frac{dT}{dt} \tag{10.4}$$

where T is the increase of temperature from the stabilized value (temperature measured in the stator), k_T is the thermal conductivity of the sample, also called 'diffusion factor', κ is the heat capacity and ρ_S the density of the liquid, and finally $\mathcal{P}_j$ appears to be a volumic density of power.

After a short lapse of time Δt is the heat diffusion in the sample volume is fast enough, which can be assumed to be the case for a very small volume of water in the neighboring of the lipid surface :

$$\Delta T = \mathcal{P}_j . \frac{\Delta t}{\kappa \, \rho_S} \tag{10.5}$$

for water at 10^oC the product $\kappa.\rho_S$=4.19 10^6 J.K^{-1}.m^{-3}). A fast calulation predicts an increase of 10 degres when applying a 1 s pulse, of power as low as 1.5 mW, in a volume

of 35 μl. Since we decided here to study aqueous mixtures, water will be considered with more attention. We propose here to investigate the mechanism of dielectric absorption in HR-MAS sample.

We introduced the factor σ_{eff} in a previous section (Eq. 4.5), to include the high-frequency dynamical effects of the dipoles, is to be related to Joule's dissipated power $\mathcal{P}_j$:

$$\mathcal{P}_j = \sigma_{eff}.\mathbf{E}_1^2 \tag{10.6}$$

here $\mathbf{E}_1$ is the RMS of electric field applied at high frequency,

Finally we see how losses from the dielectric or conductive properties of the sample lead to energy dissipation through Joule's effect. The sample's effective conductivity [126, 12, 70] couples to the effective local field strengh $\mathbf{E}_1$, and dissipation leads to heating. This may result in unwanted phase transitions due to the temperature change and, in some extreme cases, even to the degradation or destruction of the sample. Finally, sample loss also changes the matching required, and lowers the Q factor of the probe circuit hence it affects the signal-to-noise ratio of the NMR signal. These conclusions have been already intuited in 1979 by Gadian and Robinson [61].

10.2.2 The dieletric dispersion model

James C. Maxwell defines the dielectric absorption as a phenomenon observable in insulating material. He writes in 1864 : 'When the dielectric, of which the condensator is formed is not a perfect insulator, the phenomena of conduction are combined with those of electric displacement. The condenser, when left charged, gradually loses its charge, and in some cases, after being discharged completely it gradually acquires a new charge of the same sign as the original charge, and this finally disappears' [100]. Displacement currents play, for our concern, the most remarkable role in the dispersion caused by the NMR sample. A dispersive sample represents a lossy element in the RF circuit of the probe, and leads to a strong frequency shift downwards. This is due to the influence of the sample's dielectric contribution on the equivalent coil to sample capacitance [61]. To describe dispersion, the frequency dependance is to be introduced in the expression of conductivity and permittivity .

From the original definition of displacement current, the Maxwell-Ampere equation can be written to have :

$$\vec{J} + \frac{\partial \vec{D}}{\partial t} = \sigma \vec{E} + i\omega\epsilon_o\epsilon\vec{E}$$

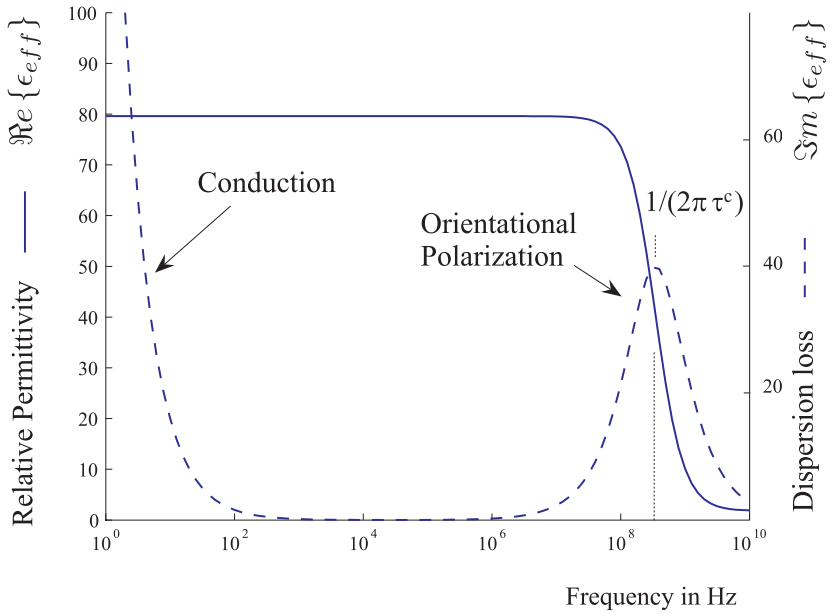

FIG. 10.2 – *Graphical representation of the real part of the dielectric constant (ϵ' full line) and the imaginary part of the effective conductivity of water ($\Im m\{\epsilon_{eff}\}$ dashed line). The relaxation time τ^c can be as small as $4.7\,10^{-10}s$ when the water is linked to phospholipidic head groups [126], but normally this one is in the order of $8.27\,10^{-12}s$ (for water at 25° [15]). The variation of ϵ' from 78.8 ($\omega = 0$) to 1.8 ($\omega = \infty$) is called dielectric decrement. the imaginary part amplitudes where calulated using the Kramers-Kronig implementation of CST. The conductivity at low frequencies is added to the Debye dispersion model, whose relaxation constant is given here. In the range of frequencies where NMR takes place, the dispersion is mostly caused by the rotational motions of the electrically polarized water molecules.*

$$\begin{aligned} &= \epsilon_o \sigma_{eff} \vec{E} \\ &= i\omega \epsilon_o \epsilon_{eff} \vec{E} \end{aligned} \tag{10.7}$$

where σ_{eff} is expressed in S/m, in the expression of the Joule's heat, only the real part plays a role[24]. This refers the definitions of effective conductivity and permittivity given as dimensionless numbers by Eqs.4.5 and 4.6. The two terms of this equation leads us to clarify two distinct types of heat dissipation mechanisms encountered in some NMR literature inspired by the work of Gadian and Robinson in 1979 [61].

Dielectric properties determine the response of a material to an electromagnetic field. The dielectric properties refer to a complex number $\epsilon(\omega)$ consisting of (i) a real portion the dielectric constant ϵ', and (ii) an imaginary portion contributing to the dielectric loss

[24] a rigourous treatment of this complex number can be found on p 18 of [12], this concept was also formulated on p 312 of [78] to distinguish the static and the high-frequency effects

factor. The dielectric constant is an indication of the polarizability of the molecules and to their ability to store electric energy [15, 124, 102]. A related quantity is the power dissipation per unit mass, also known as the specific absorption rate (SAR), this is given by $\mathcal{P}_j$ (as in Eq. 10.5) divided by the density of the material (ρ_S introduced at the beginning of this chapter). At sub-MHz frequencies, an exposure to electric field results in conductive power dissipation, caused by the translational friction of current carriers (ions in electrolyte solutions). With fields in the MHz and GHz range, an additional component, caused this time by rotation, or flexion of the molecular dipoles, dominates the dielectric relaxation. With increase in frequency, this component, known as dielectric power dissipation, ultimately prevails.

The figure 10.2 displays on the left axis the real part of the dielectric constant of water, and on the right, the imaginary parts of ϵ_{eff} comprising the low frequency conductivity losses, and the high frequency contribution from the imaginary part ϵ''.

From the derivation of Debye equation, the loss factor of a solution with a distribution of k relaxation times τ^c is :

$$\begin{aligned} \Re e\left\{\epsilon_{eff}\right\} &= \epsilon_{inf} + \sum_{k=1}^{n} \frac{\Delta\epsilon_k}{1+(\omega.\tau_k^c)^2} \\ \Im m\left\{\epsilon_{eff}\right\} &= \frac{\sigma_{ion}}{\omega\epsilon_o} + \sum_{k=1}^{n} \frac{\Delta\epsilon_k\,\omega.\tau_k^c}{1+(\omega.\tau_k^c)^2} \end{aligned} \tag{10.8}$$

where $\Delta\epsilon_k$ is the dielectric decrement $(\epsilon_o - \epsilon_{inf})$ which may also change from one type of water molecules to another depending on the chemical environment, and τ^c represents the dielectric relaxation time (also called correlation time). In principle, the latter is inversely proportional to the rotational diffusion coefficient of the water molecules, and characterizes the time required for the electric polarization to decay after a polarizing field is withdrawn [105].

The curve plotted in Fig. 10.2, considers the ideal case of a first order relaxation (n=1) often encountered in water. The imaginary part of the dielectric constant (dashed line), follows a lorentzian frequency dependence. Physically, as the frequency of the external field $\mathbf{E}_1$ approaches $1/\tau^c$ the molecular dipoles starts to lag behind the field, and continue to do so until the frequency becomes so high that the dipoles do not longer respond at all. The inability of the molecules to instantaneously align with the applied electromagnetic field leads to dissipation of electromagnetic energy into heat. From the corresponding frequency dependence of σ_{eff} we admit that the temperature increase will follow a progression which

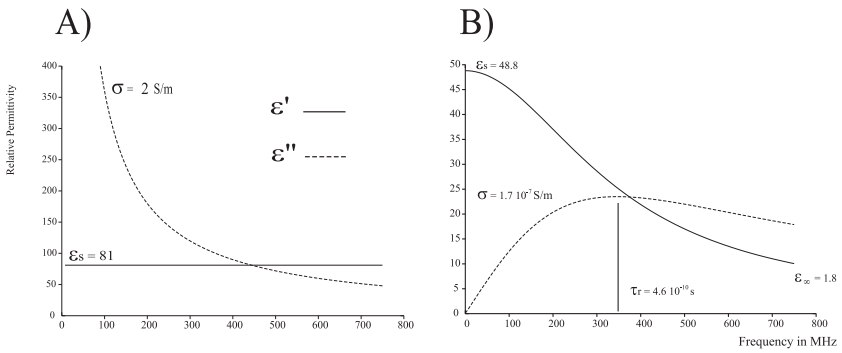

FIG. 10.3 – *Models of relative dielectric permittivity, employed by CST. The left one is not suited for high frequency behaviors were dielectric decrement plays a role, and should be reserved to simpler cases. The right one encloses this one (the singularity at static frequencies is not observable) and it adds the consideration of the dispersion caused by Orientational polarization and described trough the Debye model.*

is mostly proportional to ω^3 as it has been stated elsewere [132]. The reason is that σ_{eff} increases according to the square of the frequency before the first dielectric resonance and that the electric energy increases, at least, linearily with ω.

We know from different sources [124, 12, 126, 78], that even at low NMR frequencies the contributions to the loss factor due to the conduction and the polarization can be easily separated, in such a way that the increase of temperature can be ascribed to ϵ''[25]. Therefore, in our range of frequencies, we can neglect the contribution of the static conductivity. We use the expression of the complex permittivity presented in Eq. 4.7 to characterize the losses, in the NMR samples of our numerical simulations.

We introduce here two dispersion models of sample involved in our CST simulations given in Fig. 10.3. The left side is called 'Kappa' model, it considers the low frequency behavior, and the right one plots the effective permittivity. The Kappa model is typically used to describe the relative permittivity of salty water (σ_{ion}=2 S/m) whose real part equals 81 and whose imaginary part is decreasing monotonously with frequency. For the model of Fig. 10.3B, the correlation time τ^c was taken to be of 4.6 $.10^{-10}$ s, compared to the shorter delay of $\sim$ 9 $.10^{-12}$ s found in free water. The given static conductivity is 1.7 10^{-7}S/m. The static permittivity in this case is 48.8, and at the higher frequency limit thus becomes 1.8 (the dielectric decrement is half what is expected for normal water). This sample model is considered for the simulations involved in Fig. 11.4 and predicts better the dielectric losses, than the conductivity model also employed by CST. This last may be contained in the model of Fig. 10.3B.

[25]This is not fully the case when considering dielectric resonance at very high frequencies, due to atomic and electronic polarization but such will not happen before 10^{13}Hz [124, 12]

The variable pitch coil, introduced in Fig. 8.5 and whose electromagnetic distribution has been elucidated at 500 MHz in chapter 8, serves to illustrate the importance of displacement currents in the sample. Current density calculated by CST in the lossy dielectric regions is expressed in A/m^2. The calculations presented here are identical to those of an already cited paper [70] whose main concern is the influence of solvents on the quality factor of cryo-probe coils. The two models used to represent the water sample loading the structure gave similar results : with the conductivity model of Fig. 10.3A the maximum of current density's magnitude was 136 A/m^2, for the Debye model of Fig. 10.3B this value was smaller (77 A/m^2), but the simulations resulted in similar phase and magnitude distributions for both models. The current vectors are aligned with the main axis of the coil OZ and their phase is the same a the electric field distribution $\mathbf{E}_1$. The top and bottom edges of the cylinder represent a singularity where the current is particularily intense, but the maximum stays definitively in the middle of the sample. This central location of the current density makes the heating obtained trough RF irradiation, particularily insensitive to additional cooling. Attempts to preserve samples from degradation by freezing them may serve only because this completely changes the dielectric properties of the coil loading. Of course then the question of biological relevance has to be addressed.

For a variable pitch coil, defined as in section 8.2 the loading with a sample whose dispersion follows a law similar to what has been presented by Fig. 10.3B. This material loading increases the amount of electric energy in the sample volume. The results presented by Figs. 10.5 and 10.6 focus on the specific influence of the imaginary part of the dielectric permittivity. This parameter (ϵ'') whose maximum stands in a frequency range comprised between 200 MHz and 1.5 GHz in the case presented here, is controled by τ^c.

Using the simulation presented in section 8.2 we proved that the sample dielectric loss significantly changes the $\mathbf{E}_1$ field distribution in the coil. When considering the Debye model of dielectric dispersion in water, Fig. 10.6 clearly shows that the longer the dielectric correlation time is, the higher the amount of electric energy stored in the sample will be (this is consistent with Fig. 10.5). This is to be expected because the lag of the water dipole is more important in a viscous environement, than in a fluid media. The salt concentration adds to the polar viscosity of the solution, by constraining the water dipole in a certain position. This is possible due to polarization constraints.

We have derived the value of the power loss density inside the sample, taken as an homogeneous cylinder of slowly relaxing water. This model introduces some 'dipolar viscosity' by the dieletric relaxation time. It emerges from the graph 10.6 that such 'viscosity' will increase the amount of electric field. In practice this is still faw away from realistic cellular material, such as in biopsy samples. The heterogeneity helps, in a certain sense,

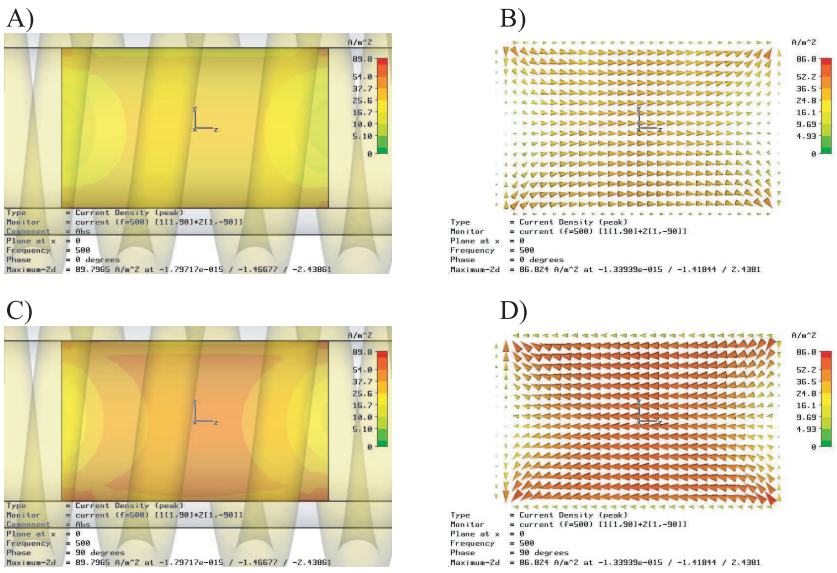

FIG. 10.4 – *Current density, calculated inside the lossy water sample. The simulation was done with CST on the already introduced 4 mm variable pitch coil. The sample is a cylinder of 5 mm length and 3 mm in diameter. It is contained in a non-lossy ceramic cylinder of 18 mm of length and 4 mm of outer diameter representing the ZrO_2 rotor. Since the field is polarized it is treated as a complex, whose time phase is to be considered. The first line corresponds to a phase reference, the second is quadrature shifted. The left column corresponds to the so called 'absolute' (abs) value of the field, this is a sum of spacial components (X,Y,Z). (A) is 'abs' at 0^o and (C) the same at 90^o. The right columns gives the corresponding distribution as a vector field.*

to lower the microscopic field. In all cases, temperature increase in real biological systems requires a complete treatment of a diffusion equation like Eq. 10.4, including the complex heat transport mechanisms of the living systems.

Finally the power loss density expressed in Eq. 10.6, can be caculated in the sample volume. With the input signal used by CST (corresponding to 1W power) the integration of power distribution proves that 20 mW will be stored in the sample (one percent of the power sent to the coil). The maximum of heat deposition is located close to the wire. Rotation by MAS stores the sample against the walls, and distributes this heat. The heating will penetrate the sample from within, thermal cooling will be useless as soon as the material properties (linked to the dilectric relaxation time) permit such effect.

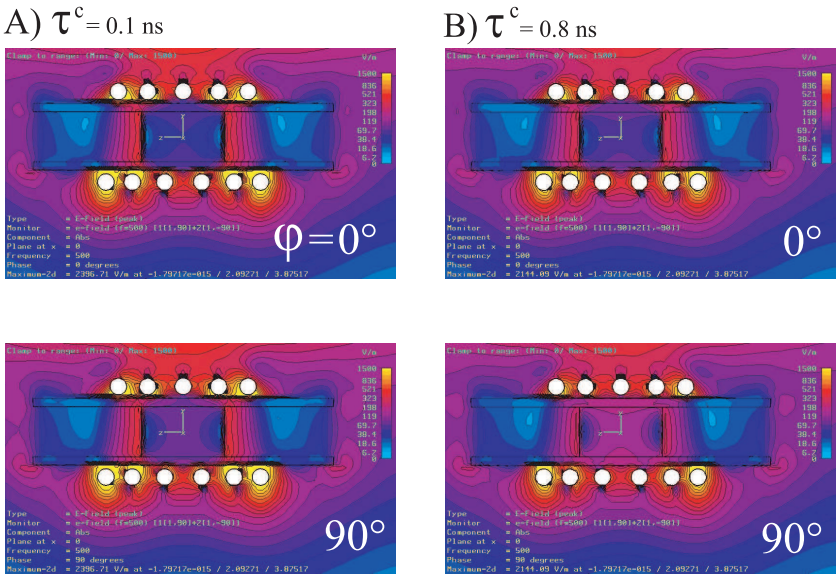

FIG. 10.5 – *Distribution of the Electric field, treated as a complex field. As in the Fig. 10.4 the line correspond to a quadratude phase shift. The two colums correspond to different dielectric correlation times. Same scale was used to sort levels of electric field up to 1500 V/m. The plane selected was a OYZ passing by the coil holder, and cuting the 5.5 wires at the opposite side.*

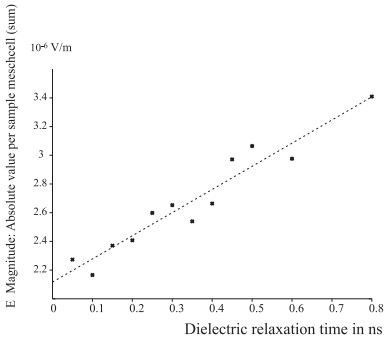

FIG. 10.6 – *Magnitude of the Electric field sum of components, the integration was done all over the sample volume and divided by the number of meshes. The same variable pittch coil was excited at the coil ends by waves as in section 8.2. Same number of meschcells was keept by the solver for each of these problems. The sample's dielectric correlation time τ^c was tunned from 0.1 to 0.8 ns.*

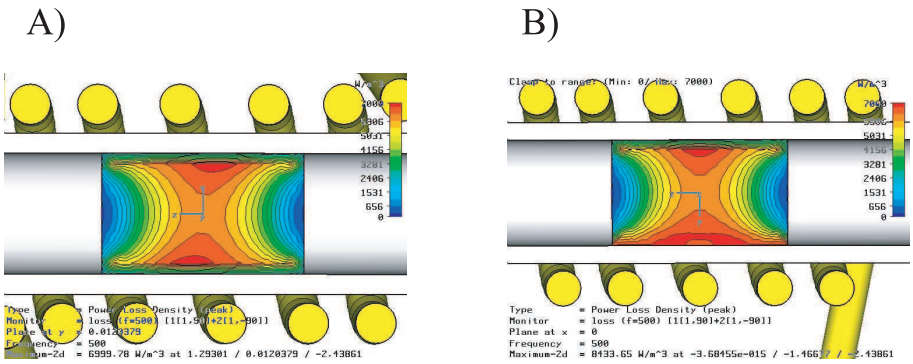

FIG. 10.7 – *Distribution of the powel loss denstity in $W.m^{-3}$, in the two axial planes of the sample. The contour levels show a difference between both planes, (A) is a 'coronal' view presenting a symettric pattern, (B) is a 'sagittal' view where it is clear that the heating is directly associated with the presence of the wires in the lower part of the figure.*

10.3 Relative influence of the inductive and dielectric losses

The alternating field $\mathbf{B}_1$ from the RF coil induces currents in a conducting sample which dissipates power. The power dissipation can be expressed as an effective resistance R_m in series with the recieving coil. Hoult and Lauterburg [73], have considered the influence of this mechanism on MRI sensitivity. For a solenoidal coil of radius a, length $2g$, and n ($>> 1$) turns, Gadian and Robinson [61] give the following formula :

$$R_m = \frac{\pi \omega_o^2 \mu_o^2 n^2 b^4 g \sigma_{eff}}{16(a^2 + g^2)} \tag{10.9}$$

where b is the sample radius, of cylindrical shape.

The same authors, based on RF literature [136], cited by [73], start from the following formula for the equivalent series resistance (ESR) R_e resulting from dielectric losses.

$$R_e = \frac{\omega_o^3 L^2 C_d}{Q_d} \tag{10.10}$$

The dielectric loss factor of the sample has been introduced within the *power factor of distributed capacity* $(1/Q_d)$ to indicate that the (ESR) depends on the sample's dielectric dispersion (Eq.101 on p 84 of [136]). The distributed capacitance from turn to turn C_d can be decomposed in two terms using the circuit analogy with lumped elements corresponding to volumes where the field in well known. Some of the $\mathbf{E}_1$ goes directly from turn to turn and is designated by a lossless capacitance (C_1) whereas some other field lines go trough the lossy sample and experience dispersion (C_2). The equivalent circuit description of the

mentioned paper (Fig.1 in [61]), was redeveloped in the recent work of Minard and Wind [105]. This approach clearly is a example of what has been explained in Chapter 3.4 of the present work : the electromagnetic distribution need to be known prior to any 'lumped elements decompostion' of the field.

The predominance of dielectric heating over other sources of electromagnetic heating as magnetic induction, has been clearly established at high-frequencies. This last heating source arises when the alternating field induces eddy currents in a conducting sample. Indeed it plays a role in imaging where the sample size is considerable, and the fields are rather low (less than 100 MHz). At high fields and for our small sample volumes the impact of induction is negligible. For example : in a four turn coil at 350 MHz the equivalent resistance linked to magnetic induction is 40 times smaller that the one linked to dielectric losses (Fig. 9 in [105])

10.4 Conservative and non-conservative $\mathbf{E}_1$

From a recent discussion found in [64, 92, 44] the dielectric heating was introduced trough the distinction between *conservative* and *non-conservative* electric fields. This formulation appears when expressing the Coulomb Gauge to the microscupic fields. In order to relate electric field ($\mathbf{E}$) and the vector potential ($\mathbf{A}$), plus the scalar potential (V) :

$$\vec{E} = -\frac{\partial \vec{A}}{\partial t} - \vec{\Delta} V \tag{10.11}$$

were the first term of the right member designates non-conservative field, and the last term is the conservative electric field. The microscopic distinction of $\mathbf{E}_1$ in a longitudinal part called E_Z and the transverse part $\vec{E}_t$ as done in section 3.1.2 may be useful to relate the irrotational component E_Z of the electric field to heating mechanisms. The following distinction was found in [26] :

$$E_Z = \vec{\nabla} V . \vec{Z} \tag{10.12}$$

$$\vec{E}_t = \frac{\partial \vec{A}}{\partial t} \tag{10.13}$$

The goal of reduction of the dielectric heating can be accomplished by reducing the conservative components of $\mathbf{E}_1$, while the rotational part (contributing to the magnetic field trough the Maxwell-Faraday equation) can not be altered without sacrifiing the ma-

gnetic field. This approach is still compatible with the paradigm presented in section 3.1.3.

10.5 Experimental measurment of heating in biological samples

10.5.1 NMR thermometers

Quantitation of sample heating in NMR experiments requires measurement of the sample temperature in situ. NMR thermometers based on temperature dependence of the chemical shift are available to calibrate the temperature inside the sample. For ^{1}H NMR spectroscopy one of the most popular method is to use methanol or ethylenglycol, whose OH and CH_2 peaks [139] experience a well known temperature dependence of the frequency shift. Compounds containing lanthanides like $TmDOTP_5$ (thulium 1,4,7,10-tetraazacyclododecane-1,4,7,10-tetrakis(methylene phosphonate)) also have been successfully used to measure the temperature via the ^{1}H chemical shift [132]. Other NMR nuclei contained in temperature sensitive materials are ^{13}C, ^{19}F, and ^{59}Co [125] for liquids, and ^{207}Pb [11] for solids. For lipid membranes the addition of reference compounds may interact with the sample and in practice the best method is the use of water [46] in most biological samples.

10.5.2 Using Bicelles to probe RF heating

In the following we would like to introduce some experimental work done in order to evaluate the impact of RF heating on coils used to perform HR-MAS.

Bicelle samples like DMPC/DHPC assemblies are membrane models which require a very careful temperature handling [86, 87]. In non-deuterated lipid, ^{2}H NMR allows us to investigate the exchange of water deuterium from the bath to the bound state. At the surface of the lipid bilayer a 0.5 nm layer contains water molecules that are bounded at several positions to the phospholopidic head groups. Water molecules experience different dielectric relaxation mechanisms [126] due to their exchange from the bounded layer to the non-bounded bath.

The splitting of deuterium (spin 1) resonance lines originating from the coupling of the quadrupolar moment with the local electric field gradient (arising from neighboring atoms or molecules) has been investigated in the so called swelling regime where the hydration plays a major role [52, 151]. There exists a region of temperatures between 298 and 317 K, where the bicelles form a homogeneous phase, and the quadrupolar splitting of ^{2}H in D_2O

is governed by the order parameter of the system. In this range the quadrupolar splitting increases linearly with temperature as seen in Fig. 10.8. The exact nature of the chemical exchange involved behind this ^{2}H splitting has not yet been completely elucidated, but the phase diagram is rather insensitive to variations of the salt concentration [116] and the same model can be applied to monitor the temperature increase.

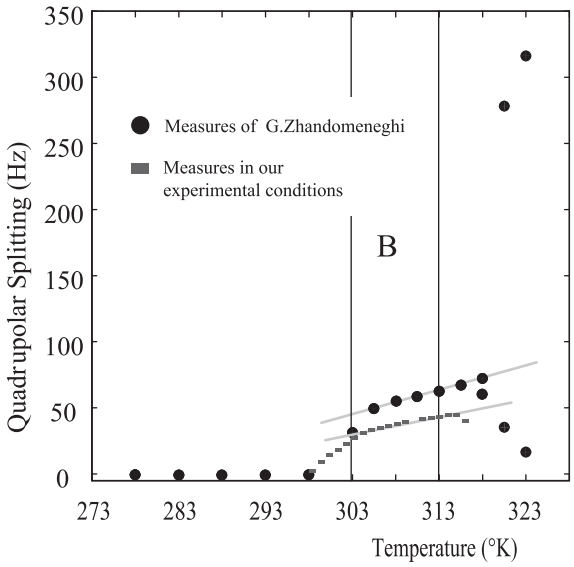

FIG. 10.8 – *Variation of $\Delta\nu_Q$ the quadrupolar splitting of water solvent as a function of temperature. 'B' indicates the bicelle phase. Data has been reproduced from [151] Linear increase of the splitting in Hz was observed also in our case, with an adjusted linear coefficient of 1.2 Hz/K.*

In order to relate the quadropolar splitting to the temperature increase produced by RF irradiation, we need to make the following hypothesis regarding the evolution of the quadrupolar splittig : the quadrupolar splitting of water solvent as a function of temperature $\Delta\nu_Q(T)$ is independent of the salt concentration in the sample. For all samples the linear increase of the splitting in Hz was observed and related to temperature through the same linear coefficient of 1.2 Hz/K. It has been published that for deuterated Head-groups the quadrupolar splitting is independent of the ionic strength of the water solvent [10], and this could explain why the membrane does not suffer from a relatively high salt concentration [26]. Moreover, it has been reported, that the phase diagram as a function of temperature of Bicelles is insensitive to differences in salt concentrations [116]. From temperature increase measurements we concluded first, that adding salt to the samples did not alter the evolution of $\Delta\nu_Q(T)$. As a consequence the same linear prediction, seen in Fig. 10.8 was applied to a series of samples whose salt-concentration,

[26] Salt is often used in order to prevent the aggregation of polar molecules in NMR tubes

and (consequently) whose dielectric time constant τ^c was increased.

Bicelles from Avanti Polar Lipids were prepared as described [29, 52, 151] at the concentration of 250 mg/ml. As proposed recently [98] the molar ratio q for the two lipids DMPC/DHPC is such that $q = 3$. The sample was prepared in a phosphate buffer of pH 6, 10% D_2O was added for the study of ^{2}H quadrupolar exchange. The sample conductivity was varied by adding PBS (a mixture of K_2HPO_4 and KH_2PO_4) to produce three different salt concentrations of 10, 50 and 100 mM. A reference sample without salt was also used. All samples were packed in a (non-spinning) 4 mm rotor. This technique was used in this study to measure the impact of power loss on salts. Such results will be presented in Fig. 11.14 of the last part to compare the solenoid coils and novel low-E coils.

The variation of the NMR line frequency vs. temperature change $\Delta\nu_{bic}/dT$, measured prior to start RF heating experiments, is equal to 1.2 Hz/K. This value is independent of the salt concentration [116, 10]. In order to ensure thermal stability, the gas flow around the sample was maintained (at a pressure of 770 mB, without spinning the sample) using a gas flow cooling unit (BCU-05), while the temperature controller (BVT-2000) was used to monitor the probe heater by measuring the temperature directly in the gas flow at the MAS stator close to the sample. Once the data were recorded at variable temperatures, these values could be used to control the increase in temperature, relative to the value of 305 K, originating from the $\mathbf{E}_1$ field of the RF coil. The pulse sequence employed to monitor the heating due to the RF electric field at the ^{1}H frequency went as follows : 0.5 s ^{1}H RF pulse prior to ^{2}H 90^o pulse followed by 1s pulse of ^{1}H CW irradiation during the ^{2}H FID acquisition to mimic a long decoupling pulse at different $\mathbf{B}_1$ fields in the range from 5 to 16 kHz. These $\mathbf{B}_1$ field amplitudes were measured by determining the length of the 360^o pulse for ^{1}H at different RF power levels for each sample and each coil. The same power level was applied 10 times before the next increment to measure RF heating step by step. The ^{2}H NMR spectra presented in Fig. 10.9 are plotted as a function of the ^{1}H $\mathbf{B}_1$ field. A phase transition occurs in the bicelle sample placed in a regular coil, when the $\mathbf{B}_1$ becomes greater than 9.5 kHz. Temperature calibration measurements with the bicelle sample show that the phase transition occurs at about 317 K. Additional sample heating due to spinning [46, 88] is avoided in our experiments because we worked with static samples. Therefore the heating of the sample results solely from the presence of the RF electric field inside the sample. Measuring the temperature increase as a function of the applied field amplitude $\mathbf{B}_1$ allows to quantify the impact of the electric field $\mathbf{E}_1$ in the coil [46, 44].

10.6 Drawbacks of RF heating

The reduction of RF heating in biologically relevant NMR samples has become a major challenge for the design of novel coils in NMR probes [92, 132, 46, 64, 105]. Since decades the principal mechanisms that lead to RF heating effects in NMR samples are well known [73, 61]. In NMR the impact on lossy samples of the RF electric field ($\mathbf{E}_1$ field), which is always accompanying the RF magnetic field ($\mathbf{B}_1$ field), is particularly noticeable at high frequencies. There are at least four effects observable which are caused by the conductivity of the NMR sample :

Frequency shift The lossy sample represents a lossy element in the RF circuit of the probe and leads to a strong dependence of the probe tuning on the conductivity or salt concentration of the sample. This is particularly noticeable for the proton RF channel of the probe ; thus for a wide range of salt concentrations also a wider ^{1}H tuning range is required. Such effect can be explained with the help of the perturbation theory developped through the equation 2.37. An important ratio called *'Magnetoelektrisches Verhältnis'* (Magnetic to electric ratio, MEV) helps in comparing one circuit with another. This MEV is calulated by dividing the frequency shift produced by a metal ball located inside a rotor ($\Delta f_{bs} = f_2 - f_1$), by the frequency shift of the rotor (f_1) refered by the frequency shift of the empty coil f_o :

$$MEV = \frac{f_2 - f_1}{f_1 - f_0} \tag{10.14}$$

since the rotor shifts the resonance towards the low frequencies $f_1 < f_0$ and the MEV is negative and (hopefully) smaller than -1.

Another parameter can be used to compare the simulated electromagnetic field distributions of different coils on one point, this is the ratio Electric to Magnetic $\mathbf{E}_1/\mathbf{B}_1$ expressed (for convenience) in V/A.

These ratios indicate clearly that the nutation field $\mathbf{B}_1$ is produced at the expenses of a certain amount of electric field $\mathbf{E}_1$. This has to be measured for each circuit and even for each coil.

Variation of the Quality factor The presence of a lossy sample lowers the Q factor of the probe circuit ; hence it affects the signal-to-noise ratio of the NMR signal. The short introduction to the quality factor presented in section 2.4 refers to the physical definition of Q as a ratio of electromagnetic energies. Equation 2.42 helps to separate different sources of loss. Indeed the circuit, including stop-circuits, condensators and transmission

lines dissipates a certain amont of energy. The coil itself and the rotor have to be handled carefully, avoiding grease that may spoil the surface of the coil and degrade the quality of the resonance. Apart from that the major source of damping of the resonnance is indeed the sample. The modification of the sample can be followed through the ratio :

$$\frac{Q_u - Q_s}{Q_u} \tag{10.15}$$

to define the *loss factor*, [132, 92, 40]. An usage of this equation was given by [92] to measure a linear increase of the temperature as a function of the following loss factor.

Alteration of the RF field From the preceding results in Figs.10.5, 10.6 and 10.7 it becomes evident that if lossy samples are brought into a given field profile, this one is altered. The presence of a lossy sample leads to a field distribution different from the previous one in air or vacuum or of a low loss sample. This has been observed together with the modification of the quality factor by those working in cryo-probes [70, 81]. The measurement of nutation fields in lossy-conductive samples has proven that the maximum values of the $\mathbf{B}_1$ field, but even more of $\mathbf{E}_1$ are altered when changing the load. What remains is the basic shape. The simulation can predict the overal distribution of the field, that has to be measured afterwards for a specific sample in the NMR magnet.

Joule heating Last but not least, as described in this chapter, losses originating from the dielectric or conductive properties of the sample lead to energy dissipation through Joule's effect. The sample couples to the $\mathbf{E}_1$ field and dissipation leads to sample heating which may result, in the case of bicelle samples, in unwanted phase transitions due to the temperature change and, in some extreme cases, even to the degradation or destruction of the sample. It results that heating by violating time reversibility make the material un-reciprocal. Thermal stability is one of the major constraints of the NMR experiments.

A convenient way to quantify the extend of RF sample heating in a given probe is to compare the values of RF input power required to produce identical 90^o pulse lengths in a lossy biological sample (P_B) and in a non-lossy reference (P_A). The power P_A delivered to the probe with a non lossy sample is dissipated in the coil inductor and other circuit components such as isolation traps, capacitors, and connecting leads. The loss in each component is proportional to the square of the $\mathbf{B}_1$ field produced in the sample coil. A quantitative analysis of the power conversion factors η introduced in the section 2.3.1 is a good approach to measure Joule heat in samples.

In addition to the definition of power conversion factors (with ν_{1nl} and ν_{1bio} denoting the nutation frequencies of a coil loaded respectively with a non-lossy ($_{nl}$) and with a lossy

($_{bio}$) sample),

$$\eta_{nl} = \nu_{1\,nl}^2/\mathcal{P}_{nl}, \qquad \eta_{bio} = \nu_{1\,bio}^2/\mathcal{P}_{bio} \tag{10.16}$$

for nonlossy samples (e.g. adamantane) and biological samples (e.g.,the reference sample of bicelle) we define the power $\mathcal{P}_{heat}$ lost in the biological sample relative to a sample without losses :

$$\mathcal{P}_{heat} = \mathcal{P}_{bio} - \mathcal{P}_{nl} \tag{10.17}$$

at the same nutation frequency (ν_{1nl}=ν_{1bio}=ν_1). The heat deposition of a biological sample,

$$q_{heat} = \frac{\mathcal{P}_{heat}}{\nu_1} = \frac{1}{\eta_{bio}} - \frac{1}{\eta_{nl}} \tag{10.18}$$

characterizes, for one given nutation field ν_1, the power dissipated in the biological sample. Hence, q_{heat} is a meaningful measurment to compare coils loaded with lossy samples [36, 64].

10.7 Conclusions on $\mathbf{E}_1$

Induced thermal effects are a reality of NMR measurements. We focused here more specifically on the high frequency phenomenae coming from dielectric dispersion and ruled by ϵ''. We proved, trough experiments and simulation that this was the major source of heating in the sample volume.

From the point of view of NMR probe engineering it is, therefore, highly desirable to design and construct NMR coils or resonators that allow to minimize RF heating of lossy NMR samples as, for example, biopsy samples, or biological membrane samples. In general low-E solutions should be anticipated for all samples whose dynamic behavior needs carefull thermal control. It is also important to remind that the electric field can not be removed from the electromagnetic distribution whithout distording the magnetic field. In the next chapter we will see that a win-win compromize has been found between $\mathbf{B}_1$ homogeneity and the reduction of $\mathbf{E}_1$. The analysis of a low-E coils in the next part shows, that the better the magnetic field homogeneity is (even at the expenses of the $\mathbf{B}_1$ maximum values), the lower the axial component of the Electric field will be.

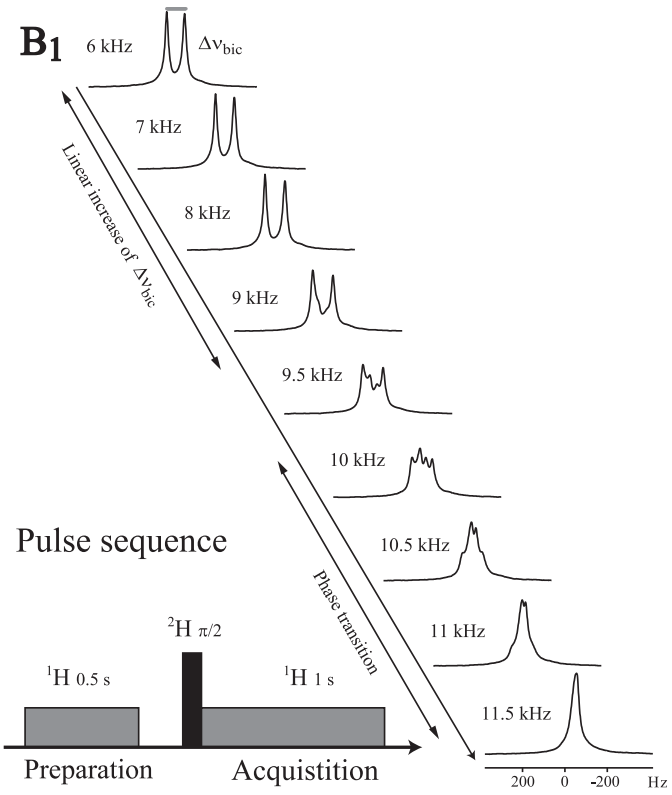

FIG. 10.9 – *Series of water ^2H NMR spectra in the DMPC/DHPC system. The quadrupolar splitting (in Hz) appears as a function of the applied $\mathbf{B}_1$ field magnitude. The measurements were done at 500 MHz (^1H), obtained with a regular 4 mm solenoidal coil on packed samples (ca. 50 μl). Alignment of bicelles was obtained after 30 min to 1 hour waiting time, the overall series of experiments took 30 to 40 min. By increasing the power level of the ^1H channel the increasing $\mathbf{E}_1$ field modifies the dynamics of water in the samples. The phase transition indicated by the vanishing splitting (lower spectrum) would corresponds to an equivalent temperature of 317 K. In a MAS stator whose temperature was stabilized at 305 K, the heating produced by the RF pulse in the ^1H channel on a 100 mM PBS salt amounts to a temperature increase up to 12 K for $\mathbf{B}_1$ field amplitudes in the range from 1 to 12 kHz.*

Part V
Introduction of a novel Low E- field coil to minimize Heating of biological samples in Solid-State multinuclear NMR experiments

11

Z-coil as an example of multinuclear low-E field resonator

11.1 Introducing optimal coils for conductive samples

From the viewpoint of NMR probe engineering it is highly desirable to design and construct NMR coils or resonators that allow to minimize RF heating of lossy NMR samples like biological membranes or protein samples. The aim of this part is to conclude with a novel coil structure, called Z-coil, which is designed for multinuclear experiments in a solid-state NMR probe. The novel Z-coil is characterized both electromagnetically as well as from the NMR experiment point of view. In general, NMR coils need to satisfy simultaneously the following requirements :

- to produce a maximum RF magnetic field at the coil and sample center ;
- to minimize the RF electric field components inside the volume occupied by the sample, hence to minimize the current density and therefore, the Joule dissipation inside the sample ;
- to provide a high homogeneity of the RF magnetic field over the sample volume.

The RF electric and magnetic field components are not independent of each other. They are linked via Maxwell's equations. The coil or resonator geometry, the surrounding RF circuit, and the sample geometry (i.e., the sample location and distribution inside the coil), represent boundary conditions, under which Maxwell's equations are to be solved. A detailed analysis shows, that for many cases minimizing the $\mathbf{E}_1$ field and homogenizing the $\mathbf{B}_1$ field by adapting the geometry of the coil comes at the expense of $\mathbf{B}_1$ field amplitude at the center of the coil. Based on the standard solenoidal or helix coil used in solid-state NMR probes (described extensively in [49]) serious attempts have been made to

improve the $\mathbf{B}_1$ homogeneity, e.g. by varying the pitch [76], or using variable-width wire [115]. On the other hand, in order to remove electric fields, a Faraday screen has been used righ inside the coil following an invention of David Cory [24]. The technique called 'distributed capacitance' may also be employed to store as much electric field as possible between the wires of the coil. The first example of this art was found in reference dedicated to heating in conductive samples from 1979 written by Alderman and Grant [2]. Again in the world of biomedical applications, the coil-structures called 'Litz' coils [39] can be mentioned here. David Doty succeded in parking the electric field in insulated crossovers. His goal was to use symmetries that allow most electric field losses to be reduced trough capacitive segmentation without affecting the current distribution. These could be used in replacement of the saddle coils commonly employed in HR-NMR. Back to solenoid, Doty involved the same fundamental concept of 'distributed capacitance'. Indeed the XC cross-coil presented in [44, 45] contains a coil whose wire cross section is such, that the larger surfaces are seeing each other, this is intended to reduce the electric field lines passing through the sample. Reducing the number of turns n is the last choice, but it proves to be extremely efficient since the dielectric losses generally increase with n^4 [105]. On one side the novel Z-coil structure to be introduced in this chapter is a continuation of this art of modifying solenoidal coils by introducing spiral coils to localize the $\mathbf{E}_1$ field in a radial plane [132, 65] outside the center of the sample and coil. On the other side, the '$\mathbf{E}_1$ field relocating' spiral coils are connected with a central loop that provides an homogeneous $\mathbf{B}_1$ field within the sample. In the present paper we will show some of the interesting features of Z-coils in comparison with the classical solenoidal coils. The electromagnetic field distribution of the Z-coil will be investigated both by calculation and by experiment. The intricate correlation that exists between the magnetic and electric field is presented. It is demonstrated that, in a multiply tuned NMR coil, the RF electric field $\mathbf{E}_1$ can not be reduced without altering the RF magnetic field. Since the detailed distribution differs from one coil to another, a comparison involving the following three distinct designs are discussed : (1) a regular coil of 5.5 turns, (2) a variable pitch coil with the same number of turns, (3) the new Z-coil structure. For each of these coils loaded with samples of different salt concentrations, the nutation fields obtained at a certain power level provide a basis to discuss the impact of the dielectric and conductive losses on the RF efficiency.

The RF heating effects caused on bicelle samples will be measured as a function of salt concentration in the sample. The Z-coil's principal advantage is to reduce the strong thermal effects produced by RF heating at high frequencies. The results obtained at 500 MHz in a 50 μl sample prove that such coil can cope with salt concentrations that are one order of magnitude higher than in traditional solenoidal coils. In other words :

the Z-Coil reduces the heating effect by an order of magnitude, so that sensitive samples can be studied at higher (one order of magnitude) salt concentrations. Reduction of RF heating is probed with a DMPC/DHPC membrane prepared in buffers of increasing salt concentrations as described in the previous part.

11.2 Z-coil resonator geometry

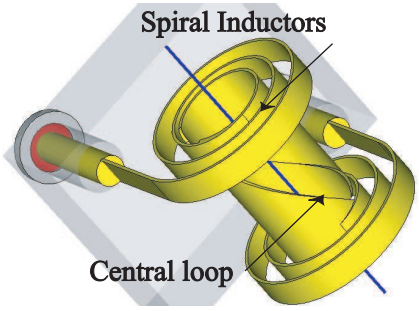

FIG. 11.1 – *Z-coil resonator with the two main construction elements : the spiral coils at opposite ends of the resonator and the central loop. The line corresponds to the path used to obtain the profiles given in Figs.11.4 and 11.9.*

The main mechanical elements and the overall geometry of the Z-coil are shown in Fig. 11.1. The Z-coil resonator consists of a copper cylinder with a helical slit. The resulting 1.5 mm wide gap carries out a 180^o turn from one end to the other end of the resonator. We refer to the cylindrical part as the core of the Z-coil. At the two extremities, two spirally wound and ribbons are connected. On the outer turns these spiral coils (Archimedes spirals, 3 turns, inner diameter 4.5 mm, outer diameter 9 mm) are soldered to the coil leads at opposite corners of the ceramic block that serves as the coil holder [153]. The Z-coil resonator is the central part of an RF circuit that provides an electrically balanced voltage distribution between the two coil leads for one, two, or even three different frequencies. An example of such a circuit can be found in [154]. It is the complete structure, depicted in Fig. 11.1, including the two spiral coils and the central core embedded in the coil holder, that defines the self-resonance frequency. The latter can be measured, for example, using a pickup coil connected through a 50Ω cable to the network analyzer. The geometric dimensions of the Z-coil are chosen in such a way that the self-resonance frequency stays above the desired proton resonance frequency (here, 630 MHz to be used in a 500 MHz RF circuit). Therefore the Z-coil appears as an inductive element in a multi-channel circuit, e.g., for a probe tuned to ^{1}H and to ^{13}C, ^{15}N or ^{2}H. In contrast to a loop-gap resonator [110, 3] the Z-coil is easily tunable to multiple frequencies. As such, it is similar to a

solenoid coil, except that the self resonant mode of the solenoid contains much more electric field inside the coil than the Z-coil. Unfortunately, away from its self-resonance frequency the Z-coil will exhibit less magnetic field than a regular coil, as is expected for such low-E structures [132, 3, 44]. However, as shown further in the present chapter, for lossy samples this apparent drawback will turn out as not significant : for lossy samples the RF efficiency of the Z-coil and the solenoidal coil almost coincide.

The assembly of a Z-coil is delicate and at the present stage requires 3 parts to be soldered together, this can be done as shown in the photography below. This resonator was actually involved in the results presented in [36].

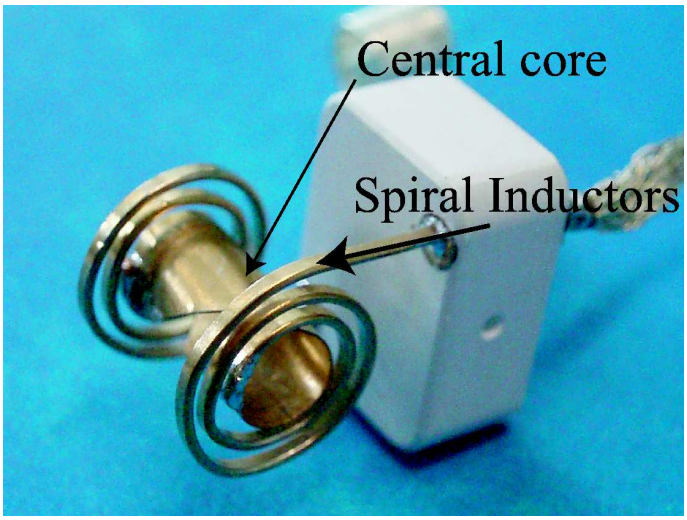

FIG. 11.2 – *Photograph of the Z-coil resonator showing the two main construction elements : (1) the spiral coils at opposite ends of the resonator and (2) the central core, similar from the point of view of structure to a 'loop-gap' where a gap, besides in extending in axial direction, carries out the currents, but does not store any TM field* ($\mathbf{E}_1$).

11.3 RF field mapping

11.3.1 Electromagnetic field simulation

We have applied computational techniques for electromagnetic fields based on first principles to evaluate the spatial distribution of the high-frequency $\mathbf{E}_1$ and $\mathbf{B}_1$ field characteristics for the Z-coil presented here. One goal was to prove by simulation that coil geometries can be found where the $\mathbf{E}_1$ field is distributed in such a way that it is minimum or negligibly small within the sample volume. Since our problem at hand has a fairly complex spatial arrangement, it was ruled out from the beginning to attempt to

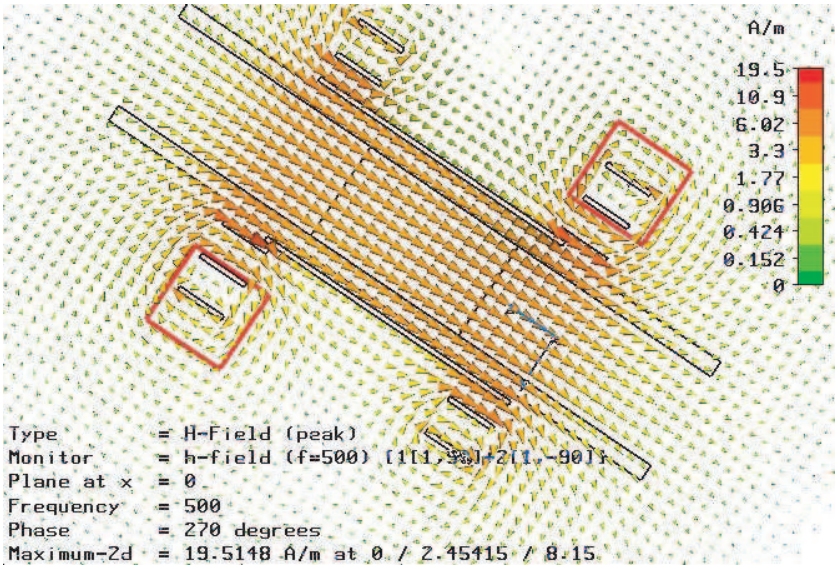

FIG. 11.3 – *Axial plane cross section of the sample-loaded Z-coil for RF field simulations. The magnetic vector field distribution is indicated by small triangles. All simulations were performed with the CST Microwave Studio (CST-MWS) transient solver. Gaussian shaped pulses were applied at both terminal ports (red squares) of the coil with opposite electric phase (to simulate a balanced circuit) at 500 MHz. A 5 mm long conductive water sample was positioned in a dielectric cylinder of 18 mm length to evalaute the impact of the complex permittivity of conductive sample.*

solve Maxwell's equations by analytical techniques. Therefore we decided to employ numerical methods based on discrete models. The Finite Integration Technique (FIT) proposed and developed by Weiland [146, 20] and implemented in the software program Microwave-Studio ® (MWS 2006) by Computer Simulation Technologies, Darmstadt (CST) has been applied to find the electromagnetic field distribution of the Z-coil. The relevance of this technique has already been demonstrated in the literature for the study of NMR coils [70, 44]. The numerical simulation was based on the Z-coil structure depicted in Fig. 11.1. The two excitation ports (in Fig. 11.3 surrounded by red squares) are fed with excitation pulses, 180^o out of phase from each other to simulate external circuit balance. A display of the magnetic vector field in an axial plane OYZ is shown in Fig. 11.3. This magnetic field distribution results from the analysis using the transient solver module of MWS applied to a Z-coil loaded with a sample consisting of a 18 mm long tube made of ZrO_2 ceramics ($\epsilon_r \sim 30$) of outer diameter 4 mm, inner diameter 3 mm, filled with a 5 mm long sample of salty water (conductivity 2 S/m) at the center of the coil. The relative permittivity ϵ_r of this solvent has a complex value whose real part is equal to 81 and whose imaginary part (loss factor) is equal to 72 at a frequency of 500 MHz.

It is interesting to note that the maximum of the magnetic field is located outside of

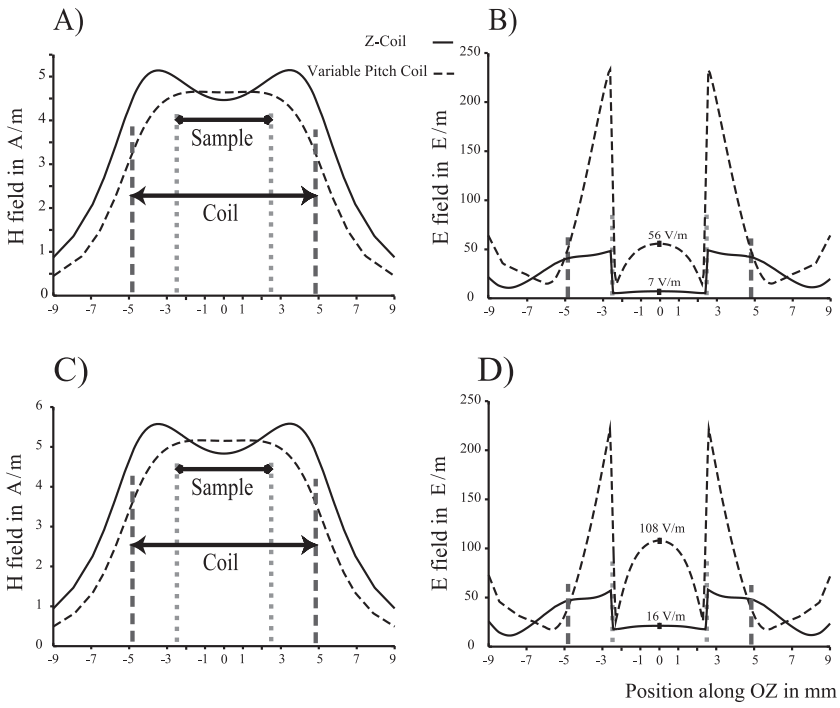

FIG. 11.4 – $\mathbf{B}_1$ *and* $\mathbf{E}_1$ *field profiles along the axis of the loaded Z-coil (full line) and variable pitch coil (dashed-line). The abscissa corresponds to a length of 18 mm. The vertical dotted lines indicate the extension of the coil and of the dispersive sample used here to load both coils. The ordinate axis of (A-C) shows the absolute value of the RF magnetic field magnitude along the coil axis. The horizontal line indicates the inhomogeneity in the maximum field region. The ordinate axis of (B-D) measures the electric field amplitude* $\mathbf{E}_1$*. The first line was obtained using a conductive model for the sample as described in the preceding chapter, the dielectric dispersion model is involved for C-D.*

the sample, close to the conducting wall of the Z-coil core. Nevertheless, the amplitude value of the field in the center of the sample is relatively high, although lower than the amplitude close to the core walls. Moreover, its distribution inside the core is highly homogeneous. Therefore it leads to the highest density that would be encountered in the field histogram of the $\mathbf{B}_1$ field [123, 137]. For the Z-coil and for the variable pitch coil the field profiles shown in Fig. 11.4C correspond to the vector component of $\mathbf{B}_1$ along the coil axis, while the distributions in Fig. 11.4b display the $\mathbf{E}_1$ field magnitude. For both distributions shown in Fig. 11.4C-D, a nonconductive sample has been assumed where the losses originate from dielectric dispersion only. The dispersion behavior in the simulation was based on a Debye model with a dielectric relaxation time of $4.6\,.10^{-10}$ s. According to Gimsa [126], this large value is characteristic for bound water on lipid headgroups of membranes. It is about 200 times larger than the relaxation time constant for nonbound water molecules (as seen in previous chapter). It is useful to consider the ratio $\mathbf{E}_1/\mathbf{B}_1$

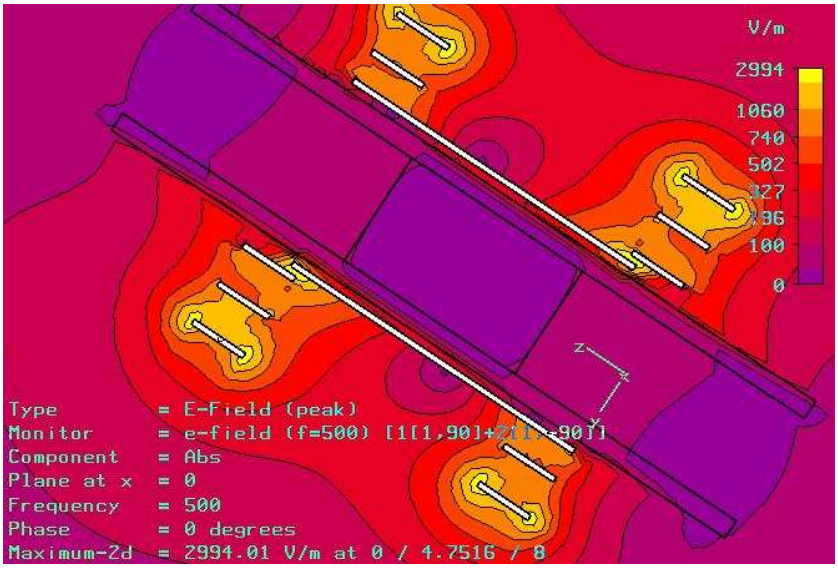

FIG. 11.5 – *Axial plane coss section representing the* $\mathbf{E}_1$ *field amplitude in a plane located at the same position as in Fig. 11.3. The maximum of the* $\mathbf{E}_1$ *field is located at the tip of the spiral coil leads. The minimum of* $\mathbf{E}_1$ *is located inside the core where the water sample is located. The contours are at 17 levels spaced from 0 to 3000 V/m (logarithmic scale).*

at a given point in space for comparing simulated fields in different coils. For the Z-coil, $\mathbf{E}_1/\mathbf{B}_1$ is computed to be approximately equal to 3.2 V/A in the center of the dispersive sample, while it reaches 21.0 V/A in the center of a variable-pitch coil (applying the same boundary conditions). The $\mathbf{E}_1$ field magnitude distribution in a plane containing the center of the core is plotted in Fig. 11.5. The plane for this contour plot coincides with the plane for the $\mathbf{B}_1$ field distribution in Fig. 11.3. We point out that the $\mathbf{E}_1$ field is concentrated in the spirals and decreases when coming closer to the core. We found furthermore by additional simulations, that the size of the gap has almost no influence on the self-resonance frequency of this coil. In practice, most of the $\mathbf{E}_1$ field is stored in the spiral coils and not in the helical gap of the core. The latter would be the case for the self-resonant mode of the loop-gap resonator.

From the RF circuit perspective, the Z-coil behaves very similar to a regular solenoid. Thus no additional means were necessary to tune or match the RF circuit of the probe. Regarding the $\mathbf{B}_1$ and $\mathbf{E}_1$ field distributions the Z-coil is different from the classical solenoidal coil. The spatial separation of the RF electric and magnetic fields in the Z-coil is much more pronounced than in a solenoidal coil [49].

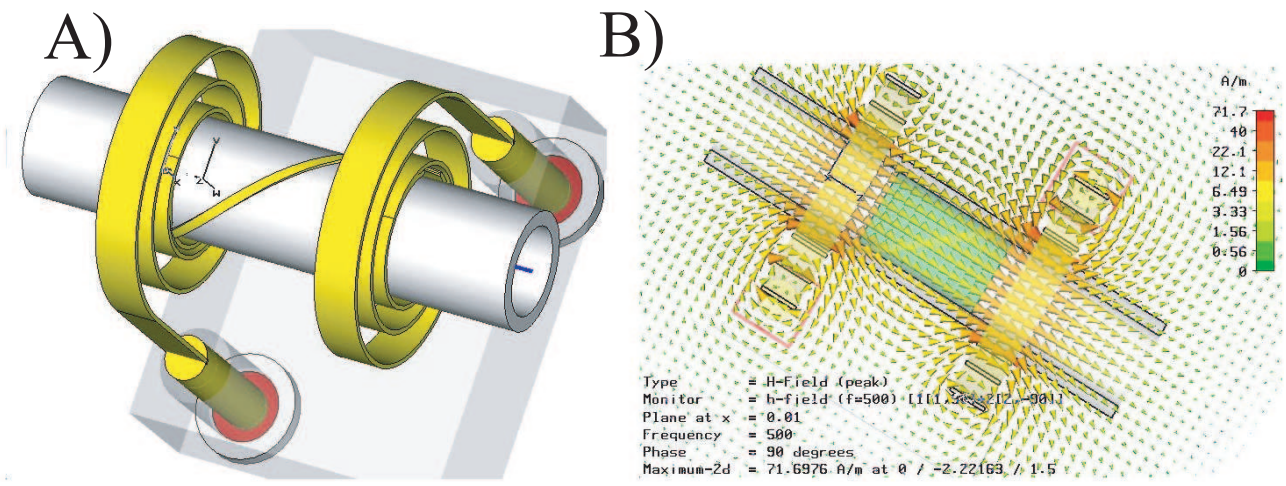

FIG. 11.6 – *CST was used to perform a EM field calculation, with the same Z-Coil structure presented in [36], but without central cylinder core. The slotted gap has been replaced by a core forming a strip of 0.5 mm width. The left side picture represents the structure, the right side (B) shows the magnetic field distribution created between the spirals.*

11.3.2 Radial field modulation in Z-coils

However the gap width plays a role for the distribution of the radial $\mathbf{B}_1$ field component, as it does in a loop-gap resonator [110] or in a scroll coil [44]. For the case of solenoidal coils we have proven in chapter 7 that the inhomogeneous distribution of the radial component of the $\mathbf{B}_1$ field leads to modulation effects in experiments performed under sample spinning conditions (e.g., MAS).This result should be extended to all coils involving helices. In order to estimate the amplitude of the radial component of the $\mathbf{B}_1$ field in the Z-coil, we performed simulations to compare the variation of the radial component of $\mathbf{B}_1$ along a circular path of 1 mm radius for a single-turn coil (loop of 4.2 mm radius, wire thickness 0.5 mm) with the radial field variation along the same path in a Z-coil (4.2 mm radius , gap width 0.5 mm). For the single-turn loop the variation of the radial $\mathbf{B}_1$ component amounts to about 10 % of the axial $\mathbf{B}_1$ component value at the loop center, for the Z-coil this variation is only ca. 2%. A similar comparison has been made for the $\mathbf{E}_1/\mathbf{B}_1$ magnitude ratio. While for the single-turn loop the value of the $\mathbf{E}_1/\mathbf{B}_1$ ratio at the center is equal to 12.7 V/A, the value of this ratio is as low as 1.9 V/A for the Z-coil.

This important result enlightened by the curve of Fig. 11.7 was a proof for us that facing the $\mathbf{B}_1$ homogeneity in the transverse plane we will come with solutions to reduce simultaneously the $\mathbf{E}_1$ in the central region. At the extreme limit of shuting down the gap, a perfect cylinder would remove completelly this modulation.

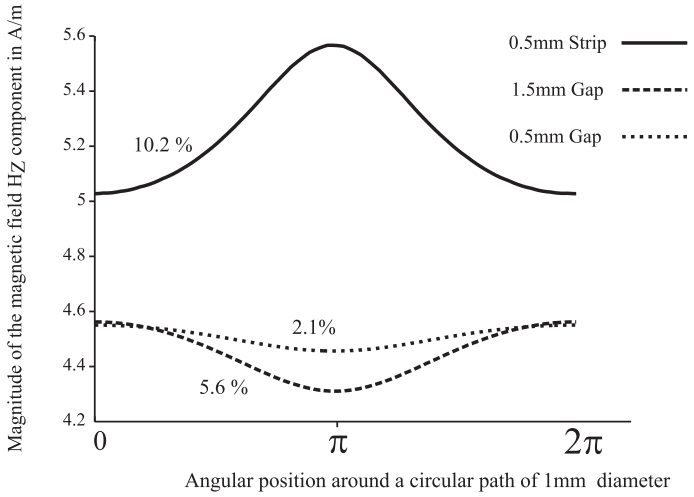

FIG. 11.7 – *Comparison of the magnitude of the magnetic field calculated by CST around a circular path. The modulation is present in all these structures, however with variable intensities. The top curve corresponds to the model Z-Coil simulated under the same conditions, but replacing the central core, by a thin wire.*

11.4 Experimental, comparative study of the different coils

11.4.1 Experimental determination of $\mathbf{B}_1$ field profiles for coils of various geometries

In order to experimentally determine the $\mathbf{B}_1$ field distribution inside resonators or coils, small metallic (e.g. spherical) bodies were positioned into the region of interest. The presence of the metallic ball leads to a local perturbation of the $\mathbf{B}_1$ field. Such so-called 'ball shift' measurements Δf_{bs} provide a mapping [97, 109] of the $\mathbf{B}_1$ distribution. In other words, the value of the frequency shift for a given position of the metallic ball is a (monotonous) function of the $\mathbf{B}_1$ field amplitude at the same location. We have used a set of Kel-F inserts containing an embedded copper ball (diameter 3 mm) to probe the field by positioning these inserts along the main axis of the coils (of length 9 mm and diameter 4.2 mm and for the solenoid with 5.5 turns and the same length and diameter) with incremental steps of 0.5 mm. The three profiles measured at a frequency of 500 MHz shown in Fig. 11.9 were taken for a regular and variable-pitch solenoidal coil as well as for the Z-coil.

As it becomes clear from Fig. 11.9, the solenoidal coil with a variable pitch has a higher $\mathbf{B}_1$ homogeneity than the regular solenoid [76, 89], but also a slightly decreased maximum value. The improved homogeneous plateau of the Z-coil exhibits simultaneously a slight

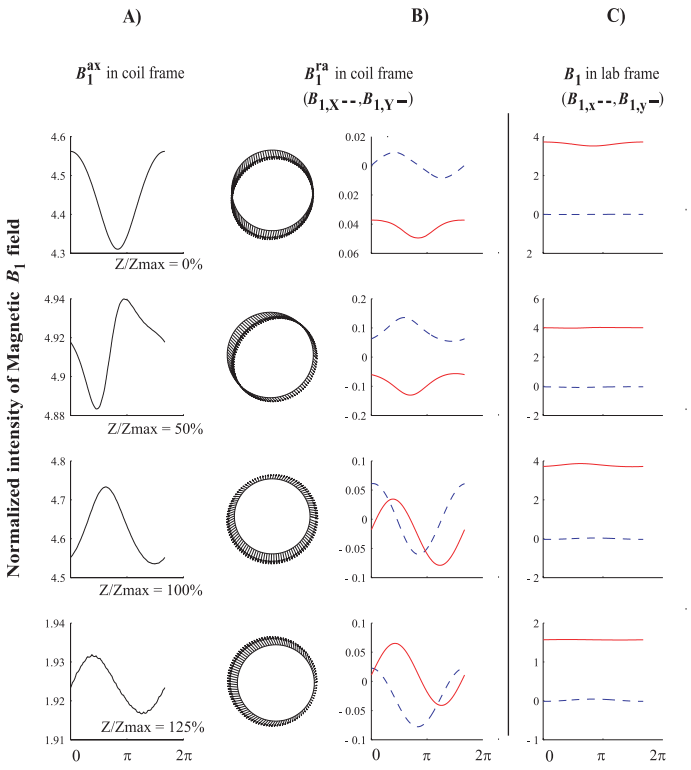

FIG. 11.8 – *Distribution of field around 1 mm of diameter circular path, similar as in Fig. 8.3. This was done to show that the modulations of the transverse plane, revealed in part 1 remain in any helicoidal structure.*

decrease of the maximum value of the ball shift in the coil center when compared to the regular solenoidal coil. The results of the profile measurement obtained for the Z-coil are in agreement with the calculated magnetic field profile shown in Fig. 11.4.

If we want to compare different coils, it is the magnetic filling factor that turns out to be relevant to relate $\mathbf{B}_1$ field magnitudes to each other at a given position inside the respective coil. In our particular case the magnetic filling factor, measured by the ball shift at the respective coil centers, is almost equal for the variable pitch and the regular coil, ζ_{bs} ∼0.0175. It is smaller for the Z-coil, where we obtained ζ_{bs} ∼0.0056, it means that from what can be measured in the coil centre, the Z-coil will have three times less magnetic filling as the solenoids.

11.5 Enhancement and sensitivity measured at 800 MHz

A prototype Z-coil was tested in a CP-MAS BL4, standard bore probehead for 800 MHz, to perform sensitivity and enhancement tests with a 4 mm Glycine sample. The question

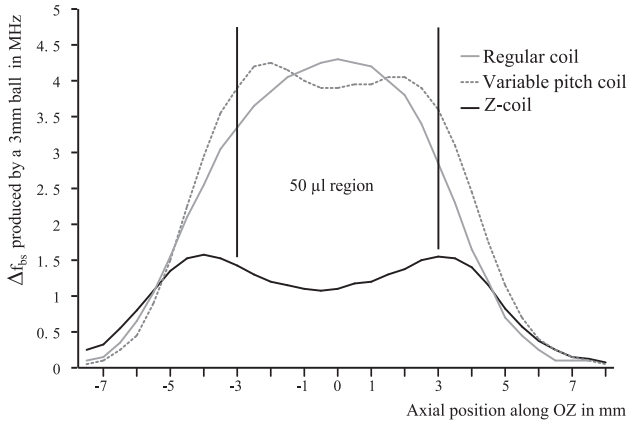

FIG. 11.9 – *RF magnetic field profile at 500 MHz for various 4 mm inner diameter coils (regular solenoid, variable-pitch solenoid, and Z-coil) obtained by ball-shift measurements. The frequency shift (Δf_{bs}) caused by the metal ball in the insert was measured by connecting an 8712ET network analyzer (Agilent technologies) to the matched probe, and recording the frequency of the wobble curve minimum. The frequency shift was taken relative to the frequency at the reflection curve minimum of an insert without ball (f_1).*

of the biological relevance of such test has been raised from various reasons : Glycine is present as a solid white powder, whose permittivity is comparable to adamantane ($\sim \epsilon = 4$).

The probe is based on a transmission line design used for for H/C/N experiments [154]. The multinuclear ability of the Z-coil is tested here for ^{13}C and ^{15}N, this test conludes with a poorer sensitivity of the Z-coil for Glycine samples compared to a regular solenoid : sensitivity figures given by Figs. 11.11 (for ^{13}C) and 11.13 (^{15}N) are 60% of the values expected for such probe with a normal coil, this reveals a quite smaller $\mathbf{B}_1$ field, at least for the low frequency chanels. On the other side enhancement figures (Fig. 11.10 for ^{13}C and Fig. 11.12 for ^{15}N) are relatively close to the theoretical values revealing a good overlaping of the frequencies involved in the cross-polarization mechanism, prooving the good spacial homogeneity of $\mathbf{B}_1$ in a Z-coil.

11.5.1 Increase of temperature in Bicelle samples

We refer to the previous chapter for the definition of NMR-thermometers. Measuring the temperature increase as a function of the applied field amplitude $\mathbf{B}_1$ allows to quantify the impact of the electric field in coils [44, 46]. Such data are shown in Fig. 11.14 for the three different coils already compared in Fig. 11.9. As can be seen from the curves in Fig. 11.14, in particular for the sample without salt (dashed lines) and 10 mM PBS salt

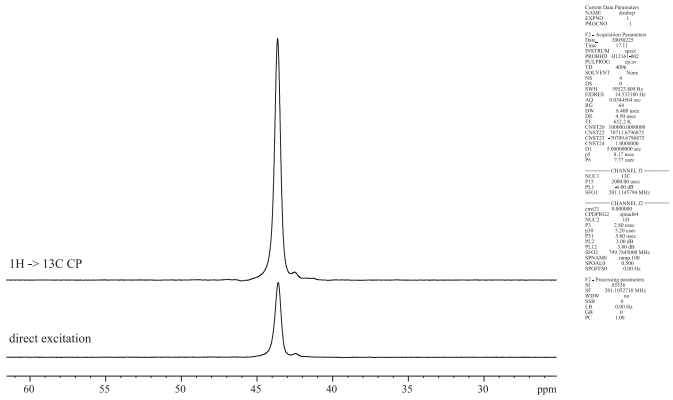

FIG. 11.10 – *CP signal enhancement measurement on the ^{13}C nucleus of a ^{15}N, ^{13}C doubly labeled glycine sample packed in a CRAMPS like 4 mm rotor (31.4 mg). The ^{13}C CP as been adjusted to a 47 kHz field during the contact pulse, during the decoupling SPINAL64 at 90 kHz was employed during 34 ms. The enhancement factor of CP as compared to direct excitation is of 3.2. Rotation speed is 11 kHz.*

(continuous line), the variable-pitch coil modification of the regular coil seems to have less $\mathbf{E}_1$ field. Semiempirically, this result is justified by the fact that a reduction of the $\mathbf{E}_1$ field in the center of the coil is possible by concentrating it where the wires are closer at both ends. On the other hand the results obtained with a salt concentration of 100mM, prove that the propagation of heat is such, that the heat generated by irradiation at the axial ends of the sample will simply diffuse to the entire volume. Therefore it can be concluded that the variable pitch coil will lead, on the long run, to results being similar to the regular solenoid. We can then suppose, that the improved axial magnetic field homogeneity, as shown in Fig. 11.9 is not a sufficient condition for an overall reduction of the $\mathbf{E}_1$ field in the coils. In other terms : Variable pitch coils are not low-E field coils.

The data in Fig. 11.14 shows that the larger the salt concentration, the higher the heating will be. This is a consequence of the fact that inductive losses, produced by the electric field are linked to the conductivity. On the other hand it is demonstrated here that the Z-coil has a lower $\mathbf{E}_1$ field than the two other coils. The temperature increase of the sample containing up to 100 mM PBS salt concentration in the Z-coil will remain comparably low to what has been measured in a regular solenoidal coil with a sample of 10 mM PBS. For the regular and the variable-pitch coil all salty samples exhibited the phase transition similar to that one shown in Fig. 10.9. This was not the case for the Z-coil at any salt concentration investigated. It was noticed that the circuit with Z-coil needed more power to generate the same $\mathbf{B}_1$ field as compared to the solenoid coils denoting a

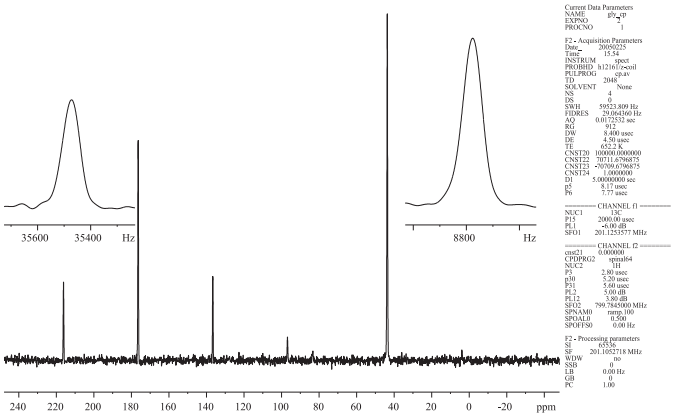

FIG. 11.11 – *Sensitivity measurement on the ^{13}C nucleus of a natural abundance glycine sample packed in a full 4 mm rotor (110 mg). The ^{13}C CP as been adjusted to a 40 kHz field during the contact pulse (2 ms), for the 1H decoupling SPINAL64 at 90 kHz was employed during 17 ms. The S/N was measured for C-α, using the function 'Sinocal' with 10 ppm noise interval, it yields at 95 :1. The rotation frequency is 8 kHz.*

poorer sensitivity. A similar observation has been made for other low-$\mathbf{E}_1$ field coils [132]. Notwithstanding of this poor maximum value, low $\mathbf{E}_1$ field capabilities of the Z-coil comes along with an improved $\mathbf{B}_1$ field homogeneity.

The data presented in Fig. 11.14 confirm in a quantitative way that the larger the salt concentration, the higher the RF heating. Furthermore it becomes evident that the Z-coil has a much lower $\mathbf{E}_1$ field than the two other coils as predicted from the computer simulation (Figs. 11.4 and 11.5). The temperature increase in the samples containing up to 100 mM PBS in the Z-coil remains comparably low when compared to a regular solenoidal coil with a sample of 10 mM PBS. For the regular and the variable-pitch coil, all salty samples exhibited the phase transition (Fig. 10.9). Thus while the replacement of the regular solenoidal coil by a variable-pitch coil is a reasonable choice for the lower salt concentrations, the Z-coil appears superior when the sample exhibits higher salt concentrations.

11.5.2 Comparison of NMR nutation fields for regular solenoids and Z-coils

Apart from the detailed electromagnetic field distribution of the coils and the quantitative evaluation of RF heating effects, it is important to measure and compare the RF efficiency of the Z-coil with that one of a solenoidal coil. For that purpose the NMR

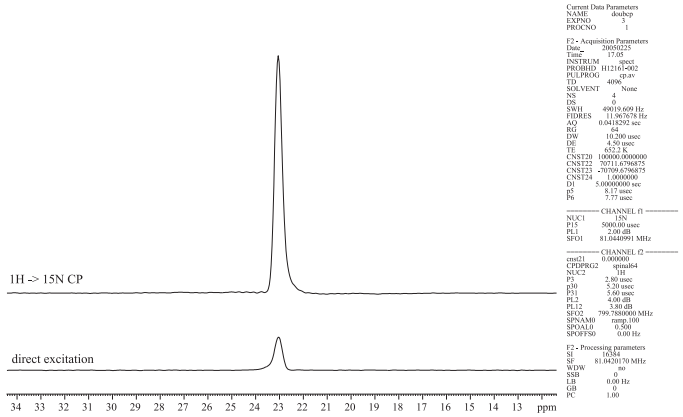

FIG. 11.12 – *CP signal enhancement measurement on the ^{15}N nucleus of a ^{15}N, ^{13}C doubly labeled glycine sample packed in a CRAMPS like 4 mm rotor (31.4 mg). The ^{15}N CP as been adjusted to a 35 kHz field during the contact pulse (5 ms), for the decoupling SPINAL64 at 90 kHz was employed during 40 ms. The enhancement factor of CP as compared to direct excitation is of 7.1. Rotation speed is 11 kHz.*

nutation field [137] was determined as a function of the RF power supplied at the input port of the ^{1}H and the ^{2}H probe channel. The data obtained from these experiments are shown in Fig. 11.15 for the bicelle sample, spinning at the magic angle at a rate of 4 kHz. The abscissa in Fig. 11.15 represents the square root of RF power, and because each curve passes through the origin and exhibits a linear behavior, only relatively few points are needed to predict the slope of each straight line. In addition to the reference bicelle sample (without salt), a sample of deuterated adamantane (same volume as the bicelle sample) spinning at a rate of 4 kHz was measured. The results from the ^{2}H probe channel are represented, in Fig. 11.15A, while the data for ^{1}H are displayed in Fig. 11.15B. The slope of each particular line defines the RF efficiency or power conversion factor η of the respective channel for the given coil with the specific sample in the coil, measured in units of nutation frequency squared per unit of power (e.g. in kHz^2/W). Focusing first on the data obtained for adamantane which represents a sample with low dielectric and no conductive losses, it becomes evident that in terms of RF efficiency (slope of straight lines in Fig. 11.15) the solenoidal coil is superior to the Z-coil for the ^{1}H as well as for the ^{2}H channel. The situation becomes different for a bicelle sample which is dielectrically lossy and conductive. The Z-coil now meets the solenoidal coil in RF performance. These findings also confirm the results reported in [61, 70, 81] : at a given power level the nutation frequency, hence the RF field amplitude, depends on the dielectric and conduction properties of the NMR sample inside the NMR coil.

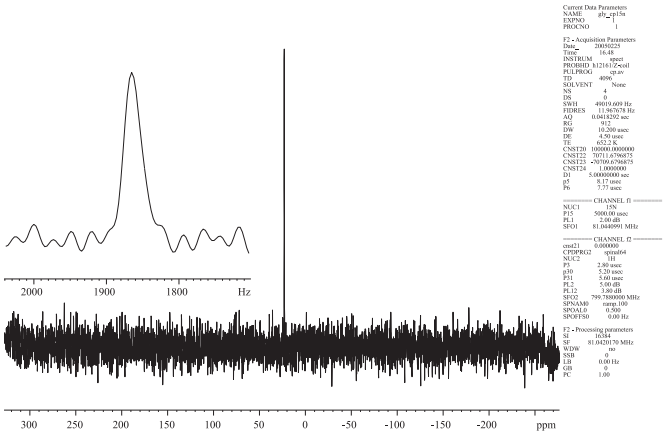

FIG. 11.13 – *Sensitivity measurement on the ^{15}N nucleus of a natural abundance glycine sample packed in a full 4 mm rotor (110mg). The ^{15}N CP as been adjusted to a 40 kHz field during the contact pulse (2 ms), for the 1H decoupling SPINAL64 at 90 kHz was employed during 40 ms. S/N measured, by the means of 'Sinocal' function, using a 10 ppm noise interval yields 18 :1. Rotation frequency is 8 kHz.*

TAB. 11.1 – *Heat deposition in samples related to the power efficiency*

Coil	η(Adamantane)	η(Bicelle)	q_{heat}
Z-coil	27.0 kHz^2/W	24.0 kHz^2/W	4.7 mW/kHz^2
Solenoid	44.9 kHz^2/W	30.2 kHz^2/W	10.0 mW/kHz^2

A quantitative analysis of the power conversion factors summarized in Table 11.1, we refer to Eq. 10.18 to calculate the heat deposition.

11.5.3 Comparison of quality factors for regular solenoids and Z-coils

Since the Z-coil has poorer magnetic field top values (Fig. 11.9), the signal to noise expected for dry samples is much less as what can be measured with a solenoid. On the other hand the heating experiments (presented in Fig. 11.14) demonstrate that the Z-coil can cope with significantly more $\mathbf{B}_1$ field than the traditional solenoid coil while keeping the electric field lower. The reason why to change to low-E field coils comes also from the fact that sensitivity is given simultaneously by the $\mathbf{B}_1$ field amplitude and the Q factor[27].

[27] both ζ and Q are derived from the same EM field distribution

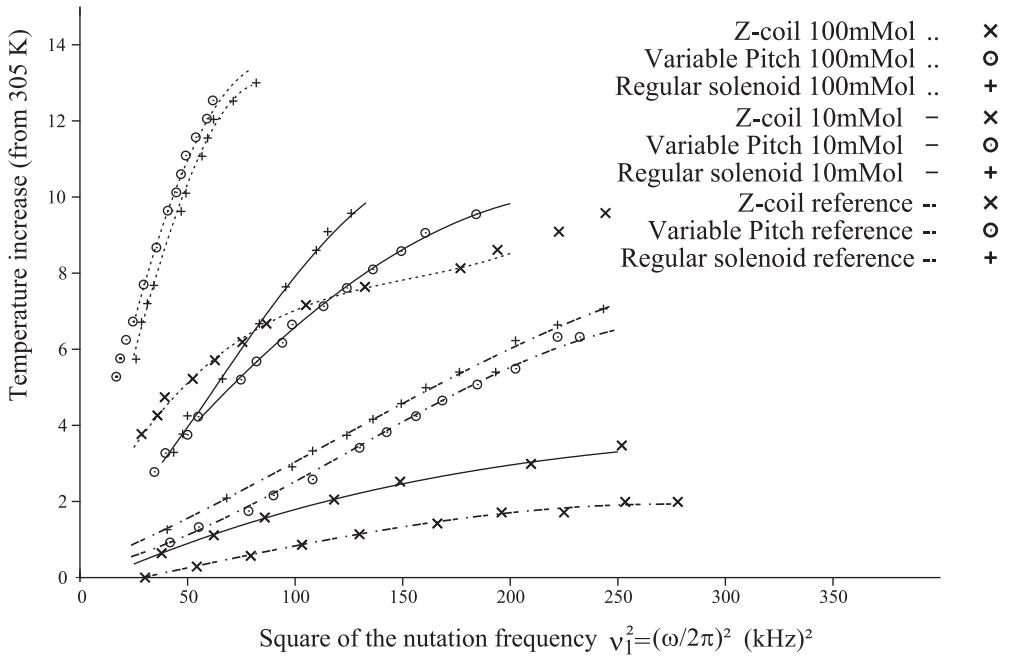

FIG. 11.14 – *Sample temperature increase induced by an increasing RF field at 500 MHz (^1H resonance frequency) as a function of the PBS concentration. The temperature increase was inferred from the ^2H quadrupolar splitting by using the same linear model for all samples.*

This last one is higher for the Z-coil than for any solenoid coil, on the same probe at the ^{1}H frequency. The large influence of the quality factor on the sensitivity has been already addressed for cryo-probes [81, 70] and was part of the discussion on reciprocity based on the work of Van der Klink [33].

The Q values used in the plot of Fig.11.16 were measured by a network analyzer (Agilent 8712ET), taking the rotors from the refrigerator to keep bicelles samples just below 10^oC. The measures of Q are given at -3dB of reflected signal amplitude. The curve of Fig.11.16 shows the strong coupling with the electric field of the regular coils. This is denoted by a rapid decrease of Q_s when increasing the salt concentration, and a strong variation between the unloaded Q_u factor and the Q_s measured with a sample. In addition the upper curve shows asymptotic behavior when the dissipation through moving charges becomes limited due to saturation of the dissipative losses in the sample. From the equation 5.25 we can extrapolate that even if the solenoid coil get three time more magnetic field than the Z-coil, it will definitivelly cease to be more sensitive, when the quality factor of the probe will drop.The low-E performance of coil can be tracked thanks

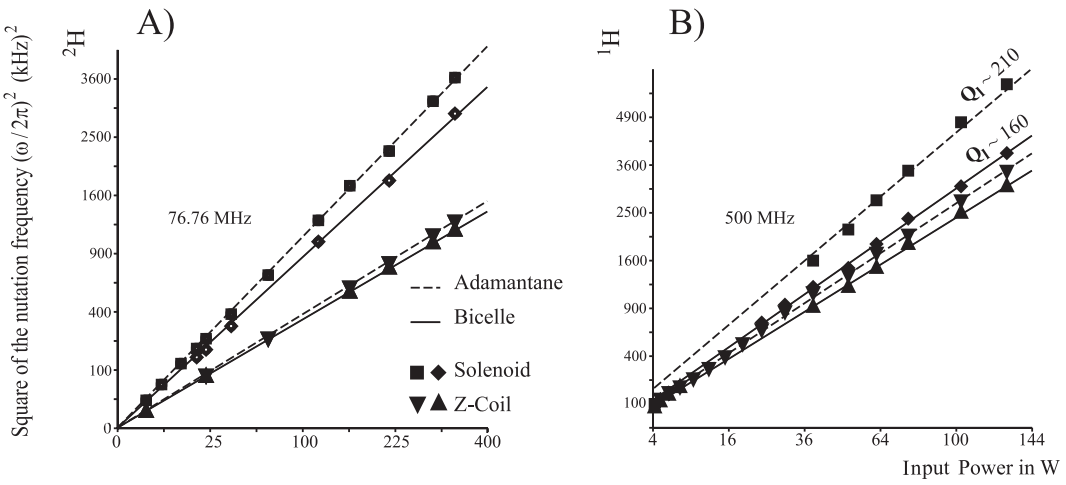

FIG. 11.15 – *Measurement of the nutation frequency squared per unit of power (A) for the ^2H channel, (B) for the ^1H channel. The nutation curves were obtained with deuterated adamantane and the reference sample of bicelles. The quality factor of the ^1H probe circuit in presence of the sample is indicated for the solenoidal coil for the adamantane (high Q value) and the bicelle sample (lower Q value). For the Z-coil the Q factor did not differ for the two samples. All data were taken under MAS at 4 kHz.*

to the heat deposition factor introduced by Gor'kov in an already mentioned paper [64]. Since Adamantane is a typical example of non-lossy sample, and Bicelles are the biological reference used also in [36], we can calculate q_{heat} for both coils used in Fig.11.15 with the reference Bicelle sample and an adamantane sample having a quality factor quite similar to the unloaded case of Fig.11.16.

$$q_{heat} = \frac{1}{\eta_{nl}} \cdot \left(\frac{Q_{nl}}{Q_{bio}} - 1 \right) \tag{11.1}$$

where η_{nl} is the power efficiency of Adamantane for each coil. In the situation described by Fig. 11.15, q_{heat} is 0.7 mW/kHz^2 for the Z-Coil, and has to be referred to 7.0 mW/kHz^2, for the case of the solenoid. From these numbers we can discuss where does it makes sense to replace the coils again to avoid loosing both the signal and the sample by electric field heating. For the PBS salt concentrated samples, the heat deposit in the sample according to 11.1 is driven by the decrease of the ^{1}H quality factor when increasing the salt concentration of the samples to 10, 50, 100 mM [28]. In the case of PBS concentrated samples the heat deposition predicted by 11.1 equals to 13.7 , 29.7 and 36.2 mW/kHz^2 in the case of a Regular coil, and 1.0 , 1.3 and 1.7 mW/kHz^2 in the case of the Z-Coil. As

[28] The corresponding static conductivities is 0.025 S/m for the reference sample and respectively, 0.31, 1.26, 2.42 S/m for the PBS concetrated samples. The conductivity of each sample was measured with a 2-pole cell CDC749 from Radiometer Analytical, also at 10^oC.

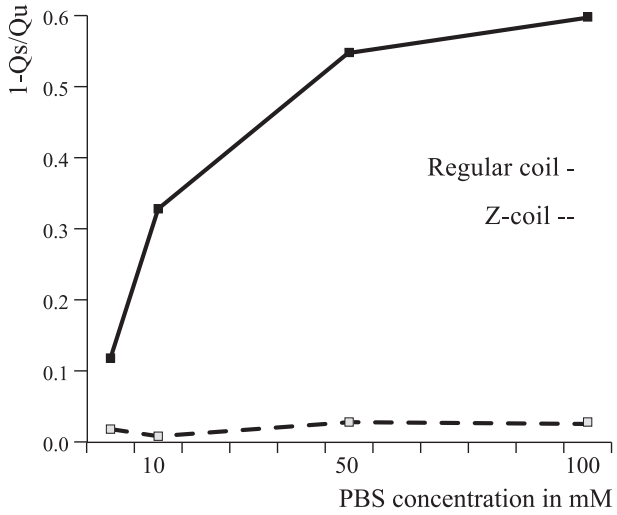

FIG. 11.16 – *Relative variation of the quality factor when loading the resonator with a conductive sample, (Q_s) compared to the empty coil, (Q_u) at 500 MHz.*

a rough estimate we can say that when the concentration is to be higher than 100 mM working with a regular coil makes no sense anymore : the power factor will be smaller than what is obtained with a Z-coil and the heat deposition is 20 times stronger.

The ratios between the quality factors of the regular coil with Bicelle and Adamantane samples ($Q_{Bic.}/Q_{Adam.}$) of the Fig.11.15B is comparable to the ratio of the two different power efficiencies $\eta_{Bic.}/\eta_{Adam.}$. The variation of this coefficient η is strongly related to the heat deposition coefficient q_{heat}.

This approach has the advantage to rely directly on the electromagnetic field energy stored in the sample volume, and it seems to us that such an approach based on measurements of quality factors has already been discussed in the past. The strong point of such method is to predict the heating before the final NMR experiment. Such measurement can be done at the network analyser testplace using a soft mW pulse to scan the frequency range under interest. Correct measurements of Q factor can be found in [79, 80].

11.6 Conclusions on Z-coil

Solenoidal coils with variable pitch or variable-wire width, and Z-coils are compatible with high impedance symmetric balanced circuits. Indeed, compared to the regular solenoid coil, the heating in the middle of the sample is already reduced for a variable pitch coil. Nevertheless, for high salt concentrations still considerable heating occurs in the sample, and both regular and the variable-pitch coil, give similar mediocre performances regarding $\mathbf{E}_1$ field. Compared to them, the Z-coil succeeds in parking the $\mathbf{E}_1$ field

between the turns of the spirals at both ends of the coil. The central loop-gap core acts as magnetic field concentrator in the center as well as a shield for the $\mathbf{E}_1$ field. It could be shown by simulation, $\mathbf{B}_1$ field profile measurements, and by NMR that the $\mathbf{B}_1$ field of a Z-coil is homogeneous and the $\mathbf{E}_1$ field is kept out of the sample volume. As part of a compromise the $\mathbf{B}_1$ field amplitudes achieved at a given probe input power level are certainly lower than the $\mathbf{B}_1$ field amplitude of a regular solenoid or variable-pitch solenoid coil. But finally thanks to its unique $\mathbf{E}_1$ field distribution, the Z-coil leads to much less severe RF heating of lossy NMR samples, keeping the sensitivity comparable to the regular coil, and thus becoming a principal alternative coil for NMR of biomembrane samples. Unfortunalty some sacrifices are also needed for multinuclear experiments. The first to consider is the boundary introduced by the poor multinuclear-capabilities of a single coil. Moreover, a low-E coil is even less efficient than the traditional coil when used in the low-frequency range. Usage of multiple coils for multiple channels is known to solve such problem. Both liquid state [29] and also some recently developped solid state probes know this technology (EFREE coil or XC coil [44]). Orthogonal alignement of two coils, is certainly not trivial from the electromagnetic point of view but also from the mechanical angle. A second boundary introduced there, then concerns the mechanics to be used in order to hold these coils together. This aspect is critical for high-resolution probes where no background signals are allowed.

[29] The so called Bruker Direct (Coil for observation of X nuclei is inside the ^1H specific coil) or Inverse probes used in HR-NMR separate the low and high frequency channels in the inside and outside saddle coils orthogonal to each other

Conclusion

Nous concluons cette thèse sur l'analyse du champ électromagnétique des structures résonantes, utilisées par les sondes de HR-MAS.

Les géométries de bobines qui sont présentées dans ce travail sont toutes produites sur le modèle d'enroulement hélicoïdal autour de l'axe de rotation, qui est aussi l'axe de propagation de l'onde (OZ). Or, une des caractéristique propre de la structure en hélice est de n'admettre aucune symétrie. La conséquence de cette particularité est que la partie transverse du champ magnétique reste entachée d'une inhomogénéité radiale induite par les conditions aux limites : un échantillon cylindrique tournant dans un solénoïde éprouve en tout point une modulation du champ magnétique qui est d'autant plus importante que celui-ci se trouve loin du centre.

Nous présentons donc des solutions analytiques et numériques aux équations de Maxwell. La cartographie du champ électromagnétique peut donc nous permettre d'avoir accès à de nouvelles géométries hélicoïdales qui minimisent l'inhomogénéité du champ $\mathbf{B}_1$ en introduisant des conditions plus favorables.

L'étude d'une telle cartographie du champ est également justifiée par l'intérêt que nous avons porté au principe de réciprocité. En effet si S_1 et S_2 sont deux éléments d'un système d'opérateurs qui interagissent entre eux au cours du temps, le flux d'énergie produit par le premier S_1 pour perturber le second S_2 aura le même profil de champ EM que celui que S_2 utilisera à son tour pour agir sur S_1, et en d'autres termes :

Le perturbateur devient perturbé dans la mesure même de sa perturbation.

Il convient donc de maîtriser la distribution du champ pour optimiser le signal que l'aimantation microscopique (S_2) peut renvoyer à la bobine de RMN (S_1). Mais la réciprocité électromagnétique est surtout liée à la capacité qu'a le système d'être invariant. En effet l'inversion de l'axe du temps n'est théoriquement possible que pour un milieu parfaitement réciproque et seulement dans ce cas.

Malheureusement la structure de la bobine contraint celle-ci à une distribution du champ EM où la composante électrique peut être effectivement couplée au milieu par le biais de la susceptibilité diélectrique. Le nombre élevé de degrés de liberté dans l'échan-

tillon va donc permettre à la polarisation d'oeuvrer au réchauffement de celui-ci. Une partie de l'énergie fournie par la bobine sera donc forcément dispersée par effet Joule. Ce phénomène physique d'agitation thermique est d'autant plus signalé qu'il est lié à l'augmentation la fréquences utilisées par la voie proton dans les aimants à haut-champs $\mathbf{B}_o$. Dans des échantillons biologiques, la dégradation du milieu par effet microondes est observée à partir de 500 MHz.

Nous avons constaté que le seul moyen de restaurer la réciprocité (pour tirer le plus grand partie de l'augmentation de sensibilité attendue d'un aimant de haut-champ $\mathbf{B}_o$), est de développer des bobines à faible champ électrique.

Nous pouvons finallement conclure cette thèse en affirmant que, pour la géométrie hélicoïdale, une amélioration de l'homogénéité $\mathbf{B}_1$ dans le plan perpendiculaire à l'axe de rotation a des effets positifs pour la diminution du champ $\mathbf{E}_1$ dans un echantillon HR-MAS.

De manière plus profonde, cette étude cherche à dégager une solution d'irradiation qui permettrait d'arriver à une séparation spatiale des modes électriques et magnétiques (qui sont naturellement mélangés dans une bobine). Or nous savons que seul un résonateur peut s'affranchir de ce problème. Mais il est clair que les bobines allant vers un comportement de type résonateur, ne peuvent pas résoudre le problème des sondes utilisées pour l'étude des protéines. En effet celles ci se doivent d'être multinucléaires (aux frequences ^{1}H/13C/^{15}N par exemple) et un résonateur ne peut être efficace que dans le voisinage de son mode de résonance.

Il convient donc de proposer une ouverture vers des systèmes de bobines croisées, où la haute fréquence est effectivement prise en charge par un résonateur, laissant ainsi les bases fréquences pour un solénoïde. Une telle séparation semble effectivement nécessaire, mais là encore elle ne peut se faire qu'en parfaite connaissance des conditions qui permettent au champ électromagnétique de s'établir effectivement dans l'échantillon.

Glossaire

Most used abreviations and symbols

Most used constants
c : Speed of light in vacuum $2.9979\,10^{8}$ m.s^{-1} p 27
h : Plank constant $6.62\,10^{-34}$ in $J.s$ p 90
$\hbar$: Dirac constant $h/2\pi$ p 90
k_B : Boltzmann constant $1.3806\,10^{-23}$ p94
μ_o : Vacuum permeability $4\pi.10^{-7} = 12.566\,10^{-7}$ in A.m^{-1} p 27
ϵ_o : Vacuum dielectric constant $1/\mu_o c^2 = 8.854\,10^{-12}$ in F.m^{-1} p 27

Variables
Ω : Volume in m^3 p 22
Σ : Surface in m^2 p 23
β : Angle between the static field $\mathbf{B}_o$ and the rotor axis $(0Z)$ p 12
ω_r : Mechanical rotation speed in rad.s^{-1} p11
ω_{rf} : Electrical pulsation frequency in rad.s^{-1} p 40
ϕ : Time phase of the fields expressed in radians p 85
ν_{rf} : RF frequency, in s^{-1} p 105
$\Delta\nu$: Off-resonance frequency refered to the static field, in s^{-1} p 105
V : Voltage in V p 24
C : Capacitance in Farads p 25
I : Current in A p 23
L : Inductance in Henry p 25
q : Charge in Coulomb p 22
q_Ω : Volumic charge C.m^{-3} p 30
q_σ : Surfacic charge C.m^{-2} p 30
$\vec{J_l}$: Linear density of Current in A.m^{-1} p 28
$\vec{J_s}$: Surface density of current in A.m^{-2} p 22
$\mathbf{j}_s$: Microscopic current density in J^{-1}.s^{-1}.V p 27
Q : Quality factor (dimensionless) p 37
ζ_{bs} : Magnetic filling factor : ratio of magnetic energies p 36
η : Power conversion factor in kHz^2.W^{-1} p 44
$\mathcal{P}^e$: Power sent to the probe channel in W p 43
$\mathcal{P}_j$: Dissipated power per unit volume in W.m^{-3} p 150
q_{heat} : Heat deposition in J in W.kHz^{-2} p 166

ρ_s : Material density in kg.m^{-3} p 146
$\vec{E}$: Electric field vector in V.m^{-1} also noted $\mathbf{E}_1$ p 22
$\vec{D}$: Electric flux density vector in A.s.m^{-2}, also called Displacement vector p 22
$\vec{H}$: Magnetic field in A.m^{-1} p 22
$\vec{B}$: Magnetic flux in V.s.m^{-2} p 22
Φ : Lenz induced magnetic flux in V.s p 131
$\vec{\mathcal{M}}$: Spin magnetization (inducing EMF in the NMR coil) in V.s.m^{-2} p 11
$\mathbf{P}$: Polarization in Debye p 149
τ^c : Dielectric relaxation time in s p153
χ_e : Electric susceptibility (dimensionless) p 27
ϵ : Material relative permitivity (dimensionless) p 67
χ_m : Magnetic susceptibility (dimensionless) p 27
μ : Material relative permeability (dimensionless) p 67
σ : Electric conductivity in S.m^{-1} p 31
φ : Space phase of the fields expressed in J p 97
ϱ : Density matrix p 92
J : Scalar coupling in Hz p 10
$\boldsymbol{\mu}$: Dipolar magnetic moment p 39
γ_r : Gyromagnetic ratio in A.s.rad.kg$^-$1 p 38
n : Number of turns in a solenoid coil p 117

Acronyms

NMR : Nuclear Magnetic Resonance,

RF : Radio-Frequency band (from 300 kHz to 1.3 GHz),

MAS : Magic Angle Spinning,

MEV : Magnetic to electric ratio, dimensionless p164

SNR : Signal to Noise ratio p6

TEM : Transverse Electric Magnetic mode, also called Lecher Wave p 26

Bibliographie

[1] A. Abragam, *The Principles of Nuclear Magnetism*, Oxford University Press, London, 1961.

[2] D. W. Alderman and D. M. Grant, *An Efficient Decoupler Coil Design which Reduces Heating in Conductive Samples in Superconducting Spectrometers*, J. Magn. Reson., 36 (1979), pp. 447–451.

[3] M. Alecci, I. Nicholson, and D. Lurie, *A novel multiple-tuned radiofrequency loop-gap resonator for use in PEDRI*, J. Magn. Reson. B, 110 (1996), pp. 82–86.

[4] E. Andrew, *Magic Angle Spinning*, in In Encyclopedia of Nuclear Magnetic Resonance, D. Grant and R. Harris, eds., vol. 5, Willey, New York, 1996, pp. 2891–2901.

[5] Y. Ayant, R. Gabillard, M. Soutif, J. Extermann, M. Buyle-Bodin, G. Bene, P. Denis, and P. Grivet, *Exemples Pratiques d'Appareillages*, in La Rèsonance Paramagnètique Nuclèaire,Moments Dipolaires et Quadripolaires, P. Grivet, ed., C.N.R.S, 1955, pp. 149–196.

[6] T. M. Barbara, *Cylindrical Demagnetization Fields and Microprobe Design in High-Resolution NMR*, J. Magn. Reson. A, 109 (1994), p. 265.

[7] ——, *Gradient Coils for Magic Angle Spinning Samples*. US patent 6, 255,824, 2001.

[8] T. M. Barbara and C. E. Bronnimann, *Target Field Design for Magic Angle Gradient Coil*, J. Magn. Reson, 140 (1999), pp. 285–288.

[9] V. J. Bartuska and G. E. Maciel, *A Magic-Angle Spinning system for bullet-type rotors in electromagnets*, J. Magn. Reson., 42 (1981), p. 312.

[10] B. Bechinger and J. Seelig, *Conformational changes of the phosphatidylcholine headgroup due to membrane dehydration. A ^{2}H-NMR study*, Chem. Phys of Lipids, 58 (1991), pp. 1–5.

[11] A. Bielecki and D. P. Burum, *Temperature Dependence of ^{207}Pb MAS Spectra of Solid Lead Nitrate. An Accurate, Sensitive Thermometer for Variable-Temperature MAS*, J. Magn. Reson., 116 (1995), p. 215.

[12] C. Böttcher and P. Bordewijk, *Theory of electric Polarization*, Elsevier, second ed., 1996.

[13] R. Bowtell and A. Peters, *Magic-Angle Gradient-Coil Design*, J. Magn. Reson. A, 115 (1995), p. 55.

[14] D. Canet, J.-C. Boubel, and E. Canet-Soulas, *La RMN Concepts, méthodes et applications*, Dunod, 2. ed. ed., 2002.

[15] M. Chaplin, *Water dielectric and microwave radiation*, LSBU, London South Bank, 2006.

[16] P. Charmont, A. Lesage, S. Steuernagel, F. Engelke, and L. Emsley, *Sample Restriction Using Magnetic Field Gradients in High-Resolution Solid-State NMR*, J. Magn. Reson., 145 (2000), pp. 334–339.

[17] V. Chevelkov, B. van Rossum, F. Castellani, K. Rehbein, A. Diehl, M. Hohwy, S. Steuernagel, F. Engelke, H. Oschkinat, and B. Reif, ^1H *detection in MAS Solid-State NMR Spectroscopy of Biomacromolecules Employing Pulsed Field Gradients for Residual Solvent Suppression*, J. Amer. Chem. Soc., 125 (2003), pp. 7788–7779.

[18] J. A. Chin, A. Chen, and M. J. Shapiro, *SPEEDY : Spin-Echo Enhanced Filtered Spectroscopy. A New Tool for High Resolution MAS NMR*, J. Comb. Chem., 2 (2000).

[19] W. Clark, *Pulsed nuclear resonance apparatus*, Rew.Scien.Instr, 35 (1964), pp. 316–333.

[20] M. Clemens and T. Weiland, *Discrete electromagnetism with the finite integration technique*, Prog. in Electromag. Research, 32 (2001), pp. 65–87.

[21] T. Cole, T. Kushida, and H. C. Heller, *Zero-Field Magnetic Resonance in Some Inorganic and Organic Radicals*, Journ. Chem. Phys., 38 (1963), pp. 2915–2924.

[22] M. S. Conradi and C. M. Edwards, *Low-noise circuitry for low-temperature NMR and SQUIDS*, Rev. Sci. Instrum., 48 (1977), pp. 1219–1220.

[23] D. Cory and J. Lewandowski, *Apparatus and method for the generation of Gradient Magnetic fields for high resolution NMR experiments.* US patent 5,872,452, 1999.

[24] D. Cory, J. Lewandowski, and W. Maas, *NMR probe for cross-polarization measurements.* US patent 5,539,315 A, 1996.

[25] D. Cory, J. W. M. van Os, and W. S. Veeman, *NMR Images of Rotating Solids*, J. Magn. Reson., 76 (1988), p. 543.

[26] D. Craig and Thirunamachandran, *Molecular Quantum Electrodynamics, an introduction to Radiation Molecule Interactions*, Dover, 1984.

[27] V. Cross, R. Hester, and J. Waugh, *Single Coil Probe with Transmission-line tunning for Nuclear Magnetic Double Resonance*, Rev. Sci. Instrum., 47 (1976), pp. 1486–1488.

[28] A. Csaki, *Un Spectrometre a Echos de Spins pour l'Etude de la Relaxation Nucléaire des Liquides*, Helv. Phys. Acta, XXXVI (1963), pp. 1021–1051.

[29] A. De Angelis, A. Nevzorov, S. Park, S. Howell, A. Mrse, and S. Opella, *High-resolution NMR spectroscopy of membrane proteins in aligned bicelles*, JACS, 126 (2004), pp. 15340–15341.

[30] T. de Swiet, M. Tomaselli, M. D. Hürlimann, and A. Pines, *In Situ-NMR Analysis of Fluids Contained in Sedimentary Rock*, J. Magn. Res., 133 (1998), p. 385.

[31] M. Decorps, P. Blonded, H. Reutenauer, and J. Albrand, *An Inductively Coupled, Series-Tuned NMR Probe*, J. Magn. Reson., 65 (1985), pp. 100–109.

[32] P. Dejon and M. Spraul, *Test Head for NMR Spectrometer*. US patent 4,851,780, 1989.

[33] J. V. der Klink, *The NMR Reciprocity theorem for Arbitrary Probe Geometry*, J. Magn. Reson, 148 (2001), pp. 147–154.

[34] H. Desvaux and P. Berthault, *Study of dynamic processes in liquids using off-resonance RF irradiation*, Prog. in NMR Spect., 35 (1999), pp. 295–340.

[35] S. Dey and R. Mittra, *A locally conformal finite difference time domain (FDTD) algorithm for modeling three-dimensional perfectly conducting objects*, IEEE Microw. and Guided Wave Letters, 7 (1997), pp. 273–275.

[36] B. Dillmann, K. Elbayed, H. Zeiger, M. Weingertner, M. Piotto, and F. Engelke, *Novel low-E field Coil to minimize Heating of Bio-Membrane samples in solid-state Multinuclear NMR Experiments*, J.Magn.Reson, in press, (2007).

[37] B. Diu, C. Guthmann, D. Lederer, and B. Roulet, *Elements de Physique Statistique*, Hermann, Paris, 1995.

[38] D. Doskocilovà, D. Duc Tao, and B. Schneider, *Effects of macroscopic spinning upon linewidth of NMR signals of liquids in magnetically inhomogeneous systems*, Czech. J. Phys., B 25 (1975), p. 202.

[39] D. Doty and C. Entzminger, G. Hauck, *Error-Tolerant RF Litz coils for NMR/MRI*, J.Magn.Reson., 140 (1999), pp. 17–31.

[40] F. Doty, *Probe design and construction*, vol. 6, Grant DM, Harris RK, Wiley : Chichester, 1996.

[41] F. Doty, G. Entzminger, and Y. Yang, *Magnetism in High-Resolution NMR Probe Design. I : General Methods*, Concepts in Magnetic Resonance, 10 (1998), pp. 133–156.

[42] ——, *Magnetism in High-Resolution NMR Probe Design. II : HR-MAS*, Concepts in Magnetic Resonance, 10 (1998), pp. 239–260.

[43] F. Doty, J. Kulkarni, G. Entzminger, S. Shevgoor, K. Shevgoor, J. Staab, and X. C., *Reducing decoupler heating by an order of magnitude in triple-resonance MAS NMR probes at 750 MHz.* Poster 45 ENC Asilomar, 2004.

[44] F. Doty, J. Kulkarni, C. Turner, G. Entzminger, and A. Bielecki, *Using a cross-coil to reduce RF heating by an order of magnitude in triple-resonance multinuclear MAS at high fields*, J. Magn. Reson, 182 (2006).

[45] F. D. Doty, G. Entzminger, P. Hansen, J. B. Spitzmesser, A. Boman, J. Staab, J. Yi, J. Doty, and L. Holte, *A New, Self- Cooling, Low-^1H- Background, Fast MAS Design for High Resolution ^1H NMR on Biological Macromolecule*, in 43rd ENC, Asilomar, 2002.

[46] S. Dvinskikh, V. Castro, and D. Sandström, *Heating caused by radiofrequency irradiation and sample rotation in ^{13}C magic angle spinning NMR studies of lipid membranes*, Magn. Reson. Chem., 42 (2004), pp. 875–881.

[47] K. Elbayed, M. Bourdonneau, J. Furrer, T. Richert, J. Raya, J. Hirschinger, and M. Piotto, *Study of the origin of the residual NMR linewidth of a peptide bound to a resin at the magic angle*, J. Magn. Reson., 136 (1999), pp. 127–129.

[48] K. Elbayed, B. Dillmann, J. Raya, M. Piotto, and F. Engelke, *Field modulation effects induced by sample spinning : application to high-resolution magic angle spinning* , J. Magn. Reson., 174 (2005), pp. 2–26.

[49] F. Engelke, *Electromagnetic Wave Compression and Radio Frequency Homogeneity in NMR Solenoidal Coils : Computational Approach*, Concepts Magn. Reson. part B., 15 (2002), pp. 129–155.

[50] F. Engelke and W. E. Mass, *High Resolution Magic Angle Spinning Spectroscopy*, Bruker Instruments, Inc., 1997.

[51] T. Farrar, *Density matrices in NMR spectroscopy*, Concepts in NMR, 2 (1990), pp. 1–12.

[52] C. Faure, L. Bonakdar, and E. Dufourc, *Determination of DMPC hydration in the L_α and $L_{\beta'}$ phases by ^2H solid state NMR of D_2O*, FEBS Letters, 405 (1997), pp. 263–266.

[53] I. Fischbach, K. Thieme, A. Hoffmann, M. Hehn, and I. Schnell, *PFG assisted selection and suppression of ^1H NMR signals in the solid state under fast MAS*, J. Magn. Reson., 165 (2003), pp. 102–115.

[54] G. Floquet, *Equations Différentielles Linéaires*, Ann. Ecole Norm., 2 (1883), pp. 47–88.

[55] H. Förster, *NMR-Spektroskopie in der biochemischen Forschung*, Bruker-Report, (1979).

[56] K. Foster, A. Lozano-Nieto, P. Riu, and T. Ely, *Heating of tissues by microwaves : A model analysis*, Bioelectromagnetics, 19 (1998), pp. 420–428.

[57] M. Franzoni and P. Levstein, *Manifestations of the absence of spin diffusion in multipulse NMR experiments on diluted dipolar solids*, Phys. Rev. B, 72 (2005), p. 235410.

[58] T. Fritzhanns, S. Hafner, D. E. Demco, H. W. Spiess, and F. H. Laukien, *Pulsed Field Gradient Selection in Two-Dimensional Magic Angle Spinning NMR of Dipolar Solids*, J. Magn. Reson., 134 (1998), pp. 355–359.

[59] C. Fry, J. Iwamiya, T. Apple, and B. Gerstein, *Doubly Wound Coils for Solid-State Double-Resonance and Multiple- Pulse NMR*, J. Magn. Reson., 63 (1985), pp. 214–216.

[60] C. A. Fyfe, J. Skibstedt, H. Grondey, and H. Meyer zu Altenschildesche, *Pulsed Field Gradient Multiple Quantum MAS NMR Spectroscopy of Half-Integer Spin Quadrupolar Nuclei*, Chem. Phys. Lett., 281 (1998), pp. 44–48.

[61] D. Gadian and F. Robinson, *Radiofrequency losses in NMR experiments on electrically conducting samples*, J.Magn.Reson, 34 (1979), pp. 449–455.

[62] A. Garroway, *Magic-angle spinning of liquids*, J.Magn.Reson, 49 (1982), pp. 168–171.

[63] M. Goldman, V. Fleury, and M. Guéron, *NMR frequency shift under sample spinning*, J. Magn. Reson. Series A, 118 (1996), pp. 11–20.

[64] P. Gor`kov, E. Chekmenev, C. Li, M. Cotten, J. Buffy, N. Traaseth, G. Veglia, and W. Brey, *Using low-E resonators to reduce RF heating in biological samples for static solid-state NMR up to 900 MHz*, J.Magn.Reson., 185 (2007), pp. 77–93.

[65] S. Grant, L. Murphy, R. Magin, and G. Friedman, *Analysis of multilayer radio frequency microcoils for nuclear magnetic resonance spectroscopy*, IEEE Trans.Magn., 37 (2001), pp. 2989–2998.

[66] M. Guenneugues, P. Berthault, and H. Desvaux, *A Method for Determining* $\mathbf{B}_1$ *Field Inhomogeneity. Are the Biases Assumed in Heteronuclear Relaxation Experiments Usually Underestimated*, J.Magn.Reson, 136 (1999), pp. 118–125.

[67] T. Gullion and J. Schaefer, *Rotational echo double resonance NMR*, J.Magn.Reson, (1989), pp. 196–200.

[68] R. Harrington, *Time-Harmonic Electromagnetic Fields*, John Wiley and Sons, New York, an ieee press classic reissue ed., 1961.

[69] S. M. Holl, R. A. McKay, T. Gullion, and J. Schaefer, *Rotational-Echo Trriple-Resonance NMR*, J. Magn. Reson., 89 (1990), pp. 620–626.

[70] T. Horiuchi, M. Takahashi, J. Kikuchi, and H. Yokoyama, S.and Maeda, *Effect of dielectric properties of solvents on the quality factor for a beyond 900 MHz cryogenic probe model*, J.Magn.Reson, 174 (2005), pp. 34–42.

[71] D. Hoult, *The principle of reciprocity in signal strength calculations- A mathematical guide*, Concepts in NMR, 24 (2000), pp. 173–187.

[72] D. Hoult and B. Bhakar, *NMR signal reception : virtual photons and coherent spontaneous emission*, Concepts in Magn. Reson., 9 (1997), pp. 277–297.

[73] D. Hoult and P. Lauterbur, *The Sensitivity of the Zeugmatographic Experiment Involving Human Samples*, J. Magn. Reson., 34 (1979), pp. 425–433.

[74] D. Hoult and R. Richard, *The Signal-to-Noise of the Nuclear Magnetic Resonance Experiment*, J. Magn. Reson., 24 (1976), pp. 71–85.

[75] R. E. Hurd, *Gradient-enhanced spectroscopy*, J. Magn. Res., 87 (1990), pp. 422–428.

[76] S. Idziak and U. Haeberlen, *Design and Construction of a High Homogeneity RF Coil for Solid-State Multiple-Pulse NMR*, J. Magn. Reson., 50 (1982), pp. 281–288.

[77] E. Insko, M. Elliott, J. Schotland, and J. Leigh, *Generalized Reciprocity*, J. Magn. Reson, 131 (1998), pp. 111–117.

[78] J. Jackson, *Classical Electrodynamics*, John Wiley and Sons, New York 1975, third ed., 1999.

[79] D. Kajfez, *Q Factor*, Vector Forum, Oxford MA, 1994.

[80] D. Kajfez and Guillon.P, *Dielectric Resonators*, Artech House, Dedham, MA, 1986.

[81] A. Kelly, H. Ou, R. Withers, and V. Dotsch, *Low-conductivity buffers for high-sensitivity NMR measurements*, Journal of the American Chemical Society, 124 (2002), pp. 12013–12019.

[82] T. Kotnik and D. Miklavčič, *Theoretical evaluation of the distributed power dissipation in biological cells exposed to electric fields*, Bioelectromagnetics, 21 (2000), pp. 385–394.

[83] A. Kubo, T. Spaniol, and T. Terao, *The Effect of Bulk Magnetic Susceptibility on Solid State NMR Spectra of Paramagnetic Compounds*, Journal of Magnetic Resonance, 133 (1998), pp. 330–340.

[84] P. Kuchel, B. Chapman, W. Bubb, P. Hansen, C. Durrant, and M. Hertzberg, *Magnetic Susceptibility : Solutions, Emulsions, and Cells*, Concepts in Magnetic Resonance, Part A, 18A (2003), pp. 56–71.

[85] E. Kůpce, P. A. Keifer, and M. Delpierre, *Adiabatic TOCSY MAS in liquids*, J. Magn. Reson., 148 (2001), pp. 115–120.

[86] N. Lancelot, K. Elbayed, A. Bianco, and M. Piotto, *Measurement of scaled residual dipolar couplings in proteins using variable-angle sample spinning*, Journal of Biomolecular NMR, 29 (2004), pp. 259–269.

[87] N. Lancelot, K. Elbayed, and M. Piotto, *Applications of variable-angle sample spinning experiments to the measurement of scaled residual dipolar couplings and ^{15}N CSA in soluble proteins*, Journal of Biomolecular NMR, 33 (2005), pp. 2–26.

[88] B. Langer, I. Schnell, H. W. Spiess, and A.-R. Grimmer, *Temperature calibration under ultrafast MAS conditions*, J. Magn. Reson., 138 (1999), p. 182.

[89] M. Leifer, *RF Solenoid with Extended Equiripple Field Profile*, J. Magn. Reson. A, 105 (1993), pp. 1–6.

[90] G. Leu, X. W. Tang, S. Peled, W. Maas, S. Singer, D. G. Cory, and P. N. Sen, *Diffusive MASS NMR Studies of Transport in Porous Materials*, Chem. Phys. Lett., 332 (2000), pp. 344–350.

[91] M. H. Levitt and Freeman, *NMR Population Inversion Using a Composite Pulse*, J. Magn. Reson., 33 (1979), pp. 473–476.

[92] C. Li, Y. Mo, J. Hu, E. Chekmenev, C. Tian, F. Gao, R. Fu, P. Gor´kov, W. Brey, and T. Cross, *Analysis of RF heating and sample stability in aligned static solid-state NMR spectroscopy*, J.Magn.Reson, 180 (2006), pp. 51–57.

[93] G. Lippens, M. Bourdonneau, C. Dhalluin, R. Warrass, T. Richert, C. Seetharaman, C. Boutillon, and M. Piotto, *Study of Compounds Attached to Solid Supports Using High Resolution Magic Angle Spinning NMR*, Curr. Org. Chem., 3 (1999), pp. 147–169.

[94] W. E. Maas, A. Bielecki, M. Ziliox, F. H. Laukien, and D. G. Cory, *Magnetic Field Gradients in Solid State Magic Angle Spinning NMR*, J. Mag. Reson., 141 (1999), pp. 29–33.

[95] W. E. Maas, F. H. Laukien, and D. G. Cory, *Gradient, High Resolution, Magic Angle Sample Spinning NMR*, J. Am. Chem. Soc., 118 (1996), pp. 13085–13086.

[96] C. Mahony, L. K. Forbes, S. Crozier, and D. M. Doddrell, *A Novel Approach to the Calculation of RF Magnetic and Electric Field for NMR Coils of Arbitrary Geometry*, J. Magn. Reson. Series B, 107 (1995), pp. 145–151.

[97] L. Maier and J. Slater, *Field strength measurement in resonant cavities*, Journ. Appl. Phys., 23 (1952), pp. 68–77.

[98] I. Marcotte and M. Auger, *Bicelles as model membranes for solid and solution-state NMR studies of membrane peptides and proteins*, Concepts in Magn. Reson A, 24A(1) (2005), pp. 17–37.

[99] G. Mateescu and A. Valeriu, *2D NMR, Density Matrix and Product Operator Treatment*, Prentice Hall, Englewood Cliffs, 1993.

[100] J. Maxwell, *A Dynamical theory of the Electromagnetic Field*, Royal Society Transactions, CLV (1864), pp. 66–76.

[101] R. A. McKay, *Double Tuned Single Coil Probe for Nuclear Magnetic Resonance Spectrometer*. US Patent 4,446,431, 1981.

[102] D. McQuarrie, *Statistical Mechanics*, University Science Books, Susalito, California, 2000.

[103] S. Meiboom and D. Gill, *Modified Spin-Echo Method for Measuring Nuclear Relaxation Times*, Rev. Sci. Instrum., 29 (1958), pp. 688–691.

[104] K. Minard and R. Wind, *Solenoidal Microcoil Design - Part I : Optimizing RF Homogeneity and Coil Dimensions*, Concepts in Magnetic Resonance, 13 (2001), pp. 128–142.

[105] ——, *Solenoidal Microcoil Design - Part II : Optimizing Winding Parameters for Maximum Signal-to-Noise Performance*, Concepts in Magnetic Resonance, 13 (2001), pp. 190–210.

[106] P. Murphy, *Applications of pulsed nuclear magnetic resonance to chemistry : Multiple-Pulse NMR, cross polarization magic-angle spinning and instrumental design*, thesis, Iowa State University, 1979.

[107] P. D. Murphy and B. C. Gerstein, *The Design of a Single Coil Double Resonance NMR Probe for Combined Magic Angle Spinning Double Resonance Experiments*, technical report, US Department of Energy, 1978.

[108] J. Murphy-Boesch, *An in Vivo NMR Probe Circuit for Improved Sensitivity*, J. Magn. Reson., 54 (1983), pp. 526–532.

[109] E. Paulson, R. Martin, and K. Zilm, *Cross polarization, radio frequency field homogeneity, and circuit balancing in high field solid state NMR probes*, J.Magn.Reson, 171 (2004), pp. 314–323.

[110] W. Piasecki and W. Froncisz, *Field distributions in loop-gap resonators*, Meas.Sci.Technol, 4 (1993), pp. 1363–1369.

[111] M. Piotto, M. Bourdonneau, J. Furrer, A. Bianco, J. Raya, and K. Elbayed, *Destruction of Magnetization during TOCSY Experiments Performed under*

Magic Angle Spinning : Effect of Radial $\mathbf{B}_1$ *Inhomogeneities*, J. Magn. Reson., 149 (2001), pp. 114–118.

[112] M. Piotto, K. Elbayed, J.-M. Wieruszeski, and G. Lippens, *Practical aspects of shimming a high resolution magic angle spinning probe*, J.Magn.Reson, 173 (2005), pp. 84–89.

[113] M. Piotto, V. Saudek, and V. Sklenar, *Gradient tailored excitation for single-quantum NMR spectroscopy of* H_2O *solutions*, J. Biomol. NMR, 2 (1992), p. 661.

[114] W. S. Price, *Gradient NMR*, Ann. Rep. NMR, (1995).

[115] A. Privalov, S. Dvinskikh, and H. Vieth, *Coil Design for Large-Volume High-B1 Homogeneity for Solid-State NMR Applications*, J. Magn. Reson. A, 123 (1996), pp. 157–160.

[116] G. Raffard, S. Steinbruckner, A. Arnold, J. Davis, and E. Dufourc, *Temperature-composition diagram of Dimyristoylphosphatidylcholine-dicaproyl-phosphatidyl-choline 'Bicelles' self-Orienting in the magnetic field. A solid-state* ^2H *and* ^{31}P *study.*, vol. 16, Langmuir, 2000.

[117] R. Rhea, *Filters and an oscillator using a new Solenoid Model*, Appl.Micro.& Wireless, (2000), pp. 30–42.

[118] V. H. Rumsey, *Reaction Concept in Electromagnetic Theory*, Phys. Rev., 94 (1954), pp. 1483–1491.

[119] G. Schauss, B. Blümich, and H. W. Spiess, *Conditions for Generating Rotating Gradients in MAS NMR Imaging*, J. Magn. Reson., 95 (1991), p. 437.

[120] P. N. Sen, Y. Liu, G. Leu, and D. G. Cory, *Detection of motion through susceptibility fields in two-dimendional exchange diffusivee-MASS experiments*, Chem. Phys. Lett., 366 (2002), pp. 588–594.

[121] S. Sensiper, *Electromagnetic wave propagation on helical structures (a review and survey of recent progress)*, Proc. Inst. Radio Eng., 43 (1955), pp. 149–161.

[122] A. J. Shaka, C. J. Lee, and A. Pines, *Iterative Schemes for Bilinear Operators ; Application to Spin Decoupling*, J. Magn. Reson., 77 (1988), p. 274.

[123] L. Shizhe, Q. Yang, and M. Smith, *RF coil optimization : evaluation of B1 field homogeneity using field histograms and Finite Element calculations*, Mag. Reson. Imag., 12 (1994), pp. 1079–1087.

[124] A. Sihvola, *Electromagnetic mixing formulas and applications*, IEE Electromagnetic waves series 47, Padstow, 1999.

[125] W. Sikorski, A. Sanders, and H. Reich, *Tris(trimethylsilyl)methane as an internal* ^{13}C *NMR chemical shift thermometer*, Magn.Reson.Chem., 36 (1998), pp. S118–S124.

[126] M. Simeonova and J. Gimsa, *The influence of the molecular structure of lipid membranes on the electric field distribution and energy absorption*, Bioelectromagnetics, 27 (2006), pp. 652–666.

[127] C. Slichter, *Principles of Magnetic Resonance*, Springer-Verlag, Heidelberg, third ed., 1989.

[128] A. Sodickson and D. G. Cory, *Shimming a High-Resolution MAS Probe*, J. Mag. Res., 128 (1997), pp. 87–91.

[129] L. Stark, *Lower modes of a concentric line having a helical inner conductor*, Journal of Applied Physics, 25 (1954), pp. 1155–1162.

[130] E. O. Stejskal and J. D. Memory, *High Resolution NMR in the Solid State*, Oxford University Press, New York, 1994.

[131] M. E. Stoll, A. J. Vega, and R. W. Vaughan, *Simple Single-coil Double Resonance NMR Probe for Solid State Studies*, Rev. Sci. Instrum., 47 (1977), pp. 800–803.

[132] J. Stringer, C. Bronnimann, C. Mullen, D. Zhou, S. Stellfox, Y. Li, E. Williams, and C. Rienstra, *Reduction of RF-induced sample heating with a scroll coil resonator structure for solid-state NMR probes*, J. Magn. Reson, 173 (2005), pp. 40–48.

[133] Y. Sun and G. Maciel, *The Tilted Coil for NMR Experiments*, J. Magn. Reson. A, 105 (1993), pp. 145–150.

[134] D. Swanson and W. Hoefer, *Microwave circuit modeling using electromagnetic field simulation*, Artech House Microwave Library, Boston London, 2003.

[135] P. Tekely and M. Goldman, *Radial-field sidebands in MAS*, J. Magn. Reson., 148 (2000), pp. 135–141.

[136] F. E. Terman, *Radio engineers' handbook*, McGraw-Hill, 1. ed., nachdr. ed., 1943.

[137] H. Torrey, *Transient nutations in nuclear magnetic resonance*, J. Appl. Phys., 23(1) (1952), pp. 68–77.

[138] R. Turner, *A Tagret Field Approach to Optimal Coil Design*, Journal of Physics D, 19 (1986), p. L147.

[139] A. Van Geet, *Calibration of the methanol and glycol nuclear magnetic resonance thermometers with a static thermistor probe*, Anal.Chem., 40 (1968), p. 2227.

[140] P. Van Zijl and C. Moonen, *Complete Water Suppression for Solutions of large Molecules based on Diffusional differences between Solute and Solvent (DRY-CLEAN)*, J. Magn. Res., 87 (1990), p. 18.

[141] D. Vanderhart, *Magnetic Susceptibility and High Resolution NMR of Liquids and solids*, in In Encyclopedia of Nuclear Magnetic Resonance, D. Grant and R. Harris, eds., vol. 5, Willey, New York, 1996, pp. 2938–2946.

[142] D. Vanderhart, W. Earl, and A. Garroway, *Resolution in ^{13}C NMR of Organic Solids Using High-Power Proton Decoupling and Magic-Angle Sample Spinning*, Journal of Magnetic Resonance, 44 (1981), pp. 361–401.

[143] M. Vera and J. B. Grutzner, *The Taylor vortex : The Measurement of Viscosity in NMR Samples*, J. Am. Chem. Soc., 108 (1986), pp. 1304–1306.

[144] P. Vizmuller, *Filters with helical and folded helical resonators*, Artech House, Inc, Norwood, MA, 1987.

[145] A. Webb, *Radiofrequency microcoil in magnetic resonance*, Progress in nuclear magnetic resonance spectroscopy, 31 (1997), pp. 1–42.

[146] T. Weiland, *A Discretization method for the solution of Maxwell equations for Six-Component Fields*, AEÜ, 31 (1977), pp. 116–120.

[147] J.-M. Wieruszeski, G. Montagne, G. Chessari, P. Rousselot-Pailley, and G. Lippens, *Rotor Synchronization of Radiofrequency and Gradient Pulses in High-Resolution Magic Angle Spinning NMR*, J. Magn. Res., 152 (2001), pp. 95–102.

[148] R. A. Wind and C. S. Yannoni, *Spin Imaging in Solids using Synchronously Rotating Field Gradients and Samples.* US Patent 4, 301,410, 1981.

[149] K. Yee, *Numerical solution of initial boundary value problems involving Maxwell's equation in isotropic media*, IEEE Trans. on Antennas and Prop., AP-14 (1966), pp. 302–307.

[150] F. Zäheringer, *Behavior of ^1H NMR nutation signals : computer simulation and experimental investigation.* Internship report, University of Konstanz, 2005.

[151] G. Zandomeneghi, *Variable-Angle Spinning NMR techniques for the study of lipid bilayers and bilayer associated peptides*, thesis, ETH Zürich, 2003.

[152] H. Zeiger and B. Dillmann, *A Radio Frequency Coil Arrangement for Magnetic Resonnance Measurements and a Probe Head for Measuring Resonance Signals by utilizing such a Radio Frequency Coil Arrangement.* GB patent 2,426,345 A, 2006.

[153] ——, *Hochfrequenz-Spulenanordnung für Messungen mit magnetischer Resonanz und Probenkopf zur Aufname von Resonanzsignalen unter Verwendung einer derartigen Hochfrequenz-Spulenanor.* DE 10 2005 024 773 B3, 2006.

[154] ——, *Test head for NMR spectrometer.* US patent 7,106,061 B2, 2006.

[155] F. Zelaya, S. Crozier, S. Dodd, R. McKenna, and D. Doddrell, *Measurement and Compensation of Field Inhomogeneities Caused by differences in Magnetic Susceptibility*, J. Magn. Reson A, 115 (1995), pp. 131–135.

[156] W. Zhang and D. G. Cory, *First Direct Measurement of the Spin Diffusion Rate in a Homogenous Solid*, Phys. Rev. Lett., 80 (1998), pp. 1324–1327.

Résumé

Une expérience de RMN du solide dans un échantillon d'origine biologique, où la haute résolution est nécessaire, requiert un traitement spécifique permis par la technologie des sondes HR-MAS. Un tel instrument met en oeuvre une bobine et un rotor dans lequel se trouve l'échantillon. Après une description de ces deux composants essentiels nous verrons comment la rotation de l'un par rapport à l'autre présente un intérêt évident pour la résolution des spectres, mais fait aussi apparaître des artéfacts qu'il est nécessaire d'expliquer. Une approche géométrique ne suffisant pas pour comprendre les interactions de la vitesse de rotation sur la distribution des fréquences de nutation, nous allons consacrer la deuxième partie de ce travail à une étude de certains concepts de l'électrodynamique classique, appliqués aux sondes utilisées. Ainsi seront abordés : les conditions aux limites, la cartographie du champ par perturbation de l'énergie électromagnétique, les méthodes de résolution numérique des équations de Maxwell. Enfin un chapitre sera consacré au principe de réciprocité, indispensable pour comprendre l'acquisition du signal RMN, et un autre traitera du problème de propagation d'onde (equation de Helmholtz), avec un regard attentif pour le cas du solénoïde (utilisé actuellement dans les sondes de HR-MAS). Dans une troisième partie, ces concepts théoriques permettront de comprendre l'interférence entre la rotation et la distribution de champ $\mathbf{B}_1$. La description d'un tel phénomène requiert en effet une résolution de l'équation maîtresse de l'évolution de l'opérateur densité (Equation de Liouville-von Neumann). La répartition spatiale du champ électromagnétique calculée par des méthodes analytiques et numériques, intervient dans expression de l'hamiltonien qui domine l'équation de Liouville. D'autre part l'inhomogénéité radiale de la distribution de champ magnétique est mise en évidence dans différentes expériences de RMN. A la fin de la troisième partie, l'inhomogénéité radiale de $\mathbf{B}_1$ est charactérisée, aussi bien par de simples expériences de nutation, que dans celles d'écho, où de spin-locking (MLEV-DIPSI). Cette thèse s'appuie sur le fait que la recherche de l'homogénéité dans la distribution du champ magnétique, permet simultanément de réduire l'amplitude du champ électrique au centre du rotor (Equation de Maxwell-Ampère). Les effets du champ électrique sont bien connus dans le domaine des microondes. Comme cela est démontré dans la quatrième partie, les ondes radio utilisées par la RMN, peuvent aussi provoquer l'échauffement d'un échantillon. Dès lors qu'un tel rechauffement peut être directement associé à la distribution de champ RF, il est bien évident qu'une série de bobines innovantes à faible champ électrique doivent être développées. Notre approche a permis de concevoir une nouvelle lignée de bobines à faible champ électrique qui (i) maîtrisent l'inhomogéneité radiale de $\mathbf{B}_1$, et (ii) reduisent l'effet joule. Ces bobines sont donc mieux adaptées à l'étude d'échantillons d'intéret biologique tels que ceux prélevés sur des biopsies.

Mots-clés: Inhomogénéité $\mathbf{B}_1$, Matrice densité, faible champ $\mathbf{E}_1$, Bobines, HR-MAS

Kurzfassung

Es ist dank HR-MAS-Probenköpfen möglich, ein hochaufgelöstes NMR-Experiment für eine Festkörperprobe von biologischem Interesse aufzusetzen. Die wichtigsten Bauteile dieser Instrumente sind die Spulen und die Rotoren, die die Probe enthalten. Bei der so genannten Rotation unter dem magischen Winkel (Magic Angle Spinning, MAS) wird die Probe um die Spulenachse gedreht. Wir erklären den Vorteil dieser Methode und stellen die Hypothese auf, dass die Rotationsgeschwindigkeit den Effekt von NMR- Radiofrequenzimpulse (RF-Impulse) beeinflusst. Ein geometrischer Ansatz reicht nicht aus, um den komplexen Zusammenhang von mechanischer Rotation und Quantenübergängen zu verstehen, deshalb besteht der zweite Teil dieser Arbeit daraus, bestimmte Elementde der klassischen Elektrodynamik, angewandt auf Probenkopftechnik, einzuführen.

Es werden Konzepte der Abbildung elektromagnetischer Felder dargestellt, die sich ergeben (i) aus Simulationen auf der Grundlage der Maxwellschen Gleichungen oder (ii) aus Experimenten durch Störungsrechnung und die Reziprozität in der Messung von NMR-Signalen. Ein Kapitel beschäftigt sich mit der Wellenausbreitung in zylindrischen Strukturen, wobei die Trennung in axiale und radiale Komponenten eingeführt wird.

Der dritte Teil zeigt, wie diese grundlegenden Konzepte benutzt werden können, um die Interferenz zwischen mechanischer Bewegung und Evolution der Magnetisierung unter einer bestimmten RF-Feld-Verteilung. Zur Beschreibung dieser Phänomene ist die Herleitung der Master-Equation für die Evolution der Dichtematrix (Lioville-von-Neumann-Gleichung) erforderlich. Die berechnete Feldverteilung, die den RF- Hamilton-Operator bestimmt, ist von unschätzbarem Wert für die Voraussage der Evolution der Kernmagnetisierung. Auf der anderen Seite werden experimentelle Nachweise für die Radialkomponente des RF-Feldes dargestellt und anhand von NMR-Impulssequenzen, wie z. B. einfachen Nutationsexperimeten, erläutert. SchlieSSlich zeigt sich, dass bei komplexen Spin-Lock-Methoden (MLEV-DIPSI) dieses scheinbar theoretische Problem auch bei häufig angewandten NMR- Experimenten für biochemische Anwendungen von Bedeutung ist.

Ein anderer Aspekt der HR-MAS von biologischen Proben ist die Anforderung, die Erwärmung durch RF-Dissipation so klein wie möglich zu halten. Diese Arbeit vertritt die These, dass es möglich ist, eine Spule zu entwickeln, die das E-Feld minimiert und gleichzeitig eine verbesserte B1-Homogenität aufweist. RF- Aufheizung wird mit Hilfe der Maxwell-Ampere-Gleichung beschrieben. Diese behandelt die Wechselwirkung der dielektrischen Verluste in der Probemit der Verteilung des elektrischen Feldes, die durch den RF-Impuls erzeugt wird. Da sich diese Arbeit hauptsächlich mit der Entwicklung von Hochfeldprobenköpfen befasst, ist es nötig, neuartige Spulen mit niedrigem E-Feld einzuführen, um eine Veränderung der untersuchten Proben bei hohen Frequenzen zu vermeiden.

Diese Spule ist sicherlich besser für die biomedizinische Anwendungen geeignet, insbesondere für das Studium von Biopsie-Proben.

Stichtwörter: $\mathbf{B}_1$ inhomogeneität, Statstischer Operator (Dichteoperator), niedere $\mathbf{E}_1$, Spulen, HR-MAS

Abstract

It is possible, thanks to HR-MAS probeheads, to set up a high resolution NMR experiment for a solid sample of biological interest. The most valuable components of these instruments are the coils and the rotors, containing the sample. Magic angle spinning (MAS) consists in rotating the sample around the coils principal axis. We will explain the advantage of this technique and hypothesize why does the rotation speed influences the effects of NMR radio frequency (RF) pulses. A geometrical approach is not sufficient to understand the intricate relationship between mechanical rotation and quantum transitions, and that's why the second part of our work will be devoted to introducing certain features from classical electrodynamics, applied to probehead engineering.

Concepts involved in the electromagnetic (EM) field mapping, obtained from (i) simulations based on Maxwell's equations or, from (ii) experiments via the perturbation methods and the reciprocity in NMR signal measurements, will be presented. A chapter will be dedicated to wave propagation in cylindrical structures, to introduce the separation of axial and radial components of the field.

The third part will show how those fundamental concepts can be deployed to understand the interference between a mechanical rotation movement and the evolution of magnetization under a certain RF field distribution. Describing this phenomenon requires deriving the master equation for the density matrix evolution (Liouville-von Neumann equation). The calculated field distribution, governing the RF Hamiltonian, is then of invaluable help in predicting the evolution of the nuclear magnetization. On the other hand experimental evidence of the RF field radial component, is shown and explained through NMR pulse sequences such as simple nutation experiments. Finally complex spin locking schemes (MLEV-DIPSI) are bringing this type of apparently theoretical problem into the most popular NMR experiments for Biochemists.

Another aspect of HR-MAS in sample of biological interest is the requirement of minimum RF heat deposition. This work defends the thesis of a possible improvement of the low-$\mathbf{E}_1$ field capabilities of a coil together with the improved magnetic field $\mathbf{B}_1$ homogeneity. RF heating will be approached through the Maxwell-Ampere equation in the fourth part. This will treat the interaction of the sample's dielectric dispersion with the EM field distribution produced during the RF pulses. Since this study is oriented toward high-field probe developments, it is necessary to introduce novel low-$\mathbf{E}_1$ coil to prevent sample degradation at high frequencies. Our philosophy has made it possible to invent a type of coil, which manages simultaneously to (i) reduce the radial field inhomogeneity, and (ii) minimize the Joule heating in the sample region.

These coils are certainly better suited for biomedical applications, in particular the study of samples such as biopsies.

Keywords: $\mathbf{B}_1$ inhomogeneity, Density matrix, low-$\mathbf{E}_1$ field, coils, HR-MAS